POLYMER INFILTRATED NANOPOROUS GOLD: KINETICS AND OPTICAL PROPERTIES OF NOVEL POLYMER NANOCOMPOSITES

Weiwei Kong

A DISSERTATION

in

MATERIALS SCIENCE AND ENGINEERING

Presented to the Faculties of the University of Pennsylvania

in

Partial Fulfillment of the Requirements for the

Degree of Doctor of Philosophy

2024

Supervisor of Dissertation

Russell J. Composto, Professor, Materials Science and Engineering, University of Pennsylvania

Graduate Group Chairperson

Ling Li, Associate Professor, Materials Science and Engineering

Dissertation Committee

Eric Detsi, Associate Professor, Materials Science and Engineering

Zahra Fakhraai, Professor, Chemistry

Daeyeon Lee, Russell Pearce and Elizabeth Crimian Heuer Professor, Chemical and Biomolecular Engineering

Robert A. Riggleman, Professor, Chemical and Biomolecular Engineering

Dedicated to my mom, dad, partner, cats, and friends.

ACKNOWLEDGEMENT

I would like to first thank the funding agencies that supported this thesis. This work was supported by the National Science Foundation's (NSF) Division of Materials Research under grant DMR-1905912 and DMR-2407300. Additionally, this thesis was also supported by the donors of ACS Petroleum Research Fund under ACS/PRF 62482-ND7. I also acknowledge the support from the Vagelos Institute for Energy Science and Technology (VIEST) through the 2023-24 VIEST Graduate Fellowship. This work was performed at the Laboratory for Research on the Structure of Matter (LRSM) at the University of Pennsylvania and supported by the National Science Foundation Partnerships for International Research and Education Program (NSF-PIRE), Grant #1545884. I would also like to acknowledge use of the Dual Source and Environmental X-ray Scattering facility operated by the Laboratory for Research on the Structure of Matter at the University of Pennsylvania (NSF MRSEC DMR-1720530). The equipment purchase was made possible by an NSF MRI grant (17-25969), an ARO DURIP grant (W911NF17-1-0282), and the University of Pennsylvania. Additionally, this work was carried out in part at the Singh Center for Nanotechnology, which is supported by the NSF National Nanotechnology Coordinated Infrastructure Program under grant NNCI-2025608. Lastly, I would like to gratefully acknowledge the use of facilities and instrumentation supported by the Materials Science and Engineering Departmental Laboratory at the University of Pennsylvania.

Next, I would like to thank those people who assisted me on my academic path from day 1 of PhD to completing this thesis. First, I would like to thank my PI, Prof. Russell J. Composto, for providing a lot of academic support and guidance throughout. PhD is not at all an easy journey, and I am grateful to have Russ as my advisor. I really appreciate that Russ provided me

with an incredible amount of freedom during those five years. Whenever I have a research-related idea popping up, Russ always supports it and encourages me to try it out. I am grateful for how Russ' encouragement transformed me into an independent thinking scientist. I also appreciate that Russ encouraged me to attend the APS conferences since my PhD year 2. The attendance at APS academically broadens my horizon and allows me to "think outside of the box". I am also thankful that Russ provided me with a lot of mentoring opportunities, two undergrads and one master student, that allowed me to enhance my leadership skills and big-picture project organization skills. Thank you!

Then, I would like to appreciate those professors that provided me with a lot of help and guidance in academics and in life. First, I would like to thank my committee members, Prof. Daeyeon Lee, Prof. Robert A. Riggleman, Prof. Zahra Fakhraai, and Prof. Eric Detsi. Prof. Lee has provided me with a lot of guidance on analyzing the data. I am grateful that Prof. Lee allowed me to use tons of his group's equipment (dynamic water contact angle, ellipsometry, QCM-D for my undergrad) while providing a lot of academic insights into my studies. Thank you for being so generous! Prof. Riggleman provided a lot of distinct helpful feedback on my research. I am lucky to have two publications in collaboration with Prof. Lee and Prof. Riggleman. Prof. Fakhraai provided me with a lot of guidance on ellipsometry modeling in my first year, when I had no clue what an ellipsometer is, and provided me with a lot of useful suggestions on my thesis via each year's update. I would like to thank Prof. Detsi for teaching me to dealloy 12k Au-Ag alloy, which is the essential membrane used for this entire thesis. Additionally, Prof. Detsi provided me with a lot of useful suggestions for my work. Besides my committee members, I would like to thank a couple of other professors – Prof. Karen I. Winey

and Prof. Eric Stach. Prof. Winey provided a lot of guidance on the SAXS analysis, and she is so nice to be that I am so grateful for. I would like to thank Prof. Stach for being on my committee for 3 years. I still remember the helpful suggestions and encouragements he provides in my proposal and updates. I wanted to quit the PhD program in my first semester, but Prof. Stach encouraged me during his office hours, which made me decide to stay. Thank you all for your help, guidance, nicety, encouragement and trust.

Next, I would like to thank all my collaborating students and my mentees that made this thesis possible. First, I would like to acknowledge Anastasia Neuman. Anna is such a wonderful computational scientist. I feel very honored to have her on two of my projects. She is incredibly talented, smart, and nice! Anna made my thesis much more complete and more convincing. I would also like to thank Mengjie Fan, who collaborated with me on the optical study. She was so generous to run XPS for us and help with data analysis. Additionally, I would like to thank my mentees, Sahana Sunder, Isa (Chuyi) Pan, and Rongyue Lin. Thank you all for working with me for 1-3 years! Thank you for all your hard work which transformed into part of my thesis and shaped me into a better mentor. I am very happy to see all three of you are heading to PhD programs and wish you all the best in the future.

I would like to acknowledge those colleagues who helped me through those 4.5 years. I would like to thank Dr. Shawn Maguire for the foundation work on this thesis and tons of mentoring during my first year. Additionally, I would like to thank Dr. Katie Rose, Dr. Michael Boyle, Dr. Connor Bilchad, Prof. Christopher O'Bryan, Dr. Jaehyun Kim, Dr. Yechan Kim, Dr. Hyunsu Lee, Dr. Yitian Zhou Dr. Chien Hua Tu and Dr. Jinseok Park for equipment training, research suggestions and being so kind in general. Also, I would like to thank Aria Zhang and

Katie Sun for helping me with characterization equipment at different stages. I would also like to acknowledge everyone else in Composto and Winey labs that helped maintain those two labs and sustain a sustainable and healthy research environment. I would also like to thank my friends (Dr. Tian Ren, Anirban Majumder, Kaiwen Wang and others) in Lee lab for a lot of research discussion, help in training, and help to open the lab door in off times. I also could not possibly accomplish my PhD without Dr. Kristin Field, Pat Overand, Vicky Lee, John Russell, Irene Celements, Steve Szewczyk, Dr. Jamie Ford, Prof. Paul Heiney and Dr. Matthew Brukman.

I would like to thank all my friends for their mental support in those 4.5 years. Yuran Zhu, you have been a great friend of mine since UG sophomore year. Thank you for being with me during my PhD. I miss the time when we watched ZhenHuanZhuan together again and again. Wish you the best of luck in your last couple months of PhD! Chenzhen Zhang, my good friend in middle school and one of my best friends since then. Life has magically brought us together and reunited over and over. We are meant to be great friends. Thank you for always being on my side. Hope you finish your PhD happily! Additionally, I would like to acknowledge Wenxiao Deng, Yihui Zhang, Yue Jiang, Yewei Huang, Yuhang Ye, and Jiaxin Liu. Thank you for always being so supportive and positive in those years.

Finally, I would like to thank my parents, my partner, and my maine coons. My parents have provided a lot of emotional and financial support during those five years. My partner Xiyu has provided me with unconditional support and love through those years we are together. For a lot of the time, he helps me to recover my negative emotions and drag me out of the mental traps. It is not easy to be with someone continuously having a lot of mental stress and anxiety but thank you for always being there. My cats (Polly and Styrene) also give me unconditional love and

companionship. Polly and Styrene were always my stimulus to finish my experiments quickly and efficiently in the lab. I would like to end with one of my favorite quotes:

"Per aspera ad astra"

ABSTRACT

POLYMER INFILTRATED NANOPOROUS GOLD: KINETICS AND OPTICAL PROPERTIES OF NOVEL POLYMER NANOCOMPOSITES

Weiwei Kong

Russell J. Composto

One of the biggest challenges in the field of polymer nanocomposites (PNCs) is to disperse high nanofiller loadings into the polymeric matrix. The high loading and uniform dispersion are limited by the unfavored polymer/nanofiller thermodynamics and the tendency for nanofiller to aggregate. In this thesis, these are circumvented by using nanoporous gold (NPG) as a scaffold for polymers to fill. The ultra-high loading (>50 vol%) is achieved by infiltrating polymer melts into NPG to produce a polymer infiltrated nanoporous gold (PING) composite. This novel composite provides promises for the next generation advanced materials for coating, optical sensors, actuators, and batteries. This thesis contributes to the better understanding of polymer kinetics under moderate confinement by varying the interfacial energy between polymer and pore wall and investigating the temperature dependence of infiltration. Confinement enhances polymer kinetics while decreasing the infiltration time dependence on M_w due to the combined effect of loss in entanglement and adsorbed chain fraction. When polymer and the wall interfacial energy is stronger, a physiosorbed layer forms, resulting in slower kinetics compared to that for weaker interfacial energy. The temperature dependence of the polymer kinetics inside NPG follows the bulk WLF behavior at lower confinement degrees, while the kinetics deviate from the bulk WLF at higher confinement levels due to the decrease in thermal expansion

coefficient. Those fundamental studies on polymer kinetics enable the optimization of preparing PING composites for the use of industrial scale applications and encourage additional studies such as ion conductivities of PING. The optical properties study established UV-Vis spectroscopy as a new approach to track polymer kinetics while simultaneously broadening the potential PING applications to optically responsive membranes. This thesis presents a pathway of fabricating PING composite while kinetics studies as well as the optical study enable scientists to better understand polymers behavior under confinement and advance the toolbox for creating interconnected polymer/filler systems at high filler concentrations.

TABLE OF CONTENTS

LIST OF TABLES

LIST OF FIGURES

CHAPTER 1. INTRODUCTION

1.1 Motivation

Polymeric materials play an essential role in our daily lives due to their versatility, durability, and cost-effectiveness. Commercially, those materials are used in a wide range of products, such as packaging and automotive parts. Their lightweight nature and resistance to corrosion make them ideal for applications in various industries. As a result, polymeric materials have become the most processed materials in the world each year. As of the year of 2015, a report by Plastic Europe reveals that the global production of plastics exceeds 330 million tons while the demand and production keeps increasing each year [1]. Below in Figure 1.1 are examples of polymer product usage in our daily life. Plastic bags, used in grocery stores and for general packaging, are made out of polyethylene (PE) which is composed of repeating units of two hydrocarbon chains as shown below. Aside from plastic bags, PE has tons of other applications such as insulation layers and containers. Interestingly, by replacing the two hydrogens on the same carbon into fluorine atoms, polyvinylidene fluoride (PVDF) can be fabricated. Because of the dual fluorine atoms attached to the carbon backbone, the chemical and physical properties of the materials are significantly tuned. For instance, PVDF has a melting temperature of 174°C, making the material more stable over a bigger temperature range. Thus, as shown in Figure 1.1, PVDF has been used for pipeline applications such as offshore pipeline, oil pipeline and water purification pipeline, where material stability and durability across a wide temperature range is required.

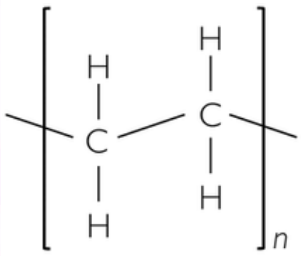

Polyethylene

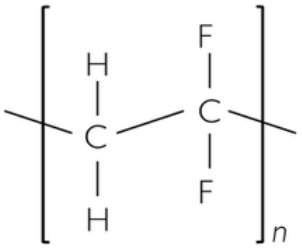

Polyvinylidene fluoride

Figure 1.1. Top. demonstration of plastic bags [2] fabricated out of polyethylene and the chemical structure of polyethylene. Bottom. Visualization of pipeline tubes [3] made out of polyvinylidene fluoride and the chemical structure of polyvinylidene fluoride.

Homopolymer provided limited performance in certain areas, such as mechanical response and material stability. Polymer nanocomposites (PNCs) provide much enhanced performance. PNCs are composed of nanofiller and polymeric materials as shown in Figure 1.2. More introduction on the PNCs will be introduced in the next section.

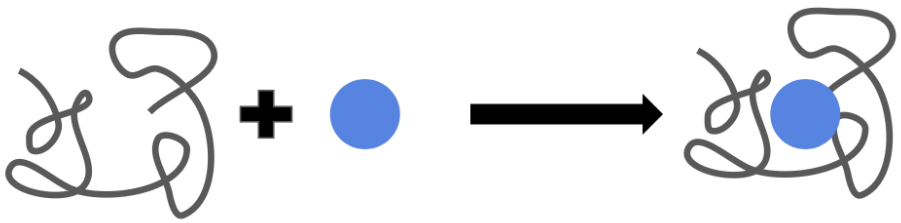

Figure 1.2 Scheme of combining the inorganic nanofiller and the polymer matrix resulting in the polymer nanocomposite. The lines represent the polymer matrix, and the blue dot represents the inorganic nanoparticle.

1.2 Polymer Nanocomposites

Polymer nanocomposites (PNCs) have been widely studied in academic, national and industrial laboratories[4–6]. PNCs are broadly defined as a mixture of an inorganic nanofiller dispersed within a polymeric matrix, resulting in a material with properties that the individual components would not exhibit by themselves. PNCs have been utilized in applications involving gas separation membranes [7,8], optically responsive devices [9–11], mechanical reinforcement [12,13], and ion conduction[14]. The unique properties of PNCs depend on factors such as inorganic nanofiller type, dispersion, loading, as well as the polymer matrix characteristics.

Nanofillers of different shapes and sizes have been used in literature to fabricate PNCs [15]. Nanofillers can be generally classified into three types: two-dimensional filler (layered structure), one dimensional filler (fibrous structure) and zero dimensional filler (spherical structure) [15]. The scheme of the precedingly mentioned nanofillers are depicted in Figure 1.3.

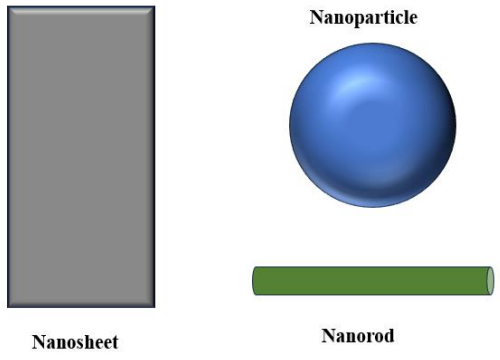

Figure 1.3 Scheme of the three types of nanofillers.

The layered 2D nanofiller structure, such as layered silicate [16], graphene [17], or MXene [18], has been widely studied. An example of layered silicate nanofiller dispersion inside a polymeric matrix is shown in Figure 1.4. For instance, Podsiadlo et al (2007) utilized Montmorillonite (MCM) clay nanosheet to fabricate a PNCs with poly(vinyl alcohol) (PVA), and the resulting PNCs have been proved to have ultra-high strength and stiffness [19].

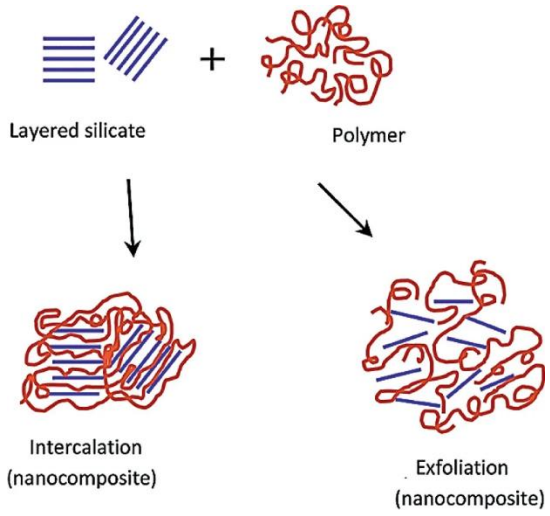

Figure 1.4 Scheme of dispersing layered silicate structure inside polymer matrix to form nanocomposites [20]. The figure is taken from reference 20 with permission.

1D nanofillers, such as nanofibres and nanorods, also received wide attention in academia because nanorods possess anisotropy. When dispersing inside a polymer matrix, the anisotropic nature enables nanorods to display a large range of surface plasmonic resonances [21]. For instance, Hore and Composto (2010) uniformly distributed polyethylene glycol (PEG) grafted Au nanorod inside a poly(methyl methacrylate) (PMMA) matrix as shown in the following Figure 1.5. It is found that the plasmon resonance can be precisely tuned by controlling the nanorod spacing and orientation [11].

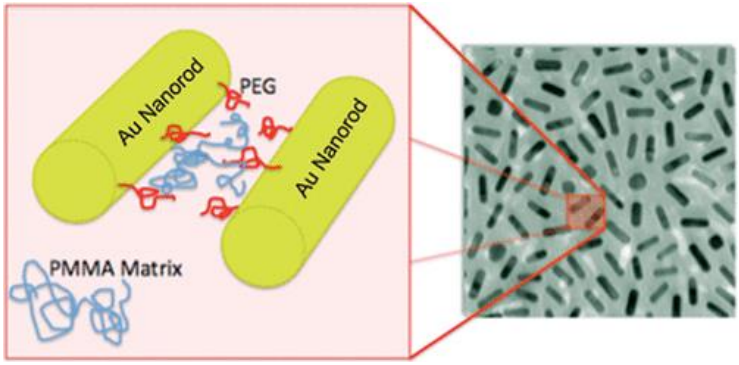

Figure 1.5 Schematic and visualization of PEG grafted Au nanorod dispersed inside the PMMA matrix[11]. The figure is taken from reference 11 with permission.

Last but not least, 0D nanofillers such as nanoparticles [22], nanoclusters[23] and quantum dots [24], have also received wide attention due to its iso-dimensional low aspect ratio. For instance, Maguire et al (2021) used polymethyl methacrylate (PMMA) grafted silica nanoparticles to disperse in poly(styrene-ran-acrylonitrile) (SAN) matrix at enhanced temperature.

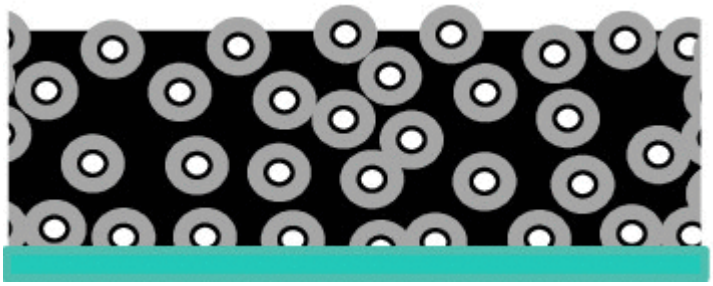

Figure 1.6 PNCs fabricated by dispersing PMMA grafted silica nanoparticles into SAN matrix [22]. The figure is taken from reference 22 with permission.

Though an extended variety of nanofiller types can be used to fabricate PNCs, nanofiller dispersion inside the polymeric matrix is limited, resulting in limited nanofiller loading. Depending on processing conditions, the NPs can disperse by thermodynamic or kinetic trapping

or aggregate as NPs self-assemble to reduce unfavorable NP/matrix interactions. However, this general approach does not ensure a homogenous dispersion of NPs particularly when a high loading is required where initial interparticle spacing is on the length scale of the NP size. For instance, Krook et al (2019) investigated the miscibility of nanoplates in a lamellar diblock copolymer and found that the equilibrium interparticle spacing is 6.4 nm[25], implying limited and conditional miscibility of NP inside the polymer matrix. In another study by Krook et al (2018), when the concentration of monodisperse nanoplates increases to 0.05 vol% in the block copolymer (BCP) assembly, the nanoplates disrupt the lamellae structure of BCP resulting in a disordered system[26]. Thus, nanofiller dispersion in polymer matrices in most nanocomposites is limited to low loadings.

Preparing PNCs with a high loading of NPs is a challenge because most combinations of polymer and bare NPs result in aggregation of NPs. Though traditional PNCs typically contain low to moderate concentrations of inorganic nanofiller, for instance, commercial tires only contain ~ 22 wt% carbon black nanofiller[27], novel methods have been developed to increase NP loading. Lu et al (2003) performed free radical polymerization of monomers in the presence of NPs, thus trapping the NPs at a loading as high as 86 wt% (ca. 22 vol%) in the PNC[28]. Similarly, LaNasa and Hickey (2020) fabricated ultra-high loading PNCs by using a surface-induced ring-opening metathesis polymerization pathway to graft polymer chains on silica nanoparticles[29]. Srivastava and Kotov (2008) explored approaches to create PNCs with high loading through layer-by-layer assembly of polymers and NPs/nanowires[30]. Although these methods successfully produce PNCs with a high loading of NPs, there are some limitations to their applicability. Namely, the prior approach is limited to systems where the NP and monomer are miscible in a

common solvent before initiating polymerization, whereas, the latter approach is limited to systems where the NP and polymer are oppositely charged.

To expand the possible combinations of polymer and NPs, a novel PNC method was developed using capillary rise infiltration (CaRI)[31]. This method starts with a two-layer system – a polymer thin film over a uniformly distributed layer of NPs. This bilayer was annealed above the polymer glass transition temperature (T_g) to fill the NP interstitial space via capillarity. Using nanoindentation and contact mode AFM, these PNCs were shown to exhibit a significant enhancement in scratch and wear resistance[32], as well as high fracture toughness [33,34]. These PNCs also demonstrated increased hardness, modulus, and fracture toughness. Compared to other existing approaches for generating high NP loading PNC, CaRI is attractive because of its versatility, namely, compatibility with many NP fillers and polymer matrices, and ease of fabrication. However, in CaRI systems, the NP interstitial pore size is not uniform or homogeneous, and the random arrangement of NPs may result in colloidal level defects such as vacancies and interstitial particles. In this thesis, we adapt CaRI to fabricate a new type of PNC via infiltrating polymer into a nanoporous gold (NPG) exhibiting bicontinuous channels of gold and air. Limited research has been done utilizing NPG as a template for actuators and catalyst support[35,36]. In this thesis work, polymer infiltrated nanoporous gold (PING) is presented as a new approach to achieve an interconnected polymer and metal structure that does not require a favorable thermodynamics of mixing. We believe that the PNCs made by PING provides a simple and scalable platform to prepare membranes for actuators, gas separation and fuel cells.

1.3 Outline of the thesis

In Chapter 1, a general introduction about polymeric materials and polymer nanocomposites are introduced. This chapter illustrates the importance of polymeric materials, the wide applications of PNCs, as well as emphasizes the emergent need for fabricating PNCs with high loading of nanofiller.

Chapter 2 of this thesis introduces the theoretical background needed to better understand this research thesis. Chapter 2 first discusses the polymer melt reptation theory under bulk, including the polymer viscosity as a function of polymer molar mass and temperature. By better understanding the polymer behavior under bulk, better comparison and analysis could be made with respect to polymer kinetics under confinement conditions. Additionally, existing studies as well as theoretical background on polymer kinetics under confinement will be introduced. Starting with Lucas-Washburn Equation, liquid imbibition under capillary is first introduced. Then, the modified LWE as well as the modified LWE in comparison with the literature studies are discussed.

Chapter 3 describes the material fabrication process as well as the major characterization techniques used across this thesis. It begins with the fabrication of nanoporous gold (NPG) membrane from the alloy, followed by making polymer/NPG bilayer structure, and the annealing process. For the characterization techniques, spectroscopic ellipsometry together with the modeling process, Quartz Crystal Microbalance - Dissipation, Small Angle X-ray Scattering, Ultraviolet-Visible Spectroscopy, MD simulations and Discrete Dipole Approximation are introduced. Individual methods that are not included in this section but used in this thesis will be included in their according chapters.

In Chapter 4, a weakly attracted polymer (polystyrene (PS)) is used to infiltrate into the NPG scaffold, and the PS kinetics is investigated. PS films with molecular weights (M_w) from 424k Da to 1133k Da is infiltrated into a NPG scaffold (ca. 120 nm), with a pore radius (R_p) and pore volume fraction of 37.5 nm and 50%, respectively. The confinement ratios ($\Gamma = \frac{R_g}{R_p}$) range from 0.47 to 0.77, suggesting that the polymers inside the pores are moderately confined. The time for PS to achieve 80% infiltration ($\tau_{80\%}$) is determined using in situ spectroscopic ellipsometry at 150°C. The kinetics of infiltration scales weaker with M_w, $\tau_{80\%} \propto M_w^{1.30 \pm 0.20}$, than expected from bulk viscosity $M_w^{3.4}$. Further, the effective viscosity of the PS melt inside NPG, inferred from the Lucas-Washburn model, is reduced by more than one order of magnitude compared to the bulk. Molecular dynamics (MD) simulation results are in good agreement with experiments predicting scaling as $M_w^{1.4}$. The reduced dependence of M_w and the enhanced kinetics of infiltration are attributed to a reduction in chain entanglement density during infiltration and a reduction in polymer-wall friction with increasing polymer molecular weight. Compared to the traditional approach involving adding discrete particles into the polymer matrix, these studies show that nanocomposites with higher loading can be readily prepared, and that kinetics of infiltration are faster due to polymer confinement inside pores.

In Chapter 5, a strongly attracted polymer (poly(2vinyl-pyridine) (P2VP)) is infiltrated into the NPG and the according kinetics is studied. P2VP with molecular weights (M_w) from 51k to 940k Da, infiltration is investigated in NPG with fixed pore radius (R_p= 34 nm) under moderate confinement ($\Gamma = \frac{R_g}{R_p}$) 0.18 to 0.78. The time for 80% infiltration ($\tau_{80\%}$) scales as $M_w^{1.43}$, similar to PS, but weaker than bulk behavior. Infiltration of P2VP is slower than PS due to

stronger P2VP-wall interactions resulting in a physisorbed P2VP layer which is supported by the similar scaling of $\tau_{80\%}$ for P2VP and PS, and MD simulations. Simulations show that infiltration time scales as $M_w^{1.43}$and that infiltration is slower for stronger polymer-wall interactions. As M_w increases, effective viscosity crosses from greater than to less than bulk viscosity due to pore narrowing and a reduction in entanglements. These studies provide new insight for polymer behavior under confinement and a new route for preparing nanocomposites at high filler loadings.

Chapter 6 studies the optical response of P2VP infiltrated NPG at various infiltration extent. The optical responses of polymer infiltrated nanoporous gold are found to be directly related to the infiltration extent (IE), demonstrating that UV-Vis as a reliable tool for probing polymer kinetics tracking. P2VP with M_w of 85 - 940 kDa are infiltrated into NPG, which has a pore radius (R_p) of approximately 34 nm. The P2VP/NPG are annealed above its T_g, at 140°C, to induce infiltration. P2VP IE inside NPG is directly related to the annealing time. UV-Vis measures the optical spectra at different annealing times and suggests that the shape of the spectra changes upon longer annealing times. Upon further analysis, we found that the spectra height as well as width and area under the spectra curve, increases parabolically with the P2VP IE. Comparing the UV-Vis analysis with the in-situ spectroscopic ellipsometer results, the two methods yields statistically identical time to reach 80% IE ($\tau_{80\%}$) for all 4 M_w analyzed as well as slope of $\tau_{80\%}$ vs. M_w. UV-Vis proves to be a valid and reliable tool for tracking the polymer kinetics inside the NPG. XPS is used to investigate the P2VP:Au interfacial electron flow, which is evidenced by a binding energy peak shift. Discrete Dipole Approximation (DDA) simulation is used to study the effect of surrounding refractive index on absorbance peak shape. Optical

response shape changes are attributed to 1. interfacial electron flow from P2VP to NPG, and 2. surrounding effective refractive index change.

Chapter 7 delves into the temperature dependence of P2VP inside NPG. In this chapter, P2VP-302k and P2VP-940k are respectively infiltrated into the NPG at various temperatures. The confinement ratios for P2VP-302k and P2VP-940k are 0.55 and 0.97 respectively. It is found that across the temperature range of 130 - 180°C, those two Mw P2VP exhibit reduced viscosities under all temperatures as compared to the bulk, implying that the polymer is traveling faster inside NPG. Additionally, the $\frac{\eta_{eff}}{\eta_{bulk}}$ value is relatively constant for each individual molecular weight, while $\frac{\eta_{eff}}{\eta_{bulk}}$ is much higher for P2VP-302k as compared to P2VP-940k, implying that when traveling inside NPG, the kinetics P2VP-940k is more enhanced with respect to bulk compared with P2VP-302k. The WLF analysis reveals that the P2VP inside NPG mostly follows the bulk temperature dependence behavior, with very slight deviations.

Chapter 8 utilizes the fundamental analysis gained from the previous chapters to fabricate the next generation of novel PNCs materials that have much enhanced properties. Starting with the current ongoing work derived from this thesis, poly(ethylene glycol) (PEO) and P2VP are firstly grafted onto the NPG surfaces to generate polymer grafted NPG. Then, building onto the previous chapters, more studies on the kinetics study, with the presence of a brush wall, is suggested. Building off the polymer grafted NPG idea, a further idea, which is to functionalize NPG with polymer loops, is suggested for further research.

1.4 References

1. https://plasticseurope.org.

2. *The Journey of a Plastic Bag: From Production to Disposal*. https://postage-solutions.co.uk/blog/the-journey-of-a-plastic-bag-from-production-to-disposal/.

3. https://www.chinafluoropolymer.com/pvdf-product-in-tube-bar-sheet/pvdf-tube/pvdf-pipeline.html.

4. Balazs, A. C., Emrick, T. & Russell, T. P. Nanoparticle Polymer Composites: Where Two Small Worlds Meet. *Science* 314, 1107–1110 (2006).

5. Kim, J. *et al.* Estimation of the concentration of nano-carbon black in tire-wear particles using emission factors of PM10, PM2.5, and black carbon. *Chemosphere* 303, 134976 (2022).

6. Guth, E. Theory of Filler Reinforcement. *J. Appl. Phys.* 16, 20–25 (1945).

7. Bilchak, C. R. *et al.* Polymer-Grafted Nanoparticle Membranes with Controllable Free Volume. *Macromolecules* 50, 7111–7120 (2017).

8. Merkel, T. C. *et al.* Ultrapermeable, Reverse-Selective Nanocomposite Membranes. *Science* 296, 519–522 (2002).

9. Glor, E. C., Ferrier, R. C., Li, C., Composto, R. J. & Fakhraai, Z. Out-of-plane orientation alignment and reorientation dynamics of gold nanorods in polymer nanocomposite films. *Soft Matter* 13, 2207–2215 (2017).

10. Hore, M. J. A., Frischknecht, A. L. & Composto, R. J. Nanorod Assemblies in Polymer Films and Their Dispersion-Dependent Optical Properties. *ACS Macro Lett.* 1, 115–121 (2012).

11. Hore, M. J. A. & Composto, R. J. Nanorod Self-Assembly for Tuning Optical Absorption. *ACS Nano* 4, 6941–6949 (2010).

12. Bilchak, C. R., Huang, Y., Benicewicz, B. C., Durning, C. J. & Kumar, S. K. High-Frequency Mechanical Behavior of Pure Polymer-Grafted Nanoparticle Constructs. *ACS Macro Lett.* 8, 294–298 (2019).

13. Rittigstein, P. & Torkelson, J. M. Polymer-nanoparticle interfacial interactions in polymer nanocomposites: Confinement effects on glass transition temperature and suppression of physical aging: Polymer-Nanoparticle Interfacial Interactions. *J. Polym. Sci. Part B Polym. Phys.* 44, 2935–2943 (2006).

14. Polizos, G. *et al.* Effect of polymer–nanoparticle interactions on the glass transition dynamics and the conductivity mechanism in polyurethane titanium dioxide nanocomposites. *Polymer* 53, 595–603 (2012).

15. Fu, S., Sun, Z., Huang, P., Li, Y. & Hu, N. Some basic aspects of polymer nanocomposites: A critical review. *Nano Mater. Sci.* 1, 2–30 (2019).

16. Albdiry, M., Yousif, B., Ku, H. & Lau, K. A critical review on the manufacturing processes in relation to the properties of nanoclay/polymer composites. *J. Compos. Mater.* 47, 1093–1115 (2013).

17. Young, R. J., Kinloch, I. A., Gong, L. & Novoselov, K. S. The mechanics of graphene nanocomposites: A review. *Compos. Sci. Technol.* 72, 1459–1476 (2012).

18. Li, X., Wang, C., Cao, Y. & Wang, G. Functional MXene Materials: Progress of Their Applications. *Chem. – Asian J.* 13, 2742–2757 (2018).

19. Podsiadlo, P. *et al.* Ultrastrong and Stiff Layered Polymer Nanocomposites. *Science* 318, 80–83 (2007).

20. Mohamed, R. R. Applications of Nanocomposites in Environmental Remediation. in *Advances in Nanocomposite Materials for Environmental and Energy Harvesting Applications* (eds. Shalan, A. E., Hamdy Makhlouf, A. S. & Lanceros-Méndez, S.) 453–471 (Springer International Publishing, Cham, 2022). doi:10.1007/978-3-030-94319-6_15.

21. Link, S. & El-Sayed, M. A. Spectral Properties and Relaxation Dynamics of Surface Plasmon Electronic Oscillations in Gold and Silver Nanodots and Nanorods. *J. Phys. Chem. B* 103, 8410–8426 (1999).

22. Maguire, S. M. *et al.* Grafted Nanoparticle Surface Wetting during Phase Separation in Polymer Nanocomposite Films. *ACS Appl. Mater. Interfaces* 13, 37628–37637 (2021).

23. Herron, N. & Thorn, D. L. Nanoparticles: Uses and Relationships to Molecular Cluster Compounds. *Adv. Mater.* 10, 1173–1184 (1998).

24. Huang, P. *et al.* Greatly decreased redshift and largely enhanced refractive index of mono-dispersed ZnO-QD/silicone nanocomposites. *J. Mater. Chem. C* 4, 8663–8669 (2016).

25. Krook, N. M. *et al.* Experiments and Simulations Probing Local Domain Bulge and String Assembly of Aligned Nanoplates in a Lamellar Diblock Copolymer. *Macromolecules* 52, 8989–8999 (2019).

26. Krook, N. M. *et al.* Alignment of Nanoplates in Lamellar Diblock Copolymer Domains and the Effect of Particle Volume Fraction on Phase Behavior. *ACS Macro Lett.* 7, 1400–1407 (2018).

27. Gómez-Hernández, R., Panecatl-Bernal, Y. & Méndez-Rojas, M. Á. High yield and simple one-step production of carbon black nanoparticles from waste tires. *Heliyon* 5, e02139 (2019).

28. Lü, C. *et al.* Preparation and characterization of ZnS–polymer nanocomposite films with high refractive index. *J Mater Chem* 13, 2189–2195 (2003).

29. LaNasa, J. A. & Hickey, R. J. Surface-Initiated Ring-Opening Metathesis Polymerization: A Method for Synthesizing Polymer-Functionalized Nanoparticles Exhibiting Semicrystalline Properties and Diverse Macromolecular Architectures. *Macromolecules* 53, 8216–8232 (2020).

30. Srivastava, S. & Kotov, N. A. Composite Layer-by-Layer (LBL) Assembly with Inorganic Nanoparticles and Nanowires. *Acc. Chem. Res.* 41, 1831–1841 (2008).

31. Huang, Y.-R. *et al.* Polymer nanocomposite films with extremely high nanoparticle loadings via capillary rise infiltration (CaRI). *Nanoscale* 7, 798–805 (2015).

32. Jiang, Y., Hor, J. L., Lee, D. & Turner, K. T. Toughening Nanoparticle Films via Polymer Infiltration and Confinement. *ACS Appl. Mater. Interfaces* 10, 44011–44017 (2018).

33. Qiang, Y., Turner, K. T. & Lee, D. Role of Polymer–Nanoparticle Interactions on the Fracture Toughness of Polymer-Infiltrated Nanoparticle Films. *Macromolecules* 56, 122–135 (2023).

34. Qiang, Y., Pande, S. S., Lee, D. & Turner, K. T. The Interplay of Polymer Bridging and Entanglement in Toughening Polymer-Infiltrated Nanoparticle Films. *ACS Nano* 16, 6372–6381 (2022).

35. Biener, J., Biener, M. M., Madix, R. J. & Friend, C. M. Nanoporous Gold: Understanding the Origin of the Reactivity of a 21st Century Catalyst Made by Pre-Columbian Technology. *ACS Catal.* 5, 6263–6270 (2015).

36. Li, J., Markmann, J., Weissmüller, J. & Mameka, N. Nanoporous gold-polypyrrole hybrid electrochemical actuators with tunable elasticity. *Acta Mater.* 212, 116852 (2021).

CHAPTER 2. THEORETICAL BACKGROUND

2.1 Introduction

Polymer dynamics is the study of polymer chains' movement and response to various forces and external conditions. Unlike small molecules or simple fluids, polymers are large, flexible long chains made up of repeating monomer units, thus resulting in unique, time-dependent behaviors that range from local segmental motions to whole-chain reorientations. These motions are influenced by factors like temperature, chain length, molecular weight, interactions with surrounding chains, and number of entanglements. The study of polymer dynamics explores how these movements affect properties such as viscosity, elasticity, and mechanical strength, making it essential for understanding and designing materials for applications like elastomers, plastics, fibers, and biological systems. By examining polymer behavior and performances over different timescales and temperatures, polymer performances under specific conditions can be accurately predicted.

Polymer dynamics is an important field of study since it could facilitate future academic research as well as industrial productions. For instance, in the manufacturing industry, polymer dynamics is essential for processes like extrusion, injection molding, and 3D printing, where flow properties under stress and temperature dictate product quality and consistency. In the automotive and aerospace industries, knowledge of polymer dynamics helps design lightweight and long-lasting materials that can withstand mechanical stress and temperature fluctuations in addition to aging, improving the overall performances. In the academic research labs, polymer dynamics have been investigated under many different scenarios. For instance, studies have been

done on polymer kinetics under moderately confined [1,2] and extreme confined [3,4] conditions to investigate the effect of confinement on polymer kinetics. Additionally, the concept of polymer kinetics has been used in fabrication of batteries, gas membranes, and optically responsive materials.

In this chapter, theoretical background on polymer kinetics under different scenarios will be introduced. Firstly, governing equations and physics of polymer kinetics under bulk will be introduced, which includes the unentangled polymer dynamics, entangled polymer dynamics, and WLF relationship. Then, theoretical background on polymer kinetics under confinement will be elaborated, which includes subsections on liquid imbibition governing by Lucas-Washburn Equation, and polymer viscosity under different effects (extreme confinement and dead zone). This theoretical background section is essential for better understanding Chapter 4 - 7.

2.2 Polymer Dynamics under Bulk

Plenty of factors influence the polymer melt viscosity, such as chain length, chain branch dispersity, temperature etc. In the following subsections, the unentangled polymer dynamics and entangled polymer dynamics, together with the effect of temperature will be discussed. In these subsections, the polymers are assumed to be linear and free of influences from branches.

2.2.1 Unentangled polymer dynamics

For polymer chains with a small number of repeating units, the chains are too short to form entanglements. The unentangled polymer viscosity could be described by the Rouse model

as shown in Equation 2.1, where η is the polymer viscosity, $\boldsymbol{\zeta}$ is the friction coefficient per Kuhn segment, b is the Kuhn length, and N is the number of Kuhn segments.

$$\eta \approx \frac{\zeta}{b} N \qquad \text{Eq. 2.1}$$

From Equation 2.1, theoretically the polymer viscosity of the unentangled chain is proportional to the monomeric friction coefficient as well as the number of Kuhn segments. However, in reality, the polymer isothermal viscosity is not directly proportional to the number of Kuhn segment because $\boldsymbol{\zeta}$ is dependent on the polymer chain length for unentangled polymers [5]. The glass transition temperature (T_g) is also dependent on the chain length. As the polymer chain get longer, the polymer coil tends to have less degree of free volume, thus induce an increase in T_g. The T_g relation with respect to the chain length could be expressed by the following Equation 2.2.

$$T_g = T_{g,\infty} - \frac{C}{M_n} \qquad \text{Eq. 2.2}$$

C is a constant depending on the polymer type, and typically is in range of $10^4 - 10^5$ K*g/mol. As a result, polymer with $M_n > 10^4 - 10^5$ g/mol experiences minimal influence of M_n on T_g while adopting the long chain limiting value $T_{g,\infty}$ [5]. Thus, when studying the unentangled polymer viscosities, constant $T - T_g$ should be used for a fair comparison rather than keep the temperature isothermal.

2.2.2 Entangled polymer dynamics

Polymers with high M_n possess different behaviors than polymers with low M_n because of the entanglements. Entanglements describe the topological constraints where polymer chains are intertwined with each other, thus impeding the degree of movement. The entangled polymer dynamics can be well captured by the reptation model as shown in the following Figure 2.1.

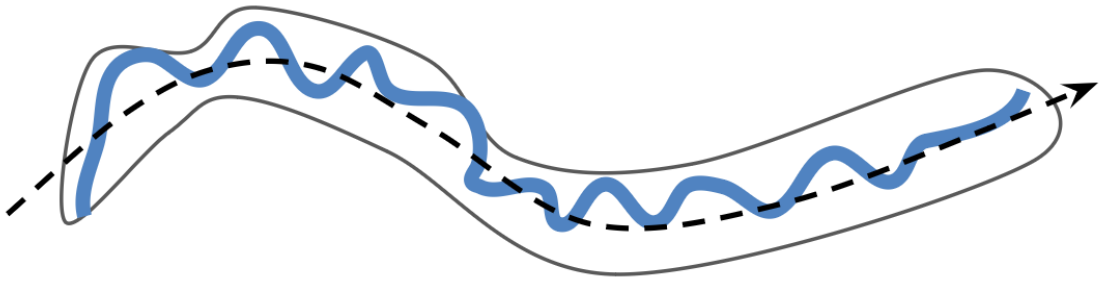

Figure 2.1. Polymer reptation model scheme. The blue curves represent the entangled polymer chains. The gray confined area depicts the constrained tube-like region created by the other chains. The dashed black line represents the primitive path of travel.

This model envisions each polymer chain as being confined within a "tube" created by surrounding entangled chains. The motion of a chain is limited because it can only move forward or backward along this tube, like a snack reptate inside a channel. The “tube” can be considered as consisting of (N/N_e) number of sections of size a, with each section containing N_e monomers, and the polymer chains are considered as random walks of each individual entanglement strands. The bulk viscosity of the entangled polymer can be approximated as Equation 2.3.

$$\eta \approx \frac{\zeta b^2}{v_o} \frac{N^3}{N_e^2} \qquad \text{Equation 2.3}$$

Combining Equation 2.1 and 2.3, the polymer viscosity can be predicted as proportional to the polymer molecular weight. For unentangled polymers, (M<M_c), the viscosity prediction follows the Rouse model, while for entangled polymers, the viscosities follow the reptation model. The summary is shown in the following Equation 2.4.

$$\eta \sim M \; for \; M < M_c \qquad \text{Eq. 2.4}$$

$$\eta \sim M^3 \; for \; M > M_c \qquad \text{Eq. 2.4}$$

In experimental measurements, entangled polymer has exhibited an exponent of 3.4 across different studies [6–9]. Thus, $\eta \sim M^{3.4}$ is more commonly used to predict the entangled polymer viscosity [5].

2.2.3 Williams-Landel-Ferry (WLF) Relation

Polymer time-temperature superposition (TTS) is a fundamental concept in polymer physics, allowing the prediction of a polymer's viscoelastic behavior over a broad range of timescales based on data collected at varying temperatures. This principle relies on the fact that polymer chains exhibit time-dependent relaxation processes that are sensitive to temperature. When a polymer is subjected to stress, it responds by deforming at different rates depending on the temperature; higher temperatures generally speed up the relaxation and motion of the chains, while lower temperatures slow them down. By shifting experimental data along the time or frequency axis to account for these temperature effects, TTS creates a "master curve" that spans many orders of magnitude in time or frequency. This master curve represents the material's response as if the measurements were all taken at a single reference temperature, simplifying the

analysis and prediction of long-term polymer behavior. TTS is especially valuable for materials scientists and engineers, as it enables the extrapolation of short-term data to predict long-term performance in applications like automotive components, medical devices, and structural materials.

Arrhenius Equation, shown in Equation 2.5, is the simplest form to describe the temperature dependence on the polymer viscosity, where E_a is the polymer activation energy.

$$\eta \sim exp\left(\frac{E_a}{kT}\right) \qquad \text{Eq. 2.5}$$

The E_a is typically a constant at elevated temperatures above T_g. As a result, as the temperature increases, the net difference between the E_a and the thermal potential stored within the polymer gets larger, thus inducing a reduced viscosity.

To better understand the temperature dependence on the polymer free volume, the Doolittle equation, a modification of the Arrhenius equation, is introduced (Equation 2.6).

$$\eta \sim exp\left(\frac{B}{f}\right) \qquad \text{Eq. 2.6}$$

In the Doolittle equation, f is the fraction of the free volume, and B is an empirical constant. Based on the Doolittle equation, as free volume f decreases, the exponential term grows much enhanced, leading to a sharp increase in viscosity. The free volume fraction, f, is related to the temperature of the polymer melt because as the temperature increases, the polymer density will decrease, thus resulting in a free volume density and a reduced effective E_a for the polymers to reptate. The free volume fraction is assumed to be linearly related to the temperature as shown in Equation 2.7.

$$f = \alpha_f (T - T_\infty) \qquad \text{Eq. 2.7}$$

Where in the equation α_f is the thermal expansion coefficient, and T_∞ is the Vogel temperature where the free volume is 0. The Vogel temperature is usually 50K below the T_g, and it has been found that $f_g \approx 0.025$ at the T_g [5].

Combining the Doolittle equation and the free volume temperature dependence relationship, the Williams-Landel-Ferry (WLF) equations can be calculated as shown below:

$$\frac{\eta}{\eta_0} = exp\left(\frac{B}{f_0}\frac{(T_0 - T)}{(T - T_\infty)}\right) \qquad \text{Eq. 2.8}$$

Where in the WLF expression, T_0 is the reference temperature that yields a free volume f_0 and η_0. The WLF has found to well describe polymer temperature dependence over the range of T_g<T<T+100K [5]. A simplified WLF equation can be seen in Equation 2.9.

$$log\,(a_T) = -\frac{C_1(T - T_r)}{(C_2 + T - T_r)} \qquad \text{Eq. 2.9}$$

Where a_T is the time scale shift factor and can be expressed as $a_T = \frac{\eta}{\eta_0}$. C_1 and C_2 are constants that are related to the f_g and α_f such that $C_1 = \frac{B}{2.303 f_g}$ and $C_2 = \frac{f_g}{\alpha_f}$.

In short, the WLF equation is a powerful tool which allows researchers to construct a "master curve" of polymer behavior by shifting experimental data taken at different temperatures and used for predicting polymer behavior and performance over a wide range of temperatures and time scales. The WLF analysis is mostly used in Chapter 7, where the polymer temperature dependence behavior inside moderately confined NPG is investigated.

2.3 Polymer Kinetics under Confinement

In this section, the polymer kinetics under confinement will be discussed. Firstly, the Lucas-Washburn Equation (LWE), which describes the liquid imbibition behavior under a narrow channel will be described. Then, the derivation of LWE for polymer imbibition under confinement will be shown. This section of theoretical background is highly relevant to chapters 4 - 7.

2.3.1 Liquid Imbibition under Capillary

Capillarity, also known as capillary action, is the phenomenon that liquid voluntarily moves in narrow tubes or porous materials due to the outcome of the interplay between cohesive and adhesive forces. Cohesive forces are the attraction between molecules of the liquid, while adhesive forces occur between the liquid molecules and the surface of the wall. In narrow spaces, like a thin tube, adhesive forces can pull the liquid up the walls of the tube, while cohesive forces help maintain the liquid column's integrity. This effect is responsible for various natural and daily life observations. For instance, water travels from the root to the leaves in plants as shown in Figure 2.2.

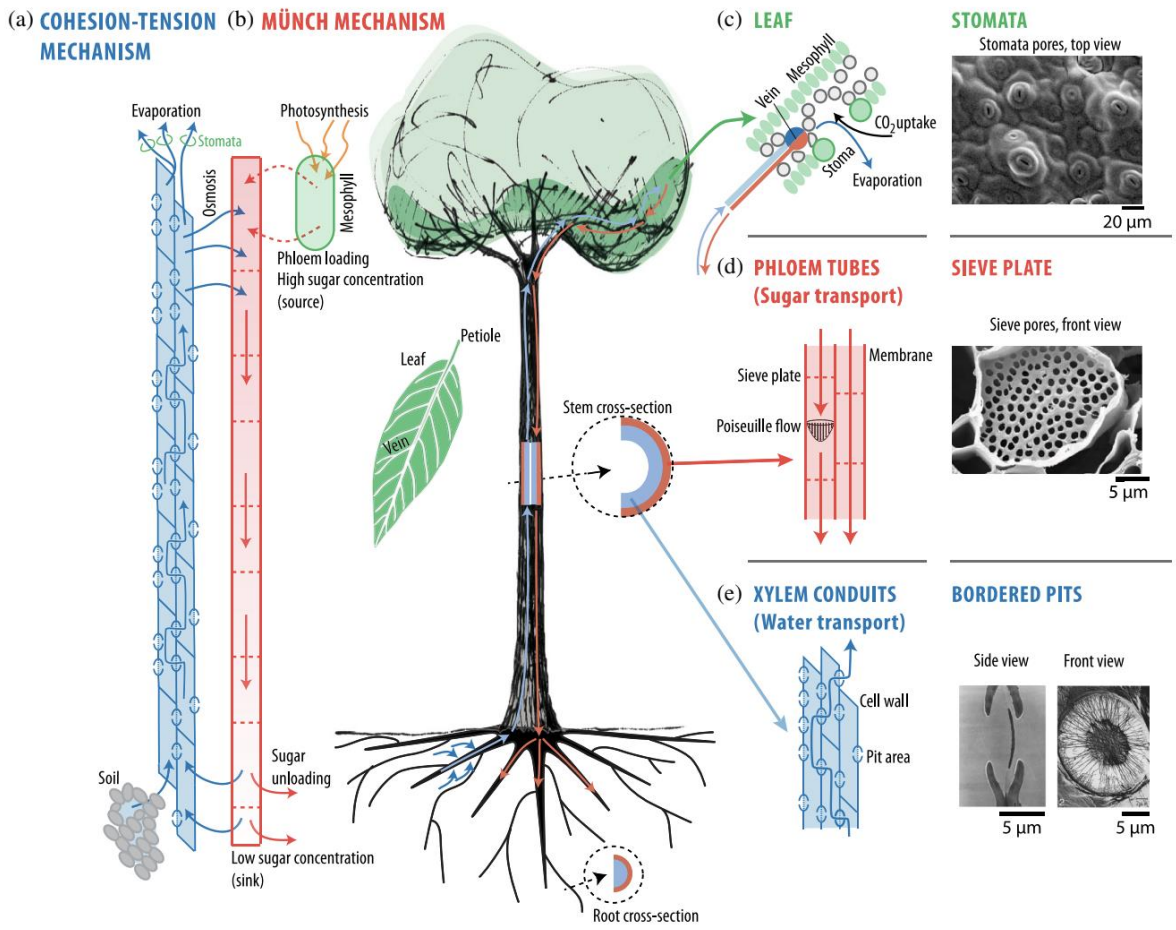

Figure 2.2 Scheme of vascular tree transport in trees [10]. The figure is taken from reference 10 with permission.

The capillary effect can be more readily visualized by fluid traveling inside a narrow channel. Below in Figure 2.3 is a schematic of simple fluid imbibition inside a cylindrical pore. In the Figure, the R is the radius of the narrow pore, h is the height that the liquid traveled.

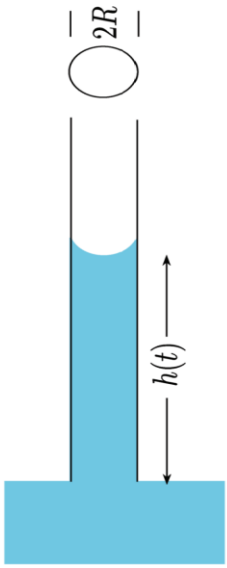

Figure 2.3 Schematic of liquid imbibition inside a cylindrical channel [11]. The figure is taken from reference 11 with permission.

For Newtonian fluids, the capillary effect is described by the Lucas-Washburn Equation (LWE)[12,13].

$$h(t) = t^{0.5}\sqrt{\frac{R_{pore}\Upsilon\, cos\theta_e}{2\eta_o}} \qquad \text{Eq. 2.10}$$

In the equation, $h(t)$ is the height infiltrated by the liquid, t is the infiltration time, R_{pore} is the radius of the pore, Υ is the surface tension of the liquid, θ_e is the equilibrium contact angle, and η_o is the fluid viscosity. The LWE assumes that the size of the fluid particle is an order of magnitude smaller than the radius of the channel, which enables the fluid to be treated as a continuum medium [11,12]. The imbibition liquid effective viscosity can be calculated from the LWE. From the LWE, it is implied that the liquid travel inside a confinement intrinsically follows a h ~ $t^{0.5}$ relationship. The scaling of polymer infiltration height $h(t)$ with $t^{0.5}$ is well-

documented. For example, polyethylene (PE) infiltrated into cylindrical anodized alumina oxide (AAO) nanopores exhibited LWE scaling such that flux ~ $t^{0.5}$, although the molecular weight dependence differed from bulk behavior[14]. Similar behavior was observed in molecular dynamics simulations of unentangled polymers in CaRI experiments[15]. Polyethylene oxide (PEO) chains infiltrated into confined AAO cylindrical nanopores where $R_g \gg R_{pore}$ again exhibited LWE scaling ~ $t^{0.5}$ [16]. However, though the h ~ $t^{0.5}$, the dynamics of the polymer under LWE deviates from the LWE prediction since the polymer behaves much more complex than simple fluid. In the next section, the derivation of polymer melt predicted under confinement will be shown.

2.3.2 Polymer kinetics under confinement

2.3.2.1 Effect of confinement

When the polymer coil size is on the same magnitude of the pore size, the confirmation of the polymer chain would be perturbed. The free energy of the polymer chain is enhanced in confined pores as compared to the bulk polymer due to the change in entropy conformation, thus the driving force is reduced in a confined scenario, which could be described by Equation 2.11 [11].

$$\Upsilon_{eff} = \Upsilon cos\theta_e - \Delta f \frac{R}{2} \qquad \text{Eq. 2.11}$$

Where in this equation, Δf is the change in free energy under confinement with respect to in bulk. This change in the free energy could be estimated by the blob model [17], where polymer chains are divided into smaller "blob" sections. Since the change in free energy per monomer inside the blob can be described by $\Delta f = k_B T \frac{N}{g}$, where g is the number of monomers inside each blob. Assuming ideal chains, the number of monomers per blob could be calculated by $g =$

$(2R/b)^2$, where b is the kuhn length of the monomer. The number density of the polymer chain is $\frac{1}{v_0 N}$, where v_0 is the monomer value. By combining the preceding three expressions, the change in free energy density[11] is shown in the following equation.

$$\Delta f = k_B T \frac{b^2}{4 v_0 R^2} \qquad \text{Eq. 2.12}$$

According to Yao et al (2018), the ratio of the two terms from the Eq. 2.12 could be used to determine the effect of the confinement on the polymer fluids [11]. The smaller the ratio is, the less confinement effect that the polymer fluids undergo. For instance, the experimental study [16] of poly(ethylene oxide) (PEO) in anodized aluminum oxide (AAO) pores yields this ratio to be 0.014, thus the confinement effect is very small in this case to contribute to the enhancement in viscosity [11]. In this section, the confinement effect of the isolated ideal chain is discussed. The confinement effect on the polymer melt chain reptation will be further discussed in later this chapter.

2.3.2.2 Effect of dead zone

For a simple fluid imbibition under capillary effect, a no-slip boundary is assumed. As a result, theoretically the fluid will travel with a parabolic profile front. However, polymer melt chains could be very different from simple fluids. When the interaction strength between the polymer and the wall is strong, the polymer in contact with the wall could be adsorbed, thus creating a dead zone with thickness ΔR. The presence of the dead zone decreases the radius that the polymer could travel through. To take the dead zone into consideration of the confinement, the effective radius, $R_{eff} = R - \Delta R$, is defined. Assuming that the polymer travels

parabolically with velocity ($v = \Delta P \frac{R^2}{8\eta_0 h}$) within the R_{eff} and the polymer is driven by the Laplace pressure ΔP, where $\Delta P = \frac{2\Upsilon \cos\theta_e}{R}$, the fluid front advancing rate can be calculated as shown below [11].

$$\frac{dh}{dt} = v\frac{R_{eff}^2}{R^2} = \frac{R_{eff}^4}{8\eta_0 h \ R^2}\frac{2\Upsilon \cos\theta_e}{R} \qquad \text{Eq. 2.13}$$

By replacing the η_0 with η_{eff} using the relation that $\frac{dh}{dt} = \Upsilon \cos\theta_e R/4\eta_{eff} h$ in the previous equation and compare with the LWE, the following relation can be attained [11].

$$\frac{\eta_{eff}}{\eta_0} = \left(\frac{R_{eff}}{R_{pore}}\right)^4 \qquad \text{Eq. 2.14}$$

From the previous equation, even a small dead zone could induce a significant increase on η_{eff}, resulting in reduced kinetics.

2.3.2.3 Polymer Reptation Under Confinement

As the pore radius is further reduced with respect to the polymer size, the polymer macroscopic flow is mainly driven by the pressure gradient as shown in the following Figure 2.4.

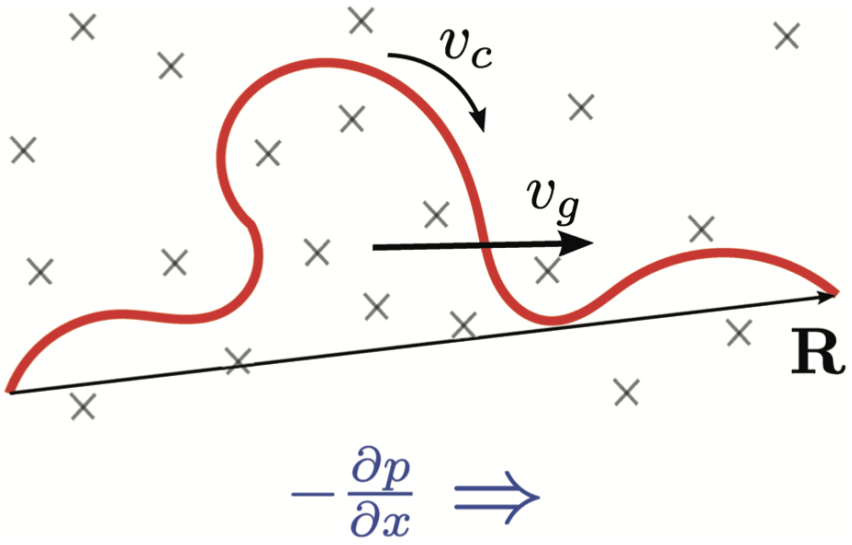

Figure 2.4. Scheme of repetition motion of polymer chain under pressure gradient [11]. The figure is taken from reference 11 with permission.

The polymer chain velocity [11] could be calculated by Equation 2.15, where l^2 is the cross section, R_x is the x-component of the end-to-end vector, N is number of segment, $\boldsymbol{\zeta}$ is the friction coefficient per kuhn segment, and v_c is the chain's velocity over the reptation tube.

$$v_c = \frac{l^2}{\zeta N} R_x \left(-\frac{\delta p}{\delta x}\right) \qquad \text{Eq. 2.15}$$

The average velocity of the polymer center of mass (v_g) can then be calculated by using $< v_g > = \frac{R_x}{L} v_c$, thus yield $< v_g >$ expression [11] as shown in Equation 2.16, where L is the contour length of the tube, N_e is the entanglement number of segments and a_t is the tube diameter. Those three terms follows the relationship [11] that $L = (N/N_e)a_t$ and $a_t = \sqrt{N_e}b$. The R_x is assumed to be ideal chain such that $< R_x^2 > = \frac{1}{3} N b^2$.

$$< v_g > = \frac{l^2 a_t}{3\zeta N} \left(-\frac{\delta p}{\delta x}\right) \qquad \text{Eq. 2.16}$$

During the reptation under confinement, only a fraction of the chain (ϕ) will participate in the reptation process, thus an additional parameter needs to be taken into consideration. Additionally, the pressure gradient could be regarded as the average fluid pressure gradient over, thus simplified $-\frac{\delta p}{\delta x}$ into $2\gamma cos\theta_e$. The cross-section fluid retention rate (ħ) is then expressed by Equation 2.17, assuming $l^2 = a_t^2$.

$$ħ = \phi \frac{N_e^{\alpha} b^3}{3\zeta N} \frac{2\gamma cos\theta_e}{hR} \qquad \text{Eq. 2.17}$$

2.3.2.4 Polymer viscosity under confinement summary

Combining the effect of dead zone and the reptation under confinement effect, Yao et al. (2018) developed a model to account for polymer effective viscosity deviations from bulk viscosity scaling[11]:

$$\frac{\eta_{eff}}{\eta_0} = \left[\left(\frac{R_{eff}}{R_{pore}}\right)^4 + \phi \frac{8N_e^{\alpha} b^3 \eta_0}{3\zeta N {R_{pore}}^2}\right]^{-1} \qquad \text{Eq. 2.18}$$

Here, the effective polymer viscosity, η_{eff}, deviates from the bulk viscosity, η_0, due to two phenomena which dominate in distinct regimes of confinement. The first term in Equation 2.18 captures the dead zone effect, in which strong adsorption of chains to the capillary surface creates a zone of thickness ΔR where polymer imbibition is blocked. The reduced pore size increases η_{eff}, leading to infiltration dynamics slower than bulk behavior. The dead zone effect is expected to dominate when the polymer radius of gyration is much smaller than the pore radius, $R_g \ll R_{pore}$. Adapted from the work of Johner et al. (2010), the second term in Equation

2.18 describes reptation-like flow under confinement, which models infiltration as plug through a capillary[18]. This term dominates in highly confined systems, i.e. when $R_g \gg R_{pore}$. Polymers confined in a reptation tube much smaller than their bulk length scale is driven by the capillary pressure gradient and infiltrate with a scaling of $\sim N^1$, showing enhanced mobility over bulk.

2.4 Polymer Properties and Conformation under Confinement

2.4.1 Polymer Properties under confinement

Confinement can perturb polymer characteristics and properties compared to bulk behavior [1,2,16,19–35]. Previous work has shown that polymers can exhibit a higher T_g in confined geometries [1,4,36–38], depending on the nature of the interactions of the polymer with the confining surfaces. As confinement increases, the polymer segmental relaxation dynamics slow down, and T_g increases [39]. For example, Maguire et al. (2021) found that the T_g of PS and P2VP increased by 6°C and 20°C respectively when confined in NPG with a pore size (R_p) greater than the radius of gyration (R_g) [1] as shown in the following Figure 2.5.

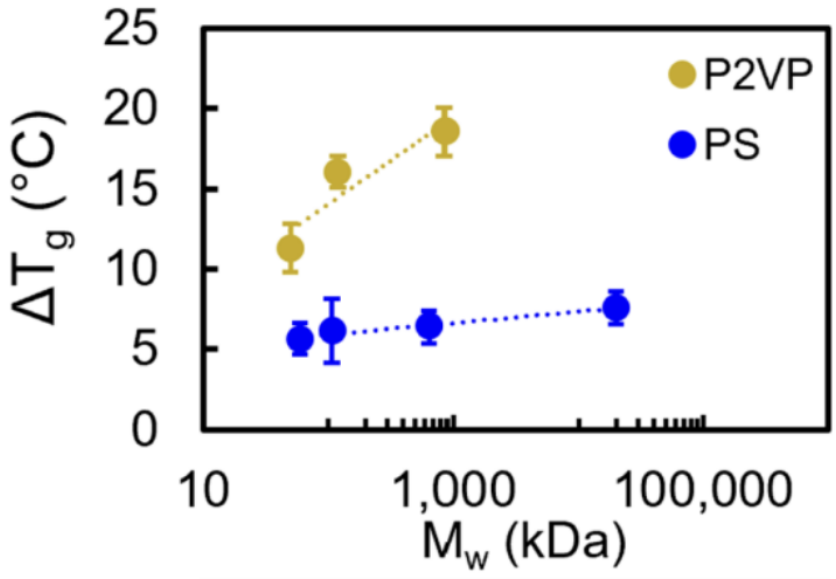

Figure 2.5. The T_g difference between the confined PS and P2VP and the bulk. PS exhibits a relative stable T_g increase for all M_w while P2VP shows a higher T_g increase while simultaneously more dependent on M_w. Figure adapted from reference 1 with permission.

In a complementary study, for PS highly confined in packed nanoparticles ($R_g < R_p$), the T_g increased by 57°C compared to the bulk [38]. Despite this increase in T_g for completely filled nanocomposites, polymer infiltration into confined or semi-confined pores shows enhanced kinetics [2–4,15,36,40]. For entangled PS infiltrating NPG under moderate confinement, the effective viscosity decreased by over an order of magnitude relative to the bulk viscosity, and this difference increased as M_w increased [2]. For entangled PS infiltration in highly confined SiO_2 packing, the effective viscosity also decreased [3]. However, for unentangled PS and P2VP infiltrating into SiO_2, a significant slowdown is observed [4]. The seemingly conflicting effect of confinement on polymer infiltration kinetics has remained largely unresolved.

2.4.2 Polymer Conformation under confinement

The polymer chains conformations are distorted when confined in pores, and this distortion, simultaneously, influences polymer dynamics. While studying polymer infiltration inside confined channels, interesting and seemingly conflicting observations have been made. Some studies [4,36] found that confinement decreases polymer kinetics. For instance, Hor et al (2018) infiltrated unentangled PS and P2VP into densely packed NP stackings and found the polymer viscosities for both PS and P2VP increases ~ 100x [4]. On the other hand, other researchers found that confinement enhances polymer kinetics [1,3]. The seemingly conflicting observations raise the need to further investigate fundamentals on polymer conformation on the molecules or atomic scales.

Simulation has been used as a versatile tool to probe chain conformations. Polymer melt chain conformation, which can be quantified by the radius of gyration R_g, has been both studied through experiment [41–43] and simulation [2,44]. For instance, small angle neutron scattering (SANS) has been used to probe the polymer conformations in polymer nanocomposites [41–43]. Studies have found polymer chains to exhibit enhanced dimensions [41], reduced dimensions [42], and unperturbed dimensions [42] through SANS. The ensemble averaging and the isotropic nature partially account for the experimental conflicting observations of the chain conformation [44]. Molecular dynamics (MD) simulations, on the other hand, are more conducive to further analyzing polymer conformation under confinement.

MD simulations from previous studies found that the polymer melt under confinement changes polymer conformation, thus impacting diffusing rate. For instance, Meyer et al (2007) used the MD simulation to probe the 2D melt performance and found 2D melt dynamics is even

faster than that predicted from the Rouse model [45]. Building on this work, Sussman et al (2014) used the same approach to analyze the entangled polymer melt confined in thin films and cylinders [46]. As shown in Figure 2.6, the red dashed line and the blue solid lines are calculated from the following equation 2.19.

$$\alpha^2_{film} \equiv \frac{1}{h}\int_0^h \frac{R^2_{ee,z,film}(z')\,dz'}{R^2_{ee,z,bulk}/\sqrt{3}} \qquad \text{Eq. 2.19}$$

Where in the equation α is the mean end-to-end vector normal to the wall. The equation appears to be a good prediction for the simulated end-to-end distance vector. It is found that under different degrees of confinement, the chains are compressed in the direction normal to the surface and elongated parallel to the surface [46]. At high values of δ, which implies that the polymers are no longer under extreme confinement, the chain conformation behaves more resembling the bulk conformation.

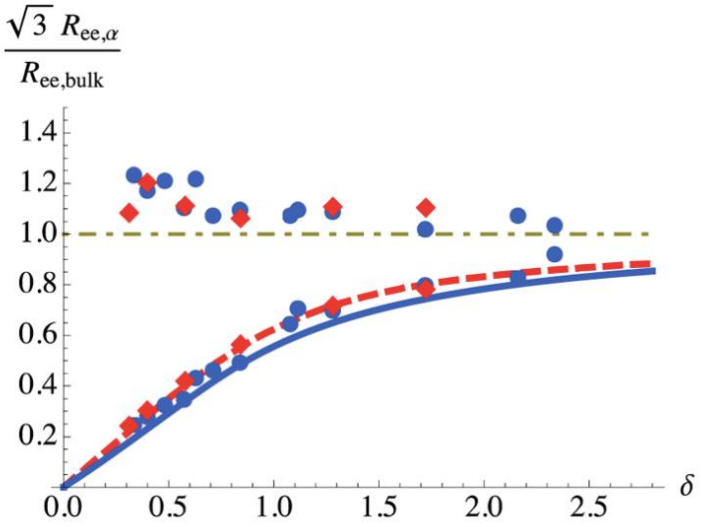

Figure 2.6. Root mean square component of the end-to-end distance vector of the cylindrically confined (blue circles and line) polymer melt as well as thin film confined (red diamond, dashed line) polymer melt. The blue solid line

and the red dashed line are the ones predicted from the equation, and the symbols are the simulation value. The gray dash-dotted line represents the bulk value of $R_{ee,bulk}/3$. δ is the confinement parameter such that $\delta \equiv 2r_{eff}/R_{ee,bulk}$. The upper points above the dot-dashed lines are the component parallel to the surface while the lower point is the component normal to the surface. The figure is adapted from reference 46 with permission.

While the polymer melt under confinement experiences changes in its chain dimensions in different directions, it also experiences a decrease in the number of entanglements. Sussman et al (2014) also found that as the polymer gets more confined, the number of entanglements of the melt chain decreases as shown in Figure 2.7.

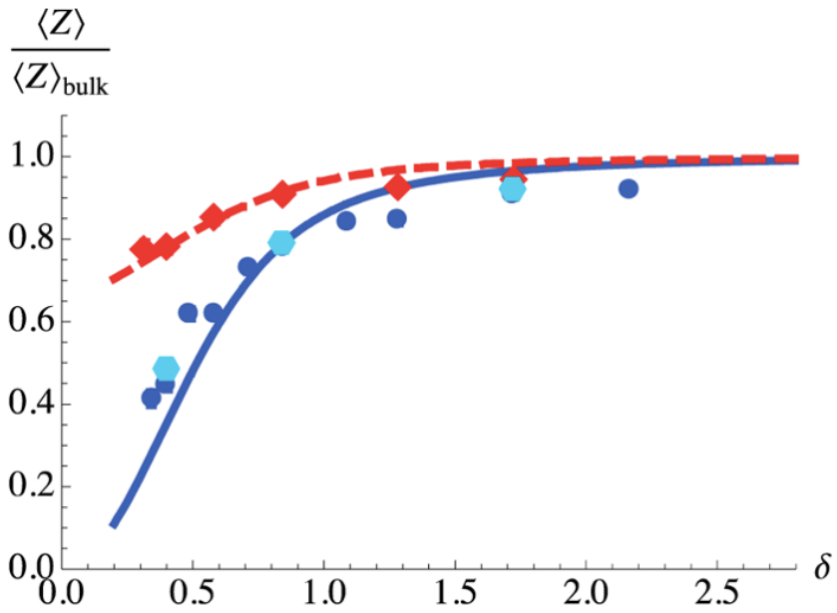

Figure 2.7. Normalized number of entanglements per chain with respect to the bulk for cylindrical confinement (blue) and thin film confinement (red). The figure is adapted from reference 46 with permission.

In summary, many simulations work has been conducted to probe the molecular level chain properties. It has been found that confinement in general changes the geometrical shape of

the chains as well as decreases the number of entanglements. These insights are critical to analyze polymer infiltration inside NPG under different conditions in the next coming chapters.

2.5 Summary

In this chapter, a comprehensive review has been provided on the theoretical and experimental topic needed to analyze the research presented in this thesis. The polymer kinetics under bulk has been introduced first, which includes the unentangled polymer kinetics, entangled polymer kinetics and the WLF relations. The polymer bulk performance sets an excellent baseline for the confined polymer to compare with and later analyze the data. The bulk polymer kinetics has been extensively used for analysis in Chapter 4, 5 and 7. Followed by the bulk polymer behavior, the polymer kinetics under confinement has been discussed. First, the LWE which describes the liquid imbibition inside narrow channels is introduced. Then, the polymer viscosity under confinement is built upon the LWE, with a detailed analysis on the effect of confinement, effect of dead zone, and reputation under confinement. This section is highly related to Chapter 4-7. Lastly, the polymer properties and conformation under confinement is reviewed. The confined polymer T_g as well as chain shape conformation are discussed, which is relevant to Chapters 4-7. This chapter provides an exhaustive overview of the theoretical backgrounds needed to better understand this thesis.

2.6 References

1. Maguire, S. M. *et al.* Effect of Nanoscale Confinement on Polymer-Infiltrated Scaffold Metal Composites. *ACS Appl. Mater. Interfaces* **13**, 44893–44903 (2021).

2. Kong, W. *et al.* Capillary filling dynamics of polymer melts in a bicontinuous nanoporous scaffold. *J. Chem. Phys.* **160**, 044904 (2024).

3. Venkatesh, R. B. & Lee, D. Conflicting Effects of Extreme Nanoconfinement on the Translational and Segmental Motion of Entangled Polymers. *Macromolecules* **55**, 4492–4501 (2022).

4. Hor, J. L., Wang, H., Fakhraai, Z. & Lee, D. Effects of polymer–nanoparticle interactions on the viscosity of unentangled polymers under extreme nanoconfinement during capillary rise infiltration. *Soft Matter* **14**, 2438–2446 (2018).

5. Rubinstein, M. & Colby, R. H. *Polymer Physics*. (Oxford University Press, Oxford ; New York, 2003).

6. Fox, T. G. & Flory, P. J. Viscosity—Molecular Weight and Viscosity—Temperature Relationships for Polystyrene and Polyisobutylene [1,2]. *J. Am. Chem. Soc.* **70**, 2384–2395 (1948).

7. Fox, T. G. & Flory, P. J. Further Studies on the Melt Viscosity of Polyisobutylene. *J. Phys. Chem.* **55**, 221–234 (1951).

8. Colby, R. H., Fetters, L. J. & Graessley, W. W. The melt viscosity-molecular weight relationship for linear polymers. *Macromolecules* **20**, 2226–2237 (1987).

9. Pearson, D. S., Fetters, L. J., Graessley, W. W., Ver Strate, G. & Von Meerwall, E. Viscosity and self-diffusion coefficient of hydrogenated polybutadiene. *Macromolecules* **27**, 711–719 (1994).

10. Jensen, K. H. *et al.* Sap flow and sugar transport in plants. *Rev. Mod. Phys.* **88**, 035007 (2016).

11. Yao, Y., Butt, H.-J., Floudas, G., Zhou, J. & Doi, M. Theory on Capillary Filling of Polymer Melts in Nanopores. *Macromol. Rapid Commun.* **39**, 1800087 (2018).

12. Washburn, E. W. The Dynamics of Capillary Flow. *Phys. Rev.* **17**, 273–283 (1921).

13. Lucas, R. Ueber das Zeitgesetz des kapillaren Aufstiegs von Flüssigkeiten. *Kolloid-Z.* **23**, 15–22 (1918).

14. Hu, G. & Cao, B. Flows of Polymer Melts through Nanopores: Experiments and Modelling. *J. Therm. Sci. Technol.* **8**, 363–369 (2013).

15. Shavit, A. & Riggleman, R. A. The dynamics of unentangled polymers during capillary rise infiltration into a nanoparticle packing. *Soft Matter* **11**, 8285–8295 (2015).

16. Yao, Y. *et al.* Complex dynamics of capillary imbibition of poly(ethylene oxide) melts in nanoporous alumina. *J. Chem. Phys.* **146**, 203320 (2017).

17. Semenov, A. N. & Obukhov, S. P. Fluctuation-induced long-range interactions in polymer systems. *J. Phys. Condens. Matter* **17**, S1747–S1775 (2005).

18. Johner, A., Shin, K. & Obukhov, S. Nanofluidity of a polymer melt: Breakdown of Poiseuille's flow model. *EPL Europhys. Lett.* **91**, 38002 (2010).

19. Shin, K. *et al.* Enhanced mobility of confined polymers. *Nat. Mater.* **6**, 961–965 (2007).

20. Tu, C.-H., Zhou, J., Doi, M., Butt, H.-J. & Floudas, G. Interfacial Interactions During In Situ Polymer Imbibition in Nanopores. *Phys. Rev. Lett.* **125**, 127802 (2020).

21. Kimmich, R., Fatkullin, N., Mattea, C. & Fischer, E. Polymer chain dynamics under nanoscopic confinements. *Magn. Reson. Imaging* **23**, 191–196 (2005).

22. Mangal, R., Srivastava, S. & Archer, L. A. Phase stability and dynamics of entangled polymer–nanoparticle composites. *Nat. Commun.* **6**, 7198 (2015).

23. Keddie, J. L., Jones, R. A. L. & Cory, R. A. Size-Dependent Depression of the Glass Transition Temperature in Polymer Films. *Europhys. Lett. EPL* **27**, 59–64 (1994).

24. Choi, J., Clarke, N., Winey, K. I. & Composto, R. J. Fast Polymer Diffusion through Nanocomposites with Anisotropic Particles. *ACS Macro Lett.* **3**, 886–891 (2014).

25. Tarnacka, M. *et al.* The Impact of Molecular Weight on the Behavior of Poly(propylene glycol) Derivatives Confined within Alumina Templates. *Macromolecules* **52**, 3516–3529 (2019).

26. Ediger, M. D. & Forrest, J. A. Dynamics near Free Surfaces and the Glass Transition in Thin Polymer Films: A View to the Future. *Macromolecules* **47**, 471–478 (2014).

27. Schneider, H. M., Frantz, P. & Granick, S. The Bimodal Energy Landscape When Polymers Adsorb. *Langmuir* **12**, 994–996 (1996).

28. Lange, F. *et al.* Large-Scale Diffusion of Entangled Polymers along Nanochannels. *ACS Macro Lett.* **4**, 561–565 (2015).

29. Roth, C. & Dutcher, J. Mobility on Different Length Scales in Thin Polymer Films. in *Soft Materials* (eds. Marangoni, A. & Dutcher, J.) 1–38 (CRC Press, 2004). doi:10.1201/9780203027004.ch1.

30. Choi, J. *et al.* Universal Scaling of Polymer Diffusion in Nanocomposites. *ACS Macro Lett.* **2**, 485–490 (2013).

31. Askar, S., Wei, T., Tan, A. W. & Torkelson, J. M. Molecular weight dependence of the intrinsic size effect on *T* g in AAO template-supported polymer nanorods: A DSC study. *J. Chem. Phys.* **146**, 203323 (2017).

32. Schneider, G. J. Dynamics of nanocomposites. *Curr. Opin. Chem. Eng.* **16**, 65–77 (2017).

33. Gam, S. *et al.* Macromolecular Diffusion in a Crowded Polymer Nanocomposite. *Macromolecules* **44**, 3494–3501 (2011).

34. Bocquet, L. Nanofluidics coming of age. *Nat. Mater.* **19**, 254–256 (2020).

35. Bansal, A. *et al.* Quantitative equivalence between polymer nanocomposites and thin polymer films. *Nat. Mater.* **4**, 693–698 (2005).

36. Hor, J. L., Wang, H., Fakhraai, Z. & Lee, D. Effect of Physical Nanoconfinement on the Viscosity of Unentangled Polymers during Capillary Rise Infiltration. *Macromolecules* **51**, 5069–5078 (2018).

37. Hor, J. L. *et al.* Nanoporous Polymer-Infiltrated Nanoparticle Films with Uniform or Graded Porosity *via* Undersaturated Capillary Rise Infiltration. *ACS Nano* **11**, 3229–3236 (2017).

38. Wang, H. *et al.* Dramatic Increase in Polymer Glass Transition Temperature under Extreme Nanoconfinement in Weakly Interacting Nanoparticle Films. *ACS Nano* **12**, 5580–5587 (2018).

39. Venkatesh, R. B. *et al.* Polymer-Infiltrated Nanoparticle Films Using Capillarity-Based Techniques: Toward Multifunctional Coatings and Membranes. *Annu. Rev. Chem. Biomol. Eng.* **12**, 411–437 (2021).

40. Ring, D. J., Riggleman, R. A. & Lee, D. Critical Contact Angle to Induce Capillary Rise of Polymers in Nanopores Does Not Depend on Chain Length. *ACS Macro Lett.* **8**, 31–35 (2019).

41. Mackay, M. E. *et al.* General Strategies for Nanoparticle Dispersion. *Science* **311**, 1740–1743 (2006).

42. Jouault, N. *et al.* Polymer Chain Behavior in Polymer Nanocomposites with Attractive Interactions. *ACS Macro Lett.* **5**, 523–527 (2016).

43. Crawford, M. K. *et al.* Chain Conformation in Polymer Nanocomposites with Uniformly Dispersed Nanoparticles. *Phys. Rev. Lett.* **110**, 196001 (2013).

44. Bailey, E. J., Riggleman, R. A. & Winey, K. I. Polymer Conformations and Diffusion through a Monolayer of Confining Nanoparticles. *Macromolecules* **53**, 8171–8180 (2020).

45. Meyer, H., Kreer, T., Cavallo, A., Wittmer, J. P. & Baschnagel, J. On the dynamics and disentanglement in thin and two-dimensional polymer films. *Eur. Phys. J. Spec. Top.* **141**, 167–172 (2007).

46. Sussman, D. M., Tung, W.-S., Winey, K. I., Schweizer, K. S. & Riggleman, R. A. Entanglement Reduction and Anisotropic Chain and Primitive Path Conformations in Polymer Melts under Thin Film and Cylindrical Confinement. *Macromolecules* **47**, 6462–6472 (2014).

CHAPTER 3. EXPERIMENTAL METHODS AND CHARACTERIZATION TECHNIQUES

3.1 Introduction

For most scientific experiments, the procedures involve four different steps: 1. Sample preparation, 2. Sample processing, 3. Sample characterization and 4. Data analysis. In this thesis dissertation, sample preparation involves spin coating polymer thin films onto substrates, followed by depositing nanoporous gold (NPG) scaffold on top of the polymer thin film to form the bilayer system. Sample processing includes procedures such as annealing the bilayer system at an elevated temperature to induce certain degrees of infiltration. Sample characterization involves sample optical properties measurement, surface characterization and structure characterization. Data analysis is different for each project, and thus will be discussed separately in each according chapter.

3.1.1 Experimental Review of Capillary Rise Infiltration (CaRI)

In this thesis, we study moderately confined polymers inside NPG scaffold, which fills in current academia research gaps in both infiltration membrane geometries and the polymer confinement ratio ranges. This section 3.1.1 will conduct a generic review of existing research on CaRI kinetics inside different confined membranes.

Previous CaRI studies have been mostly focused on polymers inside highly confined nanochannels, but the moderately confined polymers have remained relatively unexplored. Using CaRI, polydimethylsiloxane (PDMS) infiltration was investigated into a dense silica NP packing

with a confinement ratio, $\Gamma = \frac{R_g}{R_p}$, varying from 0.6 to 1.5. This system[1] exhibited a crossover in diffusive behavior at $\Gamma = 1$, with $D \propto N^{-1}$ for $\Gamma > 1$ and a scaling exponent between 0 and -1 for $\Gamma < 1$. Research of CaRI infiltration has also been conducted at highly confined regimes. PS infiltration into similar silica NP packings at much higher degrees of confinement[2], Γ varying from 2 to 15, exhibited viscosity scaling $\eta_{eff} \sim N^{0.8}$.

The polymer infiltration has been studied inside geometries of 2D silt, cylindrical nanochannels and interstitials between the nanoparticle (NP) packings, but studies remain unexplored for NPG geometry, where the gold ligaments are bicontinuously interconnected. In previous work, studies have been conducted to infiltrate polymers into 2D slit geometry[3], densely packed nanoparticles [1,2,4–10] and anodized aluminum oxide (AAO) pores [11–14] using the CaRI approach.

This thesis investigates the polymer kinetics and optical properties inside semi-confined bicontinuous NPG scaffolds. The confinement parameters Γ lies in between 0.18 to 0.97 across all chapters in the thesis, where the polymers undergo moderate degrees of confinement. The NPG, on the other hand, has been widely used for research in optical sensing [15] and battery applications [16,17]. However, NPG has not been used for infiltration studies. In the remainder of Chapter 3, the general experimental procedures and the characterization techniques will be discussed in detail.

3.2 Preparation of Polymer Infiltrated Nanoporous Gold (PING) Films

Preparation of the PING films includes three steps – 1. Dealloy and pre-anneal NPG, 2. Prepare polymer/NPG bilayer, and 3. Annealing bilayer system. In the following section, those three steps will be discussed in more detail.

3.2.1 Preparation of NPG membrane

NPG is crucial in this thesis as it is used as the structure and template for measuring polymer kinetics during the PING formation. 120 nm thick NPG are prepared using a gold alloy anodic corrosion methodology[18]. A Au-Ag (12 karat) foil with $Au_{35}Ag_{65}$ at %, is purchased and used as received. 15.8 M Nitric Acid is used to selectively etch Ag from the 12-karat composite. As the Au-Ag foil is immersed in nitric acid, HNO_3 first dissolves the less noble Ag atoms at the interface, leaving behind the Au rich layer. Subsequently, the Au atoms nucleate and grow Au-rich islands, which in turn exposes the underlying layer containing Ag. The Au islands eventually form the bicontinuous structure used in this study. The NPG formation process is captured by Figure 3.1 modeled by kinetics Monte Carlo Simulation[19].

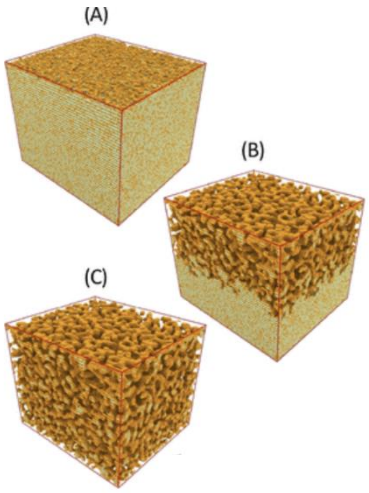

Figure 3.1. NPG porosity evolution generated through kinetics Monte Carlo simulations[19]. Part a depicts the initial 12k Ag/Au alloy in immediate contact with the acid at the interface. Part b shows the dealloying process, where the gold ligaments are gradually formed and interconnected. At this stage, there are still some minor residual Ag atoms left. Part c describes the completed etching process, where the whole structure is now composed of a bicontinuous NPG structure with minor Ag atoms residing. The figure is taken from reference 19 with permission.

The fabrication and structural characterization of the NPG has been previously studied [16,17,20]. Due to the high mobility of the gold atoms, the NPG scaffolds are annealed at 175°C for 3 h prior to forming a bilayer unless otherwise noted specifically. This pre-annealing step prevents structural changes in the NPG during polymer infiltration at 150°C [21] as shown in the following Figure 3.2. Pre-annealing prevents NPG coarsening is evidenced by the stable scattering peak position as shown in Figure 3.2. In this thesis, NPG refers to pre-annealed NPG.

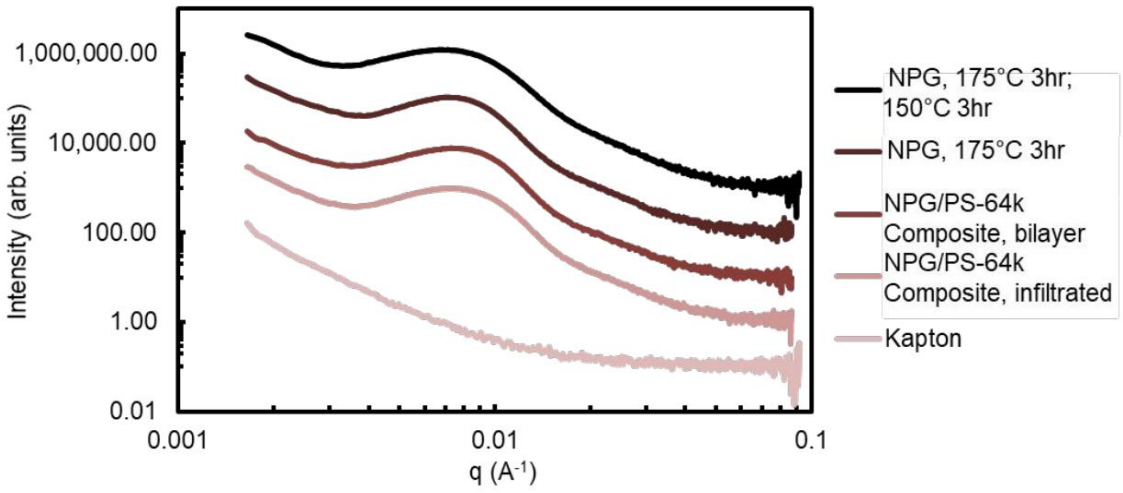

Figure 3.2. SAXS profiles of the NPG films and composites after the thermal processing techniques[21] . The figure is taken from reference 21 with permission.

3.2.2 Preparation of polymer/NPG bilayer structure

To prepare the polymer/NPG bilayer structure, firstly polymer thin films are prepared. In this thesis, polystyrene and poly(2-vinylpyridine) (P2VP) are used to make thin films. Firstly, PS and P2VP are dissolved in toluene and methanol respectively to make 2.4 wt% solutions, followed by slight heating (40°C) and constant stirring overnight. PS and P2VP solutions are then spin coated onto substrates (silicon wafer or glass substrate, depending on the nature of the project) at 4000 rpm for 1 min. After spin coating, the thin films are annealed in a Mettler hot chamber at 70°C under argon gas flow to ensure the solvent is completely evaporated. The resulting thin film thickness (90 - 500 nm) is characterized by a reflectometer. To form the NPG/PS bilayer, the pre-annealed NPG (1cm x 1cm) is floated onto a DI-H_2O surface. The suspended NPG is then lifted from underneath by a silicon wafer previously coated with a thin

PS film. The bilayer is then dried on a hot plate at 60°C until water is completely evaporated from the sample surface.

3.2.3 Thermal Annealing of polymer/NPG bilayer system

In this thesis, two types of thermal annealing are used – in situ annealing and ex situ annealing. For the ellipsometry measurements, in-situ annealing is applied while for the UV-Vis measurement, ex-situ annealing is used. For in-situ annealing, Linkam THMSEL350V heating stage with a vacuum chamber is used. The accuracy of the heating stage is 0.1°C with respect to the set temperature. The heating rate is 30°C/min, and the sealed chamber ensures a continuous flow of N_2 to prevent polymer degradation. The samples are heated to 70°C and held at this temperature for 5 minutes to ensure equilibrium before ramping to 150°C. Subsequently, the temperature is heated at a rate of 30°C/min and then held at 150 °C to study infiltration. The in-situ annealing enables us to study the instantaneous optical change of the materials in combination with ellipsometry. Similarly, ex-situ annealing is also used in this thesis. Ex-situ annealing is applied through the Mettler heating stage, where the temperature and annealing time can be precisely controlled. The Mettler heating stage is connected to an Argon gas tank, where continuous inert gas flow could well prevent polymer degradation during the infiltration process. The ex-situ heating is mainly used in the UV-Vis optical absorbance measurements.

3.3 Characterization Techniques

In the following sections, the major experimental characterization techniques involved in this thesis will be described and introduced.

3.3.1 Spectroscopic Ellipsometry (SE)

SE is an optical measurement tool to probe the change in the state of polarized light when being reflected off a material's sample surface. In this thesis, SE (J.A. Woollam, Alpha SE) is used to determine the infiltration extent of polymer in the NPG. The utilized wavelength range is 380-900nm. A Linkam THMSEL350V heating stage with a vacuum chamber is used for heating. The accuracy of the heating stage is 0.1°C with respect to the set temperature. The heating rate is 30°C/min, and the sealed chamber ensures a continuous flow of N_2 to prevent polymer degradation. The samples are heated to 70°C and held at this temperature for 5 minutes to ensure equilibrium before ramping to 150°C. Subsequently, the temperature is heated at a rate of 30°C/min and then held at 150 °C to study infiltration. Because the bulk PS/P2VP T_g is 100°C, temperatures higher than 100°C will induce polymer infiltration into NPG. As a result, the infiltration time refers to the time after when the heating plate reaches 100°C. The heating stage takes ca. 1.7 min to ramp from 100°C to 150°C. During infiltration, the temperature is stably held at 150°C. Effective Medium Approximation (EMA) Model with two material constitutes (see SI for further information) is used to capture the change in optical constants within the NPG composite as polymer fills the pores and approaches the top surface. The infiltration extent (IE) is given by, $IE = \frac{(n_t - n_i)}{(n_f - n_i)}$. The initial refractive index, n_i , is calculated by averaging the refraction index values during the first six min (i.e., prior to the PS infiltration). The final refractive index (after complete infiltration), n_f, is calculated by averaging the refraction index during the last two minutes when infiltration is complete.

3.3.1.1 SE modeling

The PS-NPG bilayer and PING nanocomposite can be modeled through a multilayer ellipsometry model [22]. Prior to infiltration, the topmost layer, which is in contact with air, can be modeled as a composite that is composed of a certain percentage of gold and air; the middle layer is a uniform polymer thin film; and the bottom layer is the silicon substrate. The initial refraction index of the top layer at 632.8 nm (n_i) is ~ 0.85, and the percentage of air measured is ~50% from the model. Take PS/NPG infiltration as an example, during the infiltration process, the polymer reptates into the porous region, thus changing the refraction index of the porous part from 1 (n of air) to 1.59 (n of PS), thus resulting in an overall increase in n for the topmost layer. After the PS fully infiltrates into the NPG to form a PING, all of the pores from NPG are filled with PS, and the refractive index of the top layer stops increasing. The final refraction index of the PING composite layer at 632.8 nm (n_f) is ~ 1.25.

3.3.2 Quartz Crystal Microbalance with Dissipation (QCM-D)

QCM-D is an extremely surface sensitive technique that measures adsorption of polymer or small molecules on the quartz crystal surface. The quartz crystal, depicted in Figure 3.3, has two electrodes on both sides, serving as the resonating sensor. When polymer adsorbs to the QCM-D sensor surface, the thickness of the quartz crystal increases, thus resulting in a shift in the acoustic resonance frequency[23]. The resonance frequency shift can be used to calculate the area mass density of the adsorbed material through the Sauerbrey equation as listed in Equation 3.1, when the adsorbed mass is small relative to the mass of the crystal and is evenly distributed as well as rigidly bounded.

$$\Delta f = -\frac{2f_0^2}{\sqrt{\rho_q G_q'}} \frac{\Delta m}{A} \qquad \text{Eq. 3.1}$$

Where in this equation Δf is the shift in resonance frequency, f_0 is the resonance frequency of the fundamental mode, ρ_q is the density of the quartz crystal, G_q' is the elastic shear modulus of the crystal, Δm is the change in adsorbed mass, and A is the area of the sensor [24,25]. Similarly, the dissipation effect of the QCM-D is related to the ratio of energy loss per cycle to the total energy stored in the system such that $D = \frac{E''}{2\pi E'}$, where E'' and E' are the loss modulus and the stored modulus respectively[25].

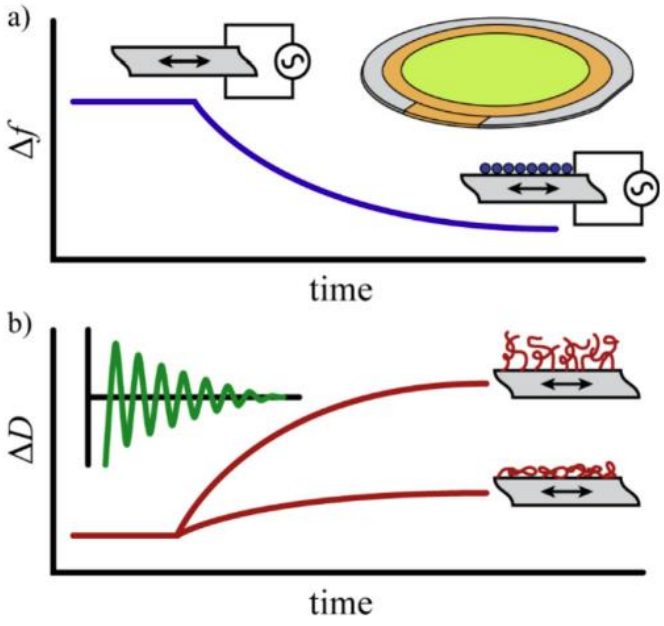

Figure 3.3 QCM-D working mechanism when polymers or particles are being adsorbed to the surface. (a) frequency change of the crystal when small molecules are adhered to the crystal surface; (b) dissipation change of the crystal when polymer chins are adsorbed to the surface[23]. The figure is taken from reference 23 with permission.

In this thesis, QCM-D is used to measure the polymer brush adsorption to the gold surface. The polymer adsorption measurements are performed using a Q- sense Analyzer QCM-D instrument. Prior to adsorption studies, the Au coated QCM-D sensors are loaded into the QCM-D flow cell and equilibrated in the DI-H_2O for an extended period of time until the drift in the measured frequency is < 1 Hz/hr. Once equilibrated, adsorption studies are performed by pumping the desired polymer solution into the flow cell at a flow rate of 50 mL/min and capturing the first 7 harmonics. After complete grafting, the polymer solution is replaced by the DI-H_2O and the harmonics are monitored for an additional 15 min.

3.3.3 Small Angle X-ray Scattering (SAXS)

X-ray scattering measures the intensity of the X-rays being scattered by a material as a function of scattering angle. In this study, SAXS is used to determine the NPG pore size and distribution. Dual Source and Environmental X-Ray Scattering (DEXS, Xenocs Xeuss 2.0) at University of Pennsylvania is used for measuring NPG ligament-ligament distance. Six tubes with sample to detector distance of 6390 mm results in a q_0 range of 0.003-0.09 $Å^{-1}$. Cu K_α, with a wavelength of 1.54 Å, is used as the light source. NPG samples are peeled off from the substrate using Kapton tape. The scattering data is collected for 1 h for each sample. The collected spectra are then azimuthally integrated into a curve for analysis. A control scattering collection of pure Kapton tape is also performed for 1 h to eliminate any effect from the tape on the scattering curve.

3.3.4 Ultraviolet-Visible Spectroscopy (UV-Vis)

UV-Vis is an analytical instrument that measures the adsorption of the light in the UV and the visible light range. In this thesis, UV-Vis is used to measure the absorbance of the polymer/NPG at different infiltration extents. Absorbance spectra were obtained using a Varian Cary Win 5000 UV-VIS-NIR Spectrophotometer with a wavelength range of 200-1000 nm. Measurements of the absorbance data were taken at various stages of infiltration with a frequency of 2 nm/sweep. The P2VP: NPG bilayer, atop of glass substrate, were annealed at 140℃ for different annealing times, inducing different polymer infiltration extents inside NPG. The absorbance spectra of glass is also taken and is included in the SI.

3.4 Computation Methods

In this thesis, two computational methods are used across the studies. The molecular dynamics (MD) simulation is used to better understand the polymer molecules' movement inside NPG. Compared to conducting and analyzing wet-lab experimental results, MD simulations provide us with more insights on individual molecule responses for different stimuli or environment on a microscopic level. The Discrete Dipole Approximation (DDA) computation, on the other hand, allows us to predict the optical responses under different systems. In the following sections, the basic physics of those two computation approaches, as well as the methodology used for this thesis, will be introduced.

3.4.1 Molecular Dynamics (MD) simulations

MD simulation is a very well-grounded methodology to study the molecule dynamics on a microscopic scale[26]. Utilizing the Newtonian mechanics, MD simulations are enabled to capture the position, structure, and motions of every single atom that made up the simulation system[26]. In the MD simulations, the intramolecular forces are calculated through the potential energy function, and the motions (velocities) of the atoms are assigned through the Maxwell-Boltzmann distribution[26]. In this thesis, the MD simulations provide us with more insights on polymer dynamics as well as polymer structure and interaction with the NPG wall, when the polymer is traveling inside moderately confined NPG. The detailed methodology is described in the following paragraphs.

Entangled polymer melts are simulated using a modified coarse-grained bead-spring Kremer-Grest (KG) model [27]. Nonbonded monomers interact through the LJ potential $U_{ij}^{nb} = 4\epsilon\left[\left(\frac{\sigma}{r}\right)^{12} - \left(\frac{\sigma}{r}\right)^{6}\right] - 4\epsilon\left[\left(\frac{\sigma}{r_{cut}}\right)^{12} - \left(\frac{\sigma}{r_{cut}}\right)^{6}\right]$ for $r \le r_{cut} = 2.5\sigma$. Units are non-dimensionalized using the potential strength, ϵ; monomer size, σ; and unit time, $\tau = \sigma\left(\frac{m}{\epsilon}\right)^{\frac{1}{2}}$, where m is the monomer mass. Monomers bonded together on the same chain interact via a finitely extensible nonlinear elastic (FENE) potential $U_{ij}^{b} = -0.5kR_0^2 \ln\left[1 - \left(\frac{r}{R_0}\right)^2\right] + 4\epsilon\left[\left(\frac{\sigma}{r}\right)^{12} - \left(\frac{\sigma}{r}\right)^{6}\right] + \epsilon$ with $k = \frac{30\epsilon}{\sigma^2}$ and $R_0 = 1.5\sigma$. The original KG model is modified by the additional of an angular harmonic potential $U_{ang} = \frac{K_\theta}{2}(\theta - \theta_0)^2$ where $K_\theta = 10$ per radian^2 is the interaction strength and $\theta_0 = 120°$ is the equilibrium bond angle. This potential increases the average number of

entanglements per chain without requiring long chain lengths, giving an average number of monomers between entanglements of $< N_e > \approx 17.5$ [28].

Polymer films are generated by random growth of polymers in a simulation box with walls on the top and bottom, followed by the application of soft potentials to push overlapped monomers apart. For efficient equilibration of entangled polymers, connectivity-altering Monte Carlo moves are used [29,30]. Films are equilibrated at high temperature, $T = 1.2$, and a time step of $\Delta t = 0.002\tau$. Equilibration proceeds until diffusive behavior of the center of mass mean squared displacement (MSD) is observed. The MSD is calculated with a moving time origin for improved statistics, and three independent film configurations are generated for each system.

All polymers in this study are above the entanglement degree of polymerization. The number of monomers per chain are 25, 50, 100, 150, and 200, with N/N_e approximately equal to 1.5, 3.0, 6.0, 8.5, and 11.5, respectively. The entanglement statistics during the equilibration of chains are included in Figure S7 of the Supporting Information. The polymer density is $0.85/\sigma^{-3}$. The films have dimensions $L_x = L_y = 100\sigma, L_z = 40\sigma$. The polymer films are placed on a 2σ thick support consisting of immobile LJ particles with a configuration taken from the middle 2σ of a larger film.

A simulation box with hard walls at the top and bottom and dimensions $L_x = L_y = 100\sigma, L_z = 400\sigma$ is randomly filled with two types of LJ particles. A repulsive LJ potential is applied to induce spinodal decomposition. Simulations are run until the average ligament-to-ligament distance reaches the desired value, and then one of the two particle types is deleted, creating a nanoporous structure. LJ particles which are separated from the surface, or those with

no nearest neighbors, are removed to create a nanoporous structure. The top and bottom surfaces are deleted, and the structure is placed 1σ from the top of the free surface of the supported polymer film. The LJ potential between particles within the nanoporous structure and polymer atoms can be modified depending on the system i.e., $\epsilon = 1.0$ and $\sigma = 1.0$ for PS/NPG infiltration while $\epsilon = 5.0$ and $\sigma = 1.0$ for the P2VP/NPG system. Here, we create a nanoporous structure with an average pore radius $R_{pore} = 6.27\sigma$. The confinement ratio is defined as the polymer radius of gyration within a bulk melt over the pore radius, $\Gamma = R_g/R_{pore}$. The polymer is allowed to infiltrate the nanoporous structure during constant NVT dynamics at $T = 1.2$. Simulation images of the nanoporous gold structure, as well as initial and post-infiltration polymer configurations, are shown in Figure 3.4

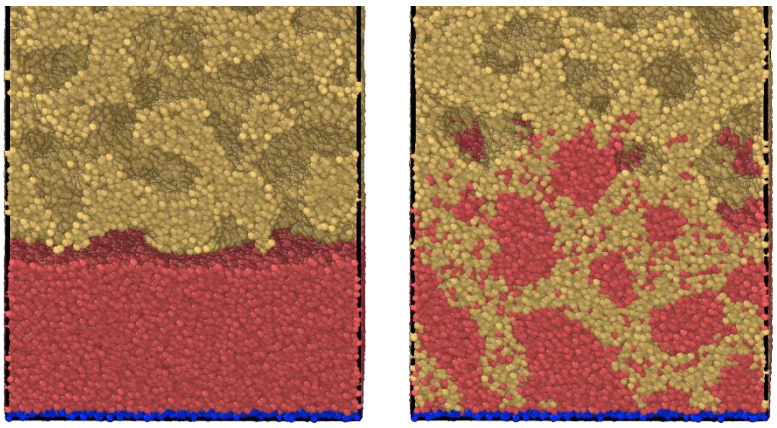

.

Figure 3.4. Particles that make up the nanoporous structure are shown in gold, polymer beads are shown in red, and particles within the thin support structure at the bottom of the polymer layer are shown in blue. The system is periodic in x and y directions. Figure adopted from ref. 22 with permission.

3.4.2 Discrete Dipole Approximation (DDA)

DDA enables researchers to better understand and calculate the responses between a system and an electromagnetic wave[31]. In this thesis, DDA is used to simulate the optical response of the NPG/polymer composite as a function of infiltration extent. The optical properties are the extinction coefficient, localized surface-plasmon resonance (LSPR) wavelength, and LSPR absorption strength, which are calculated using the MATLAB toolbox [32,33]. The incident light is demonstrated in the form of an electric field. In this simulation, the incident light is set to be polarized in x direction and propagated in z direction. The scatterer in this study is the gold ligament, since the light absorption coefficient of P2VP or air is negligible. The T-shape model, as shown in Figure 1, is used to simplify the NPG ligament structure while introducing plasmon hybridization effects to reduce the sensitivity upon change of medium dielectric constant [34,35]. To construct the "T" nanostructure, two nanorods are connected, with one origin defined at the center of the other ligament. Those two rods have longer axes set to be parallel to the y and z axis respectively and perpendicular to the polarization direction.

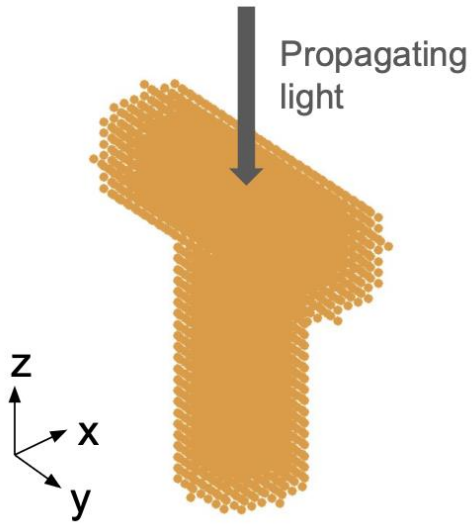

Figure 3.5. The T-shape structure is used to model the ligaments in the NPG using the DDA simulation. The dimensions are r = 25 nm and L = 125 nm for both rods forming the T-shape.

The T-shape model is placed in the Cartesian coordinate and discredited into a cubic array of dipoles. The polarizability of each dipole is calculated by the Clausius-Mossotti relationship[36] as shown in Equation 3.2 below.

$$\alpha_i = \frac{3d^3}{4\pi}\left(\frac{\epsilon_i - 1}{\epsilon_i + 2}\right) \qquad \text{Equation. 3.2}$$

where ϵ_i is the dielectric constant of dipole i, and d is the lattice constant. This preceding expression is further corrected by Draine and Goodman to the widely used lattice dispersion relation[37] as shown in Equation 3.3,

$$\alpha_i^{LDR} = \frac{\alpha_i}{1+(\alpha_I/d^3)[(b_1+m^2b_2+m^2b_3S)(kd)^2-i(2/3)(kd)^3]} \qquad \text{Equation. 3.3}$$

where b_1=-1.891531, b_2=0.1648469, b_3=-1.770004, m is the refractive index, and S is a real number associated with the polarization of the incident radiation such that $S=\sum_{j=1}^{3}(\hat{\alpha}_j\hat{e}_j)^2$, where $\hat{\alpha}$ and $\hat{e}$ are unit vectors pointing in the propagation and polarization directions of the incident radiation.

As the ligament diameter size is observed to be around 50 nm by AFM images, which is comparable to the mean free path of gold conduction electrons (42 nm at room temperature), the bulk dielectric constant fails to describe the plasmon behaviors [38]. Thus, to account for the increasing electron collisions at nanoparticle surface, a correction to the dielectric constant is needed in DDA calculation, expressed as Equation 3.4 [38],

$$\varepsilon_{NP}(\omega, r_{eff}) = \varepsilon_{bulk}(\omega) + \frac{\omega_p^2}{\omega^2 + i\Gamma_0\omega} - \frac{\omega_p^2}{\omega^2 + i\Gamma(r_{eff})\omega} \quad \text{Equation. 3.4}$$

where ε_{bulk} is the bulk dielectric constant at wavelengths from 400 to 800 nm obtained from Johnson and Christy [39], ω is the frequency of the incident light, $\omega_p = 1.35 \times 10^{16} \text{rad} \cdot s^{-1}$ is the gold plasma frequency [40], $\Gamma_0 = 1.07 \times 10^{14} \text{rad} \cdot s^{-1}$ is the electron collision frequency in bulk gold[40], $r_{eff} = (3V/4\pi)^{1/3}$ represents for the effective radius where $V = 2\pi \times L \times r^2 - 8/3 \times r^3$ for the T-shape model, with r = 25 nm and L = 125 nm. $\Gamma(r_{eff})$ is the corrected collision frequency given by $\Gamma(r_{eff}) = \Gamma_0 + A\frac{V_F}{r_{eff}}$, where A = 1 is the empirical parameter for gold, and $V_F = 1.4 \times 10^6 \text{ m/s}$ is the Fermi velocity [41].

Since each dipole interacts with the incident electromagnetic field, to calculate the dipole moment and absorption coefficient, there are contributions from both re-radiating dipoles and the incident E field. The re-radiating dipoles are assumed to be instantaneously re-radiated given such small spacing. Thus, the final electric field received at each dipole consists of two components, $E_i = E_{inc} - \sum_{j \neq i} A_{ij} P_j$,where $P_j = \alpha_j E_j$ is the polarization of dipole j. The interaction tensor A_{ij} can be determined by an off-diagonal matrix according to the Green's tensor of electric field of radiation derived from the vector Helmholtz equation [33] as shown in Equation 3.5,

$$A_{jk} = \frac{\exp(ikr_{jk})}{r_{jk}} \times [k^2(\hat{r}_{jk}\hat{r}_{jk} - I_3) + \frac{ikr_{jk} - 1}{r_{jk}^2}(3\hat{r}_{jk}\hat{r}_{jk} - I_3)] \quad \text{Equation. 3.5}$$

where I_3 is the 3×3 identity matrix, $r_{jk} = |r_j - r_k|$, and $\hat{r}_{jk} = (r_j - r_k)/r_{jk}$.

The diagonal tensors for self-radiation can be defined as the inversion of polarizability, $A_{jj} = \alpha_j^{-1}$. Thus, the original system of linear equations can be simplified as Equation 3.6 below:

$$\sum_j A_{ij} P_j = E_{inc} \qquad \text{Equation. 3.6}$$

which can be solved by standard numerical methods and used to obtain the dipole polarizability.

During polymer infiltration, the surrounding of the gold ligament changes from air to a bilayer of air and P2VP. To calculate the medium dielectric constant, effective medium approximation is used based on the characteristic matrix technique, thus, the optical properties of the bilayer structure can be determined by $n_{eff}^2 = (n_1^2 h_1 + n_2^2 h_2)/h$ [42], where $n_1 = 1.0003$ and $n_2 = 1.54$ are the refractive index of air and P2VP accordingly, while h_2, h_1, and h are the height of the infiltrated portion, residual portion, and the total height of the model which equals to 150 nm.

Finally, given polarizabilities of each dipole and the incident light electric field, the absorption (C_{abs}) and scattering cross sections (C_{sca}) can be calculated, respectively via the following two equations [33],

$$C_{abs} = \frac{4\pi k}{|E_0|^2} \sum_{i=1}^{N} \{ Im[P_i (\alpha_i^{-1})^* P_i^*] - \frac{2}{3} k^3 |P_i|^2 \} \qquad \text{Equation. 3.7}$$

$$C_{sca} = \frac{4\pi k}{|E_0|^2} \sum_{i=1}^{N} Im(E_i^* P_i) - C_{abs} \qquad \text{Equation. 3.8}$$

where E_i^*, P_i^*, and α_i^* represent the complex conjugates. The sum of two cross sections is the extinction cross section, C_{ext}. The absorption, scattering, and extinction efficiency coefficients are defined as the following equations and will be used for analysis in the result section.

$$Q_{abs} = \frac{C_{abs}}{\pi\alpha_{eff}^2} \quad \text{Equation. 3.9}$$

$$Q_{sca} = \frac{C_{sca}}{\pi\alpha_{eff}^2} \quad \text{Equation. 3.10}$$

$$Q_{ext} = Q_{abs} + Q_{sca} \quad \text{Equation. 3.11}$$

3.5 References

1. Venkatesh, R. B. & Lee, D. Interfacial Friction Controls the Motion of Confined Polymers in the Pores of Nanoparticle Packings. Macromolecules **55**, 8659–8667 (2022).

2. Venkatesh, R. B. & Lee, D. Conflicting Effects of Extreme Nanoconfinement on the Translational and Segmental Motion of Entangled Polymers. Macromolecules **55**, 4492–4501 (2022).

3. Manias, E. et al. Intercalation Kinetics of Long Polymers in 2 nm Confinements. Macromolecules **33**, 7955–7966 (2000).

4. Venkatesh, R. B. et al. Effect of polymer–nanoparticle interactions on solvent-driven infiltration of polymer (SIP) into nanoparticle packings: a molecular dynamics study. Mol. Syst. Des. Eng. **5**, 666–674 (2020).

5. Hor, J. L., Wang, H., Fakhraai, Z. & Lee, D. Effects of polymer–nanoparticle interactions on the viscosity of unentangled polymers under extreme nanoconfinement during capillary rise infiltration. Soft Matter **14**, 2438–2446 (2018).

6. Huang, Y.-R. et al. Polymer nanocomposite films with extremely high nanoparticle loadings via capillary rise infiltration (CaRI). Nanoscale **7**, 798–805 (2015).

7. Qiang, Y., Pande, S. S., Lee, D. & Turner, K. T. The Interplay of Polymer Bridging and Entanglement in Toughening Polymer-Infiltrated Nanoparticle Films. ACS Nano **16**, 6372–6381 (2022).

8. Qiang, Y., Turner, K. T. & Lee, D. Role of Polymer–Nanoparticle Interactions on the Fracture Toughness of Polymer-Infiltrated Nanoparticle Films. Macromolecules **56**, 122–135 (2023).

9. Ren, T. et al. Increase in the effective viscosity of polyethylene under extreme nanoconfinement. J. Chem. Phys. **160**, 024909 (2024).

10. Hor, J. L., Wang, H., Fakhraai, Z. & Lee, D. Effect of Physical Nanoconfinement on the Viscosity of Unentangled Polymers during Capillary Rise Infiltration. Macromolecules **51**, 5069–5078 (2018).

11. Shin, K. et al. Enhanced mobility of confined polymers. Nat. Mater. **6**, 961–965 (2007).

12. Tu, C.-H., Zhou, J., Butt, H.-J. & Floudas, G. Adsorption Kinetics of cis -1,4-Polyisoprene in Nanopores by In Situ Nanodielectric Spectroscopy. Macromolecules **54**, 6267–6274 (2021).

13. Tu, C.-H., Zhou, J., Doi, M., Butt, H.-J. & Floudas, G. Interfacial Interactions During In Situ Polymer Imbibition in Nanopores. Phys. Rev. Lett. **125**, 127802 (2020).

14. Yao, Y., Butt, H.-J., Zhou, J., Doi, M. & Floudas, G. Capillary Imbibition of Polymer Mixtures in Nanopores. Macromolecules **51**, 3059–3065 (2018).

15. Detsi, E., Salverda, M., Onck, P. R. & De Hosson, J. Th. M. On the localized surface plasmon resonance modes in nanoporous gold films. J. Appl. Phys. **115**, 044308 (2014).

16. Welborn, S. S., Van Der Meer, S., Corsi, J. S., De Hosson, J. Th. M. & Detsi, E. Using X-Ray Scattering to Elucidate the Microstructural Instability of 3D Bicontinuous Nanoporous Metal Scaffolds for Use in an Aperiodic 3D Tricontinuous Conductor–Insulator–Conductor Nanocapacitor. ACS Appl. Mater. Interfaces **13**, 11721–11731 (2021).

17. Ng, A. K., Welborn, S. S. & Detsi, E. Time-dependent power law function for the post-dealloying chemical coarsening of nanoporous gold derived using small-angle X-ray scattering. Scr. Mater. **206**, 114215 (2022).

18. Ding, Y., Kim, Y.-J. & Erlebacher, J. Nanoporous Gold Leaf: Ancient Technology Advanced Material. Adv. Mater. **16**, 1897–1900 (2004).

19. Wittstock, G. et al. Nanoporous Gold: From Structure Evolution to Functional Properties in Catalysis and Electrochemistry. Chem. Rev. **123**, 6716–6792 (2023).

20. Welborn, S. S. & Detsi, E. Small-angle X-ray scattering of nanoporous materials. Nanoscale Horiz. **5**, 12–24 (2020).

21. Maguire, S. M. et al. Effect of Nanoscale Confinement on Polymer-Infiltrated Scaffold Metal Composites. ACS Appl. Mater. Interfaces **13**, 44893–44903 (2021).

22. Kong, W. et al. Capillary filling dynamics of polymer melts in a bicontinuous nanoporous scaffold. J. Chem. Phys. **160**, 044904 (2024).

23. O'Bryan, C. S. et al. Electrochemically deposited molybdenum disulfide surfaces enable polymer adsorption studies using quartz crystal microbalance with dissipation monitoring (QCM-D). J. Colloid Interface Sci. **614**, 522–531 (2022).

24. Johannsmann, D. Gravimetric Sensing. in The Quartz Crystal Microbalance in Soft Matter Research 191–204 (Springer International Publishing, Cham, 2015). doi:10.1007/978-3-319-07836-6_8.

25. Dixon, M. C. Quartz crystal microbalance with dissipation monitoring: enabling real-time characterization of biological materials and their interactions. J. Biomol. Tech. JBT **19**, 151–158 (2008).

26. Soares, T. A. et al. Guidelines for Reporting Molecular Dynamics Simulations in JCIM Publications. J. Chem. Inf. Model. **63**, 3227–3229 (2023).

27. Kremer, K. & Grest, G. S. Dynamics of entangled linear polymer melts: A molecular-dynamics simulation. J. Chem. Phys. **92**, 5057–5086 (1990).

28. Kumar, R., Goswami, M., Sumpter, B. G., Novikov, V. N. & Sokolov, A. P. Effects of backbone rigidity on the local structure and dynamics in polymer melts and glasses. Phys. Chem. Chem. Phys. **15**, 4604–4609 (2013).

29. Mavrantzas, V. G., Boone, T. D., Zervopoulou, E. & Theodorou, D. N. End-Bridging Monte Carlo: A Fast Algorithm for Atomistic Simulation of Condensed Phases of Long Polymer Chains. Macromolecules **32**, 5072–5096 (1999).

30. Banaszak, B. J. & de Pablo, J. J. A new double-rebridging technique for linear polyethylene. J. Chem. Phys. **119**, 2456–2462 (2003).

31. Chaumet, P. C. The Discrete Dipole Approximation: A Review. Mathematics **10**, 3049 (2022).

32. Loke, V. L. Y., Pinar Mengüç, M. & Nieminen, T. A. Discrete-dipole approximation with surface interaction: Computational toolbox for MATLAB. J. Quant. Spectrosc. Radiat. Transf. **112**, 1711–1725 (2011).

33. Draine, B. T. & Flatau, P. J. Discrete-Dipole Approximation For Scattering Calculations. J. Opt. Soc. Am. A **11**, 1491 (1994).

34. Omrani, M., Mohammadi, H. & Fallah, H. Ultrahigh sensitive refractive index nanosensors based on nanoshells, nanocages and nanoframes: effects of plasmon hybridization and restoring force. Sci. Rep. **11**, 2065 (2021).

35. Funston, A. M., Novo, C., Davis, T. J. & Mulvaney, P. Plasmon Coupling of Gold Nanorods at Short Distances and in Different Geometries. Nano Lett. **9**, 1651–1658 (2009).

36. Purcell, E. M. & Pennypacker, C. R. Scattering and Absorption of Light by Nonspherical Dielectric Grains. Astrophys. J. **186**, 705 (1973).

37. Draine, B. T. & Goodman, J. Beyond Clausius-Mossotti - Wave propagation on a polarizable point lattice and the discrete dipole approximation. Astrophys. J. **405**, 685 (1993).

38. Romann, J., Wei, J. & Pileni, M.-P. Computational Matching of Surface Plasmon Resonance: Interactions between Silver Nanoparticles and Ligands. J. Phys. Chem. C **119**, 11094–11099 (2015).

39. Johnson, P. B. & Christy, R. W. Optical Constants of the Noble Metals. Phys. Rev. B **6**, 4370–4379 (1972).

40. Genzel, L., Martin, T. P. & Kreibig, U. Dielectric function and plasma resonances of small metal particles. Z. F**r Phys. B Condens. Matter Quanta **21**, 339–346 (1975).

41. Ashcroft, N. W., Mermin, N. D. & Smoluchowski, R. Solid State Physics. Phys. Today **30**, 61–65 (1977).

42. El-Haija, A. J. A. Effective medium approximation for the effective optical constants of a bilayer and a multilayer structure based on the characteristic matrix technique. J. Appl. Phys. **93**, 2590–2594 (2003).

CHAPTER 4. CAPILLARY FILLING DYNAMICS OF POLYMER MELTS IN A BICONTINUOUS NANOPOROUS SCAFFOLD

This chapter was previously published as Weiwei Kong, Anastasia Neuman, Aria C. Zhang, Daeyeon Lee, Robert A. Riggleman, Russell J. Composto; Capillary filling dynamics of polymer melts in a bicontinuous nanoporous scaffold. *J. Chem. Phys*. 28 January 2024; 160(4): 044904. R.J.C and R.R conceived and planned for the project. W.K. developed the experimental procedures and conducted all experimental measurements and analysis besides AFM measurements. A.N. conducted all simulation development and analysis. A.C.Z. took AFM images. W.K and A.N. wrote the manuscript.

4.1 Introduction

Polymer nanocomposites (PNCs) have been widely studied in academic, national and industrial laboratories[1–3]. PNCs are broadly defined as a mixture of an inorganic nanofiller dispersed within a polymeric matrix, resulting in a material with properties that the individual components would not exhibit by themselves. PNCs have been utilized in applications involving gas separation membranes [4,5], optically responsive devices[6–8], mechanical reinforcement[9,10], and ion conduction[11]. The unique properties of PNCs depend on factors such as inorganic nanofiller type, dispersion, loading, as well as the polymer matrix characteristics. In most research, the fabrication of PNCs relies on mixing inorganic nanoparticles (NP) into a polymer matrix. Depending on processing conditions, the NPs can disperse by thermodynamic or kinetic trapping, or aggregate as NPs self-assemble to reduce unfavorable NP/matrix interactions.

However, this general approach does not ensure a homogenous dispersion of NPs particularly when a high loading is required where initial interparticle spacing is on the length scale of the NP size. For instance, Krook et al (2019) investigated the miscibility of nanoplates in a lamellar diblock copolymer and found that the equilibrium interparticle spacing is 6.4 nm[12], implying limited and conditional miscibility of NP inside the polymer matrix. In another study by Krook et al (2018), when the concentration of monodisperse nanoplates increases to 0.05 vol% in the block copolymer (BCP) assembly, the nanoplates disrupt the lamellae structure of BCP resulting in a disordered system[13]. Thus, nanofiller dispersion in polymer matrices in most nanocomposites is limited to low loadings.

Preparing PNCs with a high loading of NPs is a challenge because most combinations of polymer and bare NPs result in aggregation of NPs. Though traditional PNCs typically contain low to moderate concentrations of inorganic nanofiller, for instance, commercial tires only contain ~ 22 wt% carbon black nanofiller[14], novel methods have been developed to increase NP loading. Lu et al (2003) performed free radical polymerization of monomers in the presence of NPs, thus trapping the NPs at a loading as high as 86 wt% (ca. 22 vol%) in the PNC[15]. Similarly, LaNasa and Hickey (2020) fabricated ultra-high loading PNCs by using a surface-induced ring-opening metathesis polymerization pathway to graft polymer chains on silica nanoparticles[16]. Srivastava and Kotov (2008) explored approaches to create PNCs with high loading through layer-by-layer assembly of polymers and NPs/nanowires[17]. Although these methods successfully produce PNCs with a high loading of NPs, there are some limitations to their applicability. Namely, the prior approach is limited to systems where the NP and monomer are miscible in a

common solvent before initiating polymerization, whereas, the latter approach is limited to systems where the NP and polymer are oppositely charged.

To expand the possible combinations of polymer and NPs, a novel PNC method was developed using capillary rise infiltration (CaRI)[18]. This method starts with a two-layer system – a polymer thin film over a uniformly distributed layer of NPs. This bilayer was annealed above the polymer glass transition temperature (T_g) to fill the NP interstitial space via capillarity. Using nanoindentation and contact mode AFM, these PNCs were shown to exhibit a significant enhancement in scratch and wear resistance[19], as well as high fracture toughness [20,21]. Compared to other existing approaches for generating high NP loading PNC, CaRI is attractive because of its versatility, namely, compatibility with many NP fillers and polymer matrices, and ease of fabrication. However, in CaRI systems, the NP interstitial pore size is not uniform or homogeneous, and the random arrangement of NPs may result in colloidal level defects such as vacancies and interstitial particles. In this paper, we adapt CaRI to fabricate a new type of PNC via infiltrating polymer into a nanoporous gold (NPG) exhibiting bicontinuous channels of gold and air. Limited research has been done utilizing NPG as a template for actuators and catalyst support[22,23]. In our approach, polymer infiltrated nanoporous gold (PING) is presented as a new approach to achieve an interconnected polymer and metal structure that does not require a favorable thermodynamics of mixing. In a previous study, spectroscopic ellipsometry was shown to be a sensitive tool to characterize the thermal properties of fully infiltrated PNCs[24]. In prior studies on the CaRI of polymers into nanoparticle films, polymer infiltration kinetics was also found to depend on polymer molecular weight, the extent of confinement, the presence of

water and polymer-surface interactions [25–29]. We believe that the PNCs made by PING provides a simple and scalable platform to prepare membranes for actuators, gas separation and fuel cells.

The mechanism of polymer infiltration into nanoporous gold is capillary rise, a phenomenon where liquid spontaneously fills a narrow channel without the assistance of external forces. For Newtonian fluids, the capillary effect is described by the Lucas-Washburn Equation (LWE)[30,31].

$$h(t) = t^{0.5}\sqrt{\frac{R_{pore}\Upsilon\, cos\theta_e}{2\eta_o}} \qquad \text{Eq. 1}$$

In Eq. 1, $h(t)$ is the height infiltrated by the liquid, t is the infiltration time, R_{pore} is the radius of the pore, Υ is the surface tension of the liquid, θ_e is the equilibrium contact angle, and η_o is the fluid viscosity. The LWE assumes that the size of the fluid particle is an order of magnitude smaller than the radius of the channel, which enables the fluid to be treated as a continuum medium [30,32]. The scaling of polymer infiltration height $h(t)$ with $t^{0.5}$ is well-documented. For example, polyethylene (PE) infiltrated into cylindrical anodized alumina oxide (AAO) nanopores exhibited LWE scaling such that flux ~ $t^{0.5}$, although the molecular weight dependence differed from bulk behavior[33]. Similar behavior was observed in molecular dynamics simulations of unentangled polymers in CaRI experiments[34]. Polyethylene oxide (PEO) chains infiltrated into confined AAO cylindrical nanopores where $R_g \gg R_{pore}$ again exhibited LWE scaling ~ $t^{0.5}$ [35]. Interestingly, these studies found that low molecular weight PEO chains exhibited slower than theoretically predicted infiltration, whereas high molecular weight chains exhibited faster infiltration.

For these studies of capillary filling of PEO in nanopores, Yao et al. (2018) developed a model to account for these deviations from bulk viscosity scaling[32]:

$$\frac{\eta_{eff}}{\eta_0} = \left[\left(\frac{R_{eff}}{R_{pore}}\right)^4 + \phi\frac{8N_e^g b^3\eta_0}{3\zeta N{R_{pore}}^2}\right]^{-1} \qquad \text{Eq. 2}$$

Here, the effective polymer viscosity, η_{eff}, deviates from the bulk viscosity, η_0, due to two phenomena which dominate in distinct regimes of confinement. The first term in Equation 2 captures the dead zone effect, in which strong adsorption of chains to the capillary surface creates a zone of thickness ΔR where polymer imbibition is blocked. Accounting for this dead zone, the effective pore radius is defined as $R_{eff} = R_{pore} - \Delta R$. The reduced pore size increases η_{eff}, leading to infiltration dynamics slower than bulk behavior. The dead zone effect is expected to dominate when the polymer radius of gyration is much smaller than the pore radius, $R_g \ll R_{pore}$. Adapted from the work of Johner et al. (2010), the second term in Equation 2 describes reptation-like flow under confinement, which models infiltration as plug through a capillary[36]. This term dominates in highly confined systems, i.e. when $R_g \gg R_{pore}$. Polymers confined in a reptation tube much smaller than their bulk length scale is driven by the capillary pressure gradient and infiltrate with a scaling of $\sim N^1$, showing enhanced mobility over bulk. In. Eq. 2, ϕ is the fraction of chains participating in reptation, N_e is the entanglement length of the chains, b is the Kuhn length of the polymers, ζ is the friction coefficient of one Kuhn segment, and α is a general scaling exponent.

Deviations from the LWE have been observed both experimentally and computationally, with a variety of molecular weight scaling exponents [28,34,37,38]. Beyond the dead zone effect and

modified reptation contributions enumerated in Equation 2, confinement can change other materials parameters that impact capillary rise infiltration of polymers in pores. For example, in previous studies of PEO [35], experiments and self-consistent field theory simulations for a mixture of long and short PEO chains show that shorter chains infiltrate faster than predicted by theory [39]. Such experiments demonstrate the complex relationship between materials parameters and infiltration height expressed in Equation 1.

The interaction between the infiltrating polymer and the scaffold surface is one such parameter. Diffusion of entangled polystyrene (PS) in a 2D slit geometry of alkylammonium modified mica-type silicates was found to scale inversely with molecular weight ($D \propto N^{-1}$) [40]. The weaker dependence than expected from reptation ($D \propto N^{-2}$) was attributed to attractive interactions between the polymer and confining surface. Using *in situ* nanodielectric spectroscopy, the infiltration kinetics of *cis*-1,4-polyisoprene (PI) in AAO nanopores proved quite different when the nanopores were silanized, a process which decreases PI-AAO adsorption[41]. Molecular dynamics simulations of polymer infiltrates into random close-packed NPs in the presence of solvent exhibited infiltration times with a non-monotonic dependence on polymer-NP interaction strength[28]. Infiltration dynamics increases in speed as the polymer-NP attraction increases until a strong-adhesion limit is broached, beyond which infiltration slows. The system in the present work, PS infiltration inside NPG, does not exhibit strong polymer-surface attraction, existing well below this strong-adhesion limit.

The entanglement density of polymers is often cited as an explanation for the capillary infiltration dynamics of polymers. Using small angle x-ray scattering (SAXS) to follow PS

infiltration into AAO cylindrical nanopores, an effective viscosity scaling of $\eta_{eff} \sim N^{1.5\pm0.1}$ was found for $R_g \gg R_{pore}$ and attributed to a confinement-induced reduction in entanglements during infiltration[37]. In another study PEO infiltration under strong confinement in AAO pores exhibits an effective viscosity scaling as $\eta_{eff} \sim N^{1.0}$, suggesting Rouse dynamics [35]. Recent molecular dynamics simulations of polymer infiltration into a cylindrical nanopore measured a reduction in entanglements during capillary infiltration which scales inversely with capillary radius[38]. These observations align with work studying non-infiltrating polymers under confinement. Experimental study of ultrathin PS films revealed a decrease in entanglement density with decreasing film thickness[42]. Simulations of entangled polymers under thin film confinement demonstrate that uniaxial compression of chains drives chain segregation, reducing the number of accessible interchain contacts and thus reducing entanglements [43,44]. Further computational studies extended this finding to cylindrical confinement [45,46] and tortuous networks with multiple confinement length scales[47]. Entanglements are of particular interest in this work, in which entangled PS chains infiltrate into a NPG scaffold.

As exemplified by Equation 2, infiltration kinetics depend strongly on the degree of confinement. The confinement ratio, Γ, is defined as $\Gamma = R_g/R_{pore}$, where R_g is the radius of gyration of the polymer, and R_{pore} is the radius of the pore. Using CaRI, polydimethylsiloxane (PDMS) infiltration was investigated into a dense silica NP packing with a confinement ratio, Γ, varying from 0.6 to 1.5. This system[25] exhibited a crossover in diffusive behavior at Γ = 1, with $D \propto N^{-1}$ for $\Gamma > 1$ and a scaling exponent between 0 and -1 for $\Gamma < 1$. PS infiltration into similar silica NP packings at much higher degrees of confinement[26], Γ varying from 2 to 15, exhibited viscosity scaling $\eta_{eff} \sim N^{0.8}$. Beyond the pore radius, the pore geometry is an

important factor in infiltration kinetics. Work comparing the infiltration of PS into AAO with a tortuosity close to 1 versus infiltration into tortuous porous glass finds an inverse scaling of infiltration velocity with tortuosity[48].

The present study quantitatively measures the kinetics of entangled PS infiltration into NPG under moderately confined conditions where R_g is slightly less than the R_{pore}. The experimental confinement ratio Γ varies from 0.47 to 0.77. The infiltration time scales with PS molecular weight as $\tau_{80\%} \propto M_w^{1.30 \pm 0.20}$, straying from bulk viscosity scaling with $M_w^{3.4}$. Further, the PS viscosity extracted from infiltration studies is reduced by over an order of magnitude compared to the bulk. This study of a moderately confined polymer is an important contribution to the field because of the bicontinuous pore geometry with zero-mean curvature, compared to studies of concave cylindrical pores of AAO and convex pore of nanoparticle packings. The unique properties of this system drove us to use molecular dynamics simulations of polymer infiltration into NPG to illuminate experimental findings. Simulation results well agree with experimental scaling, $\tau_{infiltration} \propto N^{1.4}$. These simulations provide insights into the mechanism of infiltration by analyzing transient chain level behavior such as the fraction of chains adsorbed to the gold surface, entanglement density, and chain R_g during infiltration. These simulation properties and their implications on experimental polymer infiltration kinetics are expounded upon in this work.

4.2 Materials & Method

Please refer to Chapter 3 for part of the materials and methods.

Samples. The polystyrene (PS) samples with different molecular weights were purchased and used as received. Important molecular characteristics and length scales are described in Table 4.1.

Table 4.1. Characteristics of PS and confinement parameter values

Sample Name	M_w (Da)	PDI	R_g (nm)	$\Gamma = R_g/R_{pore}$
PS-424k	424,000	1.06	17.8	0.47
PS-610k	609,500	1.06	21.4	0.57
PS-807k	806,815	1.03	24.6	0.66
PS-954k	954,000	1.06	26.7	0.71
PS-1031k	1,031,454	1.06	27.8	0.74
PS-1133k	1,115,960	1.02	28.9	0.77

The PS in these studies are entangled with weight average molecular weights ranging from 424 kDa to 1,116 kDa and have a low polydispersity (PDI), less than 1.06. The calculated radius of gyration (R_g) is given by $R_g = \sqrt{\frac{b^2 N}{6}}$. The R_g is calculated from the Kuhn length, b = 1.8 nm for PS, and the number of Kuhn segments, $N = \frac{M_w}{M_o}$, where the Kuhn monomer molar mass for PS is

720 Da[49]. Solutions of PS and toluene are prepared using 2.4 wt.% of polymer. The PS solution is stirred overnight. Then, the solutions are spin coated onto silicon wafers (1 cm x 1 cm) at 4000 rpm for 1 minute. After that, the polymer films are annealed at 100°C in the Mettler heating stage (Mettler FP-82) under argon flow for 10 minutes to ensure complete evaporation of the solvent. The resulting polymer thickness range from 150-500 nm as measured by reflectometer (Filmetrics F3UV).

Water Contact Angle Goniometry. Static and Dynamic Water Contact Angles are used to measure the surface energy of the NPG/PS composite. Uniform DI-H_2O droplets were deposited onto the sample surface using a Gilmont Micrometer Dispenser. The system is illuminated using a Stocker Yale Imagelite Lite Mite - Model 20. Pictures of the water droplets were captured using a Sony CCD N50 Video Camera Module with a Navitar Zoom 7000 close-focusing macro video lens mounted on an optical table. The captured pictures are analyzed using Image J, plugin "LB-ADSA," which uses the Young-Laplace equation to fit the shape of the water droplet for the exact contact angle.

Atomic Force Microscopy (AFM). Bruker Icon AFM with tapping mode is used to probe the surface morphology of the NPG/composite. The images collected are 2*2 μm^2. Tapping mode AFM tips, Tap300Al, have a tip height of 17 μm and radius of 10 nm. The AFM images are analyzed using Gwyddion software.

Scanning Force Microscopy (SEM). FEI Quanta 600 SEM is used to detect the secondary electron signals at 15kV. The images are taken top-down to measure the ligament-ligament distance and in cross-section to measure the NPG thickness as well as infiltration extent. SEM images analysis also utilizes Gwyddion software.

4.3 Results and Discussion

Characterization of Nanoporous Gold (NPG).

In this study, polymer is infiltrated into the pores of a nanoporous gold (NPG) scaffold. The scaffold is prepared by dealloying a ca. 100 nm film with nominal composition $Au_{35}Ag_{65}$ at. %. In the gold-alloy etching process, also known as depletion gilding or gold coloration[50], the less-noble (Ag) element is removed, leaving behind Au adatoms that diffuse to form Au clusters and eventually Au ligaments. The resulting structure is bicontinuous with gold ligaments and nanopores as shown in Figure 4.1a. Figure 4.1a (inset) shows a cartoon of the NPG structure, that defines d which is the average distance from the center of one ligament to the center of an adjacent ligament. Because pristine NPG spontaneously coarsens at moderate temperature, post-dealloying coarsening is needed to stabilize the structure. Both thermal and chemical coarsening has been studied [51–55] . Because the NPG/PS infiltration studies utilize thermal annealing at 150°C (i.e. above the PS glass transition temperature), the NPG was thermally coarsened at 175°C for 3 h prior to preparing the NPG/PS bilayer. Our prior study showed that this treatment prevented NPG coarsening during infiltration at 150 °C [24].

Small-angle X-ray scattering (SAXS), SEM and AFM were used to characterize the structure of the NPG. Figure 4.1b shows the SAXS intensity versus wavenumber (q) before and after coarsening the NPG at 175°C for 3 h. For as-prepared NPG, the maximum-intensity peak position is located at 0.00873 $Å^{-1}$, corresponding to d = 89 nm, with a small shoulder at 0.02139 $Å^{-1}$ which corresponds to d = 36 nm. This shoulder may reflect scattering from Au

nanoparticles (NP) resulting from incomplete ligament formation. Upon annealing, the maximum intensity moves to lower q, q_{max} = 0.00513$Å^{-1}$, and the shoulder disappears suggesting dissolution of the Au NP. For bicontinuous structures, the ligament-ligament distance is given by d = 1.23 * $\frac{2\pi}{q_{max}}$ [53,56], where the factor of 1.23 accounts for the random arrangement of ligaments. For as prepared NPG, d is 89 nm, whereas after thermal treatment d = 150 nm. The full width at half maximum (FWHM) of the annealed NPG is shown in SI Fig. A1. The broadness of the scattering peak reflects the heterogeneity of the pore size which is verified in SEM and AFM images. For annealed NPG, the lower bound of the FWHM is $q_{FWHM,lower}$ = 0.00218 $Å^{-1}$, corresponding to $d_{upper} = 355\ nm$. The upper bound is $q_{FWHM,upper}$ = 0.00829 $Å^{-1}$, corresponding to $d_{lower} = 93\ nm$. The calculation can be verified through the SEM/AFM images in Figure 4.1, as some pores have larger values in the longitudinal direction. As noted previously, this thermal treatment is sufficient to lock in the NPG structure during polymer melt infiltration at 150°C. For all subsequent discussion, "NPG" will refer to the coarsened structure.

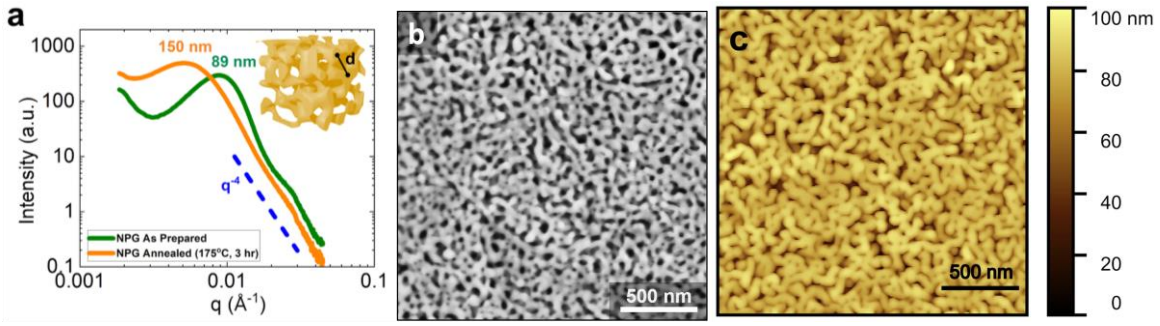

Figure 4.1. NPG structural analysis. A) SAXS spectra of as-prepared and coarsened (175°C, 3 h) NPG film. The maximum q values are used to determine d values of 89 nm and 150 nm, respectively. The high q region scales as q^{-4}. The inset defines d as the ligament to ligament spacing. Inset cartoon adopted from Welborn and Detsi (2020).

B.) SEM and c) AFM height images of coarsened NPG in a top-view. White and gold colors, respectively, represent the ligaments of the NPG. Dark regions in both images correspond to open pores.

The coarsened NPG was also characterized by real space methods, namely SEM and AFM. Figure 4.2b is an SEM image showing that the NPG displays an interconnected network structure when viewed top down. Line-scans (see SI, Fig. A2) are used to determine the ligament-ligament distance, d = 146 ± 9 nm, which is in good agreement with SAXS (Fig. 4.1a). Figure 4.2c is an AFM height image of the coarsened NPG exhibits a network of gold ligaments. By taking a 2D correlation function, the ligament-ligament distance can be determined from the distance between peak heights as shown in SI (Fig. A3). To randomize measurements, correlations were determined at -45°, 0°, 45°, 90°. From AFM, the ligament spacing was found to be 114 ± 39 nm, which is less than the values from SAXS and SEM. The large uncertainty may result from limited resolution due to the tip radius (10 nm) as it traverses the narrow pores (75 nm). This resolution limit is evident upon comparing the narrower ligament widths in the SEM image (Fig. 4.1b) compared to the broader widths in the AFM height image (Fig. 4.1c).

Pore volume is another important characteristic of the NPG. In addition to d, the pore volume fraction and pore radius were determined for the NPG. As modeled via ellipsometry and calculated from 2D correlation function analysis of the AFM image (Fig. A3), the porosity of the NPG is approximately 50% by volume, which agrees well with our previous study[24] . As shown in Fig. 4.1a, the ligament-ligament distance is the sum of the ligament width plus the diameter of the pore. Thus, the average radius of the pore is given by $R_{pore} = \frac{d}{4}$, which is 37.5 nm in this study.

Characterization of NPG/PS before and after complete infiltration.

Before investigating the kinetics of infiltration, the initial NPG/PS bilayer and the NPG/PS composite (PING) after complete infiltration were characterized. The preparation of NPG/PS on a silicon substrate was described in the Materials and Methods section. Figure 4.2a shows a cross-sectional SEM image of a bilayer with a 120 ± 4 nm thick NPG top layer (white) over a 80 ± 3 nm thick PS layer (dark). The edges of both films are observed as well as the gold ligaments on top of the NPG. Figure 4.2b presents a cross-section image of PS-424k in the NPG after complete infiltration at 150°C for 3 h. The final thickness of PING is 128 ± 8 nm. From Figure 4.2, PS-424k appears to completely fill the pores. The NPG thickness before and after infiltration are within experimental uncertainty, indicating that the NPG takes up the PS without swelling.

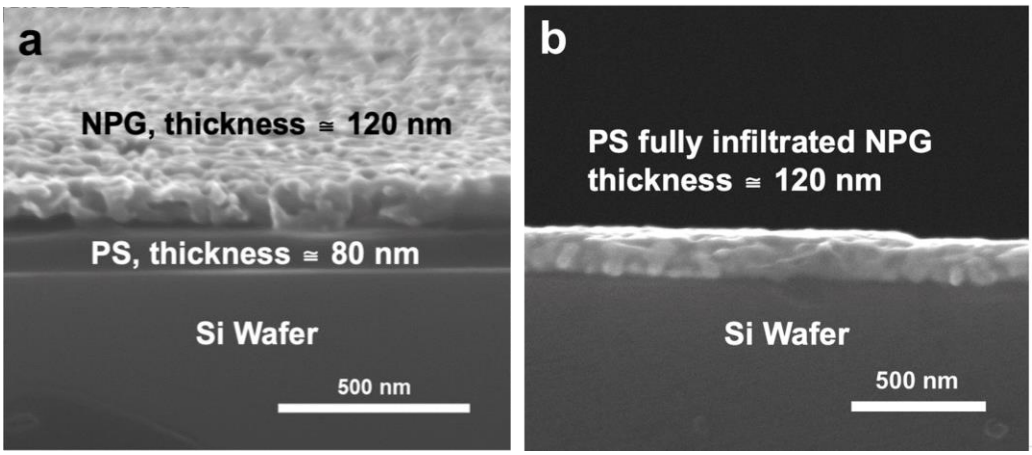

Figure 4.2. a) Cross-sectional SEM image of the prepared bilayer. The top-most, middle and bottom layers represent the NPG (120 nm), the PS film (80 nm), and the silicon substrate. The tilt angle is 5°. b) Cross-sectional SEM image of the NPG after complete infiltration by the PS-400k after annealing for 3 h at 150C.

The surface characteristics and properties of the fully infiltrated NPG/PS films were also determined. As polymer infiltrated the NPG from below, the color of the film became progressively dimmer as shown in Figure A4 as the film transitioned from initial to partial to complete infiltration. Tapping mode AFM was used to characterize the topography of the NPG/PS-424k film before and after complete infiltration as shown in Figure 4.3. The AFM tip radius is 10 nm. Before infiltration (t = 0 s), the NPG (~ 120 nm) lies on top of the PS-424k film (~ 80 nm) and, as expected, the height image in Fig. 4.3a is very similar to that in Fig. 2c for the neat NPG film. The bicontinuous gold ligament structure (bright features) can be clearly visualized. The height scale bar from 0 to 100 nm was chosen to be the same as that of Fig. 4.1c. The surface roughness of the bilayer is R_q = 3.3 ± 0.7 nm, implying that the surface is relatively rough due to the open pores at the surface. However, after complete infiltration, Figure 4.3b shows that the surface becomes smoother with ligaments (bright spots) rising at most ca. 50 nm above the background. This decrease in roughness is attributed to the PS domains (dark) filling the pores between ligaments. Quantitatively, the surface roughness decreases to R_q = 1.8 ± 0.1 nm.

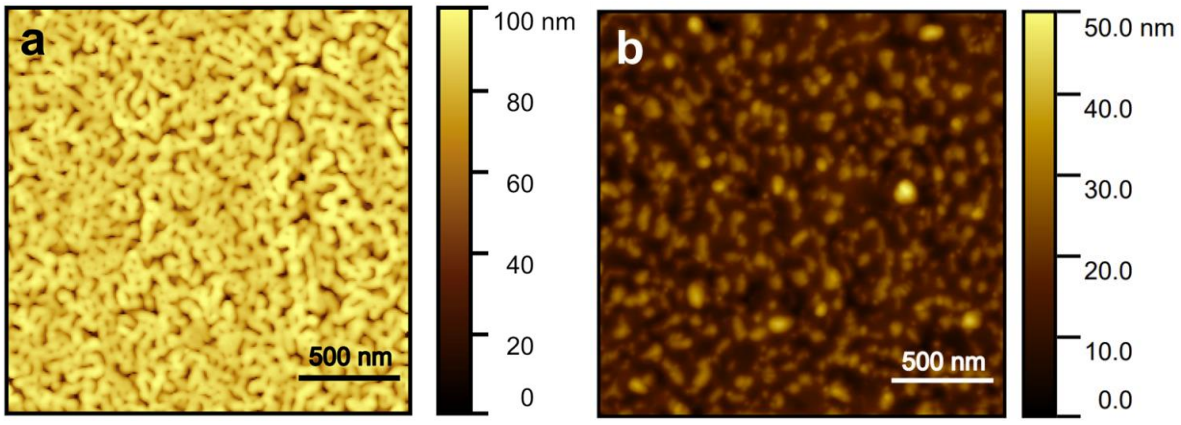

Figure 4.3. a) AFM height image of NPG (ca. 100 nm) over PS-424k film (ca. 100 nm). Surface roughness is R_q = 3.3 ± 0.7 nm. The structure is similar to that in Figure 2c. b. AFM height image of the NPG after complete infiltration by PS-424k after annealing at 150°C for 3 h. Surface roughness is R_q = 1.8 ± 0.1 nm

To further investigate surface properties, water contact angles were measured on a pure PS-954k film, a solid gold film and a fully infiltrated NPG/PS-954k film. As shown in Figure 4.4a, the equilibrium water contact angle for PS-900k is θ = 89.9 ± 0.7°, in good agreement with literature[57]. Because it is porous, the NPG absorbs water and delaminates from the substrate. Thus, a solid gold film was used as a surrogate for the NPG film. The gold wafer, made by sputtering a layer of gold on a silicon wafer, exhibits a water contact angle θ = 64.4 ± 2.7°, which is in good agreement with the range of values from the literature [58], 60 to 65° . Given that the porosity of the NPG is ca. 50%, the water contact angle for fully infiltrated NPG can be estimated by averaging the contact angles of PS-954k and gold, and is 77.2°. This estimate assumes a smooth surface and does not account for the effect of nanoscale roughness shown in Fig. 4.3b. As shown in Figure 4.4, the measured contact angle for the NPG/PS-954k film is slightly larger, θ = 80.1 ± 0.5°, than the simple rule of mixtures prediction. This small difference might be attributed to PS domains that partially spread over the gold ligaments on the top surface. Nevertheless, because θ < 90°, the top of the NPG/PS-954k film appears to contain both PS domains and gold ligaments at the surface. The water contact angle results are qualitatively consistent with the AFM height map shown in Figure 4.3b that displays patches of PS (dark) and gold ligaments (bright). Thus the AFM results suggest that PS does not spread across the entire surface to form a uniform wetting layer over the gold ligaments. AFM phase images shown in Figure A5 of the SI support this conclusion. In addition to the static contact angle, we have also

measured the dynamic water contact angle on fully infiltrated NPG/PS-954k as shown in Fig. A6. Future studies will apply ToF-SIMS to quantify the relative areas of PS and gold on the surface.

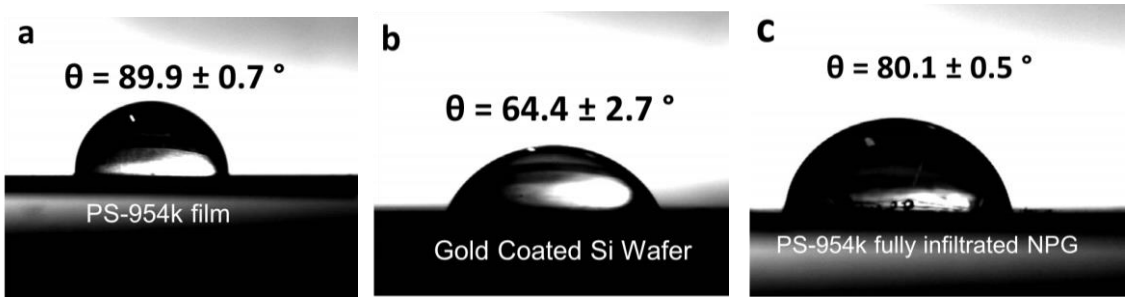

Figure 4.4. Room temperature water contact angle measurements on a) PS-954k film, b) solid gold film on silicon, and (c) NPG after complete infiltration by PS-954k.

Kinetics of Polystyrene Infiltration into the NPG Scaffold.

After characterizing the initial and final states, the kinetics of polystyrene infiltration into a NPG scaffold is investigated using *in-situ* spectroscopic ellipsometry (SE). The infiltration extent (IE) is determined from the refractive index of the top layer at time t, n_t, via $IE = \frac{(n_t - n_i)}{(n_f - n_i)}$, where n_i is the initial refraction index of the top layer, and n_f is the final refraction index of the top layer (see SI for details). Figure 4.5a shows infiltration height for PS-424k, PS-807k and PS-1133k in the NPG plotted versus $t^{1/2}$. The time for 80% infiltration which corresponds to a height of 96 nm is used to compare the different molecular weights. At 80% infiltration, the infiltration times are 9.6 min, 22.5 min and 62.9 min, respectively. According to the LWE (Eq. 1), $h \sim t^{1/2}$. Figure 4.5a shows that PS infiltration height scales linearly with $t^{1/2}$, indicating that the LWE is obeyed for infiltration of PS into the nanoporous scaffold. Other

polymer infiltration studies in nanoconfined systems, such as polymer infiltrating into SiO_2 nanoparticle assemblies and AAO membranes, also exhibit the relationship $h \sim t^{1/2}$ [26,59]. Figure 4.5b,c shows the IE as a function of annealing time for PS-954k infiltrating into NPG at 150°C. From 0 to 10 min, PS-954k fills approximately 35% of the NPG; however, from 10 to 20 min, PS-954k only fills an additional 23% of the NPG. The slower kinetics of PS infiltration is reflected by the parabolic shape with a negative concavity shown in Fig. 4.5b. According to the classical LWE model, the capillary driving force becomes weaker as infiltration increases resulting in a slowing down of the advancing polymer front. To compare infiltration times as a function of PS molecular weight, the time to infiltrate 80% of the NPG, $\tau_{80\%}$, was chosen. This time point was convenient for several reasons. First, the 80% filling fraction value can be more accurately measured than the 100% value which is approached asymptotically as shown in Figure 6b. Further, using $\tau_{80\%}$ allows for a higher molecular weight range to be explored using reasonable annealing times. Figures 4.5a and 4.5b show that $\tau_{80\%}$ = 38.8 min for PS-954k infiltrating into the NPG at 150°C.

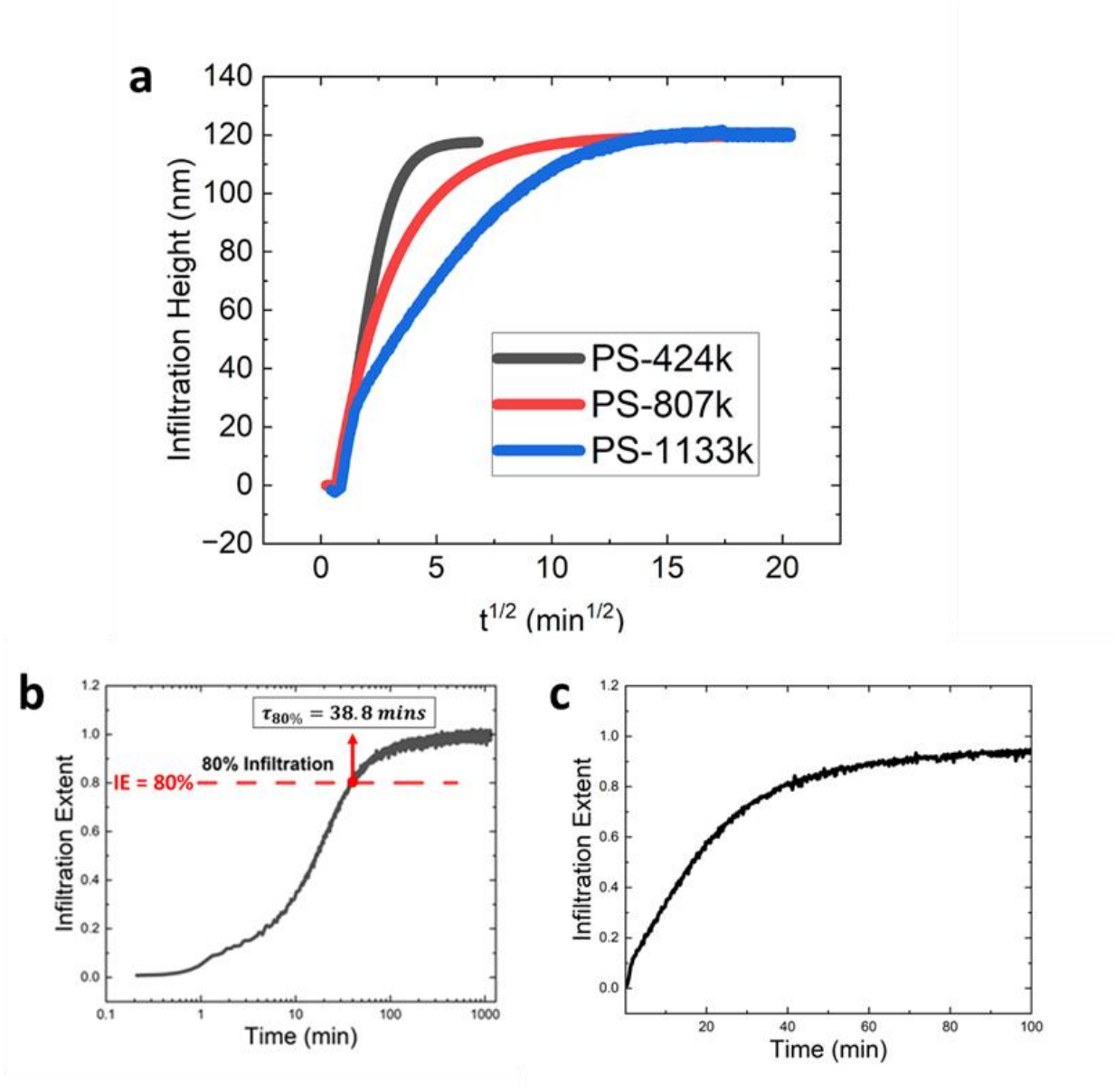

Figure 4.5. (a) Infiltration height of PS-424k, PS-807k, and PS-1133k into NPG at 150°C. Because the height increases linearly as $t^{1/2}$, the LWE captures the time dependence for PS infiltration into nanoporous scaffolds in this study. (b) Plot of PS-954k infiltration extent as a function of the log time . (c). Plot of PS-954k infiltration extent as function of linear scale between t = 0 and t = 100 mins. The time to reach 80% infiltration is represented in the insets and has a value of 38.8 min for PS-954k at 150°C.

Using $\tau_{80\%}$ measurements from SE, the kinetics of polystyrene infiltration into NPG was measured for weight-average molecular weights (M_w) from 424k to 1133k g/mol. For a pore radius of 37.5nm, the confinement ratio Γ ranges from 0.47 and 0.77 as shown in Table 4.1. Figure 4.6 shows how infiltration time increases as M_w increases upon annealing at 150°C. For example, PS-424k (R_g = 17.3nm) exhibits $\tau_{80\%}$ = 9.69 min, which is 5x faster than infiltration of PS-1133k (R_g = 28.9 nm) where $\tau_{80\%}$ = 49.9 min. Note that the PS in this study (Table 4.1) have M_w values above the entanglement molecular weight of PS (M_e = 17k g/mol) [49] and therefore the bulk melt viscosity (η) scales as $\eta \propto M_w^{3.4}$ [49,60,61]. From the LW relationship, $\boldsymbol{\tau} \sim \eta$, and therefore if bulk viscosity controls the molecular weight dependence of infiltration, $\tau_{80\%} \propto M_w^{3.4}$. However, as shown in Fig. 4.6, $\tau_{80\%} \propto M_w^{1.30 \pm 0.20}$, demonstrating that the molecular weight dependence of infiltration in NPG is much weaker than expected from bulk behavior.

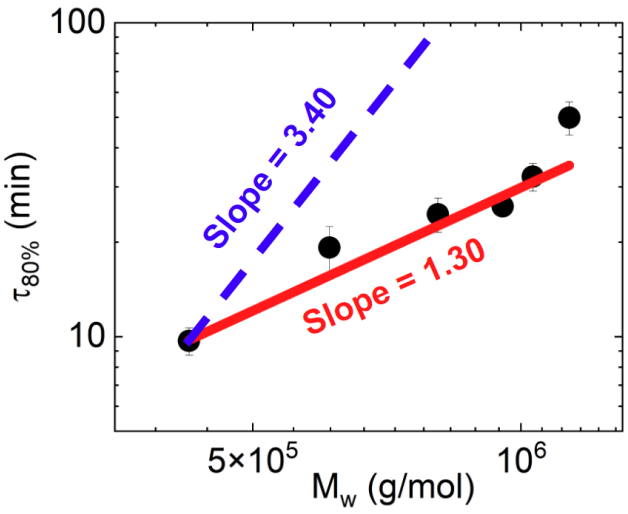

Figure 4.6. Infiltration time as a function of polystyrene molecular weight at 150°C. In these studies $\tau_{80\%}$ represents the time for PS to infiltrate 80% into the NPG scaffold. The scaling of $\tau_{80\%}$ with molecular weight is weaker than expected from bulk viscosity where $\tau_{80\%} \propto M_w^{3.4}$.

Next, we compare experimental results with prevailing models. For $R_g \gg R_{pore}$ and $\Gamma \gg 1$, Johner, Shin and Obukhov (2010) developed a theoretical model that captures reptation of polymers under strong confinement. The pressure gradient within the pores results in enhanced mobility and faster infiltration[36] where $\tau \propto M_w^1$. In previous experiments under confinement [35,37], the PS and PEO infiltration time in nano-sized cylindrical pores were found to scale as $\tau \propto M_w^{1.4}$ and $\tau \propto M_w^{0.9}$, respectively. Additionally, polymer infiltration in a densely packed SiO_2 nanoparticle scaffold scaled[26] as $\tau \propto M_w^{0.8}$. Though the polymers used in these studies were entangled, the scaling behavior approximately suggests that $\tau \propto \eta \propto M_w^1$. Thus, for both the model and experiments where $\Gamma > 1$, the infiltration rate exhibits a weaker dependence on M_w than expected from bulk behavior.

Infiltration time (Figure 4.6) can be used to determine the effective viscosity (η_{eff}) of PS. Using a modified Lucas-Washburn Equation (LWE) that accounts for tortuosity[62], the height that PS travels at time t is:

$$h^2 = \left(\frac{\Upsilon R_{pore} cos\,\theta}{4\,\eta_{eff}\,\tau^2}\right) t \qquad \text{Eq. 5}$$

where Υ is the surface tension of PS at 150°C, R_{pore} is the average pore which is 37.5 nm, τ is the tortuosity factor of the NPG [63] which is taken as 1.5, θ is the contact angle between PS and gold. The contact angle for PS on silica is reported as 20° and used here [26]. To further support this choice, the contact angle of PS on Au was estimated. Namely the PS contact angle on a planar Si wafer[71] was measured to be 6.9°, whereas relationship between the PS contact angle on

planar Si and planar gold[65] is $\boldsymbol{\theta}_e^{Au} = 1.9\,\boldsymbol{\theta}_e^{Si}$. Thus, the PS contact angle on Au is estimated to be ca. 13°. Note: this estimate excludes the effect of roughness and curvature. Further, because the difference in cos$\boldsymbol{\theta}$ is only a few percent, the value of 20° is a reasonable estimate to calculate the effective viscosity from Eq. 4.1. Calculations for the surface tension and bulk viscosity are given in the SI. As shown in Figure 4.7, the effective viscosity of PS infiltrating inside the NPG is lower than that of the bulk (η_{bulk}). For 424k-PS, η_{eff} is $7.0 * 10^6$ Pa*s and η_{bulk} is $2.9 * 10^8$ Pa*s, which is 40x greater than the viscosity of the confined polymer. For 1133k-PS, the reduction in viscosity is even larger with $\eta_{eff} = 3.8 * 10^7$ Pa*s and $\eta_{bulk} = 8.4 * 10^9$ Pa*s resulting in a difference of more than two orders of magnitude. As shown in Figure 4.7, the difference in $\eta_{bulk} - \eta_{eff}$ increases as M_w increases. As observed in MD simulations in Figure 4.9, one possible explanation is that the reduction in entanglement density increases as M_w increases. In summary, the PS infiltration time exhibits a weaker dependence on M_w than expected from bulk behavior and PS viscosity inside the nanopores is greatly reduced relative to bulk viscosity. In addition to predicting the scaling behavior of infiltration time with M_w, the next section will investigate the mechanism of infiltration using molecular dynamics simulations.

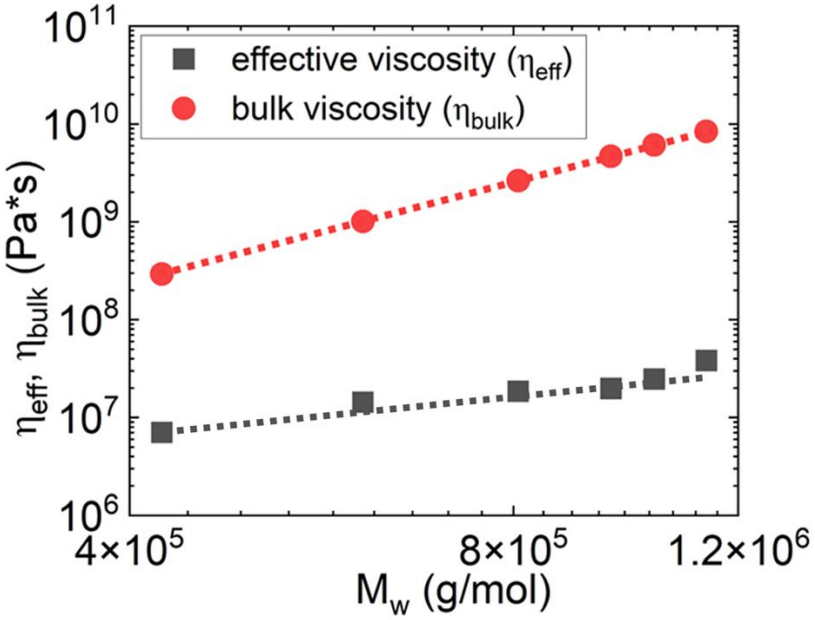

Figure 4.7. The effective viscosity of PS in the NPG and bulk viscosity as a function of molecular weight at 150°C. Red circles represent the bulk viscosity values calculated at the same molecular weight as the NPG studies. The dashed red line is a fit that scales as $M_w^{3.4}$. The gray squares represent the effective viscosity determined from the infiltration times given in Figure 7. The effective viscosities of PS confined in the NPG are much lower than the bulk values.

Molecular Dynamics (MD) Simulations of Polymer Infiltration into NPG.

To compare experimental results with simulations, molecular dynamics is used to determine the height of the polymer front as it infiltrates into the NPG. The methods section describes the system (Chapter 3) and simulation details. The height of the polymer front is calculated from $\rho(z)$, the local polymer density in the z direction. The infiltration front can be tracked as the z threshold z′, where $\int_0^{z'} \rho(z)dz = 0.99\rho_{total}$, or at which 99% of the total polymer density is contained. This threshold is depicted via a dashed red line in Figure 1 at $\boldsymbol{\tau} = 0$

(initial configuration) and **τ** = 330000 (after infiltration). The difference between this height and the bottom of the nanoporous gold structure, $z' - z_{gold}$, is referred to as $h_{99}(t)$. The infiltration rate, $\dot{h^2}_{99}$, is calculated from the slope of the linear region when plotting ${h^2}_{99}$ versus time. To compare with experimental scaling of $\tau_{80\%}$ with molecular weight (Figure 4.6), $1/\dot{h}^2_{99}$, which is proportional to the infiltration time, $\tau_{infiltration}$, is plotted versus the number of monomers per chain N on a log-log plot. In previous works simulating polymer dynamics during capillary rise, in addition to tracking the infiltration front, the infiltration of the bulk of the polymer is characterized via the z threshold z′′, where $\int_0^{z''} \rho(z)dz = 0.85\rho_{total}$, or at which 85% of the total polymer density is contained[34]. The dynamics of the infiltration front more closely match the experimental conditions tracked in this work and are thus reported here. The bulk infiltration dynamics are included in Figure A9 of the Supporting Information for completeness.

Figure 4.8 shows infiltration rate and infiltration time for N = 25, 50, 100, 150 and 200 monomers. Those five polymer chain lengths incorporate the range for PS used in the experiments, as N approximately ranges from 30 to 90 for the PS used in the experiments. Note that N/N_e increases from 1.5 to 11.5, respectively, for our simulated system. Figure 4.8a shows that the progression of infiltration slows down as polymer length increases. For each polymer, a linear regime is observed as expected from the LWE model. Figure 9b shows that infiltration time increases with N and that this time scales as $N^{1.4}$. This result is in good agreement with the experimentally observed scaling shown in Figure 4.6, where $\tau_{80\%} \propto M_w^{1.30 \pm 0.20}$. As discussed previously, this scaling deviates significantly from that expected for bulk behavior, $\tau_{80\%} \propto M_w^{3.4}$.

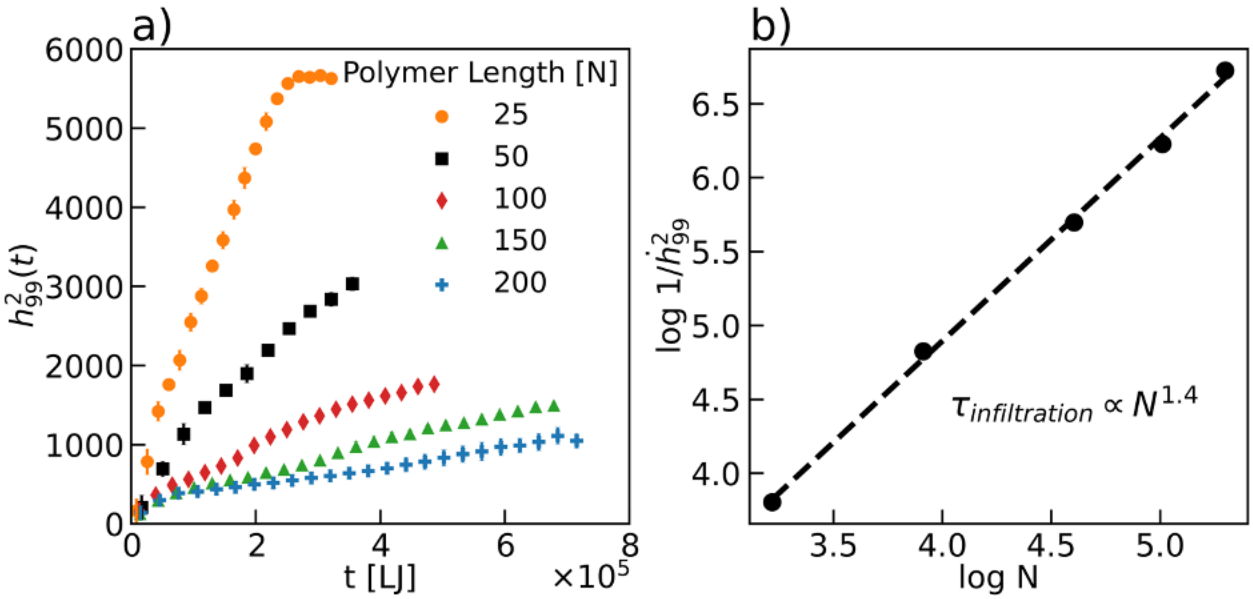

Figure 4.8. (a) The square of the infiltrated polymer film height h_{99}^2 as a function of simulation time. Each color corresponds to a different polymer chain length, N, as noted in the legend. An average of triplicate runs is shown, with error bars included on the plots. (b) Inverse infiltration rate $1/\dot{h}_{99}^2$ as a function of the number of monomers. A log-log scale is used to show the scaling of infiltration time with N, $\tau_{infiltration} \propto N^{1.4}$.

The difference between the scaling from simulations and the $\tau \sim N^1$ behavior predicted by the model in Equation 4.2 may be attributed to several factors. The confinement ratio, Γ, in the simulations ranges from 0.46 to 1.35. The shorter chain lengths are not in the highly confined regime required for this reptation-like flow and lack sufficient entanglements to be considered within the reptation regime. In addition, the tortuosity of the gold surface changes the expected pressure gradient in comparison to an ideal cylindrical capillary[36].

Previous studies have shown that confinement reduces the number of entanglements in polymer chains compared to the bulk value [37,42,43,45,47]. A reduction in entanglements decreases polymer viscosity, thus leading to faster infiltration than predicted by bulk behavior. Figure 4.9a

shows the change in the average number of entanglements per chain, $\Delta < Z >$, over the duration of infiltration for all chain lengths. Only infiltrated chains, i.e. chains with a center-of-mass z position above the bottom of the nanoporous gold structure, are considered for the average number of entanglement analysis. The Z1+ algorithm[66] is used to analyze entanglements in all simulations. All chain lengths show a decrease in entanglements as infiltration time increases, consistent with the experimentally observed decrease in viscosity. As chain length and thus the degree of confinement increases, the magnitude of $\Delta < Z >$ increases from about -0.5 to -2.0 entanglements per chain for N = 25 and 250, respectively. Rather than using the loss of entanglements, comparing entanglement length, N_e, as chain length increases provides a clearer comparison. If the change in entanglements is sufficient to explain the confined polymer viscosity, one would expect $\eta \propto 1/N_e$, giving $\frac{\eta_{infiltrated}}{\eta_{bulk}} \propto \frac{Ne_{bulk}}{Ne_{infiltrated}}$. The ratio of bulk entanglement length versus infiltrated entanglement length during the course of infiltration is included in Figure A10 in the Supporting Information. Figure 4.9b shows $\frac{Ne_{bulk}}{Ne_{infiltrated}}$ versus Γ at the final simulation time point for each chain length, capturing the total change in the entanglement length over the course of infiltration. This ratio increases as N increases; if entanglements played a dominant role in the changes in the infiltration rate, we would thus expect smaller deviations from bulk viscosity for higher molecular weight polymers. However, with the dynamic scaling found experimentally and computationally in this work, $\frac{\eta_{infiltrated}}{\eta_{bulk}} \propto \frac{N^{1.4}}{N^{3.4}} \propto N^{-2}$, one would expect larger deviations from bulk viscosity as N increases. The experimental results in Figure 4.7 show this latter trend; namely, the difference in $\eta_{bulk} - \eta_{eff}$ increases as M_w increases. Although a reduction in entanglements can enhance infiltration

kinetics, the change in entanglement per chain does not explain the scaling observed in this study.

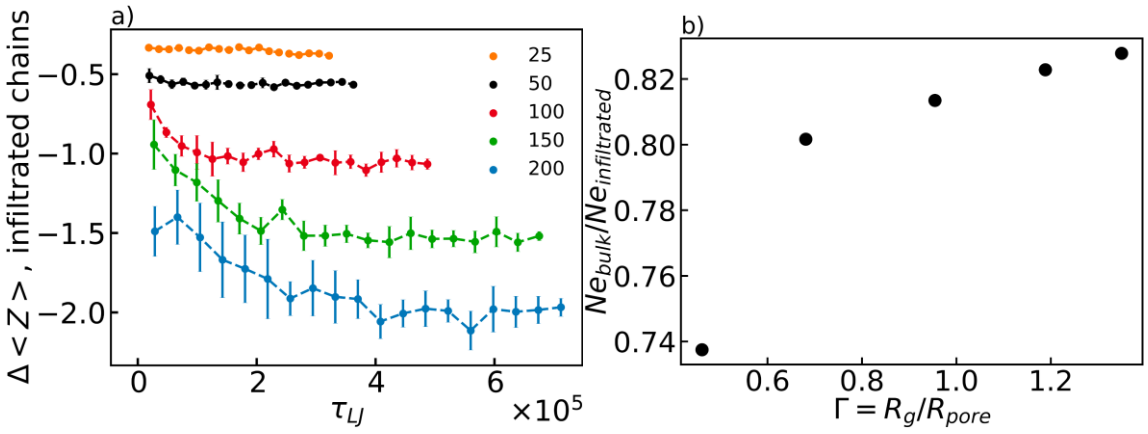

Figure 4.9. Effect of confinement on entanglements. (a) The decrease in the average number of entanglements per chain over the course of infiltration, $\Delta < Z > = < Z >_t - < Z >_{bulk}$. (b) $\frac{Ne_{bulk}}{Ne_{infiltrated}}$ at the final simulation time point versus the confinement ratio Γ.

The model from Yao et al (2018) assumes that chains obey Gaussian equilibrium statistics and are not deformed by flow[32,36]. There have been conflicting results with regards to the shape of polymers during capillary infiltration, with reports of both unperturbed dimensions[37] and chain extension in the direction of flow[38]. The reduction in entanglements for confined polymers is thought to be driven by chain compression in the confined dimension which reduces the pervaded volume of chains and thus the number of available interchain contacts [42,43]. Confinement of significantly long polymers can even drive chain segregation [44,46]. This chain segregation produces an entropic barrier to polymer diffusion, as chains must adopt highly extended conformations to exchange positions with neighboring chains. Figure 4.10 shows the normalized one-dimensional radius of gyration in each direction for free (open circles) and

highly adsorbed (solid circles) chains. Values are normalized to the bulk polymer Rg in each direction such that a value of 1 represents a chain that has retained bulk dimensions in that respective direction. Free chains are defined as those chains with no polymer beads within 1.5σ of any gold surface bead, while highly adsorbed chains have at least half of the total chain length within 1.5σ of any gold surface bead. There is clear extension in the direction of infiltration (z direction) for both free and adsorbed chains, with the extent of chain stretching scaling with the degree of confinement. Highly adsorbed chains retain bulk shape in the x and y directions for all confinement ratios, while the most confined free chains (Γ = 1.35) are compressed in the confined x and y directions.

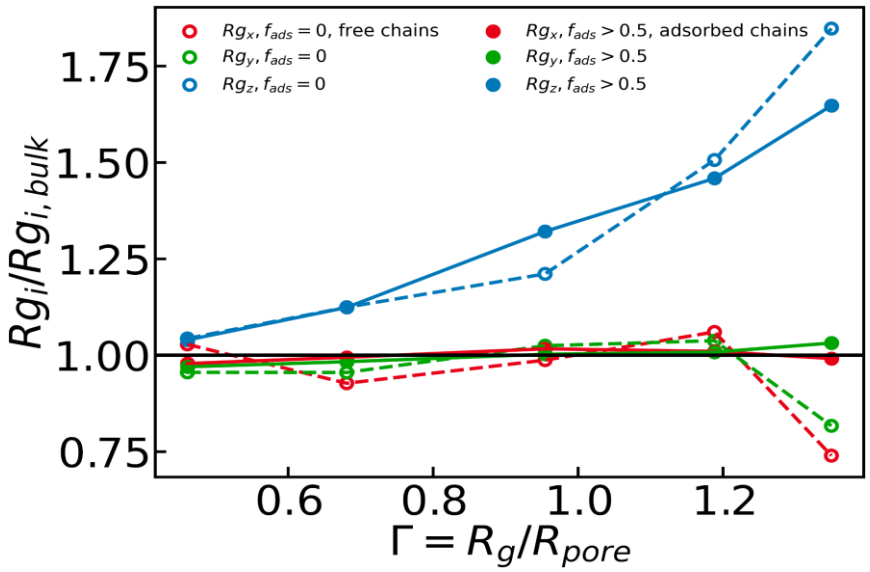

Figure 4.10. Normalized one-dimensional radius of gyration in each direction, split into free (open circles) and highly adsorbed (closed circles) chains. Free chains are defined as those with no polymer beads within 1.5σ of any gold surface bead, while highly adsorbed chains have at least half of the total chain length within 1.5σ of any gold surface bead. The x-axis corresponds to increasing chain length, plotted as the confinement ratio, R_g/R. Chain extension in the z-direction is observed for both free and adsorbed chains.

Although the dead zone effect is expected to slow infiltration compared to bulk behavior, the opposite effect to that observed in this system, we investigate if a dead zone could be present in simulations. To probe for a dead zone, we calculate $\frac{dz}{dt}$, the instantaneous velocity in the z direction of the center of mass of each polymer chain within the simulations. The effect of polymer surface adsorption on $\frac{dz}{dt}$ is quantified via the number of adsorbed beads out of the total number of beads of chain length *N* for each polymer. A bead is considered adsorbed if the chain bead is within 1.5σ of a gold surface bead. Figure 4.11a shows the z velocity dependence on the fraction of adsorbed beads per polymer, f_{ads}. The adsorbed fraction, f_{ads}, varies from 0 to 1 where $f_{ads} = 0$ represents a free chain not interacting with the gold surface and $f_{ads} = 1$ represents a chain fully adsorbed to the gold surface. For all chain lengths, the z velocity of the polymers decreases as the fraction of adsorbed beads increases. Despite this, even the longest chains exhibit motion at high f_{ads}, with $\frac{dz}{dt} > 0$. The lack of dead zone behavior is consistent with the experimental system because chains do not have a strong affinity for the gold surface, and thus are less likely to strongly and permanently adsorb to the surface.

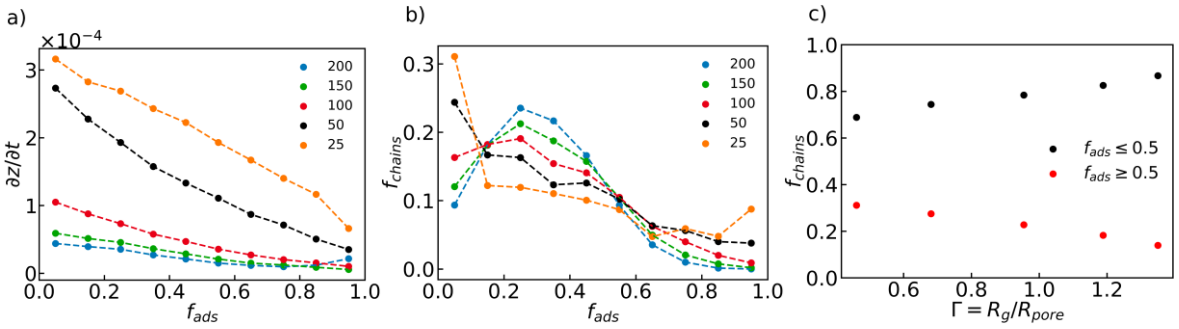

Figure 4.11. (a) Chain center of mass z velocity $\frac{dz}{dt}$, versus the fraction of adsorbed polymer beads for each chain length. A monomer is adsorbed if the chain bead is within 1.5σ of any gold surface bead. The adsorbed fraction is defined as $f_{ads} = (\frac{\#\ of\ adsorbed\ beads}{N})$. (b) The fraction of total chains (f_{chains}) at each adsorbed fraction for each chain length. (c) The fraction of highly adsorbed chains $f_{ads} \geq 0.5$ (red) and the fraction of weakly adsorbed chains $f_{ads} \leq 0.5$ (black) versus the confinement ratio Γ.

Figure 4.11b shows the fraction of total chains at each value of f_{ads}. This fraction is calculated using all time points throughout the course of infiltration. The two shortest chain lengths, N = 25 and N = 50, have radii of gyration smaller than the characteristic pore radius, $\Gamma < 1$. The highest fraction of chains for these polymers under low confinement are the free chains, with $f_{ads} < 0.1$. Once the radius of gyration is near or exceeds the pore radius, as is true for the other chain lengths (N=100, 150, 200), excluded volume interactions press chains toward the pore walls, and the largest fraction of chains exist in a partially adsorbed state.

In Figure 4.11b, above $f_{ads} \approx 0.6$, one sees that the number of chains with a large absorbed fraction decreases with increasing N. Despite the bias away from completely free chains, the fraction of slower moving, highly adsorbed chains is lower for longer chains. Figure 4.11c depicts this trend, plotting the fraction of highly adsorbed chains $f_{ads} \geq 0.5$ in red and the fraction of weakly adsorbed chains $f_{ads} \leq 0.5$ in black for each simulated Γ. This finding aligns well with previous works [39,67,68] demonstrating through both experiment and simulation that surface adsorbed polymer concentration scales inversely with molecular weight. A model for the probability distribution of adsorbed monomers has been developed previously[69] in which the mean value of f_{ads} is located at $f_{mean} \sim f_{max} - N^{-1/6}$ where f_{max} is the maximum adsorbed

fraction. Such a model is for equilibrium distributions, which are not captured in Figure 4.11b, but demonstrates the N dependence of the adsorbed fraction. Previous research has also shown that polymer diffusion near surfaces exhibits non-monotonic behavior, at first increasing with increasing surface coverage until a maximum is reached and diffusion slows as macromolecular crowding at the surface dominates[70] . Combined with work demonstrating that shorter chain lengths have faster adsorption dynamics[59], one would expect lower surface coverage with increasing N, as shown in Figure 4.11, and thus higher diffusion within the nanoporous gold in comparison with bulk diffusion.

Previous simulation work modeling the dynamics of polymers confined in nanoparticle packings found that polymer segments in contact with nanoparticle surfaces experienced higher local friction, and thus slower dynamics[71]. When the authors compared a polymer nanocomposite system with a lower polymer fill fraction, $\phi_{poly} = 0.2$, to a system with higher polymer fill fraction, the higher $\phi_{poly} = 0.87$ system contained a notable number of chains with faster dynamics than the $\phi_{poly} = 0.2$ system. Since both systems have the same amount of available nanoparticle surface area, but there are more polymer chains in the more filled system, the polymers in the $\phi_{poly} = 0.2$ system have a higher percentage of polymer segments adsorbed to nanoparticle surfaces than the polymers in the $\phi_{poly} = 0.87$ system. The deviation in f_{ads} between the two systems leads to a difference in local friction, explaining the enhanced dynamics in the $\phi_{poly} = 0.87$ system [71,72]. A similar argument can be applied to the system studied here. As depicted in Figure 4.11, on average f_{ads} decreases with increasing chain length. The local friction due to surface adsorption in the system thus decreases with increasing chain length. The capillary force balance is between the pressure gradient and the frictional force. Under constant

capillary pressure, the frictional force decreases with increasing chain length. One would thus expect larger deviations from bulk dynamics with increasing N due to a larger driving force during infiltration, which agrees well with the $\frac{\eta_{infiltrated}}{\eta_{bulk}} \propto \frac{N^{1.4}}{N^{3.4}} \propto N^{-2}$ experimental scaling behavior depicted in Figure 4.7, where the decrease from bulk viscosity grows with chain length.

This work bears several similarities with recent work by Zhou et al simulating capillary rise of polymer chains in cylindrical nanopores[38], justifying a comparison of the results in that work with the findings outlined here. The system studied in the aforementioned work involves an ideal cylindrical pore with no tortuosity, while the current study centers on a bicontinuous network of pores. Zhou's work simulates chain lengths from N = 1 to N = 400, varying from well below to well above the entanglement length for the simulation method used, Ne ≈ 84 . In the present paper, only chain lengths above the entanglement length, Ne ≈ 17, are simulated, ranging from N = 25 to N = 200. The confinement ratio in the simulations described here ranges from 0.46 to 1.35 and only the chain length impacts confinement; a constant bicontinuous gold structure is used for all simulations. In Zhou's work, confinement is varied via both chain length and pore size using 3 different cylindrical pore radii. In the smallest pore size, R = 5σ, the confinement ratio ranges from near 0 to 1.5. Because this range is most similar to our study, we will focus on results in the R = 5σ capillary for highly entangled chains, N > 100; N/Ne > 1.2. For these conditions, Zhou observed faster than LWE capillary infiltration, similar to our results shown in Figure 4.8a. However, the effective viscosity was found to scale with polymer molecular weight as $\eta_{eff} \propto N^{0.33}$, a smaller exponent than the $\eta_{eff} \propto N^{1.4}$ scaling shown in Figure 4.8b. Similar to the results shown in Figure 4.10 of this work, the radius of gyration of chains infiltrated into cylindrical pores was measured, and chain extension in the direction of capillary flow was

observed. In the cylindrical nanopores, the number of entanglements decreased for all highly entangled chain lengths, similar to the findings shown in Figure 4.9a. However, in the cylindrical capillaries, $\frac{Ne_{bulk}}{Ne_{infiltrated}}$ decreases with increasing molecular weight, the opposite trend to that shown in Figure 10b. As described previously, the trend found in Zhou's work supports the idea that the decrease in entanglements is the main driving force for the change in viscosity observed in the confined cylindrical capillaries. The unique geometry of the bicontinuous nanoporous gold structure introduces more dramatic surface effects, with the fraction of chains interacting with the surface decreasing as chain length increases, as shown in Figure 4.11c. In this work, in contrast with Zhou's work, the decrease in entanglements is driven more by surface interactions than pure confinement. Previous research has demonstrated that in the presence of nanoparticles with radius on the order of the ligament-ligament distance of the gold surface simulated here, the number of entanglements near particle surfaces is lower than bulk, with more dramatic differences observed in the presence of neutral wetting surfaces[73], like the surface simulated here. As the entanglement density of chains near the surface is lower than the bulk, one would expect to see a larger impact of surfaces on the number of entanglements for the shorter chains, explaining the observation that the trend in $\frac{Ne_{bulk}}{Ne_{infiltrated}}$ shown in Figure 4.11c opposes the trend observed in cylindrical capillaries. This surface effect contributes to the difference in the scaling of viscosity with molecular weight between these two works.

The results from molecular dynamics simulations of capillary rise infiltration of weakly-interacting entangled polymers into nanoporous gold reveal two main factors driving the experimentally observed reduction in viscosity and change in infiltration scaling exponent. The

first is a reduction in chain entanglement density during infiltration. The number of entanglements decreases for all chain lengths studied, but there is a smaller delta in entanglements for larger chains. This trend means that entanglement density alone cannot fully explain the observed viscosity changes, where the decrease in viscosity increases with molecular weight. The second factor we attribute to the reduced viscosity is a decrease in the fraction of chains adsorbed with increasing polymer molecular weight. Less adsorption leads to decreasing friction with molecular weight, and thus lower viscosity.

4.4 Conclusion

In this work, the dynamic scaling of capillary rise infiltration of polystyrene as a function of molecular weight is measured inside a nanoporous gold (NPG) structure. The bicontinuous structure is characterized by SAXS, SEM and AFM. The NPG film is about 120 nm thick with a pore radius of 37.5 nm and a pore volume fraction of about 0.50. For a moderate degree of polymer confinement in the NPG ($0.47 < \Gamma < 0.77$) and entangled PS, the infiltration time scales as $\tau_{80\%} \propto M_w^{1.30 \pm 0.20}$, which is weaker than predicted if bulk viscosity dictates capillary flow. For $0.46 < \Gamma < 1.35$, molecular dynamics simulations of polymer infiltration inside NPG yields an apparent scaling $\tau_{infiltration} \propto N^{1.4}$, in good agreement with experimental studies. Using the infiltration time, the effective viscosity of entangled PS is significantly reduced compared to bulk, with the difference increasing with molecular weight. Molecular dynamics simulations of the nanoporous gold system demonstrate a reduction in entanglements for all chains, which supports the increased kinetics. However, the reduction in entanglements decreases as chain length increases, indicating that reduced entanglement alone does not explain the trend in

experimental viscosity. The simulations reveal a decrease in the fraction of highly adsorbed chains with N, which reduces polymer-wall friction with increasing polymer molecular weight. This behavior captures the observed experimental kinetics and viscosity. Through studying PS kinetics inside NPG during the formation of PING, we now better understand how to infiltrate polymers into a metal scaffold, facilitating future studies that utilize other polymeric materials to create PING that can serve as actuators, cell membranes, and optical response materials.

4.5 References

1. Balazs, A. C., Emrick, T. & Russell, T. P. Nanoparticle Polymer Composites: Where Two Small Worlds Meet. *Science* **314**, 1107–1110 (2006).

2. Kim, J. *et al.* Estimation of the concentration of nano-carbon black in tire-wear particles using emission factors of PM10, PM2.5, and black carbon. *Chemosphere* **303**, 134976 (2022).

3. Guth, E. Theory of Filler Reinforcement. *J. Appl. Phys.* **16**, 20–25 (1945).

4. Bilchak, C. R. *et al.* Polymer-Grafted Nanoparticle Membranes with Controllable Free Volume. *Macromolecules* **50**, 7111–7120 (2017).

5. Merkel, T. C. *et al.* Ultrapermeable, Reverse-Selective Nanocomposite Membranes. *Science* **296**, 519–522 (2002).

6. Glor, E. C., Ferrier, R. C., Li, C., Composto, R. J. & Fakhraai, Z. Out-of-plane orientation alignment and reorientation dynamics of gold nanorods in polymer nanocomposite films. *Soft Matter* **13**, 2207–2215 (2017).

7. Hore, M. J. A., Frischknecht, A. L. & Composto, R. J. Nanorod Assemblies in Polymer Films and Their Dispersion-Dependent Optical Properties. *ACS Macro Lett.* **1**, 115–121 (2012).

8. Hore, M. J. A. & Composto, R. J. Nanorod Self-Assembly for Tuning Optical Absorption. *ACS Nano* **4**, 6941–6949 (2010).

9. Bilchak, C. R., Huang, Y., Benicewicz, B. C., Durning, C. J. & Kumar, S. K. High-Frequency Mechanical Behavior of Pure Polymer-Grafted Nanoparticle Constructs. *ACS Macro Lett.* **8**, 294–298 (2019).

10. Rittigstein, P. & Torkelson, J. M. Polymer-nanoparticle interfacial interactions in polymer nanocomposites: Confinement effects on glass transition temperature and suppression of physical aging: Polymer-Nanoparticle Interfacial Interactions. *J. Polym. Sci. Part B Polym. Phys.* **44**, 2935–2943 (2006).

11. Polizos, G. *et al.* Effect of polymer–nanoparticle interactions on the glass transition dynamics and the conductivity mechanism in polyurethane titanium dioxide nanocomposites. *Polymer* **53**, 595–603 (2012).

12. Krook, N. M. *et al.* Experiments and Simulations Probing Local Domain Bulge and String Assembly of Aligned Nanoplates in a Lamellar Diblock Copolymer. *Macromolecules* **52**, 8989–8999 (2019).

13. Krook, N. M. *et al.* Alignment of Nanoplates in Lamellar Diblock Copolymer Domains and the Effect of Particle Volume Fraction on Phase Behavior. *ACS Macro Lett.* **7**, 1400–1407 (2018).

14. Gómez-Hernández, R., Panecatl-Bernal, Y. & Méndez-Rojas, M. Á. High yield and simple one-step production of carbon black nanoparticles from waste tires. *Heliyon* **5**, e02139 (2019).

15. Lü, C. *et al.* Preparation and characterization of ZnS–polymer nanocomposite films with high refractive index. *J Mater Chem* **13**, 2189–2195 (2003).

16. LaNasa, J. A. & Hickey, R. J. Surface-Initiated Ring-Opening Metathesis Polymerization: A Method for Synthesizing Polymer-Functionalized Nanoparticles Exhibiting Semicrystalline Properties and Diverse Macromolecular Architectures. *Macromolecules* **53**, 8216–8232 (2020).

17. Srivastava, S. & Kotov, N. A. Composite Layer-by-Layer (LBL) Assembly with Inorganic Nanoparticles and Nanowires. *Acc. Chem. Res.* **41**, 1831–1841 (2008).

18. Huang, Y.-R. *et al.* Polymer nanocomposite films with extremely high nanoparticle loadings via capillary rise infiltration (CaRI). *Nanoscale* **7**, 798–805 (2015).

19. Jiang, Y., Hor, J. L., Lee, D. & Turner, K. T. Toughening Nanoparticle Films via Polymer Infiltration and Confinement. *ACS Appl. Mater. Interfaces* **10**, 44011–44017 (2018).

20. Qiang, Y., Turner, K. T. & Lee, D. Role of Polymer–Nanoparticle Interactions on the Fracture Toughness of Polymer-Infiltrated Nanoparticle Films. *Macromolecules* **56**, 122–135 (2023).

21. Qiang, Y., Pande, S. S., Lee, D. & Turner, K. T. The Interplay of Polymer Bridging and Entanglement in Toughening Polymer-Infiltrated Nanoparticle Films. *ACS Nano* **16**, 6372–

6381 (2022).

22. Biener, J., Biener, M. M., Madix, R. J. & Friend, C. M. Nanoporous Gold: Understanding the Origin of the Reactivity of a 21st Century Catalyst Made by Pre-Columbian Technology. *ACS Catal.* **5**, 6263–6270 (2015).

23. Li, J., Markmann, J., Weissmüller, J. & Mameka, N. Nanoporous gold-polypyrrole hybrid electrochemical actuators with tunable elasticity. *Acta Mater.* **212**, 116852 (2021).

24. Maguire, S. M. *et al.* Effect of Nanoscale Confinement on Polymer-Infiltrated Scaffold Metal Composites. *ACS Appl. Mater. Interfaces* **13**, 44893–44903 (2021).

25. Venkatesh, R. B. & Lee, D. Interfacial Friction Controls the Motion of Confined Polymers in the Pores of Nanoparticle Packings. *Macromolecules* **55**, 8659–8667 (2022).

26. Venkatesh, R. B. & Lee, D. Conflicting Effects of Extreme Nanoconfinement on the Translational and Segmental Motion of Entangled Polymers. *Macromolecules* **55**, 4492–4501 (2022).

27. Hor, J. L., Wang, H., Fakhraai, Z. & Lee, D. Effect of Physical Nanoconfinement on the Viscosity of Unentangled Polymers during Capillary Rise Infiltration. *Macromolecules* **51**, 5069–5078 (2018).

28. Venkatesh, R. B. *et al.* Effect of polymer–nanoparticle interactions on solvent-driven infiltration of polymer (SIP) into nanoparticle packings: a molecular dynamics study. *Mol. Syst. Des. Eng.* **5**, 666–674 (2020).

29. Hor, J. L., Wang, H., Fakhraai, Z. & Lee, D. Effects of polymer–nanoparticle interactions on

the viscosity of unentangled polymers under extreme nanoconfinement during capillary rise infiltration. *Soft Matter* **14**, 2438–2446 (2018).

30. Washburn, E. W. The Dynamics of Capillary Flow. *Phys. Rev.* **17**, 273–283 (1921).

31. Lucas, R. Ueber das Zeitgesetz des kapillaren Aufstiegs von Flüssigkeiten. *Kolloid-Z.* **23**, 15–22 (1918).

32. Yao, Y., Butt, H.-J., Floudas, G., Zhou, J. & Doi, M. Theory on Capillary Filling of Polymer Melts in Nanopores. *Macromol. Rapid Commun.* **39**, 1800087 (2018).

33. Hu, G. & Cao, B. Flows of Polymer Melts through Nanopores: Experiments and Modelling. *J. Therm. Sci. Technol.* **8**, 363–369 (2013).

34. Shavit, A. & Riggleman, R. A. The dynamics of unentangled polymers during capillary rise infiltration into a nanoparticle packing. *Soft Matter* **11**, 8285–8295 (2015).

35. Yao, Y. *et al.* Complex dynamics of capillary imbibition of poly(ethylene oxide) melts in nanoporous alumina. *J. Chem. Phys.* **146**, 203320 (2017).

36. Johner, A., Shin, K. & Obukhov, S. Nanofluidity of a polymer melt: Breakdown of Poiseuille's flow model. *EPL Europhys. Lett.* **91**, 38002 (2010).

37. Shin, K. *et al.* Enhanced mobility of confined polymers. *Nat. Mater.* **6**, 961–965 (2007).

38. Zhang, J. *et al.* Capillary Filling of Polymer Chains in Nanopores. *Macromolecules* **56**, 2258–2267 (2023).

39. Yao, Y., Butt, H.-J., Zhou, J., Doi, M. & Floudas, G. Capillary Imbibition of Polymer Mixtures in Nanopores. *Macromolecules* **51**, 3059–3065 (2018).

40. Manias, E. *et al.* Intercalation Kinetics of Long Polymers in 2 nm Confinements. *Macromolecules* **33**, 7955–7966 (2000).

41. Tu, C.-H., Zhou, J., Doi, M., Butt, H.-J. & Floudas, G. Interfacial Interactions During In Situ Polymer Imbibition in Nanopores. *Phys. Rev. Lett.* **125**, 127802 (2020).

42. Wang, F. *et al.* Suppressed Chain Entanglement Induced by Thickness of Ultrathin Polystyrene Films. *Macromolecules* **54**, 3735–3743 (2021).

43. García, N. A. & Barrat, J.-L. Entanglement Reduction Induced by Geometrical Confinement in Polymer Thin Films. *Macromolecules* **51**, 9850–9860 (2018).

44. Lee, N.-K., Diddens, D., Meyer, H. & Johner, A. Local Chain Segregation and Entanglements in a Confined Polymer Melt. *Phys. Rev. Lett.* **118**, 067802 (2017).

45. Sussman, D. M., Tung, W.-S., Winey, K. I., Schweizer, K. S. & Riggleman, R. A. Entanglement Reduction and Anisotropic Chain and Primitive Path Conformations in Polymer Melts under Thin Film and Cylindrical Confinement. *Macromolecules* **47**, 6462–6472 (2014).

46. Pressly, J. F., Riggleman, R. A. & Winey, K. I. Polymer Diffusion Is Fastest at Intermediate Levels of Cylindrical Confinement. *Macromolecules* **51**, 9789–9797 (2018).

47. Zhang, T., Winey, K. I. & Riggleman, R. A. Polymer Conformations and Dynamics under Confinement with Two Length Scales. *Macromolecules* **52**, 217–226 (2019).

48. Luna, F. V. *et al.* Straight versus Spongy: Effect of Tortuosity on Polymer Imbibition into Nanoporous Matrices Assessed by Segmentation-Free Analysis of 3D Sample

Reconstructions. *J. Phys. Chem. C* **126**, 12765–12779 (2022).

49. Rubinstein, M. & Colby, R. H. *Polymer Physics*. (Oxford University Press, Oxford ; New York, 2003).

50. Ding, Y., Kim, Y.-J. & Erlebacher, J. Nanoporous Gold Leaf: Ancient Technology Advanced Material. *Adv. Mater.* **16**, 1897–1900 (2004).

51. Hu, K., Ziehmer, M., Wang, K. & Lilleodden, E. T. Nanoporous gold: 3D structural analyses of representative volumes and their implications on scaling relations of mechanical behaviour. *Philos. Mag.* **96**, 3322–3335 (2016).

52. Lilleodden, E. T. & Voorhees, P. W. On the topological, morphological, and microstructural characterization of nanoporous metals. *MRS Bull.* **43**, 20–26 (2018).

53. Ng, A. K., Welborn, S. S. & Detsi, E. Time-dependent power law function for the post-dealloying chemical coarsening of nanoporous gold derived using small-angle X-ray scattering. *Scr. Mater.* **206**, 114215 (2022).

54. Welborn, S. S., Van Der Meer, S., Corsi, J. S., De Hosson, J. Th. M. & Detsi, E. Using X-Ray Scattering to Elucidate the Microstructural Instability of 3D Bicontinuous Nanoporous Metal Scaffolds for Use in an Aperiodic 3D Tricontinuous Conductor–Insulator–Conductor Nanocapacitor. *ACS Appl. Mater. Interfaces* **13**, 11721–11731 (2021).

55. Wittstock, A., Biener, J. & Bäumer, M. Nanoporous gold: a new material for catalytic and sensor applications. *Phys. Chem. Chem. Phys.* **12**, 12919 (2010).

56. Michels, A. & Weissmüller, J. Magnetic-field-dependent small-angle neutron scattering on

random anisotropy ferromagnets. *Rep. Prog. Phys.* **71**, 066501 (2008).

57. Li, Y., Pham, J. Q., Johnston, K. P. & Green, P. F. Contact Angle of Water on Polystyrene Thin Films: Effects of CO_2 Environment and Film Thickness. *Langmuir* **23**, 9785–9793 (2007).

58. Erb, R. The Wettability of Gold. *The Journal of Physical Chemistry* 2412–2413 (1967).

59. Tu, C.-H., Zhou, J., Butt, H.-J. & Floudas, G. Adsorption Kinetics of *cis* -1,4-Polyisoprene in Nanopores by *In Situ* Nanodielectric Spectroscopy. *Macromolecules* **54**, 6267–6274 (2021).

60. Fox, T. G. & Flory, P. J. Viscosity—Molecular Weight and Viscosity—Temperature Relationships for Polystyrene and Polyisobutylene [1,2]. *J. Am. Chem. Soc.* **70**, 2384–2395 (1948).

61. Colby, R. H., Fetters, L. J. & Graessley, W. W. The melt viscosity-molecular weight relationship for linear polymers. *Macromolecules* **20**, 2226–2237 (1987).

62. Masoodi, R., Pillai, K. M. & Varanasi, P. P. Darcy's law-based models for liquid absorption in polymer wicks. *AIChE J.* **53**, 2769–2782 (2007).

63. Luo, J.-W. *et al.* Macroscopic transport properties of Gyroid structures based on pore-scale studies: Permeability, diffusivity and thermal conductivity. *Int. J. Heat Mass Transf.* **146**, 118837 (2020).

64. Seemann, R., Jacobs, K. & Blossey, R. Polystyrene nanodroplets [*]. *J. Phys. Condens. Matter* **13**, 4915–4923 (2001).

65. Karapanagiotis, I., Evans, D. F. & Gerberich, W. W. Dewetting dynamics of thin polystyrene

films from sputtered silicon and gold surfaces. *Colloids Surf. Physicochem. Eng. Asp.* **207**, 59–67 (2002).

66. Kröger, M., Dietz, J. D., Hoy, R. S. & Luap, C. The Z1+ package: Shortest multiple disconnected path for the analysis of entanglements in macromolecular systems. *Comput. Phys. Commun.* **283**, 108567 (2023).

67. Tarnacka, M. *et al.* The Impact of Molecular Weight on the Behavior of Poly(propylene glycol) Derivatives Confined within Alumina Templates. *Macromolecules* **52**, 3516–3529 (2019).

68. Lin, E. Y., Frischknecht, A. L., Winey, K. I. & Riggleman, R. A. Effect of surface properties and polymer chain length on polymer adsorption in solution. *J. Chem. Phys.* **155**, 034701 (2021).

69. O'Shaughnessy, B. & Vavylonis, D. Non-equilibrium in adsorbed polymer layers. *J. Phys. Condens. Matter* **17**, R63 (2004).

70. Zhao, J. & Granick, S. How Polymer Surface Diffusion Depends on Surface Coverage. *Macromolecules* **40**, 1243–1247 (2007).

71. Lin, E. Y., Frischknecht, A. L. & Riggleman, R. A. Chain and Segmental Dynamics in Polymer–Nanoparticle Composites with High Nanoparticle Loading. *Macromolecules* **54**, 5335–5343 (2021).

72. Lin, E. Y., Frischknecht, A. L. & Riggleman, R. A. Origin of Mechanical Enhancement in Polymer Nanoparticle (NP) Composites with Ultrahigh NP Loading. *Macromolecules* **53**,

2976–2982 (2020).

73. Seibert, J., Pfaller, S. & Ries, M. Investigation of the influence of nano-sized particles on the entanglement distribution of a generic polymer nanocomposite using molecular dynamics. *Math. Mech. Solids* 10812865231206547 (2023) doi:10.1177/10812865231206547.

CHAPTER 5. POLYMER-WALL INTERACTIONS SLOW INFILTRATION DYNAMICS IN BICONTINUOUS, NANOPOROUS STRUCTURES

Content in this chapter is currently under review in 2024 to *Macromolecules*, with authors Weiwei Kong, Anastasia Neuman, Laetitia Moore, Daeyeon Lee, Robert A. Riggleman, Russell J. Composto. R.J.C., D.L and R.A.R conceived and planned for the project. W.K. developed the experimental procedures and conducted all experimental measurements and analysis. A.N. conducted simulation development and analysis. L.M. conducted and analyzed a portion of simulations. W.K and A.N. wrote the manuscript. R.J.C., D.L. and R.A.R edited the manuscript.

5.1 Introduction

Polymer nanocomposites (PNCs) are of interest for commercial applications because their wide range of properties makes them attractive materials for coatings [1,2], membranes [3,4], and actuators [5]. Typically, PNCs contain inorganic nanofiller dispersed in a polymeric matrix. PNCs have been of interest in academia, national laboratories and industrial laboratories [6–8] because of their superior performance as compared to unfilled polymers. For instance, by adding nanoparticles into a polymer matrix, PNCs with ultrahigh strength and toughness can be designed as protective coatings [9,10]. In part, the properties of the PNC depend on processing conditions which determine nanoparticle dispersion and material properties, such as nanoparticle loading, nanoparticle type and matrix polymer properties. In most systems, the thermodynamics of mixing is unfavorable and nanoparticles aggregate, particularly at high loadings. Even for the rare cases where the nanoparticle and polymer have a favorable thermodynamics of mixing, slow

nanoparticle diffusion due to the high viscosity matrix can lead to kinetically trapped aggregates of nanoparticles. This arrested state is even more prevalent when producing PNCs with high loadings. For example, below 0.05 vol%, nanoplates uniformly sequester in one domain of a lamellar block copolymer (BCP), whereas at higher loadings nanoplates aggregate and frustrate BCP ordering [11,12]. In summary, PNCs with a high loading of nanoparticles (e.g., near percolation) are typically difficult to prepare while maintaining control over PNC morphology.

In our previous studies [13,14], we circumvented the difficulties of nanofiller-limited loading and inhomogeneous dispersion by infiltrating polymer into the pores of a prefabricated bicontinuous nanoporous gold (NPG). This polymer-infiltrated NPG (PING) nanocomposite exhibits inorganic loadings of ~50 vol%. PING preparation utilizes a capillary force to drive molten polymer into the NPG with pore diameters from 15 to 75 nm[15], and similar strategies have been used in previous work to infiltrate densely packed nanoparticles [16–24] and anodized aluminum oxide (AAO) pores [25–28]. Starting with a polymer film on top of the NPG, the bilayer is heated above the polymer glass transition temperature (Tg). Subsequently, capillarity drives the polymer melt through the porous network spanning the NPG thickness, resulting in a PNC that retains the original NPG structure. Capillary rise infiltration (CaRI) has been used to prepare PNCs using scaffolds of densely packed nanoparticles [16–24] and anodized aluminum oxide (AAO) pores [25–28]. Through capillary-driven infiltration, high nanofiller loading was achieved.

Confinement can perturb polymer characteristics and properties compared to bulk behavior [13,14,25,27,29–44]. The conformations of polymer chains are distorted when confined to pores with a size comparable to the polymer, and this distortion, in turn, influences polymer dynamics. Previous work has shown that polymers can exhibit a higher Tg in confined

geometries [13,19,24,45,46], depending on the nature of the interactions of the polymer with the confining surfaces. As confinement increases, the polymer segmental relaxation dynamics slow down, and Tg increases [47]. For example, Maguire et al. (2021) found that the Tg of PS increased by 6°C when confined in NPG with a pore size (Rp) greater than the radius of gyration (Rg) [13]. In a complementary study, for PS highly confined in packed nanoparticles (Rg < Rp), the Tg increased by 57°C compared to the bulk [46]. Despite this increase in Tg for completely filled nanocomposites, polymer infiltration into confined or semi-confined pores shows enhanced kinetics [14,16,19,24,48,49]. For entangled PS infiltrating NPG under moderate confinement, the effective viscosity decreased by over an order of magnitude relative to the bulk viscosity, and this difference increased as Mw increased [14]. For entangled PS infiltration in highly confined SiO_2 packing, the effective viscosity also decreased [16]. However, for unentangled PS and P2VP infiltrating into SiO_2, a significant slowdown is observed [19]. The seemingly conflicting effect of confinement on polymer infiltration kinetics has remained largely unresolved.

In this study, we investigate the effect of polymer / wall interactions on the kinetics of polymer infiltration into NPG structures. In our preceding study [14], polystyrene (PS), which weakly interacts with the NPG, exhibited a reduced effective viscosity relative to the bulk and a weaker viscosity dependence on Mw over the range 424k to 1133k Da. To better understand the underlying mechanism, molecular dynamics (MD) simulations were used to show that the weak Mw dependence and the enhanced kinetics were attributed to a reduction in the chain entanglement density and a reduction in the polymer-wall adsorption fraction as Mw increases [14]. Some prior studies indicated that interfacial energy did not affect chain-scale polymer dynamics [19,50,51]. For instance, Hor et al. (2018) investigated the infiltration of unentangled P2VP and PS

for confinement parameter $\Gamma > 1$, where $\Gamma = R_g/R_p$, and found that the normalized viscosities were impacted in the same way for stronger polymer-wall interaction system (P2VP) as well as the weaker polymer-wall interaction system (PS) [19]. However, other studies suggest that stronger interfacial interactions decrease polymer kinetics. As a comparison, Maguire et al. (2021) found that infiltration time of entangled P2VP in NPG was an order of magnitude longer than that of PS under the same conditions [13]. In summary, prior studies are inconclusive about the effect of the polymer-wall interactions on infiltration kinetics.

The present study focuses on the kinetics of infiltrating poly(2-vinylpyridine) (P2VP) into nanoporous scaffolds with Rp of 34 nm. For Mw from 51k to 940k, infiltration conditions are "moderate" with Γ ranging from 0.18 to 0.78. For comparison, $\Gamma > 1$ would correspond to stronger confinement of chains. A key finding is that infiltration time scales as $\tau_{80\%} \propto M_w^{1.43}$, which is much weaker than the prediction based on the bulk behavior, $\tau \propto$ Mw3.4. For Mw < 180,000 Da., the effective viscosities are greater than the bulk values, whereas for Mw > 180,000 Da., the effective viscosities are lower than the bulk values. This transition occurs when the Mw is approximately 5x above the bulk critical Mw and is consistent with confinement reducing chain entanglements. The similarity of the molecular weight dependence of infiltration time for P2VP and PS is attributed to a strongly bound layer in the P2VP case. To investigate the effect of polymer-wall affinity, coarse-grained MD simulations were performed for systems with varying polymer-wall interactions. MD simulations support experimental results and show that polymers with a strong attraction for the wall results in slower infiltration. MD simulations show that infiltration time scales as $\tau \sim$ Mw1.4 in good agreement with experiments. This study allows us to better understand the effect of polymer-wall adsorption on infiltration into nanoporous

channels, and to prepare nanocomposites at high filler loadings that are difficult to achieve by blending polymers and discrete particles.

5.2 Materials & Methods

Please refer to Chapter 3 for part of the Materials and Methods.

Samples. The poly(2-vinylpyridine) (P2VP) and polystyrene (PS) samples with different molecular weights were purchased and used as received. Important molecular characteristics and length scales are described in Table 5.1.

Table 5.1. Characteristics of polymer and confinement parameter values

Sample Name	Mw (Da)	PDI	Rg (nm)	$\Gamma = Rg/Rp$
P2VP-51k	50,500	1.02	6.1	0.18
P2VP-85k	85000	1.08	8.0	0.23
P2VP-153k	152,500	1.06	10.7	0.31
P2VP-302k	302,000	1.09	15.1	0.44
P2VP-417k	417,000	1.13	17.7	0.52
P2VP-643k	643,000	1.18	22.0	0.65
P2VP-940k	940,000	1.10	26.6	0.78
PS-168k	168,000	1.05	11.2	0.33

The P2VP are entangled with weight average molecular weights from 51k Da to 940 kDa and have a narrow polydispersity (PDI). The radius of gyration (R_g) is given by $R_g = b2N6$. The R_g is calculated from the Kuhn length, b = 1.8 nm and the number of Kuhn segments, $N=M_w/M_o$, where the Kuhn monomer molar mass is 720 Da [52]. P2VP and PS solutions are prepared using 2.4 wt.% of polymer in methanol and toluene, respectively. After stirring overnight, solutions are spin coated onto silicon wafers (1 cm x 1 cm) at 4000 rpm for 1 minute. After that, the polymer films are annealed at 60°C in the Mettler heating stage (Mettler FP-82) under argon flow for 10 minutes to ensure evaporation of the solvent. The polymer thicknesses range from 100-300 nm as measured by reflectometer (Filmetrics F3UV).

The T_g's for bulk PS and P2VP are nearly identical when measured at the same cooling rate, Tg = 100 ℃ [53,54]. The T_g of PS-168k and P2VP-153k films on silicon substrates were measured using *in-situ* SE. To ensure equilibrium, the polymer films were first heated to 150 ℃, held at 150 ℃ for 5 min., and then cooled down at a rate of 10 ℃/min. Analysis of the SE output to determine Tg is described in SI information (Fig. B2). The PS-168k film (90 nm) has a T_g = 97 ± 2 ℃, whereas the P2VP-153k film (130 nm) has a Tg = 98 ± 2 ℃.

Water Contact Angle Goniometry. Static Water Contact Angles are used to measure the surface energy of the P2VP: NPG composite. Uniform DI-H_2O droplets were deposited onto the sample surface using a Gilmont Micrometer Dispenser. The system is illuminated using a Stocker Yale Imagelite Lite Mite - Model 20. Pictures of the water droplets were captured using a Sony CCD N50 Video Camera Module with a Navitar Zoom 7000 close-focusing macro video lens mounted on an optical table. The captured pictures are analyzed using Image J, plugin “LB-

ADSA," which uses the Young-Laplace equation to fit the shape of the water droplet for the exact contact angle.

Atomic Force Microscopy (AFM). Bruker Icon AFM with tapping mode is used to probe the surface morphology of the NPG/composite. The images collected are 2 x 2 μm^2. Tapping mode AFM tips, Tap300Al, have a tip height of 17 μm and radius of 10 nm. The AFM images are analyzed using Gwyddion software.

Scanning Electron Microscopy (SEM). FEI Quanta 600 SEM is used to detect the secondary electron signals at 15kV. The images are taken top-down to measure the ligament-ligament distance and in cross-section to measure the NPG thickness as well as infiltration extent. SEM images analysis also utilizes Gwyddion software.

5.3 Results and Discussion

Nanoporous Gold Characterization

The pore radii of as-prepared and annealed, 175°C for 3 h, nanoporous gold (NPG) were determined by small angle x-ray scattering (SAXS). For bicontinuous structures, the ligament to ligament distance (d-spacing) is given by [56,64] $d=1.23*2\pi/q_{max}$. Figure 5.1 shows that the SAXS intensity from the as-prepared and annealed NPG exhibits distinct scattering peaks with the peak for the annealed sample shifted to lower q. In both cases the intensity scales as q^{-4} at high q. The as-prepared NPG exhibits an average d-spacing of 62 nm, whereas the d-spacing increases to 136 nm for the annealed NPG. Using a porosity of ~ 50% measured previously [13,14], the radius of pore (R_p) can be determined from the d spacing using $R_p= d/4$. Thus, the as prepared NPG has a

radius of R_p, as prepared = 15.5 nm, whereas the value for the annealed NPG is R_p, annealed = 34 nm. For the annealed NPG, a shoulder exists at q = 0.025 Å-1, corresponding to a R_p = 7.7 nm. The shoulder may reflect the scattering from smaller NPG pores or Au nanoparticles resulting from incomplete ligament formation. In our prior work [13], we demonstrated that annealing of the NPG at 175°C for 3 h prevents the NPG structure from coarsening during infiltration at 150°C at times up to 3 h. In the present study, only the annealed NPG will be utilized to study infiltration of P2VP. In the remainder of the paper, "NPG" will refer to the annealed NPG.

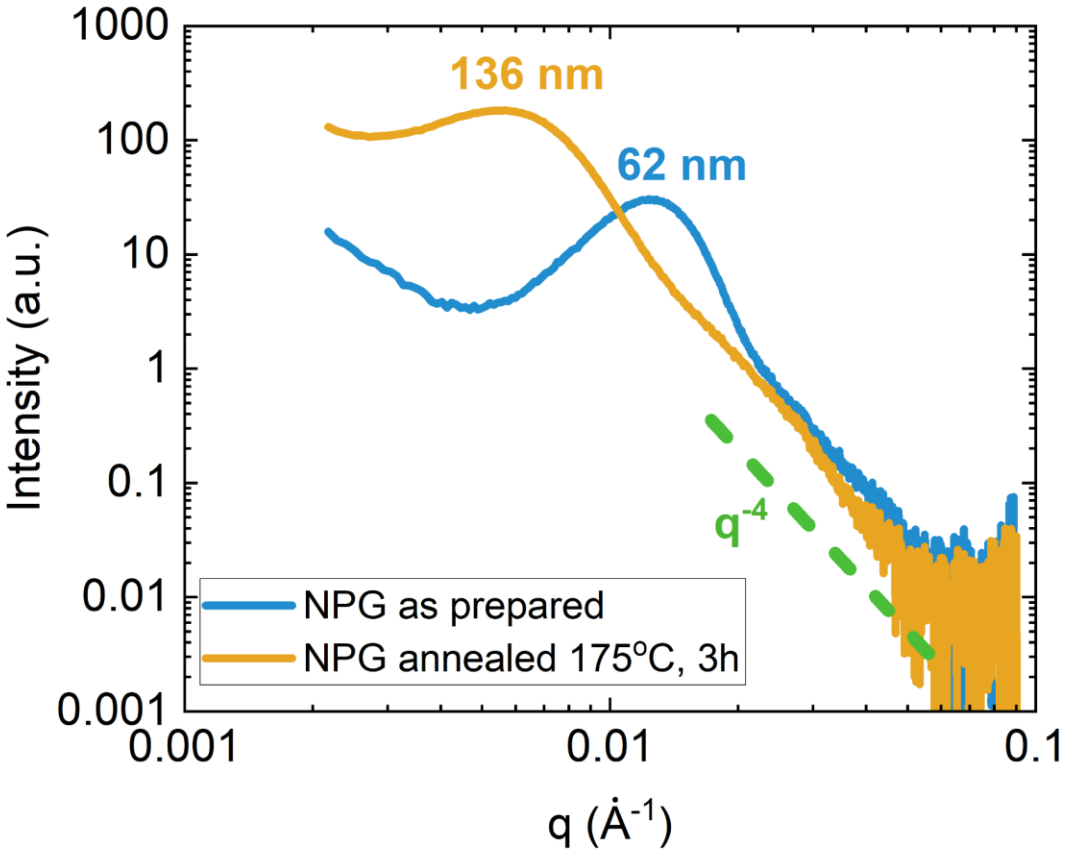

Figure 5.1. SAXS of as prepared NPG and NPG annealed at 175°C for 3 h. The characteristic peak shifts to lower q upon annealing. The d-spacings or ligament to ligament spacings increase from 62 nm to 136 nm upon annealing. At high q, the intensity scales as q^{-4}. The NPG thickness is 120 nm.

To complement SAXS, SEM images of the annealed NPG scaffolds were taken at different magnifications from increasingly smaller areas. Figure 5.2 shows the morphologies with scale bars of 5 μm, 2 μm and 500 nm (left to right). The SEM images show that the NPG ligaments are relatively uniformly distributed across the sample with few defects at higher magnifications. The uniform morphology ensures similar infiltration at different locations across the film. From this top view, the Au ligaments appear interconnected and form a bicontinuous structure of gold ligaments and open pores. From a line scan analysis, the Rp from the SEM images is 31 ± 7 nm, in statistical agreement with the SAXS results. In summary, SAXS and SEM characterization of the ca. 120 nm thick NPG are consistent with a bicontinuous structure exhibiting pores of 34 nm.

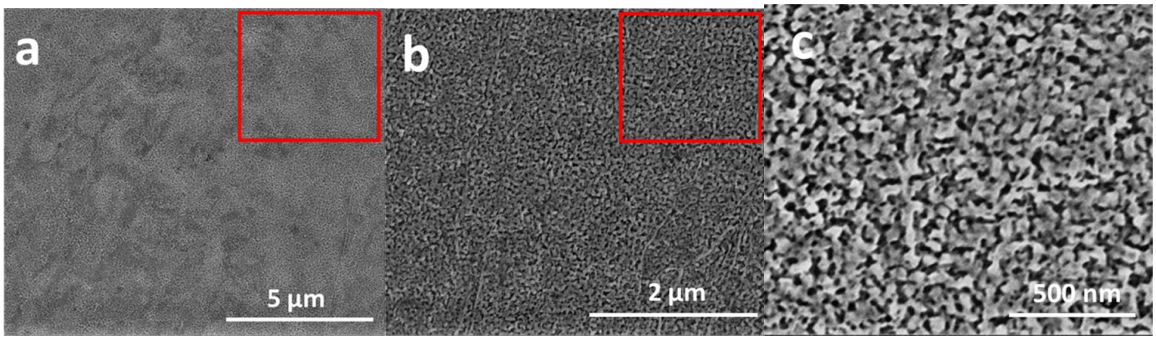

Figure 5.2. SEM images of annealed NPG at different length scales. The Au scaffold and open pores are light and dark respectively. 5.2b is taken from the region in 5.2a denoted by the red box. 5.2c taken from the region denoted by the red box 2b.

Infiltration of P2VP into the NPG scaffold

In this work, the effective viscosities as compared to the bulk, as well as the effect of polymer-wall interactions on polymer infiltration are studied by selecting a polymer, P2VP, that is attractive towards the Au surface of the scaffold. Several factors influence polymer infiltration into pores including polymer radius of gyration, polymer viscosity and polymer affinity with the wall. Polymer infiltration inside porous media is often described by the Lucas-Washburn Equation (LWE) [65,66],

$$h(t) = \sqrt{\frac{R_p \Upsilon \cos\theta_e}{2\eta_o}\, t} \qquad \text{Eq. 5.1}$$

In Eq. 5.1, $h(t)$ is the height infiltrated by the fluid (polymer), t is the infiltration time, R_p is the radius of the pore, Υ is the surface tension of the liquid, θ_e is the equilibrium contact angle, and η_o is the bulk viscosity. Originally, the LWE was derived for a Newtonian simple fluid, treated as a continuum medium, infiltrating a cylinder. According to Eq. 5.1, $t \sim h^2$, implying that if the medium is a Newtonian fluid, h^2 should be linearly related to the t of infiltration. In our previous study [14], we demonstrated that the infiltration height of polystyrene (PS) into a NPG scaffold scales as $t^{0.5}$ during the early time of infiltration in agreement with Eq. 5.1.

Using *in-situ* spectroscopic ellipsometry (SE), Figure 5.3a shows the infiltration height of P2VP-940k and P2VP-85k plotted as a function of $t^{0.5}$ at 140°C. For ease of comparison with MD results, the same data was also plotted as h^2 vs. t in the SI (Fig. B1). However, Figure 5.3a better distinguishes the difference between the P2VP-940k and P2VP-85k results when plotted as

h vs. $t^{0.5}$. The maximum height corresponds to the thickness of the NPG, 120 nm [14]. From Figure 5.3a, the P2VP-940k infiltration height deviates from linearly, even at early times, and the slope decreases with increasing time in contrast to the infiltration of PS. This slowing down may be attributed to the affinity of the P2VP for the Au surface and the weak interaction of PS with Au [14]. As described later, MD simulations of the infiltration height capture this slowing down. Figure 5.3a also shows that infiltration slows as the M_w of P2VP increases from 85k to 940k. We use $\boldsymbol{\tau}_{80\%}$ to quantify the infiltration time for P2VP to reach a height of 96 nm in the NPG. As shown in Figure 5.3a, $\boldsymbol{\tau}_{80\%}$ increases from 5 min. to 106 min. as M_w increases from 85k to 940k, respectively. The infiltration kinetics for P2VP was measured for seven values of M_w ranging from 51k to 950k, corresponding to confinement ratios from 0.18 to 0.78. For P2VP:NPG bilayers annealed at 140°C, Figure 5.3b shows that infiltration time increases as M_w increases. If bulk viscosity determines the scaling of the molecular weight dependence, then $\tau_{80\%} \propto M_w^{3.4}$. However, as shown in Fig. 5.3b, $\tau_{80\%} \propto M_w^{1.43 \pm 0.03}$, implying that the molecular weight dependence of P2VP infiltration is weaker than expected from bulk behavior. Interestingly, the scaling of the infiltration time for P2VP is similar to that of PS [14] (slope = 1.30 ± 0.20), even though P2VP and PS have different affinities for the Au surface. This observation will be discussed later. In summary, P2VP infiltration height exhibits a nonlinear h vs. $t^{0.5}$ relationship, infiltration time scales as and scales as $M_w^{1.43}$, and the scaling of infiltration times with M_w for P2VP and PS are similar.

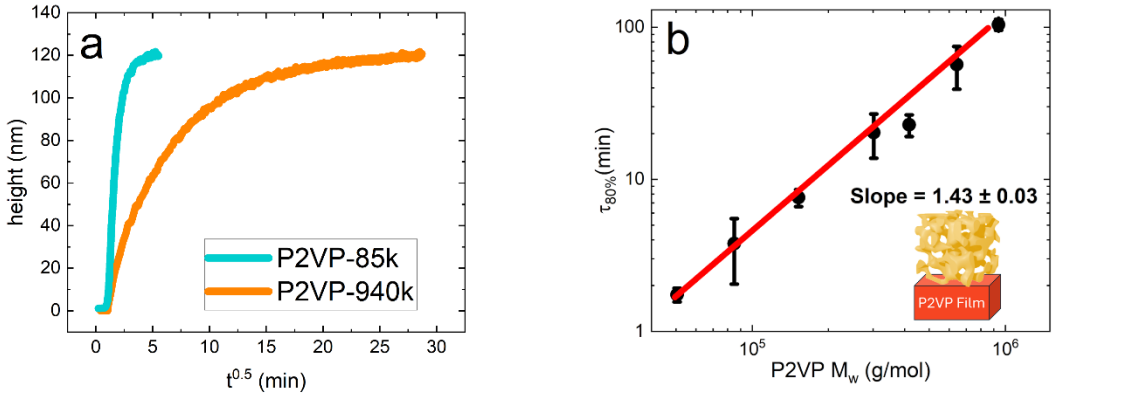

Figure 5.3. a. Infiltration height as a function of $t^{0.5}$ for P2VP-85K and P2VP-940k at 140°C. b. $\tau_{80\%}$ versus P2VP for molecular weights ranging from 51k to 940k. All M_w values are greater than M_c = 31k. The slope is 1.43. Inserted cartoon depicts the P2VP:NPG bilayer structure prior to infiltration.

The effective viscosity determined from infiltration studies can be compared to the bulk viscosity. The effective viscosity (η_{eff}) of P2VP can be calculated using a modified Lucas-Washburn Equation [67],

$$h^2 = \left(\frac{\Upsilon R_p cos\,\theta}{4\,\eta_{eff}\,\tau^2}\right) t \qquad \text{Eq. 5.2}$$

where the bulk fluid viscosity is replaced by the effective viscosity, η_{eff}. For the P2VP:NPG system, the Υ of P2VP is 37.9 mN/m [19] at 140°C, the average R_{pore} is 34 nm, τ is 1.5 [68], and θ between P2VP and gold [69] is 9°. Using these values, experimental data (e.g., Fig. 5.3) and Eq. 5.2, η_{eff} of P2VP can be determined. As shown in Figure 5.4a, the effective viscosity increases from $1.03 * 10^6$ to $6.14 * 10^7$ $Pa * s$ as M_w increases from 51k to 940k, respectively. The bulk viscosities were taken from the literature [54] and scale as $\eta_{bulk} \sim M_w^{3.4}$. Figure 5.4a shows that the effective viscosity is lower than the bulk viscosity at low M_w and greater at high M_w. This trend

is reiterated by plotting the ratio ($\frac{\eta_{eff}}{\eta_{bulk}}$) as shown in Figure 5.4b. As M_w increases, $\frac{\eta_{eff}}{\eta_{bulk}}$ is greater than 1, approaches 1 near 180k Da (Γ = 0.34), and then decreases below 1. In our previous study of PS infiltration [14], the η_{eff} was lower than the bulk for M_w values from 424k (Γ = 0.47) to 1133k Da (Γ = 0.77). For PS under confinement, we attributed this reduced η_{eff} to a decrease in entanglements and a relative reduction in the fraction of highly adsorbed chains as M_w increases. Both contributions also explain the reduction in η_{eff} for P2VP-302k (Γ = 0.44) and above, as detailed in the MD studies. However, for the range P2VP-51k to P2VP-153k, $\eta_{eff} < \eta_{bulk}$ with the viscosity difference, $\eta_{eff} - \eta_{bulk}$, decreasing as M_w increases. For unentangled P2VP (8k, Γ = 0.70 and 22k Da., Γ = 1.13) infiltrating into a dense SiO_2 structure, the effective viscosities increased by nearly 100x and 30x, respectively [19]. Although these studies are for unentangled chains and ours are above the bulk M_c (Figure 5.4), the results are consistent with each other. In summary, the effective viscosities are greater than the bulk values below 180k (Γ = 0.34) and less than the bulk values above this molecular weight.

The effective viscosity of polymer inside a channel can be divided into three regimes[23]. For low confinement, $\Gamma = \frac{R_g}{R_p} << 1$, η_{eff} increases due to the narrowing of the channel due to adsorbed polymer, also called the dead zone [70]. In the intermediate range, $0.1 < \Gamma \leq 1$, the η_{eff} decreases as confinement enhances the chain mobility due to chain elongation and reduced friction with the wall. However, for high confinement, $\Gamma > 1$, η_{eff} increases again because chains are strongly confined, resulting in an enhanced entropic barrier to infiltrate [23]. These three regimes agree with experiments [23,70]. As shown in Table 5.1, the confinement ratio in this study ranges from 0.18 and 0.78, corresponding to the second regime where η_{eff} is expected to be less

than the bulk value[23] according to Ren et al. (2024). However, for Γ = 0.18, 0.23 and 0.31, η_{eff} for P2VP is greater than the bulk values; whereas for Γ = 0.44, 0.52, 0.65 and 0.78, the effective viscosities are less than the bulk values. Based on the regimes defined above, for the P2VP:NPG system we expect $\eta_{eff} < \eta_{bulk}$, however this is only observed for Γ = 0.44 and above.

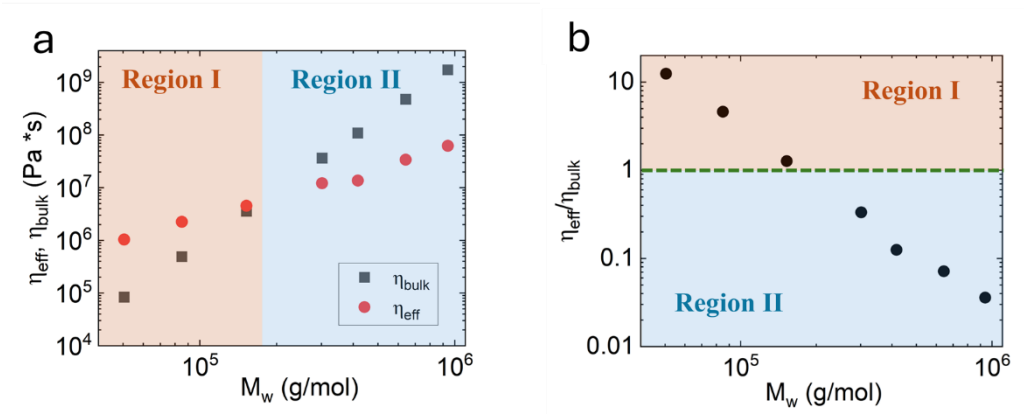

Figure 5.4. a. Effective viscosity (η_{eff}) and bulk viscosity (η_{bulk}) of P2VP as a function of $M_w$at 140°C. Effective viscosity scales as $\eta_{eff} \sim M_w^{1.4}$ while bulk viscosity scales as $\eta_{bulk} \sim M_w^{3.4}$. The M_w ranges from 51k to 940k Da., resulting in confinement ratios from 0.18 to 0.78. From M_w 51k to 153k Da. (Region I), the effective viscosities are higher than the bulk viscosity, whereas for M_w greater than 153k (Region II), the effective viscosities are lower than the bulk viscosities. In Region II, this difference increases as M_w increases. b. Using data from 4a, the ratio of $\frac{\eta_{eff}}{\eta_{bulk}}$ is plotted as a function of M_w. The ratio of $\frac{\eta_{eff}}{\eta_{bulk}}$ =1 near M_w = 180k Da.

As shown in Figure 5.4, the effective viscosities of P2VP can be divided into regions I (orange) and II (blue) with a crossover near 180k Da (Γ = 0.34). The transition suggests that ca. 180k Da represents an effective critical molecular weight (M_c) under confinement. For PEO infiltrating into cylindrical pores with R_p = 35 nm, a similar transition was observed between 100k (Γ =

0.35) and 280k Da (Γ = 0.58) [29,70]. For bulk melts, M_c separates Rouse from reptation dynamics [71] where $\eta \sim M_w$, and $\eta \sim M_w^{3.4}$, respectively. For both PS and P2VP, M_c is 31,000 Da[71]. The finding that $M_{c,confined} > M_c$ is consistent with a reduction of entanglements for weak polymer/wall attraction [14]. For stronger polymer-wall attraction (ε = 5.0), MD simulations described later indicate that confinement reduces polymer entanglement. Thus, in region 1, the higher effective viscosity is attributed to the formation of a physisorbed layer resulting in an effective pore size $R_p - \Delta R$, where ΔR is the physisorbed layer thickness [70]. Results found in Region II ($\eta_{eff} < \eta_{bulk}$) are consistent with our previous studies of PS infiltration across a similar range of Γ [14]. Because Γ is between 0.18 and 0.78, our experiments would fall into the intermediate regime described above [23]. Our results suggest that the Γ denoting the transition between the low and intermediate confinement regimes may be greater than expected.

Infiltration Kinetics of P2VP versus PS in NPG

Here we focus on how the polymer melt/Au interface impacts infiltration kinetics, noting that P2VP has a stronger attraction for Au than PS. The different interfacial properties of polar P2VP and hydrophobic PS are reflected in their water contact angle (WCA) values [14] of 60.0° (Fig. B5) and 89.9°, respectively. For comparison the WCA of gold is 64.4° [14]. Figure 5.5 compares the infiltration extent in NPG for PS-168k ($R_g = 11.2\ nm, \Gamma = 0.33$) and P2VP-153k ($R_g = 10.7\ nm,\ \Gamma = 0.31$) at 140°C. Whereas PS-168k reaches $\tau_{80\%}$ in 3.1 min, P2VP-153k is slower with $\tau_{80\%}$ = 5.8 min., nearly twice as long as PS. Similarly, PS-168k reaches 99% infiltration extent, $\tau_{99\%}$, after 7.9 min, whereas for P2VP-153k, $\tau_{99\%}$=17.9 min. The $\tau_{80\%}$ and $\tau_{99\%}$ values are both longer for P2VP as compared to PS at similar Γ. The effective viscosity of P2VP-153k

is given in Figure 5.4, whereas the value for PS-168k is calculated from Eq. 5.2 using Υ = 29.60 mN/m and θ = 20° [14]. Whereas η_{eff} for PS-168k is $1.3 * 10^6$ Pa*s, the value for P2VP-153k is $3.4 * 10^6$ Pa*s, which is 2.6x greater than PS. Because the T_g for these polymers are similar [53,54] as noted in the methods section, the slower infiltration of P2VP should be attributed to other factor(s) such as the affinity of P2VP for the Au surface of the scaffold.

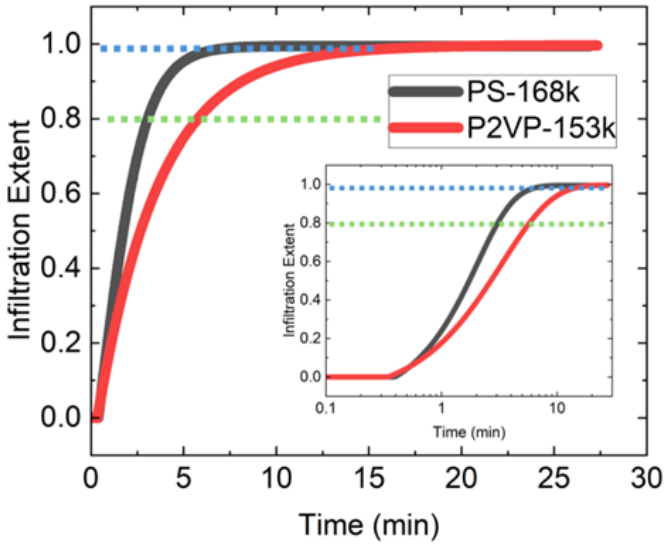

Figure 5.5. Comparison of PS-168k and P2VP-153k infiltration extent inside NPG at 140°C. The insert shows the annealing time plotted on a log scale from t = 0.4 to t = 27 mins. The green dotted line represents the 80% infiltration extent while the blue represents the 99% infiltration extent.

Surface Topography of Fully Infiltrated PING composites

After the NPG scaffold is completely infiltrated by PS-168k or P2VP-153k, the surface topography was characterized. Figures 5.6a-c show AFM phase images of pristine NPG, P2VP-153k infiltrated NPG and PS-168k infiltrated NPG, whereas Figures 6d-f represent drawings of

the cross-sections corresponding to the images in the top row. The corresponding height images are given in the SI (Fig. S4). Figure 6a shows that the surface of the pristine NPG exhibits interconnected ligaments (bright) and unfilled pores (dark). The R_p is 30.7 ± 7.3 nm, which agrees with SEM and SAXS measurements. Compared to the pristine NPG, the P2VP-153k:NPG displays a more uniform morphology suggesting a surface covered by polymer. From height images (SI), the roughness values for pristine NPG and P2VP: NPG are 15.5 nm and 5.8 nm, respectively. Furthermore, hemispherical bumps due to the P2VP appear at the surface that are ca. 15 nm high by 80 nm wide. This observation suggests that molten P2VP spreads on the Au ligaments, as sketched in Figure 6e. However, the molten hydrophobic PS doesn't spread, leaving the top-most NPG ligaments exposed as sketched in Figure 5.6f. The roughness of PS:NPG is 4.7 nm, 3x lower than the pristine NPG and slightly less than P2VP:NPG surface. After PS completely fills the NPG (phase image in Fig. 5.6c), the NPG ligaments remain visible, thus supporting the claim that PS does not form a wetting layer over the Au ligaments. In summary, the attraction of P2VP for Au produces surface features that cover the entire surface, whereas the weaker interaction between PS and Au results in a surface exhibiting a mixture of Au ligaments and PS.

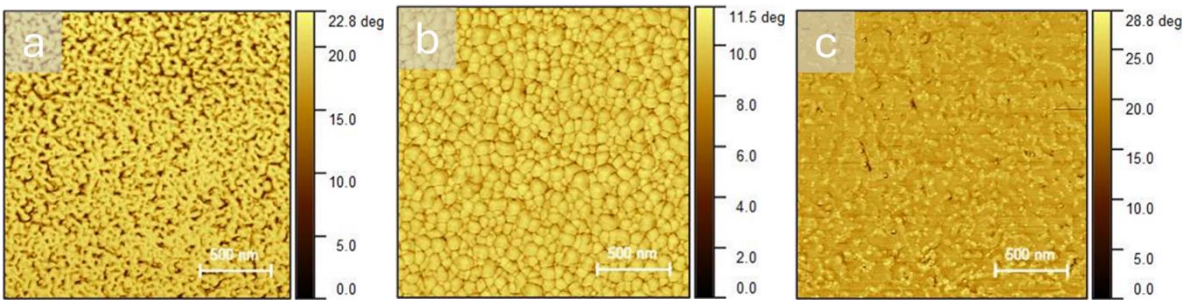

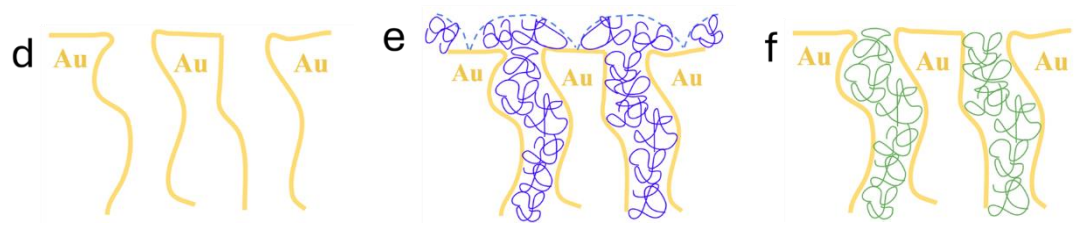

Figure 5.6. a-c. AFM phase images of NPG, P2VP:NPG and PS:NPG respectively. The P2VP and PS infiltration was carried out at 140 ℃ until the extent of infiltration was 100% (e.g., Fig. 5). d-f. Cartoon of cross-section representations of the NPG with open pores, NPG filled with P2VP (purple) and NPG filled with PS (green).

The main experimental results for P2VP infiltration into NPG are as follows. The infiltration time of entangled P2VP scales as $M_w^{1.43\ \pm 0.03}$, similar to that of entangled PS $M_w^{1.30\ \pm 0.20}$. Additionally, the effective viscosities of P2VP are greater than the bulk values for $M_w\ <$ $180{,}000\ g/mol$, but lower than the bulk values above this M_w. We attribute a crossover above the bulk M_c to polymer disentanglement under confinement as described in the next. P2VP infiltration into NPG is found to be slower than PS because of its stronger affinity for the Au surface of the pore. After complete infiltration, the surface of the NPG becomes covered by P2VP, whereas a heterogeneous surface with exposed Au ligaments is observed for PS infiltration. In the next section, MD simulations are compared with experimental results and provide insight into how molecular properties are perturbed for weak and stronger attraction between polymer-wall conditions.

Molecular Dynamics (MD) Simulations of Polymer Infiltration

To provide insight into experimental results, we performed MD simulations of infiltrating entangled polymers into nanoporous gold. Figure 5.7 shows simulation images and density profiles of polymer infiltration into the gold scaffold for weak and strong polymer/gold interaction strengths, $\varepsilon = 1.0$ and 5.0, respectively. The local density of the polymer in the z direction, $\rho(z)$, is used to calculate the height of the polymer infiltration front. To track infiltration, two thresholds are utilized: z'_{99} and z'_{85}, where $\int z'_{99}\, \rho(z)dz = 0.99\rho_{total}$ and $\int z'_{85}\, \rho(z)dz = 0.85\rho_{total,}$ indicating where 99% or 85% of the total polymer density is contained, respectively. These thresholds, represented by red dashed lines in the density plots of Figure 5.7, denote the infiltration front (z'_{99}) and the infiltration height of the bulk of the polymer (z'_{85}). Additionally, the dashed gold lines plots indicate the z position of the bottom of the nanoporous gold, z_{gold}. The polymer height, h_{99} or h_{85}, is defined as $z' - z_{gold}$ and serves as our primary measure of infiltration. This figure will be further discussed when comparing simulations with experiments.

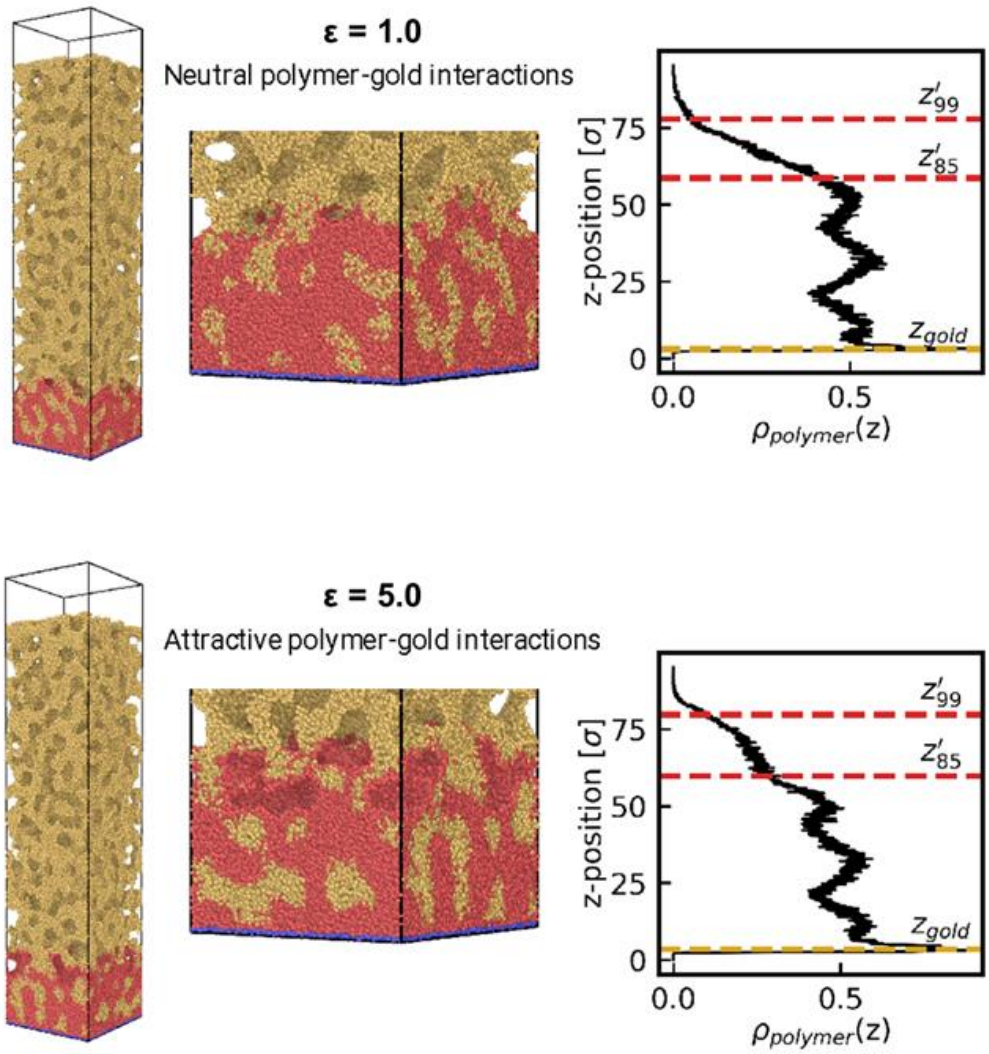

Figure 5.7. (Top) The left image shows the system configuration after τ = 762,000 for a degree of polymerization N = 50 and weak polymer-gold interaction, $\epsilon = 1.0$. The particles constituting the nanoporous structure are depicted in gold, the polymer beads are illustrated in red, and the particles within the thin support structure at the bottom of the polymer layer are shown in blue. The center image presents a zoomed-in portion of the simulation box and aligns with the density plot on the right. The plot on the right displays the density profiles of polymer chains as a function of z position. (Bottom) System configuration at τ = 860,000 for N = 50 and stronger attractive polymer-gold interactions, $\epsilon = 5.0$. The center figure again presents a zoomed-in portion of the simulation box, aligned with the density plot on the right. The plot shows the density profiles of polymer chains vs z position. For both simulations,

the entire polymer reservoir has infiltrated into the nanoporous gold, causing the gold structure to descend and fill the empty space at the bottom of the simulation box. The red dashed lines represent the height corresponding to 99% (z'_{99}) and 85% (z'_{85}) of the total polymer density, respectively. The gold dashed line denotes the bottom of the nanoporous structure (z_{gold}).

Simulations are presented for weak and strong attractive interactions between the polymer and scaffold wall. Figures 5.8a and 5.8b show how the squared infiltration heights, h^2_{99} and h^2_{85}, respectively, increase with simulation time for N = 25, 50, and 100 and polymer-gold interaction strengths ϵ = 1.0 (open symbols) and ϵ = 5.0 (solid symbols). For this range of N, N/N_e increases from 1.5 to 6.0; correspondingly, the confinement ratio, Γ, ranges from 0.46 to 0.95. For comparison, Γ for P2VP experiments are from 0.18 to 0.78 (Table 1). Figures 5.8a and 5.8b show that both h^2_{99} and h^2_{85}, respectively, increase more slowly as N increases from 25 to 100. At early infiltration times for N = 25 and 50, infiltration is faster for ϵ = 5.0 compared to ϵ = 1.0. However, at later times, the polymer with weaker interactions (open symbols) infiltrates more quickly than the stronger interaction case; this is observed for both h^2_{99} (Figure 5.8a) and h^2_{85} (Figure 5.8b). We do not observe the crossover for N = 100, which we speculate is due to the limited simulation time. For the weaker interaction case, a relatively linear relationship with time is observed for both h^2_{99} and h^2_{85}. However, for stronger attractive interaction, the h^2_{85} values increase linearity at early times whereas h^2_{99} is nonlinear for N = 25, 50 and 100. Due to this loss of linearity, the slope of the h^2_{85} plot is used to calculate the infiltration time shown in Figure 5.8c. For strong polymer attraction for the wall (ϵ = 5.0), the infiltration time scales as $N^{1.4}$ in good agreement with the experimental results for P2VP:NPG (Fig. 5.2b), where $\tau_{80\%} \propto M_w^{1.43 \pm 0.03}$. Previous MD studies [14] for ϵ = 1.0 also shows that infiltration time scales as $N^{1.4}$.

Similar scaling for the weaker and stronger attractive interactions between polymer and wall will be discussed later in the context of physisorption changing the interface for the latter case.

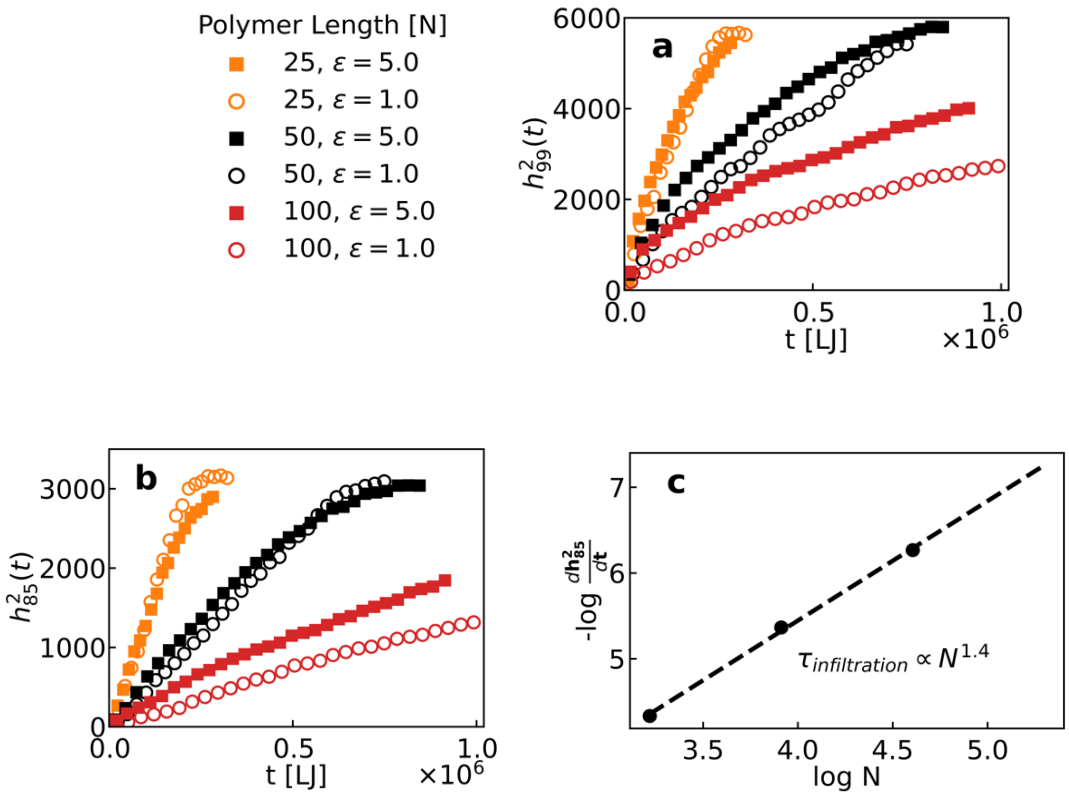

Figure 5.8. (a) The square of the infiltrated polymer height h^2_{99} as a function of simulation time for N = 25 (orange), 50 (black) and 100 (red). Height calculations for weaker and stronger polymer-gold interactions are represented by $\epsilon = 1.0$ (open circles) and $\epsilon = 5.0$ (filled squares), respectively. (b) The square of the infiltrated polymer height h^2_{85} as a function of simulation time. (c) Inverse infiltration rate, $1/\frac{dh^2_{85}}{dt}$, as a function of degree of polymerization for $\epsilon = 5.0$. The linear region of the plots in Figure 5.8b are used to calculate the infiltration rate, $\frac{dh^2_{85}}{dt}$. Taking the inverse of the infiltration rate allows the data to be interpreted as an infiltration time for more direct comparison with experimental results. A log-log plot is shown to determine scaling with polymer length. The infiltration time scales with N as $\tau_{infiltration} \propto N^{1.4}$. h^2_{85} was used rather than h^2_{99} due to the lack of linear scaling for the latter.

The presence of strong attractive polymer-surface interactions (ϵ = 5.0) may lead to the formation of a strongly adsorbed polymer layer on the gold surface that perturbs infiltration. To probe for this behavior, we calculate the instantaneous velocity in the z direction of the center of mass of each polymer chain within the simulations, $\frac{dz}{dt}$. The effect of polymer physisorption on $\frac{dz}{dt}$ is quantified by determining the fraction of adsorbed beads out of the total number of beads of chain length *N* for each polymer. We define adsorbed beads are those within 1.5σ of a gold surface bead. For N= 25, 50 and 100, Figure 5.9a shows how $\frac{dz}{dt}$ decreases as the fraction of adsorbed beads per polymer increases for $\epsilon = 1.0$ and 5.0. For reference, $f_{adsorbed} = 0$ represents a free chain that doesn't interact with the gold surface whereas $f_{adsorbed} = 1$ represents a chain fully adsorbed on the gold surface. As described in our previous work[14], a bound layer doesn't form when polymer-gold interactions are weak ($\epsilon = 1.0$); furthermore, all chain lengths exhibit motion at high $f_{adsorbed}$, with $\frac{dz}{dt} > 0$. However, when attractive polymer-gold interactions are relatively strong ($\epsilon = 5.0$), a physisorbed layer behavior is more apparent. As shown in Figure 5.9a, $\frac{dz}{dt}$ is lower for $\epsilon = 5.0$ for N = 25, 50 and 100. For all N, the velocity decreases at more rapidly with $f_{adsorbed}$ for $\epsilon = 5.0$, implying a more profound effect of adsorption when polymers are strongly attracted to the wall. Above $f_{adsorbed}$ > 0.2, $\frac{dz}{dt}$ approaches 0 for the longer chain lengths N = 50 and N = 100. For N =25, the reduction in z velocity is significantly reduced when $\epsilon = 5.0$ and approaches small values above $f_{adsorbed}$ > ca. 0.5. Overall, this analysis shows that the velocity of chains near the surface is strongly reduced by attractive interactions.

To further discern the adsorption behavior as a function of N and polymer-gold interaction strength, the fraction of total chains at each value of $f_{adsorbed}$ is determined. This fraction is calculated using all time points throughout infiltration. The results for $\epsilon = 1.0$ was presented in our previous work [14]. Briefly, the largest fractions of weakly interacting chains have a low fraction of adsorbed monomers $f_{adsorbed}$, and f_{chain} decreases mostly monotonically as $f_{adsorbed}$ increases (open circles). In simulations with stronger polymer-gold interactions ($\epsilon = 5.0$), the behavior is quite different, and the largest populations of chains are either weakly adsorbed with $f_{adsorbed} < 0.1$ or strongly adsorbed, $f_{adsorbed} > 0.9$. This data supports the physisorption of attractive chains on the pore surface that form a bound layer, while a subset of free chains infiltrate the narrowed pore.

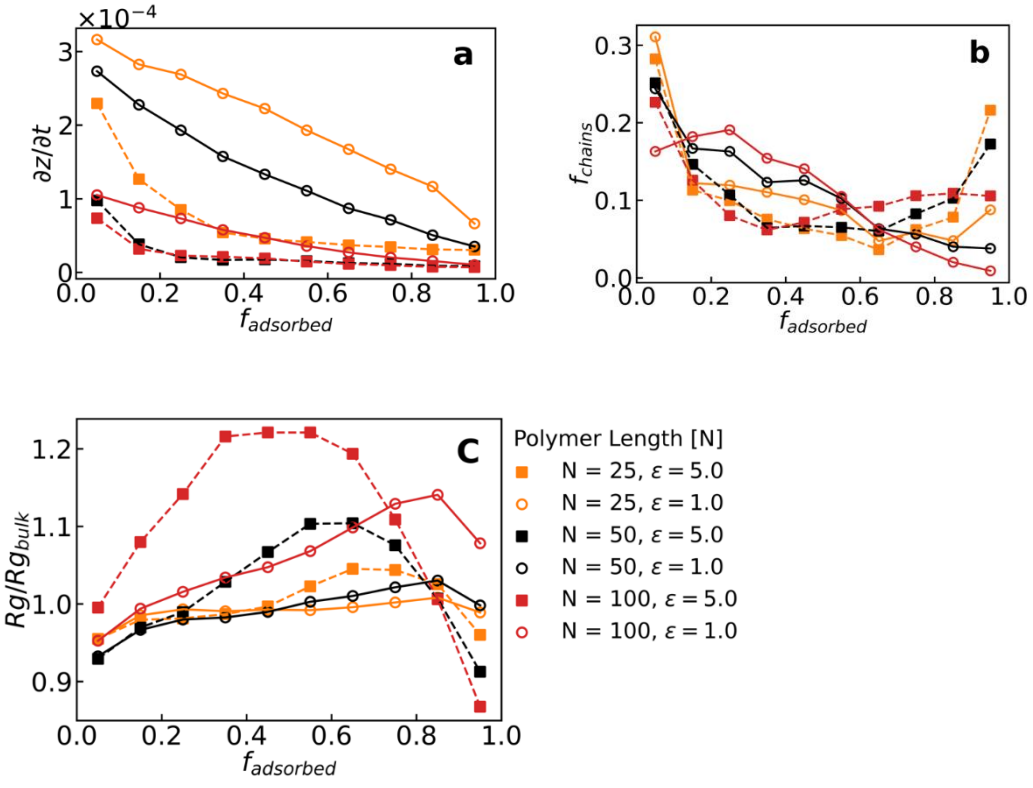

Figure 5.9. (a) Chain center of mass z velocity $\frac{dz}{dt}$, versus the fraction of adsorbed polymer chairs for N = 25, 50 and 100. A monomer is adsorbed if the chain bead is within 1.5σ of any gold surface bead. The adsorbed fraction is defined as $f_{adsorbed} = (\frac{\#\ of\ adsorbed\ beads}{N})$. For each N, open circles and closed squares represent polymer-gold interactions with $\epsilon = 1.0$ and $\epsilon = 5.0,\ respectively$. (b) The fraction of total chains (f_{chains}) at each adsorbed fraction for each N. (c) Normalized radius of gyration versus adsorbed fraction ($f_{adsorbed}$). A value of 1.0 for R_g/R_{bulk} represents a polymer size in the pore equal to the radius of gyration in the bulk.

Previous work exploring the conformations of polymers during capillary infiltration has demonstrated a variety of effects, finding both unperturbed dimensions [25] and chain extension in the direction of flow[72]. To understand the interplay between chain stretching and adsorption, we examine the impact of adsorbed fraction on the polymer chain radius of gyration. Figure 5.9c shows the normalized radius of gyration R_g/R_{bulk} for the polymer chains versus the adsorbed fraction $f_{adsorbed}$. Values are normalized to the bulk polymer R_g in each direction such that a value of 1 represents a chain that has retained bulk dimensions in that respective direction. For simulations at all chain lengths N = 25, 50, 100 with attractive polymer-gold interactions ($\epsilon = 5.0$), the R_g initially increases with increasing adsorption as the chains extend to access additional gold surface area, reaches a maximum extension, and then decreases at a very high adsorbed fraction. The effect of adsorption on the chain dimensions increases as chain length increases. The chain distortions (both stretch and compressed) are greater for the stronger attractive polymer-surface interactions. Of particular note is that the longest chains, N = 100, that are fully absorbed are strongly compressed with $\frac{R_g}{R_{bulk}} \sim 0.85$, whereas the shorter chains, N = 25 and 50, are less compressed at high adsorbed fraction, with $\frac{R_g}{R_{bulk}} \sim 0.96$ and $\frac{R_g}{R_{bulk}} \sim 0.92$

respectively. These studies show that chains absorbed to the pore wall are more strongly perturbed when interactions with the wall are stronger.

The adsorption and distortion of polymer chains leads to a reduction in entanglements within the confining nanopore. Figure 5.10 shows the decrease in the average number of entanglements per chain, $\Delta\langle Z\rangle$, over the duration of infiltration for N = 25, 50 and 100. Only infiltrated chains, i.e. chains with a center-of-mass z position above the bottom of the nanoporous gold structure (Figure 5.7), are included in the average, and the Z1+ algorithm[73] is used to analyze entanglements. As discussed in our previous work using for $\epsilon = 1.0$[14], there is a reduction in entanglements as infiltration progresses for all chain lengths. For stronger attractive polymer-gold interactions ($\epsilon = 5.0$), the change in entanglements with time depends on chain length. For N = 25, 50, and 100, the initial decrease in entanglements at the start of infiltration is larger for $\epsilon = 5.0$ (solid symbols) than $\epsilon = 1.0$ (open symbols). The larger disentanglement reduction for $\epsilon = 5.0$ is likely driven by an initial disentanglement of chains from the bulk as the chains are confined and begin to wet the gold surface. After the initial decrease in entanglements, the number of entanglements for the shorter chain lengths (N = 25 and 50), remains approximately constant, while that for the $N = 100$ chains continue to gradually decrease. Previous work has shown that chain confinement drives a reduction in entanglements via a reduction in the pervaded volume of chains and thus the number of interchain contacts [74–76]. For $N = 100$ and $\varepsilon = 5$, the larger compression and disentanglement may explain the lack of a crossover in the infiltration kinetics on the simulated time scales shown in Figure 5.8.

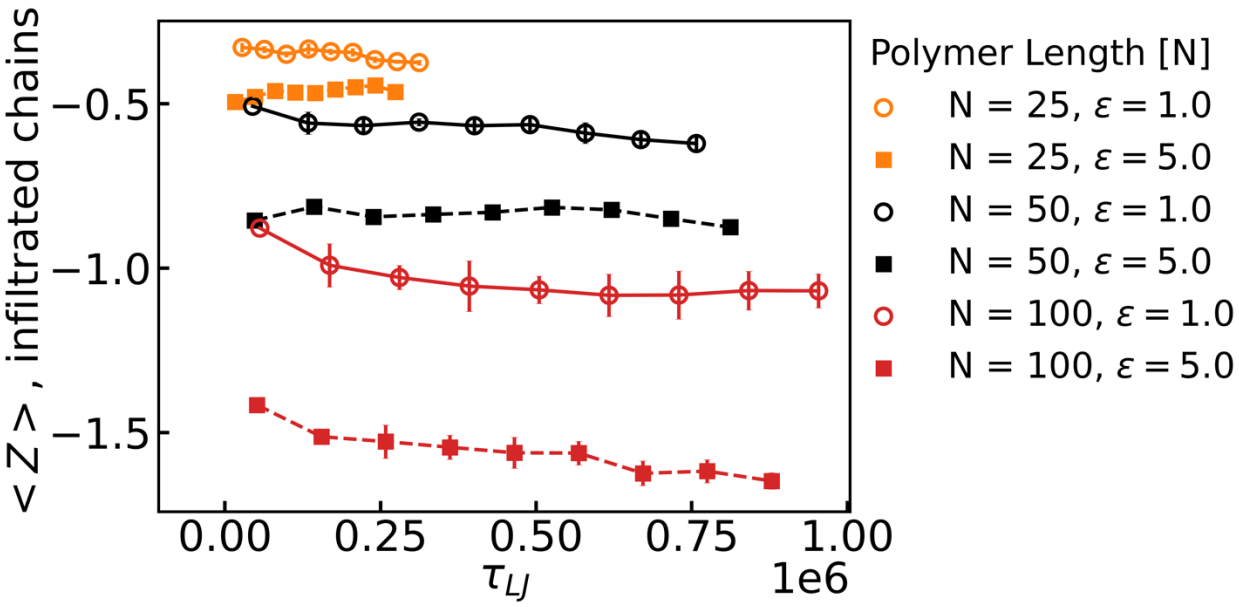

Figure 5.10. The change in average number of entanglements per chain over the course of infiltration, $\Delta\langle Z\rangle = \langle Z\rangle - \langle Z\rangle_{bulk}$. For N =100, chains have only partially penetrated the porous structure as shown in Figure 5.7. For each chain length, open circles and closed squares represent simulations using $\epsilon = 1.0$ and $\epsilon = 5.0$, respectively.

Comparison of experiment and simulation

Experiments and simulations are consistent with the formation of a physisorbed bound layer followed by infiltration of P2VP into narrowed pores in a nanoporous scaffold. In experiments, the physisorbed layer is driven by the affinity of P2VP to wet the gold surface. In simulations, for N = 50, Figure 5.7 shows the infiltration of polymer with weaker, ϵ = 1.0 (top), and stronger, ϵ = 5.0 (bottom), attractive interactions for the gold surface. Comparing the polymer infiltration front (red) for ϵ = 1.0 and ϵ = 5.0, the former shows mainly filled pores whereas the latter shows a polymer wetting layer on the pore surface at the growth front. This qualitative observation is supported by the broader front edge of the polymer density profile in Figure 5.7

for ϵ = 5.0 (bottom right). Further analysis is needed at various infiltration times to examine this precursor layer at the growth front. For ϵ = 5.0, the formation of a physisorbed layer is supported by the near zero velocities for highly adsorbed chains shown in Figure 5.9a, as well as the increase in the fraction of highly observed chains shown in Figure 5.9b. As noted later, the formation of this physisorbed layer is similar to the dead zone [70] proposed by Yao et al. (2018).

For PS and P2VP, the similar scaling of infiltration time with molecular weight, $M_w^{1.4}$, can be attributed to the formation of a physorbed P2VP covering the Au surface. Namely, the backfilling P2VP interacts with pore having the composition of P2VP (rather than Au). We attribute the similar molecular weight dependence of P2VP and PS infiltration to the weak interactions that both polymers have with the confining walls, P2VP and Au, respectively. For weak interactions (ϵ = 1.0), MD simulations yield $\tau \sim M_w^{1.4}$ [14]. Similarly, for stronger attractive interactions (ϵ = 5.0), Figure 5.8c shows that $\tau \sim M_w^{1.4}$. This agreement in scaling behavior for experiments and simulations is consistent with the formation of a physisorbed P2VP layer followed by backfilling of P2VP through the coated pore.

Lastly, P2VP is found to infiltrate more slowly than PS when compared at similar confinement ratios. Simulations in this study provide insights into four factors that influence kinetics of infiltration. First, the larger reduction in entanglement density for ϵ = 5.0 (Fig. 10) suggests that stronger adsorption increases infiltration kinetics. Second, the chain velocity along the pores is greatly reduced for ϵ = 5.0 (Fig. 9a). Third, for ϵ = 5.0, a physisorbed layer first forms and then polymer infiltrates through this narrowed pore as noted in Scheme 1. The effective radius (R_{eff}) of the pore is now $R_{eff} = R_p - \Delta R$. Previous studies [23,70] have qualitatively shown that a bound layer will increase the effective viscosity. A fourth factor is that

the physisorbed layer provides a stickier interface for the backfilling polymer than the original metal pore as noted in Scheme 1. Namely, the adsorbed polymer forms loops and tails that can entangle with backfilling polymer. As a result the local effective viscosity would increase compared to the non-slip conditions at the polymer/wall in the LW derivation. This last factor requires further investigation by experiments and simulations. Previous simulations [18,77] of solvent-driven polymer infiltration identifies dissolution-dominated and adhesion-dominated modes, which depend on the interaction strength between each component. The adhesion-dominated mode results in a slower kinetics when the interaction is strong. Our experimental and simulation studies imply that the P2VP:NPG system belongs to the adhesion-dominated mode, consistent with slower kinetics. In summary, the slower infiltration of P2VP compared to PS has its origin in the formation of the physorbed layer on the Au pore surface, which could provide entanglements while narrowing the pore size.

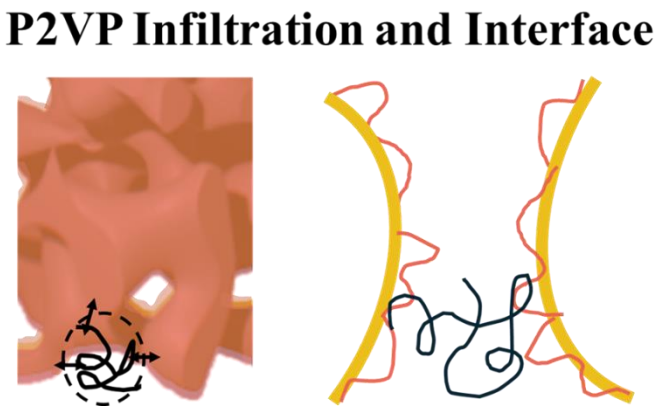

Scheme 1. Cartoons showing a macroscopic view of the physisorbed P2VP layer as a continuous coating on the Au scaffold (left), a free P2VP chain (black) infiltrating the nanopore and the ability of the P2VP chain (black) to entangle with the physisorbed P2VP chain (red molecule).

5.4 Conclusion

In this work, experiments and simulations are used to investigate the infiltration of moderately confined polymers into nanoporous scaffolds. Experimentally, poly(2-vinylpyridine) (P2VP) with molecular weights from 51k to 940k are infiltrated nanoporous gold (NPG) scaffolds to form polymer infiltrated nanoporous gold (PING) composites at 140°C. For a pore diameter of 34 nm, the confinement ratios vary from 0.18 to 0.78. In-situ spectroscopic ellipsometry is used to determine when 80% of the NPG ($\tau_{80\%}$) has been filled with P2VP. This infiltration time scales as $M_w^{1.4}$ which is similar to PS infiltration across similar confinement ratios. Both the PS and P2VP infiltration times have a much weaker M_w dependence than expected from bulk viscosity where $\tau_{bulk} \sim M_w^{3.4}$. The infiltration time for simulations with strong attractions between polymer and pore walls agree with experimental scaling results. At similar conditions, P2VP infiltration is slower than PS in the same scaffold. Simulations show that polymer with a stronger attraction to the scaffold ($\varepsilon = 5; P2VP$) infiltrates more slowly than polymer with a weaker interaction ($\varepsilon = 1; PS$). For P2VP, the effective viscosity crosses over from greater than to less than the bulk viscosity near 180 kDa. This transition is attributed to the narrowing of the pore walls and a reduction in entanglements, respectively.

Simulations of the infiltration process of polymers with strong and weak attraction for the pore wall provide important macro and molecular insights. First, the dynamics of infiltration exhibited a scaling with chain length that was consistent with experimental results. Furthermore, for chains that strongly wet the pore surface, the structure of the infiltrating polymer chains was altered compared to polymers with weaker interactions. Simulations revealed a growth in the population

of chains that have a larger fraction of their monomers adsorbed to the pore wall for the strong attraction case compared to the weaker case. This observation is consistent with the formation of a physisorbed layer on the wall. This strong attraction of polymer for the pore wall led to significant changes in the polymer conformations, disentanglement of the polymers that had infiltrated the pores, and the emergence of a population of chains with drastically reduced infiltration rate. Presumably, the disentanglement plays a key role in the change of the scaling of η_{eff} with M_w, though the precise origin of the observed scaling with $\eta_{eff} \propto M_w^{1.4}$ remains unknown.

5.5 References

1. Bilchak, C. R., Huang, Y., Benicewicz, B. C., Durning, C. J. & Kumar, S. K. High-Frequency Mechanical Behavior of Pure Polymer-Grafted Nanoparticle Constructs. *ACS Macro Lett.* **8**, 294–298 (2019).

2. Rittigstein, P. & Torkelson, J. M. Polymer-nanoparticle interfacial interactions in polymer nanocomposites: Confinement effects on glass transition temperature and suppression of physical aging: Polymer-Nanoparticle Interfacial Interactions. *J. Polym. Sci. Part B Polym. Phys.* **44**, 2935–2943 (2006).

3. Bilchak, C. R. *et al.* Polymer-Grafted Nanoparticle Membranes with Controllable Free Volume. *Macromolecules* **50**, 7111–7120 (2017).

4. Merkel, T. C. *et al.* Ultrapermeable, Reverse-Selective Nanocomposite Membranes. *Science* **296**, 519–522 (2002).

5. Liu, Y. *et al.* Electro-thermal actuation in percolative ferroelectric polymer nanocomposites. *Nat. Mater.* **22**, 873–879 (2023).

6. Balazs, A. C., Emrick, T. & Russell, T. P. Nanoparticle Polymer Composites: Where Two Small Worlds Meet. *Science* **314**, 1107–1110 (2006).

7. Kim, J. *et al.* Estimation of the concentration of nano-carbon black in tire-wear particles using emission factors of PM10, PM2.5, and black carbon. *Chemosphere* **303**, 134976 (2022).

8. Guth, E. Theory of Filler Reinforcement. *J. Appl. Phys.* **16**, 20–25 (1945).

9. Wegst, U. G. K., Bai, H., Saiz, E., Tomsia, A. P. & Ritchie, R. O. Bioinspired structural materials. *Nat. Mater.* **14**, 23–36 (2015).

10. Meyers, M. A., McKittrick, J. & Chen, P.-Y. Structural Biological Materials: Critical Mechanics-Materials Connections. *Science* **339**, 773–779 (2013).

11. Krook, N. M. *et al.* Experiments and Simulations Probing Local Domain Bulge and String Assembly of Aligned Nanoplates in a Lamellar Diblock Copolymer. *Macromolecules* **52**, 8989–8999 (2019).

12. Krook, N. M. *et al.* Alignment of Nanoplates in Lamellar Diblock Copolymer Domains and the Effect of Particle Volume Fraction on Phase Behavior. *ACS Macro Lett.* **7**, 1400–1407 (2018).

13. Maguire, S. M. *et al.* Effect of Nanoscale Confinement on Polymer-Infiltrated Scaffold Metal Composites. *ACS Appl. Mater. Interfaces* **13**, 44893–44903 (2021).

14. Kong, W. *et al.* Capillary filling dynamics of polymer melts in a bicontinuous nanoporous scaffold. *J. Chem. Phys.* **160**, 044904 (2024).

15. Ng, A. K., Welborn, S. S. & Detsi, E. Time-dependent power law function for the post-dealloying chemical coarsening of nanoporous gold derived using small-angle X-ray scattering. *Scr. Mater.* **206**, 114215 (2022).

16. Venkatesh, R. B. & Lee, D. Conflicting Effects of Extreme Nanoconfinement on the Translational and Segmental Motion of Entangled Polymers. *Macromolecules* **55**, 4492–4501 (2022).

17. Venkatesh, R. B. & Lee, D. Interfacial Friction Controls the Motion of Confined Polymers in the Pores of Nanoparticle Packings. *Macromolecules* **55**, 8659–8667 (2022).

18. Venkatesh, R. B. *et al.* Effect of polymer–nanoparticle interactions on solvent-driven infiltration of polymer (SIP) into nanoparticle packings: a molecular dynamics study. *Mol. Syst. Des. Eng.* **5**, 666–674 (2020).

19. Hor, J. L., Wang, H., Fakhraai, Z. & Lee, D. Effects of polymer–nanoparticle interactions on the viscosity of unentangled polymers under extreme nanoconfinement during capillary rise infiltration. *Soft Matter* **14**, 2438–2446 (2018).

20. Huang, Y.-R. *et al.* Polymer nanocomposite films with extremely high nanoparticle loadings via capillary rise infiltration (CaRI). *Nanoscale* **7**, 798–805 (2015).

21. Qiang, Y., Pande, S. S., Lee, D. & Turner, K. T. The Interplay of Polymer Bridging and Entanglement in Toughening Polymer-Infiltrated Nanoparticle Films. *ACS Nano* **16**, 6372–6381 (2022).

22. Qiang, Y., Turner, K. T. & Lee, D. Role of Polymer–Nanoparticle Interactions on the Fracture Toughness of Polymer-Infiltrated Nanoparticle Films. *Macromolecules* **56**, 122–135 (2023).

23. Ren, T. *et al.* Increase in the effective viscosity of polyethylene under extreme nanoconfinement. *J. Chem. Phys.* **160**, 024909 (2024).

24. Hor, J. L., Wang, H., Fakhraai, Z. & Lee, D. Effect of Physical Nanoconfinement on the Viscosity of Unentangled Polymers during Capillary Rise Infiltration. *Macromolecules* **51**, 5069–5078 (2018).

25. Shin, K. *et al.* Enhanced mobility of confined polymers. *Nat. Mater.* **6**, 961–965 (2007).

26. Tu, C.-H., Zhou, J., Butt, H.-J. & Floudas, G. Adsorption Kinetics of *cis* -1,4-Polyisoprene in Nanopores by *In Situ* Nanodielectric Spectroscopy. *Macromolecules* **54**, 6267–6274 (2021).

27. Tu, C.-H., Zhou, J., Doi, M., Butt, H.-J. & Floudas, G. Interfacial Interactions During In Situ Polymer Imbibition in Nanopores. *Phys. Rev. Lett.* **125**, 127802 (2020).

28. Yao, Y., Butt, H.-J., Zhou, J., Doi, M. & Floudas, G. Capillary Imbibition of Polymer Mixtures in Nanopores. *Macromolecules* **51**, 3059–3065 (2018).

29. Yao, Y. *et al.* Complex dynamics of capillary imbibition of poly(ethylene oxide) melts in nanoporous alumina. *J. Chem. Phys.* **146**, 203320 (2017).

30. Kimmich, R., Fatkullin, N., Mattea, C. & Fischer, E. Polymer chain dynamics under nanoscopic confinements. *Magn. Reson. Imaging* **23**, 191–196 (2005).

31. Mangal, R., Srivastava, S. & Archer, L. A. Phase stability and dynamics of entangled polymer–nanoparticle composites. *Nat. Commun.* **6**, 7198 (2015).

32. Keddie, J. L., Jones, R. A. L. & Cory, R. A. Size-Dependent Depression of the Glass Transition Temperature in Polymer Films. *Europhys. Lett. EPL* **27**, 59–64 (1994).

33. Choi, J., Clarke, N., Winey, K. I. & Composto, R. J. Fast Polymer Diffusion through Nanocomposites with Anisotropic Particles. *ACS Macro Lett.* **3**, 886–891 (2014).

34. Tarnacka, M. *et al.* The Impact of Molecular Weight on the Behavior of Poly(propylene glycol) Derivatives Confined within Alumina Templates. *Macromolecules* **52**, 3516–3529 (2019).

35. Ediger, M. D. & Forrest, J. A. Dynamics near Free Surfaces and the Glass Transition in Thin Polymer Films: A View to the Future. *Macromolecules* **47**, 471–478 (2014).

36. Schneider, H. M., Frantz, P. & Granick, S. The Bimodal Energy Landscape When Polymers Adsorb. *Langmuir* **12**, 994–996 (1996).

37. Lange, F. *et al.* Large-Scale Diffusion of Entangled Polymers along Nanochannels. *ACS Macro Lett.* **4**, 561–565 (2015).

38. Roth, C. & Dutcher, J. Mobility on Different Length Scales in Thin Polymer Films. in *Soft Materials* (eds. Marangoni, A. & Dutcher, J.) 1–38 (CRC Press, 2004). doi:10.1201/9780203027004.ch1.

39. Choi, J. *et al.* Universal Scaling of Polymer Diffusion in Nanocomposites. *ACS Macro Lett.* **2**, 485–490 (2013).

40. Askar, S., Wei, T., Tan, A. W. & Torkelson, J. M. Molecular weight dependence of the intrinsic size effect on *T* g in AAO template-supported polymer nanorods: A DSC study. *J. Chem. Phys.* **146**, 203323 (2017).

41. Schneider, G. J. Dynamics of nanocomposites. *Curr. Opin. Chem. Eng.* **16**, 65–77 (2017).

42. Gam, S. *et al.* Macromolecular Diffusion in a Crowded Polymer Nanocomposite. *Macromolecules* **44**, 3494–3501 (2011).

43. Bocquet, L. Nanofluidics coming of age. *Nat. Mater.* **19**, 254–256 (2020).

44. Bansal, A. *et al.* Quantitative equivalence between polymer nanocomposites and thin polymer films. *Nat. Mater.* **4**, 693–698 (2005).

45. Hor, J. L. *et al.* Nanoporous Polymer-Infiltrated Nanoparticle Films with Uniform or Graded Porosity *via* Undersaturated Capillary Rise Infiltration. *ACS Nano* **11**, 3229–3236 (2017).

46. Wang, H. *et al.* Dramatic Increase in Polymer Glass Transition Temperature under Extreme Nanoconfinement in Weakly Interacting Nanoparticle Films. *ACS Nano* **12**, 5580–5587 (2018).

47. Venkatesh, R. B. *et al.* Polymer-Infiltrated Nanoparticle Films Using Capillarity-Based Techniques: Toward Multifunctional Coatings and Membranes. *Annu. Rev. Chem. Biomol. Eng.* **12**, 411–437 (2021).

48. Ring, D. J., Riggleman, R. A. & Lee, D. Critical Contact Angle to Induce Capillary Rise of Polymers in Nanopores Does Not Depend on Chain Length. *ACS Macro Lett.* **8**, 31–35 (2019).

49. Shavit, A. & Riggleman, R. A. The dynamics of unentangled polymers during capillary rise infiltration into a nanoparticle packing. *Soft Matter* **11**, 8285–8295 (2015).

50. Lin, C.-C. *et al.* Do Attractive Polymer–Nanoparticle Interactions Retard Polymer Diffusion in Nanocomposites? *Macromolecules* **46**, 4502–4509 (2013).

51. Tung, W.-S. *et al.* Temperature-Dependent Suppression of Polymer Diffusion in Polymer Nanocomposites. *ACS Macro Lett.* **5**, 735–739 (2016).

52. Rubinstein, M. & Colby, R. H. *Polymer Physics*. (Oxford University Press, Oxford ; New York, 2003).

53. Jiang, N. *et al.* Thermal Properties and Segmental Dynamics of Polymer Melt Chains Adsorbed on Solid Surfaces. *Langmuir* **34**, 4199–4209 (2018).

54. Takahashi, Y., Ochiai, N., Matsushita, Y. & Noda, I. Viscoelastic Properties of Poly(2-vinylpyridine) in Bulk and Solution. *Polym. J.* **28**, 1065–1070 (1996).

55. Ding, Y., Kim, Y.-J. & Erlebacher, J. Nanoporous Gold Leaf: Ancient Technology Advanced Material. *Adv. Mater.* **16**, 1897–1900 (2004).

56. Welborn, S. S. & Detsi, E. Small-angle X-ray scattering of nanoporous materials. *Nanoscale Horiz.* **5**, 12–24 (2020).

57. Welborn, S. S., Van Der Meer, S., Corsi, J. S., De Hosson, J. Th. M. & Detsi, E. Using X-Ray Scattering to Elucidate the Microstructural Instability of 3D Bicontinuous Nanoporous Metal Scaffolds for Use in an Aperiodic 3D Tricontinuous Conductor–Insulator–Conductor Nanocapacitor. *ACS Appl. Mater. Interfaces* **13**, 11721–11731 (2021).

58. Plimpton, S. Fast Parallel Algorithms for Short-Range Molecular Dynamics. *J. Comput. Phys.* **117**, 1–19 (1995).

59. Kremer, K. & Grest, G. S. Dynamics of entangled linear polymer melts: A molecular-dynamics simulation. *J. Chem. Phys.* **92**, 5057–5086 (1990).

60. Kumar, R., Goswami, M., Sumpter, B. G., Novikov, V. N. & Sokolov, A. P. Effects of backbone rigidity on the local structure and dynamics in polymer melts and glasses. *Phys. Chem. Chem. Phys.* **15**, 4604–4609 (2013).

61. O'Shaughnessy, B. & Vavylonis, D. Non-equilibrium in adsorbed polymer layers. *J. Phys. Condens. Matter* **17**, R63 (2004).

62. Banaszak, B. J. & de Pablo, J. J. A new double-rebridging technique for linear polyethylene. *J. Chem. Phys.* **119**, 2456–2462 (2003).

63. Mavrantzas, V. G., Boone, T. D., Zervopoulou, E. & Theodorou, D. N. End-Bridging Monte Carlo: A Fast Algorithm for Atomistic Simulation of Condensed Phases of Long Polymer Chains. *Macromolecules* **32**, 5072–5096 (1999).

64. Michels, A. & Weissmüller, J. Magnetic-field-dependent small-angle neutron scattering on random anisotropy ferromagnets. *Rep. Prog. Phys.* **71**, 066501 (2008).

65. Washburn, E. W. The Dynamics of Capillary Flow. *Phys. Rev.* **17**, 273–283 (1921).

66. Lucas, R. Ueber das Zeitgesetz des kapillaren Aufstiegs von Flüssigkeiten. *Kolloid-Z.* **23**, 15–22 (1918).

67. Masoodi, R., Pillai, K. M. & Varanasi, P. P. Darcy's law-based models for liquid absorption in polymer wicks. *AIChE J.* **53**, 2769–2782 (2007).

68. Luo, J.-W. *et al.* Macroscopic transport properties of Gyroid structures based on pore-scale studies: Permeability, diffusivity and thermal conductivity. *Int. J. Heat Mass Transf.* **146**, 118837 (2020).

69. Kunz, M. S., Shull, K. R. & Kellock, A. J. Colloidal Gold Dispersions in Polymeric Matrices. *J. Colloid Interface Sci.* **156**, 240–249 (1993).

70. Yao, Y., Butt, H.-J., Floudas, G., Zhou, J. & Doi, M. Theory on Capillary Filling of Polymer Melts in Nanopores. *Macromol. Rapid Commun.* **39**, 1800087 (2018).

71. Klein, J. The self-diffusion of polymers. *Contemp. Phys.* **20**, 611–629 (1979).

72. Zhang, J. *et al.* Capillary Filling of Polymer Chains in Nanopores. *Macromolecules* **56**, 2258–2267 (2023).

73. Kröger, M., Dietz, J. D., Hoy, R. S. & Luap, C. The Z1+ package: Shortest multiple disconnected path for the analysis of entanglements in macromolecular systems. *Comput. Phys. Commun.* **283**, 108567 (2023).

74. Wang, F. *et al.* Suppressed Chain Entanglement Induced by Thickness of Ultrathin Polystyrene Films. *Macromolecules* **54**, 3735–3743 (2021).

75. García, N. A. & Barrat, J.-L. Entanglement Reduction Induced by Geometrical Confinement in Polymer Thin Films. *Macromolecules* **51**, 9850–9860 (2018).

76. Sussman, D. M., Tung, W.-S., Winey, K. I., Schweizer, K. S. & Riggleman, R. A. Entanglement Reduction and Anisotropic Chain and Primitive Path Conformations in Polymer Melts under Thin Film and Cylindrical Confinement. *Macromolecules* **47**, 6462–6472 (2014).

77. Manohar, N., Riggleman, R. A., Lee, D. & Stebe, K. J. Nonmonotonic polymer translocation kinetics through nanopores under changing surface–polymer interactions. *J. Chem. Phys.* **160**, 084908 (2024).

CHAPTER 6. OPTICAL ABSORPTION OF NANOPOROUS METAL SCAFFOLDS INFILTRATED WITH POLYMER

Content in this chapter will be submitted in 2024 to *ACS AMI*, with authors Weiwei Kong, Chuyi Pan, Rongyue Lin, Mengjie Fan, John M. Vohs, Russell J. Composto. R.J.C. and W.K. conceived and planned for the project. W.K. developed the experimental procedures and C.P. and W.K. conducted all experimental measurements. R.L. conducted simulation development. M.F conducted the XPS characterization. W.K conducted the analysis. W.K wrote the manuscript. R.J.C edited the manuscript.

6.1 Introduction

Polymer nanocomposites (PNCs), materials containing both organic and inorganic fractions, have been extensively studied in national laboratories and industry[1–3] because of their versatile use as coating [4,5], membranes [6,7] and actuators [8]. Among PNCs, those with high inorganic nanofiller loading have received particular attention because of their potential as mechanically enhanced materials [9,10]. However, high nanofiller loadings are challenging to fabricate because the thermodynamics of mixing is often unfavorable resulting in nanofiller aggregation. To circumvent limited loading and non-uniform dispersion, various approaches to infiltrate polymers into pre-fabricated membranes or nanoparticle assemblies have been developed. Examples include polymer infiltration into anodized aluminum oxide (AAO) membranes [11–16], nanoparticle assemblies [17–27] and nanoporous gold (NPG) [28,29]. In our previous studies [28,29], we fabricated polymer infiltrated nanoporous gold (PING), which has ultra-high

nanofiller loading (~ 50 vol%) by infiltrating a polymer melt into a NPG scaffold. During the fabrication of the final PING composite, polymer kinetics were investigated for conditions of moderined confinement, namely chain size slightly less than pore diameter. Polymer kinetics under confinement has received much attention recently because confinement can perturb polymer conformations [11,13,15,28–44], thus affecting adsorption, thermal properties and melt viscosity. For instance, studies have shown that polymers reptating inside confined channels exhibit an enhanced glass transition temperature (T_g) as compared to the bulk [21–23,28,45]. Among the properties, infiltration kinetics has been of special interest [23–25,28,29] as by precisely controlling the infiltration extent, properties such as optical response, mechanical performance, and surface topography could be precisely controlled and tuned. The study of polymer kinetics inside confined channels has been an essential topic to create new possibilities for membranes for stimuli-response and ion conductivity membranes.

To quantify polymer infiltration into porous media, cross-section SEM [16], small angle x-ray scattering (SAXS) [13], dielectric spectroscopy (DS) [11,12,14,15,46–49], and spectroscopic ellipsometry (SE) [21–26,28,29,45] have been used. Cross-section SEM provides direct visualization of polymer displacement inside confined pores. In the study by Hu and Cao (2012), polyethylene (PE) melt is monitored to infiltrate inside AAO templates at 130℃ [16]. PE kinetics is determined from the PE growth front (H) as a function of infiltration time [16]. Here, the infiltration height is proportional to square root of infiltration time [16], such that H(t) ~ $0.28t^{0.5}$, where H and t are in units of $10^{-6}\ m$ and s, respectively. This scaling agrees with Lucas-Washburn Equation, implying that the PE inside AAO behaves like simple fluids and the infiltration pattern can be predicted [16]. Cross-section SEM enables direct visualization of the infiltration front.

Simultaneously, this technique requires image analysis to define the height from the images. Additionally, studies have shown that electron beams could degrade the polymer [50]. Thus, cross-section SEM has limited applicability on monitoring polymer kinetics in nanopores.

SAXS has also been proved successful in monitoring polymer infiltration [13]. Shin et al. (2007) used timed resolved SAXS to detect the capillary rise of polystyrene (PS) inside AAO membrane [13]. To assess infiltration extent, multiple procedures were performed by Shin et al. (2007). Firstly, the integrated intensity (Q) is used to extract the volume fractions of the pore (ϕ_p) and the alumina (ϕ_{AO}) in the membrane using $Q \sim [\phi_U \rho_{AO}^2 + \phi_F(\rho_{AO} - \rho_{PS})^2]\phi_p\phi_{AO}$, where ρ is the electron density, and ϕ_F and ϕ_U are the volume fraction of filled and unfilled pores such that $\phi_F + \phi_U = 1$ [13]. The total flux (J) is given by

$$J = \pi r^2 \frac{\Delta l}{\Delta t} = -K \frac{\Delta(Q/Q_o)}{\Delta t} \qquad \text{Equation 6.1}$$

where r is the radius of the pore and l is the length polymer that has traveled into the membrane In Eq. 1, the flux is related to the change in Q through $K = \pi r^2 L \rho_{AO}^2/(2\rho_{AO} - \rho_{PS})\rho_{PS}$, where L is membrane length. As the pores fill with polymer, the integrated scattering intensity decreases from Q_o to Q [13]. The ϕ_U could thus be calculated through the preceding equations. Although being one of the first methods to measure infiltration, SAXS has several limitations including access to x-ray scattering, polymer degradation [51], low flux due the the thick foil over the membranes, and heavy calculations.

Dielectric spectroscopy (DS) measures dielectric properties of the membrane. A thin gold sputtered layer serves as the upper electrode while the substrate acts as the lower electrode [52–54]. DS measures the complex dielectric permittivity (ε*) as a function of frequency (w) and

temperature (T) such that ε*(w,T). The measured ε*(w,T) are fitted through the Havriliak and Negami (HN) equation:

$$\varepsilon^*_{HN}(w,T) = \varepsilon_\infty(T) + \sum_{k=1}^{2} \frac{\Delta\varepsilon_k(T)}{[1+(iw\tau_{HN,k}(T)^{m_k}]^{n_k}} + \frac{\sigma_o(T)}{i\varepsilon_f w} \qquad \text{Equation 6.2}$$

where $\Delta\varepsilon_k(T)$is the relaxation strength, $\tau_{HN,k}(T)$ is the relaxation time of m_k and n_k ($m_k n_k \leq 1$, $m_k > 0$), and ε_∞ is the dielectric permittivity at high frequency limits. The infiltration time [14] is determined from the relaxation time at maximum loss (τ_{max}).

$$\tau_{max,k} = \tau_{HN,k}(T) sin^{-1/m}\left(\frac{\pi m_k}{2(1+n_k)}\right) sin^{-1/m}\left(\frac{\pi m_k n_k}{2(1+n_k)}\right) \qquad \text{Equation 6.3}$$

Previous studies [11,12,14,15,46–49] showed that DS is a reliable method for tracking polymer kinetics inside a confined channel. However, to track kinetics, DS is an indirect method and requires complex calculations post measurement.

Spectroscopic ellipsometry (SE) is a widely used method to measure polymer infiltration [23,24,28,29]. SE detects the change in light polarization in the s-plane and p-plane after light is reflected off the front and back surfaces of a film[55]. The polarization change is represented by the amplitude ratio Ψ and phase difference **Δ**, and various optical properties, such as refractive index, extinction coefficient and optical anisotropy, can be obtained by building models to fit the Ψ and **Δ** at different wavelengths [55]. SE has been used in our previous studies investigating polystyrene (PS) and poly(2-vinylpyridine) (P2VP) infiltration into NPG [28,29]. SE can be easily adjusted to track the kinetics in situ over a period of time as the heating chamber is easier to set up than the vacuum chamber. However, SE relies on fitting parameters and approximating the infiltration front as a sharp boundary between filled and unfilled pores..

Ultraviolet-Visible (UV-Vis) Spectroscopy is an analytical technique used to study the absorption and transmission of ultraviolet and visible light by a sample. UV-Vis composed of light in the UV (200-400 nm) and visible (400-700 nm) ranges. UV-Vis spectroscopy measures absorbed, reflected and transmitted radiation by the sample. When the radiation passes through the sample, elements absorb electromagnetic radiation of different wavelengths, depending on materials shape, chemical bonds, and molecules [56]. Because specific molecular structures absorb light at characteristic wavelengths, the resulting absorption spectrum provides insights into the sample's chemical composition and electronic properties. UV-Vis has not been widely used to measure polymer infiltration. UV-Vis has proved the most reliable in nanomaterials characterization in optical properties, electronic structures, size and size distribution, and concentration [56]. In this project, we validate UV-Vis as a reliable and facile tool of polymer kinetics tracking inside nanoporous gold (NPG).

Optical properties depend on the characteristics of the material. For instance, Au nanostructure plasmon resonance shifts with separation, orientation [57] and volume fraction of the nanostructure [58]. Similar to Au nanorod, NPG are composed of gold particles which evolve into bicontinuous gold ligaments through the fabrication procedure as described in previous publication [29]. NPG has been found to exhibit unique optical properties [59–63] because of the bicontinuous structure, which causes the conducting electrons motion to be greatly suppressed [64] and induces unique localized surface plasmon resonance (LSPR) response in the visible range [65]. Utilizing the LSPR to detect peak shift under different refractive index surroundings, plasmonic sensors can be fabricated using different metals [66–68]. Unlike planar gold or gold nanorods, the optical response of NPG depends on various factors. For instance, the NPG transmission spectra

has been found to be highly related to the NPG ligament aspect ratio [63]. As the aspect ratio increases, the short-wavelength transmission peak experiences a blue shift while the long-wavelength transmission peak experiences a significant red shift [63]. The optical response of NPG also depends on the pore size [65]. Lang et al. (2011) found increasing pore size cause remarkable the LSPR red shift [65]. Different from the existing studies investigating the optical response of NPG, this work focuses on investigating the optical response of NPG under different polymer infiltration extent (IE).

In this study, the optical response during polymer infiltration of NPG is measured from the absorbance spectra from 450 nm to 700 nm. The sample consists of a NPG foil placed over a poly(2-vinyl pyridine) (P2VP) film deposited on a glass substrate. The NPG is pre-annealed for 3 h at 175℃ to prevent coarsening during infiltration at 140℃ [28]. During infiltration, the absorbance peak shifts from 517 nm to 521 nm (red shift), increases in intensity, and grows broader. Analysis of the peak height, peak width, and peak area can be used to determine the infiltration extent. In our previous study [29], the scaling of infiltration time with molecular weight M_w was measured using in-situ SE. Polymer exhibit enhanced kinetics inside NPG as compared to the bulk, and the infiltration time dependence on M_w is greatly reduced [29]. Comparison with in-situ SE shows that UV-vis produces statistically identical infiltration times as well as the same scaling of IE with M_w. This result demonstrates that changes in plasmonic absorption during infiltration correlates with polymer infiltration. Later XPS and DDA analysis suggest that the change in optical response at different IE is due to 1. interface electron flow from P2VP to NPG, and 2. change in surrounding effective refractive index. This study demonstrates that UV-Vis spectroscopy is a straightforward method to determine polymer infiltration into a nanoporous

metallic scaffold. Through better understanding the optical responses of polymer type and polymer infiltration extent inside NPG, polymer infiltrated/ partially infiltrated NPG can be applied for advanced plasmon sensors.

6.2 Materials and Methods

Part of the Materials and Methods section have been described in Chapter 3.

P2VP Bilayer Preparation

Poly (2-vinyl pyridine) (P2VP) is dissolved in butanol (≥ 99.9 %, Sigma-Aldrich), and stirred overnight. The molecular weight, radius of gyration and confinement parameter for P2VP is shown in Table 6.1.

Table 6.1. Characteristics of the P2VP.

Sample	M_w (Da)	R_g (nm)	$\Gamma = R_g/R_{pore}$
P2VP-85k	85,000	7.98	0.23
P2VP-302k	302,000	15.05	0.44
P2VP-643k	643,000	21.96	0.65
P2VP-940k	940,000	26.55	0.78

Atomic Force Microscopy (AFM)

Surface topography of the P2VP:NPG before and after full infiltration are measured using AFM. Tapping mode AFM is performed using Bruker Icon AFM with tips (TAP300AL-G-50 radius of curvature < 10 nm, Ted Pella). The images collected are 1*1 μm^2. The surface properties images are processed using Gwyddion software.

X-Ray Photoelectron Spectroscopy (XPS)

XPS is used to quantify the binding energy of elements in NPG and NPG with polymer before and after it is completely infiltrated. X-ray photoelectron spectroscopy (XPS) was performed in an ultrahigh vacuum chamber equipped with a hemispherical electron energy analyzer (Leybold-Heraeus) and an Al-Kα X-ray source (VG Microtech). The penetration depth is ~10 nm. XPS is used to quantify the electron flow at the P2VP:Au interface.

Discrete Dipole Approximation (DDA) Simulations

The Discrete Dipole Approximation (DDA) is used to simulate the optical properties of the NPG:polymer composite as a function of infiltration extent. The optical properties are the extinction coefficient, localized surface-plasmon resonance (LSPR) wavelength, and LSPR absorption strength, which are calculated using the MATLAB toolbox [69,70]. In this simulation, the electromagnetic radiation propagates in the z direction. Because the light absorption coefficient of P2VP and air are negligible, the scattering only needs to simulate the ligament structure of the NPG. A T-shape structure is found to more accurately capture experimental absorption behavior

than a Au nanorod (Figure S13). Figure 6.1 shows the T-shape structure representing the NPG. This structure captures the plasmon hybridization of the unfilled NPG as well as the reduction in intensity upon replacing air with a medium (polymer) having a dielectric constant [71,72]. As shown in Figure 6.1, the T structure is constructed of two nanorods with diameter and length of 25 nm and 125 nm, respectively.

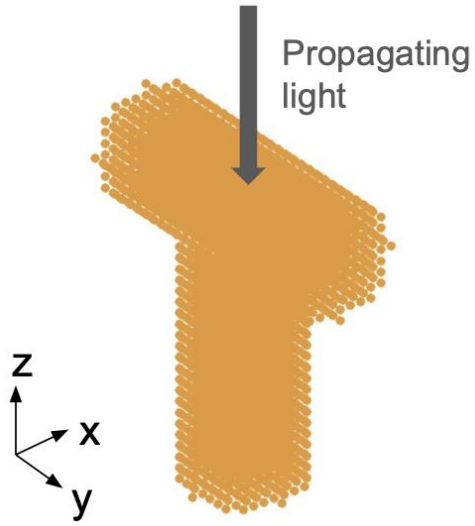

Figure 6.1. The T-shape structure used to model the ligaments in the NPG using the DDA simulation. The dimensions are r = 25 nm and L = 125 nm for both rods forming the T-shape.

6.3 Results and Discussion

Transmittance of NPG filled with air, water and polymer

Plasmon adsorption of metals depends on its surrounding medium. For example, Kim et al (2023) found that the absorbance spectra of gold nanorods experience blue shifts by grafting PS to it [73]. Detsi et al. (2014) showed that the transmittance peak wavelength position of

nanoporous gold (NPG) increases with increasing aspect ratio (AR) of the ligaments, such that doe the AR ranges from 1.2 to 1.8, peak wavelength increases from 560 to 580 nm [63]. In the present study, NPG with a pore radius (R_p) of 34 nm is used. To study the effect of the surrounding medium on NPG, transmittance spectra are compared for NPG filled with air, water and P2VP at room temperature. Absorption from the glass substrate has been subtracted from the transmission spectra. The fully infiltrated NPG was fabricated by annealing NPG: P2VP at 140℃ for 3 h as described previously [28].

The transmittance peaks of NPG are very different when the surrounding medium is varied. Figure 6.2 shows the NPG transmittance spectra in air, water, and P2VP. It is worth noting that the transmittance minimum for NPG in air is weak because of the high reflectivity of the gold in the visible light region, causing most of the light to be reflected rather than being absorbed or transmitted. When the absorbance intensity is weak, transmittance spectra better represent the optical response because $T = 10^{-A}$, where T is the transmittance intensity and A is the absorbance intensity.

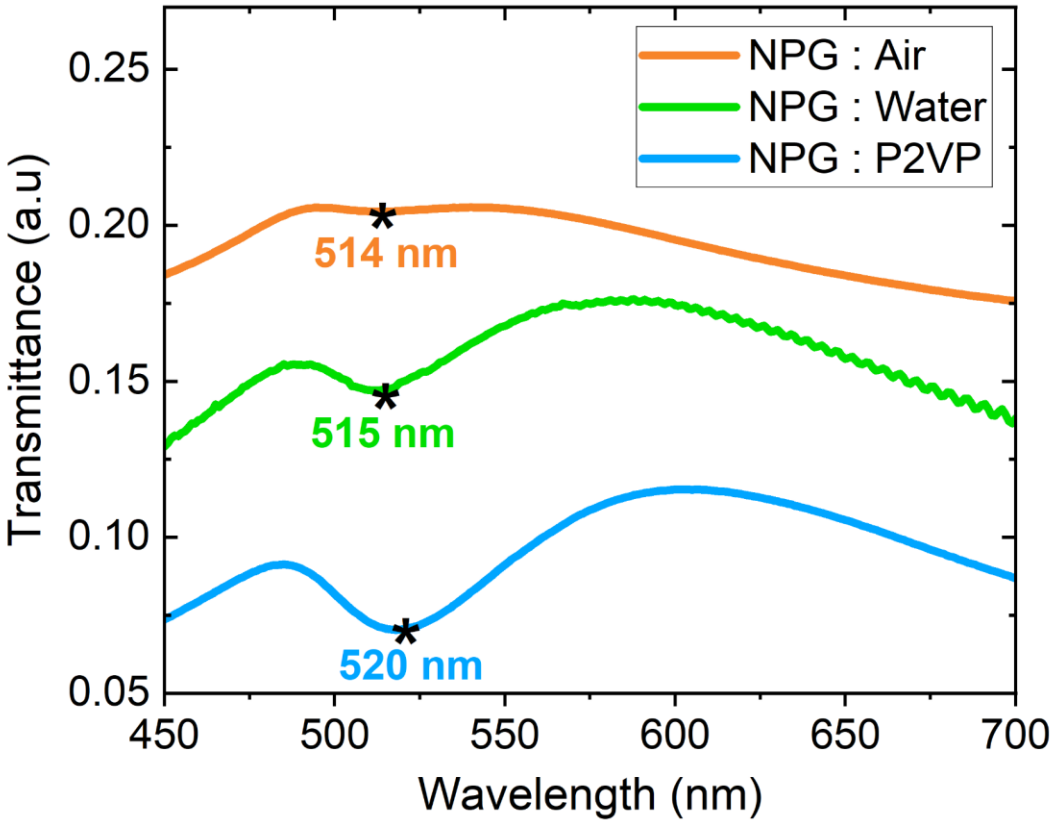

Figure 6.2. Transmittance of NPG in air, water and P2VP. As noted by the asterisk symbol, the transmittance peak minimum shifts from 514 to 515 to 520 nm as the surrounding media changes from air (orange) to water (green) to P2VP (blue). The oscillation in the transmittance curve of NPG in water is accounted for by the instability of the NPG:water interface.

The transmittance intensity increases, and the peak position redshifts as the refractive index of the surrounding medium increases. As shown in Figure 6.2, the NPG transmittance spectra exhibit shifts in minima wavelength positions, resembling the absorbance peak maxima. When the pores are filled with air, the minimum is weak and the transmittance minimum appears

at 514 nm. When pores are filled with water, the transmittance peaks become stronger relative to the minimum. Compared to air (n=1), NPG has a lower reflectivity in water (n = 1.33 @ wavelength = 632.8 nm) because the refractive index difference between gold and water is smaller than gold and air. The NPG filled with water also undergoes a red shift in the peak position (515 nm) due to the increase in the surrounding refractive index. For the NPG:Water system, the oscillations at higher wavelengths are due to interference fringes. As NPG are fully immersed in P2VP (n=1.54), the transmittance peaks become stronger than the NPG:Air and NPG:Water due to a further reduction in reflectivity of the NPG-P2VP composite. The NPG - P2VP transmittance minimum appears at 520 nm, indicating a red shift compared to air and water. NPG absorbance spectra undergoes peak red shift and higher intensity (more apparent shape) as the surrounding media refractive index increases.

Absorbance Spectra during polymer infiltration

As polymer fills the NPG film from below, the refractive index of the NPG-P2VP composite increases. As mentioned in our previous studies [28,29], the polymer kinetics inside NPG can be monitored using in-situ spectroscopic ellipsometry (SE) and modeled using effective medium approximation (EMA). Motivated by the previous section examining how the transmission of NPG depends on the medium filling the pore, the absorbance spectra of a P2VP-643k:NPG bilayer is determined at 140°C for annealing times from 0 to 300 min as shown in Figure 6.3.

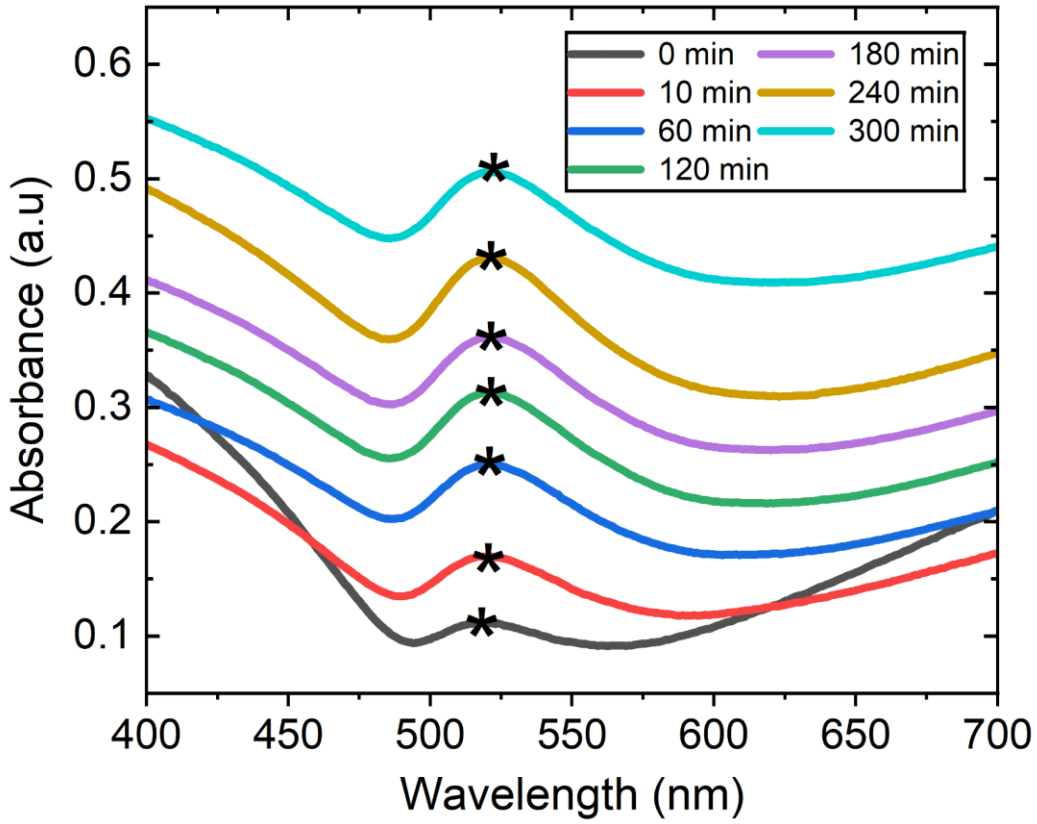

Figure 6.3. Absorbance data of P2VP-643k:NPG under various annealing times. The asterisks indicate the peak location. Absorbance for 10 min to 300 min is shifted vertically to better visualize each time point.

As annealing time increases, the absorbance peak red shifts and moves to higher wavelength. At 0 min, when P2VP-643k:NPG exhibits a discrete bilayer, the absorbance peak lies at 517 nm. In Figure 6.2, the NPG:Air sample showed a minimum in transmission near 514 nm. The P2VP absorbance spectra shows no outstanding absorbance in the range of 400-700 nm wavelength as shown in SI Figure S9. However, though there is no P2VP infiltrated into the NPG, the P2VP underneath the NPG creates a P2VP-NPG interface. The change in the interface causes the

change in the peak position which will be further discussed in the mechanism section. At 300 mins of annealing (full infiltration), the absorbance spectra peak shifts to 521 nm, increased by 4 nm as compared to the 0 min spectra. Additionally, similar to the observation from Figure 6.2, the P2VP-643k:NPG absorbance curve exhibits an increased width and an enhanced height (intensity) as annealing time increases. Absorbance measurements on P2VP-85k:NPG, P2VP-302k:NPG, and P2VP-940k:NPG at 140°C have also been performed and are shown in SI Figure S10. The trend in absorption peak position and intensity are consistent with those showing in Figure 6.3. Research has shown that the Au localized surface plasmon resonance (LSPR) is enhanced when Au is conjugated with poly(vinyl pyrrolidone) (PVP) through electron doping in the valence band through the adsorption of hydride [74]. P2VP has a stronger electron donating behavior as compared to PVP since PVP:Au has a Au-Au coordination number (CN_{Au-Au}) of 7.5 ± 0.7, while P2VP:Au has a much enhanced CN_{Au-Au} of 8.3 ± 0.7 [75]. As a result, when P2VP binds to the gold, the gold undergoes more electron doping, thus causing a much enhanced LSPR response as shown in the measurements. In the later section, the P2VP:NPG interfacial electron doping phonmena will be quantified using XPS and discussed in more detail.

UV-Vis Absorbance Analysis and Comparison of Infiltration Kinetics with SE

In this section, we relate the absorbance characteristics, namely peak height, peak width and peak area to the extent of P2VP infiltration into the NPG. As shown in Figure 6.4a, the relative peak height increases rapidly at early annealing times and then more slowly after 100 min. This parabolic behavior mimics the increase in the change of refractive index measured by the in-situ SE system in our previous publication [28,29]. From UV-vis absorption spectra, the

initial peak height (h_i) and final peak height (h_f) can be used to determine the infiltration extent, $IE = \frac{h_o - h_i}{h_f - h_i}$. The time dependence of IE calculated from UV-vis spectra is shown in Figure 6.4b. Similarly, the IE was determined from the peak width and peak area and shown in SI. The IE determined from these three approaches (height, width, area) statistically agree with each other. In the rest of the experimental study, we use the peak height approach. For the P2VP-643k:NPG system in Figure 6.3, Figure 6.4b compares the time dependence of IE for the UV-Vis (green) and in-situ SE (pink). The IE values are in excellent agreement to ca. 0.85. Between IE = 0.85 - 1.0, the UV-vis data is slightly greater than the SE values. The greater values of UV-Vis can be attributed to the P2VP wetting ahead of the growth front which in turn affects the plasmon absorption peak before P2VP backfilling occurs. Because SE uses a two layer EMA model with a well defined interface, the IE is slightly less than the values measured by UV-vis particularly near the top of the NPG due to P2VP traveling faster at the NPG:P2VP interfaces. At very long annealing times (i.e., 300 min), the IE values converge as expected for completely filled NPG.

Using data like Figure 6.4b for M_w = 85k, 302k, 643k and 940k Da., the time to reach 80% IE ($\tau_{80\%}$) is determined. Figure 6.4c shows the scaling of $\tau_{80\%}\ vs. M_w$ for the UV-Vis (green) in-situ SE (pink) methods. The $\tau_{80\%}$ values at each M_w are in statistical agreement according to their standard deviations. Additionally, we further investigate the $\tau_{80\%}\ vs. M_w$ relationship using those two approaches. Shown in our other publication, for the in-situ SE approach, $\tau_{80\%}\ vs. M_w$ displays a slope of 1.40 ± 0.03, whereas the UV-Vis approach yields 1.35 ± 0.04. The excellent agreement indicates that the UV-Vis approach is an accurate method to determine infiltration kinetics in a metallic scaffold. In this section, we measured the infiltration

extent using a new approach UV-Vis, and found it to be in excellent agreement with the more often used in-situ SE approach.

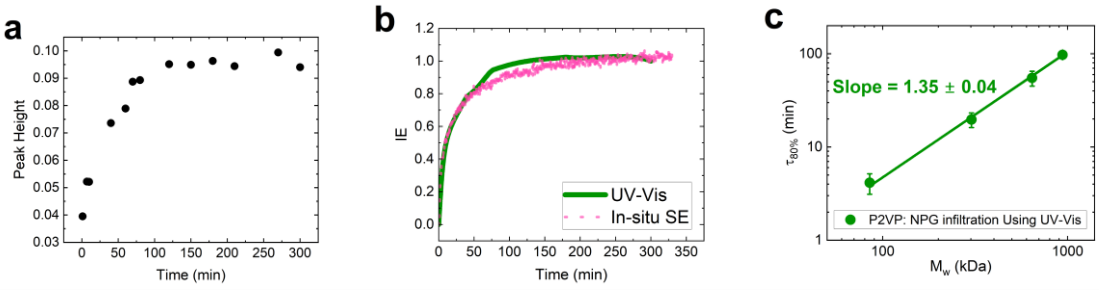

Figure 6.4. (A) UV-Vis spectra of peak height versus annealing time for P2VP-643k:NPG at 140°C . (B) Infiltration extent for P2VP-643 in NPG measured by UV-Vis and SE. (C) The times for 80% infiltration for P2VP having M_w of 85k, 302k, 643k and 940k.

The previous section demonstrated that the plasmon resonance peak can be used to quantify polymer infiltration kinetics in a nanoporous metal scaffold. Here, we investigate the contribution from the NPG:P2VP interface and the surrounding medium filling the pore. To quantify the NPG:P2VP interfacial phenomena, XPS is used to probe the binding energy of the Au 4f orbital. The interfacial contribution will be discussed in the following section. The surrounding medium effect on the absorbance shape is approached using DDA simulation, which will be elaborated in the next section.

P2VP forms a thin wetting layer on the NPG surface after complete infiltration. Figure 6.5a shows the AFM height image from the surface of a NPG (120 nm):P2VP-643k (100 nm) bilayer, whereas Figure 6.5b shows the height image after P2VP has completely infiltrated the top NPG film. Prior to infiltration, Figure 6.5a shows the ligaments (bright) and pores (dark) of

the NPG. The initial RMS roughness is 10.2 nm. Upon annealing for 5 h at 140°C to ensure complete infiltration (c.f. Figure 6.3b), the top most surface of the NPG no longer shows distinct ligaments. This observation differs from our study of polystyrene infiltration into NPG where the surface displays ligaments adjacent to PS filled pores. In contrast, Figure 6.5b shows a topography where NPG ligaments are covered by P2VP, evidenced by "blobs" appearing on the surface. Correspondingly, the RMS roughness decreases to 3.4 nm (Figure 6.5b), indicating a smoother surface as compared to the pre-infiltration sample. Figures S1-S3 show the corresponding AFM images of P2VP bilayers at M_w = 85k, 302k, and 940k Da before and after complete infiltration. Figures S4-S7 show the corresponding phase images. All images are consistent with a smooth surface after complete infiltration. To future confirm that the surface is wet by P2VP, Figure S8 compares the water contact angles (WCA) of fully infiltrated P2VP and PS, indicating surface wetting properties of P2VP. A thin P2VP wetting layer is formed atop NPG, allowing additional XPS characterizations.

After we confirm the formation of a P2VP wetting layer on top of the NPG, XPS is used to demonstrate strong coupling between plasmons in the gold due to binding of P2VP at the interface.. XPS measures the binding energy, with a probing depth of 5-10 nm. Figure 6.5c shows the gold $4f_{5/2}$ and $4f_{7/2}$ orbital binding energies before and after complete P2VP infiltration. The gold curve denotes the binding energy of pristine NPG, while the blue curve denotes the binding energy of P2VP infiltrated NPG. For both $4f_{5/2}$ and $4f_{7/2}$ orbitals, binding energy decreases after complete infiltration. The pristine NPG has $4f_{5/2}$ binding energy at 87.63 eV, while the $4f_{7/2}$ binding energy lies at 84.02 eV. The pristine NPG binding energies are in good agreement with literature values [75]. For the P2VP infiltrated NPG, the corresponding

binding energies are 87.15eV and 83.56 eV, which are 0.48 eV and 0.46 eV less than the pristine case. The lower binding energies at the P2VP:NPG interface implies that the NPG is negatively charged through electron donations from the NPG:P2VP interface stabilization [76]. The decrease in gold binding energies implies that the electrons flow from P2VP to NPG when P2VP wets the NPG. The strong electron-donating behavior of P2VP is originated from the electron-donating alkyl chains adjacent to the nitrogen atom [75], making nitrogen more electronegative, thus further enhancing the tendency for electrons to flow from P2VP to NPG upon conjugation. At the P2VP-NPG interface, electrons flow from P2VP into NPG, making NPG more electron rich and negatively charged.

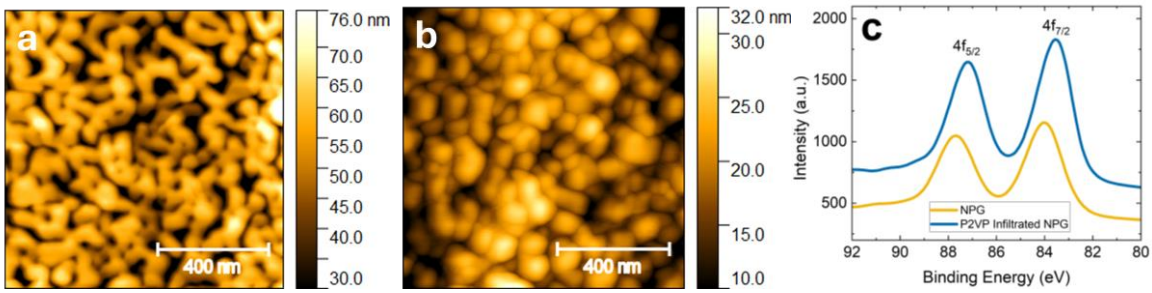

Figure 6.5. a. AFM height image of as-cast NPG:P2VP-643k composite. b. AFM height image of fully infiltrated NPG:P2VP-643k composite after annealing at 140 °C for 5 hours. Root-mean-square (RMS) roughness for (a) is 10.2 nm, RMS roughness for (b) is 3.4 nm. c. XPS spectra of gold 4f orbital for pristine NPG and P2VP infiltrated NPG.

The change in interfacial electron flow and polarity change account for the peak shift in Figure 6.3. In addition to interfacial interactions, the bulk P2VP filling the pore changes the surface plasmon resonance of the Au ligaments. Prior to infiltration, the NPG is composed of gold and air. However, after complete infiltration, the pores are filled with a dielectric, namely

P2VP. P2VP has a much higher refractive index (n = 1.54) than air (n = 1.0). Recall that infiltration is modeled in SE by a bilayer having a top thickness filled with air and a bottom layer filled with P2VP. To further investigate how this change in refractive index impacts the SPR, the Discrete Dipole Approximation (DDA) is used along with the Effective Medium Approximation (EMA).

Simulation of NPG absorption spectra using DDA

"T" shape is used in DDA simulation to capture the NPG structure and finds an absorbance peak experiencing red shifts as the medium refractive index increases. As mentioned in the method section, a "T" shape gold is constructed to mimic the structure of NPG. Previous research has used a rod shape to mimic the structure of NPG [63], however, it is found that the "T" shape could better capture the adsorption. The rod shape DDA simulation results are shown in Figure S13. To compare simulations with experimental results, DDA is used to determine the optical properties of NPG, with a focus on the transverse LSPR. To first test the accuracy and precision of the simulated T-shape model using DDA as compared to the experimental settings, the absorption behaviors of the T-shape model in three different medias are simulated. As shown in Figure 6.6, the resulting absorption peak wavelength positions of the T-shape gold ligament in air (n=1.0003), water (n=1.33), and P2VP (n=1.54) are 515, 521, and 522 nm respectively. As the media refractive index increases (from n = 1 to n = 1.54), the peak shifts towards higher wavelength. This observation is in good qualitative agreement with the experimental optical response surrounded by the same medium as shown in Figure 6.2, which yields peaks at 514 (air), 515 (water), and 520 (P2VP) nm respectively. Besides the peak position, the absorbance

peak height also increases upon increasing the surrounding medium refractive index. The peak height increases from 0.264, 0.581, to 0.815 (a.u.) upon the change of medium from n = 1 (air) to n = 1.33 (water) to n = 1.54 (P2VP), which also agrees with experimental observation as shown in Figure 6.2. Since the DDA simulation only accounts for the change in the surrounding refractive index, Figure 6.6 curves implies that the surrounding refractive index also possesses an influential effect on NPG LSPR.

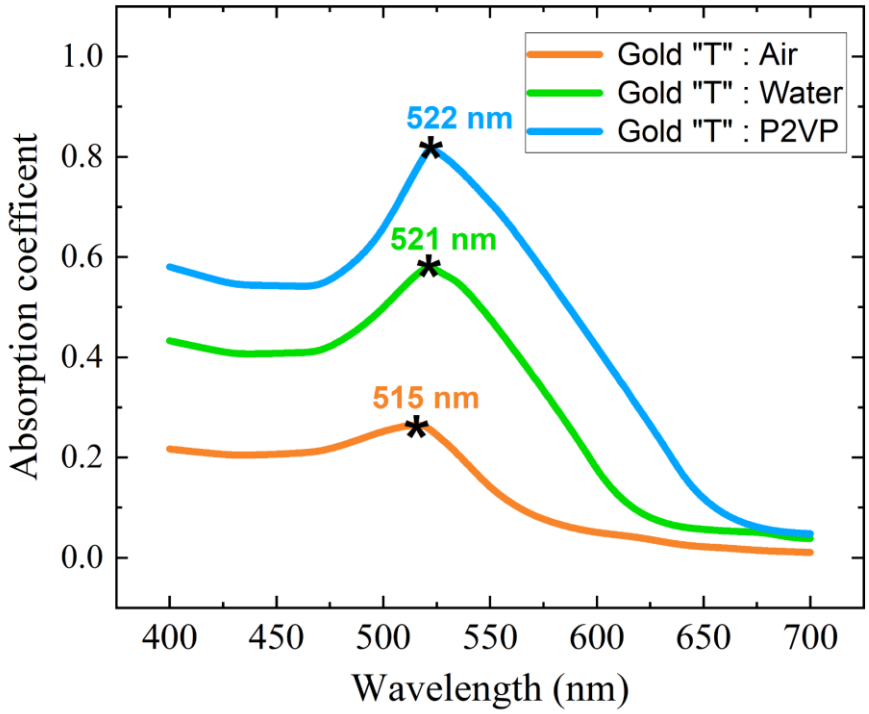

Figure. 6.6. Absorption coefficient of NPG in air, water, and P2VP by DDA simulation, with incident light wavelength from 400 to 700 nm. Plot of the above three media shows peak shift from 515 to 521 to 522 nm, peak broadening, and strong absorption effects as surrounding medium refractive index increases.

Conversion of DDA Absorbance Spectra to Infiltration Extent

To investigate the effect of P2VP infiltration extent on absorbance behavior, the optical properties of polymer-NPG bilayer/composites at different infiltration extent (IE) are simulated and calculated at incident light wavelengths from 400 to 700 nm. The total height (TH) of the T-shape gold model is 150 nm, and the infiltrated height (IH) is manually set as shown in the cartoon in Fig. 7a. The surrounding medium of the infiltrated part is set to be n = 1.54, and the infiltration extent (IE) is calculated by $IE = 100\% * \frac{IH}{TH}$. a partial infiltration scenario (i.e. Fig. 7a, IE = 0.5), while the bottom region is filled with P2VP, the non-infiltrated region remains surrounded by air (n=1.0003). As shown in Figure 6.7b, the resulting absorption coefficient curves show weak peak shift from 515 to 522 nm during infiltration, with broadened peak width as well as higher absorption peak upon increasing IE. The simulation results qualitatively agree well with the experimental observations in Fig. 6.3. Noticeably, the left shoulder of the absorption coefficient curve remains stable at ~ 470 nm during the process, which agrees with the experimental observations shown in Figure 6.3, while the red-shifted right shoulder leading to broadening effect. Interestingly, the work by Detsi et al. (2014) also shows a relatively stable left shoulder and a much shifted right shoulder when altering the NPG aspect ratios (AR). Detsi et al. (2014) found that the NPG AR could greatly influence the optical response. When the AR increases from 3.8 to 5.1 [63], the transmittance peak becomes broader and deeper. The left shoulder experiences a blue shift for ~ 3 nm while the right shoulder experiences a ~ 32 nm red shift [63]. Upon NPG structural changes or surrounding medium changes, the right shoulder experiences a more prominent shift towards the red, accounting for the peak broadening observations.

The surrounding medium refractive index also accounts for the peak shifts. Figure 6.7c clearly shows the peak experiencing a red shift as the peak position is at 515 nm before infiltration, shifted to 521 nm after IE = 0.5, and moves and keeps constant at 522 nm for higher IEs. It is interesting to note that while the P2VP reaches complete infiltration at IE = 1.0, the peak position stops shifting red at IE = 0.67. Though the peak position remains constant at 522 nm for IE = 0.67, 0.83, and 1.0, those three circumstances still induce change in peak shape (width & height).

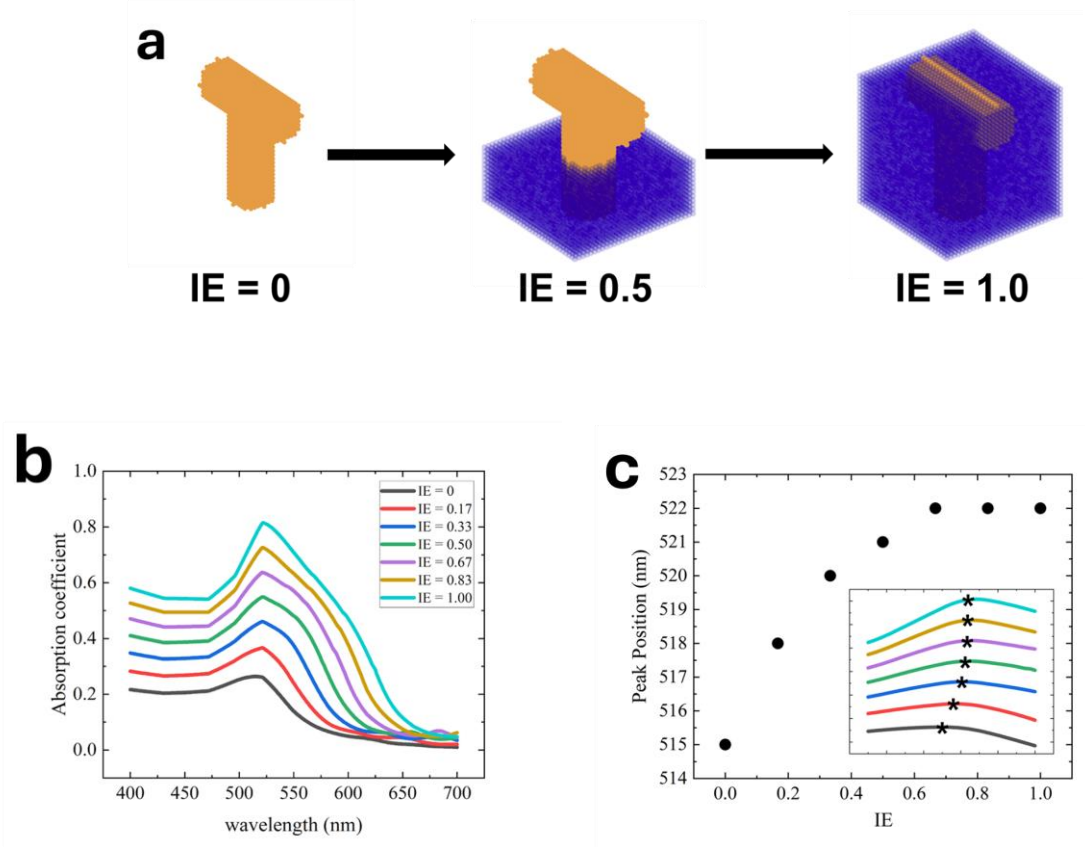

Figure. 6.7. a. DDA cartoon scheme of IE = 0, IE = 0.5, and IE = 1.0. b. absorption coefficients calculated by DDA simulation, with different infiltration extents (IE) from pure NPG to fully infiltration. IE is defined as the P2VP infiltrated height over the total height of the T-shape model. Curves showing weak peak red-shifting, peak

broadening effect, and stronger absorption with higher IE. c. the extracted peak position vs infiltration extent, inserted with a magnified figure demonstrating peak shift.

DDA: Correlation between theoretical and simulated IE

The absorbance spectra shape and shifting are directly related to the effective medium refractive index. As the polymer infiltration extent increases, the simulated peaks exhibit an enhanced peak width as well as peak height, in addition to the shift of the peak wavelength position. As we noticed similar trends for DDA as compared to the experimental observation (Figure 6.3), additional analysis of absorption spectra shape with respect to different infiltration extent is conducted. The DDA simulation circumvents the infiltration time of the P2VP:NPG infiltration process. Compared with experimental data from the UV-Vis, which shows a parabolic relationship between peak height and annealing time, the linear relationship from simulation results in circumvents of time variation. Infiltration time is eliminated as a parameter in DDA, and as shown in the experimental section, infiltration time scales parabolically to the infiltration extent. The IE in the DDA simulation is manually set as a height in the T-shape gold model box, thus there is no kinetics associated with the polymer travel. To analyze the simulated peaks under different IE, peak height, full width half maximum (FWHM), and area under the curve (AUC) are quantified and analyzed. The peak height (a.u.) increases from 0.264 to 0.815 when the IE increases from 0 to 1 as shown in Figure 6.8a. Additionally, the peak height is linearly related with IE, with Pearson's r=0.99962 and R-square (COD)= 0.99925, implying this linear correlation has high reliability and precision. The linear slope of peak height vs. IE is 0.55 ± 0.01. The AUC and FWHM are also calculated and linearly fit as a function of IE as shown in

supplemental Figure. By using the peak height, AUC, and FWHM linear fit, given a specific IE, the absorbance spectra shape can be easily predicted. The peak height, FWHM, AUC all show the same trend such that as IE increases, the according value linearly increases. The DDA simulation shows that as IE increases, the peak height, AUC and FWHM increases linearly as shown in Figure 6.8a and C15, implying that the absorbance spectra is directly related to the medium refractive index.

To further interpret the relationship between the peak shape and the IE, the manually set IE (x-axis) for the DDA simulation is compared with the calculated IE (y-axis) as shown in Figure 6.8b. The calculated IE utilizes the peak height (h) values from Figure 6.8a, and apply the equation that $Calculated\ IE\ = \frac{h - h_o}{h_f - h_o}$, where h_o = 0.264 and h_f = 0.815. The calculated IE exhibits a linear relationship with respect to the IE, with a slope of 0.99 ± 0.01, implying that the calculated IE agrees with the manual set IE, confirming that the absorbance peak shape can be used to analyze the polymer kinetics. Similar procedures are also conducted for AUC and FWHM, leading to similar results showing linear slope close to 1 (figure S16). The DDA analysis proved that the optical spectra is a valid tool for tracking polymer infiltration kinetics inside a NPG scaffold.

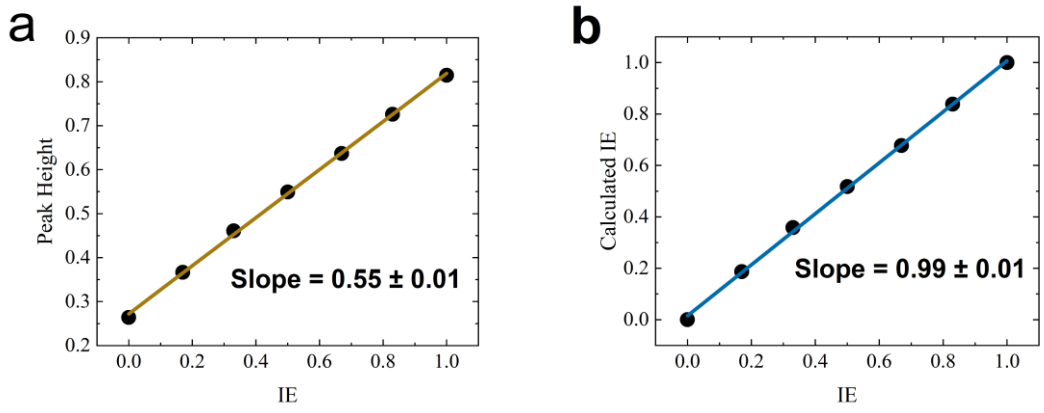

Figure. 6.8. a. peak height of P2VP infiltrated NPG with different infiltration extents from DDA simulation, linear fitting with Pearson's r=0.99962 and R-square(COD)=0.99925. Infiltration extent is defined as infiltration height / total height of the T-shape model. b. plot of calculated infiltration extent vs. pre-defined infiltration extent, slope of the linear fitting equal to 0.99 with standard error of 0.01.

6.4 Conclusion

UV-Vis is used to measure the optical responses of polymer infiltrated nanoporous gold (PING) at different annealing times. At temperatures higher than T_g, P2VP (M_w = 85 - 940 kDa) infiltrates into the 34 nm NPG bicontinuous pores. Different annealing times induce infiltration extents (IE) which range from 0 to 1. At higher annealing times, the UV-Vis optical response curve is measured to have an enlarged height and width, as well as red shifts in the peak position. Through analyzing the peak height, width, and area under the curve (AUC), it is found that those three parameters change accordingly with the IE. Upon further comparison between the UV-Vis and the previous in-situ spectroscopic ellipsometry result, it is found that those two methods yield statistically the same time to reach 80% IE ($\tau_{80\%}$) as well as slope of $\tau_{80\%}$ vs. M_w. UV-Vis proves to be a valid tool for polymer kinetics tracking, also implying that the optical response

curve properties (height, width, AUC) are directly proportional to the IE. To further investigate the physics behind the optical curve to the IE, XPS is used to find that electrons flow from P2VP to the NPG at the P2VP:NPG interface, and DDA simulation is used to found that the effective medium refractive index also accounts for the optical curve shape change. In this project, we have proved UV-Vis to be a reliable and facile tool for polymer kinetics tracking inside nanoporous scaffolds, allowing future studies of simultaneous investigation of polymer kinetics and optical properties.

6.5 References

1. Balazs, A. C., Emrick, T. & Russell, T. P. Nanoparticle Polymer Composites: Where Two Small Worlds Meet. *Science* **314**, 1107–1110 (2006).

2. Kim, J. *et al.* Estimation of the concentration of nano-carbon black in tire-wear particles using emission factors of PM10, PM2.5, and black carbon. *Chemosphere* **303**, 134976 (2022).

3. Guth, E. Theory of Filler Reinforcement. *J. Appl. Phys.* **16**, 20–25 (1945).

4. Bilchak, C. R., Huang, Y., Benicewicz, B. C., Durning, C. J. & Kumar, S. K. High-Frequency Mechanical Behavior of Pure Polymer-Grafted Nanoparticle Constructs. *ACS Macro Lett.* **8**, 294–298 (2019).

5. Rittigstein, P. & Torkelson, J. M. Polymer-nanoparticle interfacial interactions in polymer nanocomposites: Confinement effects on glass transition temperature and suppression of physical aging: Polymer-Nanoparticle Interfacial Interactions. *J. Polym. Sci. Part B Polym.*

Phys. **44**, 2935–2943 (2006).

6. Bilchak, C. R. *et al.* Polymer-Grafted Nanoparticle Membranes with Controllable Free Volume. *Macromolecules* **50**, 7111–7120 (2017).

7. Merkel, T. C. *et al.* Ultrapermeable, Reverse-Selective Nanocomposite Membranes. *Science* **296**, 519–522 (2002).

8. Liu, Y. *et al.* Electro-thermal actuation in percolative ferroelectric polymer nanocomposites. *Nat. Mater.* **22**, 873–879 (2023).

9. Wegst, U. G. K., Bai, H., Saiz, E., Tomsia, A. P. & Ritchie, R. O. Bioinspired structural materials. *Nat. Mater.* **14**, 23–36 (2015).

10. Meyers, M. A., McKittrick, J. & Chen, P.-Y. Structural Biological Materials: Critical Mechanics-Materials Connections. *Science* **339**, 773–779 (2013).

11. Yao, Y. *et al.* Complex dynamics of capillary imbibition of poly(ethylene oxide) melts in nanoporous alumina. *J. Chem. Phys.* **146**, 203320 (2017).

12. Tu, C.-H., Zhou, J., Butt, H.-J. & Floudas, G. Adsorption Kinetics of *cis* -1,4-Polyisoprene in Nanopores by *In Situ* Nanodielectric Spectroscopy. *Macromolecules* **54**, 6267–6274 (2021).

13. Shin, K. *et al.* Enhanced mobility of confined polymers. *Nat. Mater.* **6**, 961–965 (2007).

14. Tu, C.-H., Steinhart, M., Butt, H.-J. & Floudas, G. *In Situ* Monitoring of the Imbibition of Poly(*n* -butyl methacrylates) in Nanoporous Alumina by Dielectric Spectroscopy. *Macromolecules* **52**, 8167–8176 (2019).

15. Tu, C.-H., Zhou, J., Doi, M., Butt, H.-J. & Floudas, G. Interfacial Interactions During In Situ

Polymer Imbibition in Nanopores. *Phys. Rev. Lett.* **125**, 127802 (2020).

16. Hu, G. & Cao, B. Flows of Polymer Melts through Nanopores: Experiments and Modelling. *J. Therm. Sci. Technol.* **8**, 363–369 (2013).

17. Huang, Y.-R. *et al.* Polymer nanocomposite films with extremely high nanoparticle loadings via capillary rise infiltration (CaRI). *Nanoscale* **7**, 798–805 (2015).

18. Jiang, Y., Hor, J. L., Lee, D. & Turner, K. T. Toughening Nanoparticle Films via Polymer Infiltration and Confinement. *ACS Appl. Mater. Interfaces* **10**, 44011–44017 (2018).

19. Qiang, Y., Pande, S. S., Lee, D. & Turner, K. T. The Interplay of Polymer Bridging and Entanglement in Toughening Polymer-Infiltrated Nanoparticle Films. *ACS Nano* **16**, 6372–6381 (2022).

20. Qiang, Y., Turner, K. T. & Lee, D. Role of Polymer–Nanoparticle Interactions on the Fracture Toughness of Polymer-Infiltrated Nanoparticle Films. *Macromolecules* **56**, 122–135 (2023).

21. Hor, J. L. *et al.* Nanoporous Polymer-Infiltrated Nanoparticle Films with Uniform or Graded Porosity *via* Undersaturated Capillary Rise Infiltration. *ACS Nano* **11**, 3229–3236 (2017).

22. Hor, J. L., Wang, H., Fakhraai, Z. & Lee, D. Effects of polymer–nanoparticle interactions on the viscosity of unentangled polymers under extreme nanoconfinement during capillary rise infiltration. *Soft Matter* **14**, 2438–2446 (2018).

23. Hor, J. L., Wang, H., Fakhraai, Z. & Lee, D. Effect of Physical Nanoconfinement on the Viscosity of Unentangled Polymers during Capillary Rise Infiltration. *Macromolecules* **51**,

5069–5078 (2018).

24. Venkatesh, R. B. & Lee, D. Conflicting Effects of Extreme Nanoconfinement on the Translational and Segmental Motion of Entangled Polymers. *Macromolecules* **55**, 4492–4501 (2022).

25. Venkatesh, R. B. & Lee, D. Interfacial Friction Controls the Motion of Confined Polymers in the Pores of Nanoparticle Packings. *Macromolecules* **55**, 8659–8667 (2022).

26. Venkatesh, R. B. *et al.* Effect of polymer–nanoparticle interactions on solvent-driven infiltration of polymer (SIP) into nanoparticle packings: a molecular dynamics study. *Mol. Syst. Des. Eng.* **5**, 666–674 (2020).

27. Ren, T. *et al.* Increase in the effective viscosity of polyethylene under extreme nanoconfinement. *J. Chem. Phys.* **160**, 024909 (2024).

28. Maguire, S. M. *et al.* Effect of Nanoscale Confinement on Polymer-Infiltrated Scaffold Metal Composites. *ACS Appl. Mater. Interfaces* **13**, 44893–44903 (2021).

29. Kong, W. *et al.* Capillary filling dynamics of polymer melts in a bicontinuous nanoporous scaffold. *J. Chem. Phys.* **160**, 044904 (2024).

30. Kimmich, R., Fatkullin, N., Mattea, C. & Fischer, E. Polymer chain dynamics under nanoscopic confinements. *Magn. Reson. Imaging* **23**, 191–196 (2005).

31. Mangal, R., Srivastava, S. & Archer, L. A. Phase stability and dynamics of entangled polymer–nanoparticle composites. *Nat. Commun.* **6**, 7198 (2015).

32. Keddie, J. L., Jones, R. A. L. & Cory, R. A. Size-Dependent Depression of the Glass

Transition Temperature in Polymer Films. *Europhys. Lett. EPL* **27**, 59–64 (1994).

33. Choi, J., Clarke, N., Winey, K. I. & Composto, R. J. Fast Polymer Diffusion through Nanocomposites with Anisotropic Particles. *ACS Macro Lett.* **3**, 886–891 (2014).

34. Tarnacka, M. *et al.* The Impact of Molecular Weight on the Behavior of Poly(propylene glycol) Derivatives Confined within Alumina Templates. *Macromolecules* **52**, 3516–3529 (2019).

35. Ediger, M. D. & Forrest, J. A. Dynamics near Free Surfaces and the Glass Transition in Thin Polymer Films: A View to the Future. *Macromolecules* **47**, 471–478 (2014).

36. Schneider, H. M., Frantz, P. & Granick, S. The Bimodal Energy Landscape When Polymers Adsorb. *Langmuir* **12**, 994–996 (1996).

37. Lange, F. *et al.* Large-Scale Diffusion of Entangled Polymers along Nanochannels. *ACS Macro Lett.* **4**, 561–565 (2015).

38. Roth, C. & Dutcher, J. Mobility on Different Length Scales in Thin Polymer Films. in *Soft Materials* (eds. Marangoni, A. & Dutcher, J.) 1–38 (CRC Press, 2004). doi:10.1201/9780203027004.ch1.

39. Choi, J. *et al.* Universal Scaling of Polymer Diffusion in Nanocomposites. *ACS Macro Lett.* **2**, 485–490 (2013).

40. Askar, S., Wei, T., Tan, A. W. & Torkelson, J. M. Molecular weight dependence of the intrinsic size effect on *T* g in AAO template-supported polymer nanorods: A DSC study. *J. Chem. Phys.* **146**, 203323 (2017).

41. Schneider, G. J. Dynamics of nanocomposites. *Curr. Opin. Chem. Eng.* **16**, 65–77 (2017).

42. Gam, S. *et al.* Macromolecular Diffusion in a Crowded Polymer Nanocomposite. *Macromolecules* **44**, 3494–3501 (2011).

43. Bocquet, L. Nanofluidics coming of age. *Nat. Mater.* **19**, 254–256 (2020).

44. Bansal, A. *et al.* Quantitative equivalence between polymer nanocomposites and thin polymer films. *Nat. Mater.* **4**, 693–698 (2005).

45. Wang, H. *et al.* Dramatic Increase in Polymer Glass Transition Temperature under Extreme Nanoconfinement in Weakly Interacting Nanoparticle Films. *ACS Nano* **12**, 5580–5587 (2018).

46. Serghei, A., Chen, D., Lee, D. H. & Russell, T. P. Segmental dynamics of polymers during capillary flow into nanopores. *Soft Matter* **6**, 1111 (2010).

47. Serghei, A. *et al.* Density Fluctuations and Phase Transitions of Ferroelectric Polymer Nanowires. *Small* **6**, 1822–1826 (2010).

48. Serghei, A., Zhao, W., Wei, X., Chen, D. & Russell, T. P. Nanofluidics with phase separated block-copolymers: Glassy dynamics during capillary flow. *Eur. Phys. J. Spec. Top.* **189**, 95–101 (2010).

49. Houachtia, A. *et al.* Nanofluidics Approach to Separate between Static and Kinetic Nanoconfinement Effects on the Crystallization of Polymers. *Nano Lett.* **15**, 4311–4316 (2015).

50. Guohua, Y., Dezhang, Z., Haochang, P., Hongjie, X. & Shoumian, C. Beam Induced

Degradation Effect in Ion Beam Analysis of Polymer. *Chin. Phys. Lett.* **8**, 472–475 (1991).

51. Schnabel, W. *Polymer Degradation: Principles and Practical Applications*. (Hanser [u.a.], München, 1981).

52. Alexandris, S., Sakellariou, G., Steinhart, M. & Floudas, G. Dynamics of Unentangled *cis* -1,4-Polyisoprene Confined to Nanoporous Alumina. *Macromolecules* **47**, 3895–3900 (2014).

53. Politidis, C., Alexandris, S., Sakellariou, G., Steinhart, M. & Floudas, G. Dynamics of Entangled *cis* -1,4-Polyisoprene Confined to Nanoporous Alumina. *Macromolecules* **52**, 4185–4195 (2019).

54. Alexandris, S. *et al.* Interfacial Energy and Glass Temperature of Polymers Confined to Nanoporous Alumina. *Macromolecules* **49**, 7400–7414 (2016).

55. Bagley, J. D., Dennis Tolley, H. & Linford, M. R. Reevaluating the conventional approach for analyzing spectroscopic ellipsometry psi/delta versus time data. Additional statistical rigor may often be appropriate: Reevaluating the standard analysis of ellipsometry psi/delta/time data. *Surf. Interface Anal.* **48**, 186–195 (2016).

56. Rizwan, M. & Gwenin, C. Nanomaterials in renewable energy: UV-Visible spectroscopy characterization and applications. in *Nano Tools and Devices for Enhanced Renewable Energy* 103–120 (Elsevier, 2021). doi:10.1016/B978-0-12-821709-2.00017-7.

57. Hore, M. J. A., Frischknecht, A. L. & Composto, R. J. Nanorod Assemblies in Polymer Films and Their Dispersion-Dependent Optical Properties. *ACS Macro Lett.* **1**, 115–121 (2012).

58. Hore, M. J. A. & Composto, R. J. Nanorod Self-Assembly for Tuning Optical Absorption.

ACS Nano **4**, 6941–6949 (2010).

59. Yu, F. *et al.* Simultaneous Excitation of Propagating and Localized Surface Plasmon Resonance in Nanoporous Gold Membranes. *Anal. Chem.* **78**, 7346–7350 (2006).

60. Biener, J. *et al.* Nanoporous Plasmonic Metamaterials. *Adv. Mater.* **20**, 1211–1217 (2008).

61. Qian, L. H., Yan, X. Q., Fujita, T., Inoue, A. & Chen, M. W. Surface enhanced Raman scattering of nanoporous gold: Smaller pore sizes stronger enhancements. *Appl. Phys. Lett.* **90**, 153120 (2007).

62. Dixon, M. C. *et al.* Preparation, Structure, and Optical Properties of Nanoporous Gold Thin Films. *Langmuir* **23**, 2414–2422 (2007).

63. Detsi, E., Salverda, M., Onck, P. R. & De Hosson, J. Th. M. On the localized surface plasmon resonance modes in nanoporous gold films. *J. Appl. Phys.* **115**, 044308 (2014).

64. Fujita, T. *et al.* Unusually Small Electrical Resistance of Three-Dimensional Nanoporous Gold in External Magnetic Fields. *Phys. Rev. Lett.* **101**, 166601 (2008).

65. Lang, X., Qian, L., Guan, P., Zi, J. & Chen, M. Localized surface plasmon resonance of nanoporous gold. *Appl. Phys. Lett.* **98**, 093701 (2011).

66. Malinsky, M. D., Kelly, K. L., Schatz, G. C. & Van Duyne, R. P. Chain Length Dependence and Sensing Capabilities of the Localized Surface Plasmon Resonance of Silver Nanoparticles Chemically Modified with Alkanethiol Self-Assembled Monolayers. *J. Am. Chem. Soc.* **123**, 1471–1482 (2001).

67. Xu, X. & Cortie, M. B. Shape Change and Color Gamut in Gold Nanorods, Dumbbells, and

Dog Bones. *Adv. Funct. Mater.* **16**, 2170–2176 (2006).

68. Homola, J. & Piliarik, M. Surface Plasmon Resonance (SPR) Sensors. in *Surface Plasmon Resonance Based Sensors* (ed. Homola, J.) vol. 4 45–67 (Springer Berlin Heidelberg, Berlin, Heidelberg, 2006).

69. Loke, V. L. Y., Pinar Mengüç, M. & Nieminen, T. A. Discrete-dipole approximation with surface interaction: Computational toolbox for MATLAB. *J. Quant. Spectrosc. Radiat. Transf.* **112**, 1711–1725 (2011).

70. Draine, B. T. & Flatau, P. J. Discrete-Dipole Approximation For Scattering Calculations. *J. Opt. Soc. Am. A* **11**, 1491 (1994).

71. Omrani, M., Mohammadi, H. & Fallah, H. Ultrahigh sensitive refractive index nanosensors based on nanoshells, nanocages and nanoframes: effects of plasmon hybridization and restoring force. *Sci. Rep.* **11**, 2065 (2021).

72. Funston, A. M., Novo, C., Davis, T. J. & Mulvaney, P. Plasmon Coupling of Gold Nanorods at Short Distances and in Different Geometries. *Nano Lett.* **9**, 1651–1658 (2009).

73. Kim, J. *et al.* Polymer-Grafted, Gold Nanoparticle-Based Nano-Capsules as Reversible Colorimetric Tensile Strain Sensors. *Small* **19**, 2300361 (2023).

74. Ishida, R., Hayashi, S., Yamazoe, S., Kato, K. & Tsukuda, T. Hydrogen-Mediated Electron Doping of Gold Clusters As Revealed by In Situ X-ray and UV–vis Absorption Spectroscopy. *J. Phys. Chem. Lett.* **8**, 2368–2372 (2017).

75. Matsuo, A., Hasegawa, S., Takano, S. & Tsukuda, T. Electron-Rich Gold Clusters Stabilized

by Poly(vinylpyridines) as Robust and Active Oxidation Catalysts. *Langmuir* **36**, 7844–7849 (2020).

76. Tsunoyama, H. & Tsukuda, T. Magic Numbers of Gold Clusters Stabilized by PVP. *J. Am. Chem. Soc.* **131**, 18216–18217 (2009).

CHAPTER 7. EFFECT OF TEMPERATURE ON POLYMER KINETICS INSIDE SEMI-CONFINED NANOCHANNEL

Content in this chapter will be submitted in 2024 to *Soft Matter*, with authors Weiwei Kong and Russell J. Composto. R.J.C and W.K conceived and planned for the project. W.K. developed the experimental procedures and carried all experimental measurements and analysis. W.K wrote the manuscript. R.J.C. edited the manuscript.

7.1 Introduction

Polymer nanocomposites (PNCs) have received a lot of attention in industry and academia [1–3] because of their enhanced properties, making them attractive materials for coatings [4,5], actuators [6], membranes [7,8], and optical response materials [9–11]. Typically, PNCs are fabricated by adding inorganic nanofillers (NF) into a polymeric matrix, thus imparting properties that the individual component alone does not possess. The resulting PNCs properties are closely tied to the NF geometry, dispersion, and percent loading [12–16]. Various NF shapes have been used to fabricate PNCs. For instance, studies have been conducted on adding nanoparticles into polymer blends, thus creating a unique domain size [17,18]. Additionally, studies have used gold nanorod self-assembly inside a polymer matrix to tune the absorption properties across the visible spectrum [10,11]. Although inorganic synthesis methods allow for various shapes beyond spheres (e.g. plates, cubes and rods), creating PNCs with a homogeneous dispersion at high percent NP loading remains challenging. The dispersion of NFs depends on the thermodynamics of mixing or kinetically arresting of NPs to prevent aggregation. A uniform dispersion at high loading of

NF is particularly challenging when interparticle NP spacings are on the order of NP. For instance, whereas the equilibrium spacing between nanoplates in a lamellar diblock copolymer was 6.4 nm [19], the maximum loading without disrupting the lamellae structure was only 0.05 vol% [19]. Thus, the traditional method for fabricating PNCs with a good dispersion typically results in low to moderate levels of NF loading.

To circumvent limited loading as well as the tendency for NF to aggregate, infiltration of polymer into inorganic scaffolds has been growing interesting. In a study where PS is infiltrated into TiO_2 NP packings, capillary rise infiltration (CaRI)[20], was developed. Starting with a bilayer, CaRI infiltrates the underlying polymer film into densely packed nanoparticle (NP) assembly by annealing above the polymer glass transition temperature (T_g) to allow the polymer to fill interstitial sites between particles. The present approach replaces the packed NPs with a bicontinuous nanoporous gold (NPG) scaffold. A significant difference is that the pore channels are continuous and uniform rather than the "bottle" neck structure in CaRI. The NPG is a combination of the AAO scaffold which exhibits continuous pores that are linear, and the CaRI packed system with a random array of interstitial pores. Using a NPG scaffold, high loading (>50 vol%) PNCs can be prepared with polymers that weakly and strongly interact with the confining gold surface.

Here we review results using the NPG scaffold, as well as relevant studies using AAO and CaRI approaches. Previously, infiltration of polymers with weak, polystyrene (PS), and strong, poly(2-vinylpyridine) (P2VP), interactions with NPG were investigated [21]. PS with molecular weights (M_w) from 424k Da to 1133k Da are infiltrated into a 120 nm thick NPG

scaffold, resulting in confinement ratios ($\Gamma = \frac{R_g}{R_p}$) range from 0.47 to 0.77 [21]. For this moderate confined scenario, PS infiltrates faster, and exhibits a weaker dependence on M_w compared to bulk predictions which is attributed to disentanglement and reduction in polymer-wall friction as M_w increases [21]. Under moderate confinement, P2VP infiltration exhibits slower kinetics compared to PS, which is attributed to the formation of a physisorbed layer of P2VP on the NPG pore. Using CaRI, extensive studies have also been conducted [20,22–29]. For instance, for entangled PS infiltrated into SiO_2 NP packings that results in Γ ranges between 0.5 to 60, it is found that an increase in the degree of polymer confinement enhances polymer chain dynamics while slows polymer segmental dynamics [22]. Kinetics of infiltration has also been conducted using anodized aluminum oxide (AAO) membranes [30–33]. For instance, the adsorption kinetics of cis-1,4-polyisoprene (PI) inside AAO (Γ = 0.02 - 0.345) membranes suggest that the adsorption time is strongly dependent on Γ [31]. Studies of the temperature dependence of (moderately) confined entangled polymers remain limited. The infiltration of unentangled PS (Γ = 0.7 and 1.1) and P2VP (Γ = 0.7 and 1.1) into SiO_2 NP packings suggests that unentangled polymers display a significant (~100x) increase in viscosity in confined pores, and simultaneously an increase in effective viscosity normalized by bulk viscosity that appears independent of temperature [25]. In this work, the temperature dependence of the effective viscosity of moderately confined and confined P2VP is studied.

Although the effect of confinement on the temperature dependence of polymer infiltration is not extensively investigated, the temperature dependence of the bulk viscosity is well known. The Williams-Landel-Ferry (WLF) equation describes the temperature dependence of polymer viscosity (η):

$$\frac{\eta}{\eta_0} = exp\left(\frac{B}{f_0}\frac{(T_0-T)}{(T-T_\infty)}\right) \qquad \text{Eq. 7.1}$$

where T_0 is the reference temperature corresponding to free volume f_0 and η_0, and T_∞ is the Vogel temperature. The WLF describes the temperature dependence over the range of T_g < T < T+100K [34]. The time scale shift factor $a_T = \frac{\eta}{\eta_0}$ is

$$log\ (a_T) = -\frac{C_1(T-T_r)}{(C_2+T-T_r)} \qquad \text{Eq. 7.2}$$

Here, C_1 and C_2 are related to physical properties, namely the free volume at T_g, f_g, and thermal expansion coefficient, α_f, such that $C_1 = \frac{B}{2.303 f_g}$ and $C_2 = \frac{f_g}{\alpha_f}$. The WLF equation enables the construction of a "master curve" of viscosity (and other viscoelastic properties) by shifting experimental data at different temperatures which allows for predicting polymer behavior over a wide range of temperature and time scales. To investigate the effect of confinement on temperature dependence, the WLF parameters from bulk P2VP will be compared to the WLF parameters determined from P2VP infiltration into NPG.

This present study investigates how confinement influences the temperature dependence of poly(2-vinylpyridine) (P2VP) infiltration into nanoporous gold (NPG) scaffolds with R_p of 27.5 nm. Two M_w of P2VP are used – P2VP-302k which is moderately confined (Γ = 0.55), and P2VP-940k which is more confined (Γ = 0.97). P2VP-302k and P2VP-940k are infiltrated into NPG at 130 - 160°C and 150 - 180°C, respectively. At all infiltration temperatures and both M_w's, the effective viscosities (η_{eff}) of P2VP are reduced as compared to the bulk viscosities (η_{bulk}) with the reduction being greatest for the Γ = 0.97 system. For the temperature range

studied, $\frac{\eta_{eff}}{\eta_{bulk}}$ remains relatively constant for each M_w with values of 0.66 (P2VP-302k) and 0.26 (P2VP-940k). The shift factor for the moderately confined P2VP-302k agrees with the bulk WLF prediction. However, the shift factor overshoots the WLF prediction for P2VP-940k which is attributed to a reduction in thermal expansion coefficient (α_f) under confinement. The apparent activation energy ($\triangle H_{aa}$) shows that $\triangle H_{aa,bulk} \simeq \triangle H_{aa,P2VP-302k} > \triangle H_{aa,P2VP-940k}$. The lower activation energy is consistent with the larger values of $\eta_{bulk} - \eta_{eff}$ observed for the P2VP-940k system. This study provides new insight into the temperature dependence of infiltration under moderately confined and confined conditions and thus allows for optimizing processing conditions to efficiently prepare nanocomposites at high filler loadings.

7.2 Materials and Methods

P2VP Bilayer Sample Preparation.

P2VP (M_w = 302k and 940k Da.) are dissolved in butanol (≥ 99.9 %, Sigma-Aldrich), and stirred overnight. The P2VP solutions (2.4 wt %) were spin-coated (4000 rpm, 60 seconds, Laurell Technologies) onto 1x1 cm^2 cleaned SiO_2 wafers and dried at 70 °C for 10 minutes to remove the residual solvent. All films were smooth and homogeneous as-cast. Film thickness was measured with a white-light reflectometer (Filmetrics F3-UV) and ranged from 120-150 nm. Nanoporous gold (NPG) with a pore radius of 27.5 nm and a thickness of 120 nm is used in this study. The NPG is deposited on top of the P2VP polymer film. The resulting bi-layer is then dried at 70 °C for 10 minutes to remove residual H_2O. More details about the bilayer sample preparation can be referred to our previous publications [21,35].

Atomic Force Microscopy (AFM).

Surface topography of the P2VP/NPG before and after full infiltration are measured using AFM. Tapping mode AFM was performed using Bruker Icon AFM with tips (TAP300AL-G-50 radius of curvature < 10 nm, Ted Pella). The images collected are 1*1 μm^2. The surface properties images were processed using Gwyddion software.

In-Situ Spectroscopic Ellipsometry (SE).

Spectroscopic ellipsometry (SE) (J.A. Woollam, Alpha SE) is used to measure the instant refractive index of the P2VP bilayer/ composite during the infiltration process. The SE measurement wavelength range is 380 - 900 nm. A Linkam THMSEL350V heating stage is used for in-situ heating. The precision of the heating stage is 0.1°C with respect to the set temperature. The heating rate is 30°C/min. The samples are heated to 70°C and held at this temperature for 5 minutes to ensure system equilibrium. Then, the temperature is heated at a rate of 30°C/min and then held at the targeted temperature to study infiltration. Because the bulk P2VP has T_g around 100°C, temperatures higher than 100°C will induce polymer infiltration into NPG. As a result, the infiltration time refers to the time after the heating stage reaches 100°C. During infiltration, the temperature is stably held at the targeted temperature. Effective Medium Approximation (EMA) Model with two material constitutes is used to capture the change in optical constants within the NPG composite as polymer fills the pores and approaches the top surface. The detailed SE modeling has been described in our previous publications [21,35]. The infiltration extent

(IE) is given by, $IE = \frac{(n_t - n_i)}{(n_f - n_i)}$. The initial refractive index, n_i , is calculated by averaging the refraction index values during the first six min (i.e., prior to the P2VP infiltration). The final refractive index (after complete infiltration), n_f, is calculated by averaging the refraction index during the last two minutes when infiltration is complete. The 80% infiltration time ($\tau_{80\%}$) used in the analysis is the time that the P2VP infiltration front reaches IE = 0.8.

Small Angle X-Ray Scattering (SAXS).

Dual Source and Environmental X-Ray Scattering (DEXS, Xenocs Xeuss 2.0) at the University of Pennsylvania is used for measuring the NPG ligament to ligament distance. Six tubes with sample to detector distance of 6390 mm results in a q_0 range of 0.003-0.09 $Å^{-1}$. Cu K_α, with a wavelength of 1.54 Å, is used as the light source. NPG samples are peeled off from the substrate using Kapton tape. The scattering data is collected for 20 mins for each sample. The collected spectra are then azimuthally integrated for analysis. A control scattering experiment from pure Kapton tape is also performed for 20 mins to eliminate contributions from the tape to the scattering curve.

Scanning Electron Microscopy (SEM).

FEI Quanta 600 SEM is used to detect the secondary electron signals at 15kV. The images are taken top-down to measure the ligament-ligament distance and in cross-section to measure the NPG thickness as well as infiltration extent. SEM images analysis also utilizes Gwyddion software.

7.3 Results and Discussion

The infiltration membrane, nanoporous gold (NPG), is pre-annealed to prevent structural coarsening during the annealing process. NPG was prepared by using HNO_3 to selectively etch Ag atoms from 12k Au/Ag alloy. The detailed procedure has been described in a previous publication [21]. NPG structure is subject to coarsening under conditions such as temperature treatments [36,37], exposure to chemicals [38,39], or ion beam irradiation [40] due to excessive surface energy [39]. The NPG coarsening rate has been reported to be non-uniform at different stages. At the early stages, NPG coarsening scales as $t^{0.25}$ because surface diffusion dominates coarsening [39,41–43], while later stage coarsening exhibits a slower rate [44,45] and scales as $t^{0.05}$. Previous research [35] has shown that pre-annealing NPG at elevated temperatures for an extended time prevents coarsening during the infiltration process. Because a temperature range of 130 to180℃ is used in this study, the NPG is pre-annealed at 180℃ for 12 h to ensure that the structure remains stable during P2VP infiltration.

The pore radii of as-prepared and pre-annealed NPG were determined by small angle x-ray scattering (SAXS). The ligament to ligament distance (d-spacing) of the bicontinuous NPG [44,46] is given by $d = 1.23 * \frac{2\pi}{q_{max}}$. Figure 7.1 shows the scattering intensity of as-prepared and pre-annealed NPG as a function of the scattering vector q. Both scattering patterns exhibit distinct peaks, with the pre-annealed peak shifted towards the lower q. In both cases, the intensity scales as q^{-4} at high q as shown in Figure 1. The as-prepared NPG exhibits a d-spacing of 80 nm while the pre-annealed NPG has a larger d-spacing of 110 nm. Because the NPG porosity is ~ 50% measured from previous works [21,35], and also through ellipsometry modeling, the pore radius

(R_p) is given by $R_p = \frac{d}{4}$. The pore radii for the as-prepared and pre-annealed NPG are 20nm and 27.5nm, respectively. In this study, only the annealed NPG (180°C for 12 h) will be used to study the temperature dependence of infiltration time for P2VP-302k and P2VP-940k. "NPG" refers to the pre-annealed NPG in the rest of the paper.

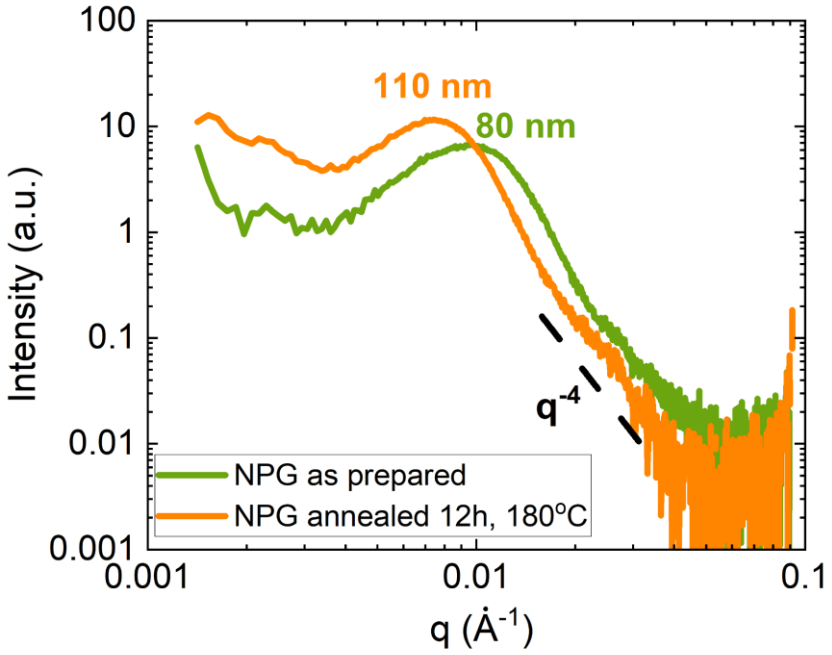

Figure 7.1. SAXS of as-prepared NPG and NPG pre-annealed at 180°C for 12 h. The scattering peak shifts to lower q upon thermal annealing. The d-spacings between ligaments increase from 80 nm to 110 nm upon annealing. At high q, the intensity scales as q^{-4}. The NPG thickness is 120 nm.

The P2VP used for infiltration are entangled with weight average molecular weights of 302k Da and 940 kDa and polydispersity (PDI). These polymers are denoted as P2VP-302k and P2VP-940k, respectively. The radius of gyration, $R_g = \sqrt{\frac{b^2N}{6}}$, is calculated from the Kuhn length,

b = 1.8 nm, and the number of Kuhn segments, $N = \frac{M_w}{M_o}$, using a Kuhn monomer molar mass of 720 Da [34]. The molecular characteristics and R_g values are listed in Table 7.1. For R_p = 27.5nm, the confinement ratios ($\Gamma = \frac{R_g}{R_p}$) of P2VP-302k and P2VP-940k are 0.55 and 0.97, respectively. Because Γ < 1, this study investigates infiltration under moderate confinement conditions. For P2VP in NPG, our previous study found that the critical molecular weight separating reduced and enhanced effective viscosity is $M_c = 180k\ Da$ which is greater than the bulk value of 47k Da. We attribute this larger value of M_c to a reduction in entanglement density due to the confining walls captured by MD simulations. Because P2VP-302k and P2VP-940k have M_w's well above 180k Da., P2VP infiltration in this study occurs in the entangled regime where the effective viscosity is expected to be less than the bulk values.

Table 7.1. Characteristics of the P2VP used in the study.

Sample	M_w (Da)	R_g (nm)	$\Gamma = R_g/R_p$
P2VP-302k	302,000	15.05	0.55
P2VP-940k	940,000	26.55	0.97

To complement SAXS, the NPG was also characterized using real space imaging, namely SEM and AFM. Figure 7.2 shows the SEM images of the NPG across a range of length scales as noted by the scale bars in Figures 7.2a, 7.2b and 7.2c, namely 3 μm, 1 μm, and 500 nm, respectively. At low magnification, Figure 7.2a shows a uniform bicontinuous morphology across a roughly 10 μm x 10μm area, with no large-scale defects (e.g. holes). At higher

magnification (Figures 7.2b and 7.2c), the pore diameters (dark) and ligaments (bright) become evident. Heterogeneity of pore size is observed with some pores being slightly smaller than the pore size determined from the characteristic length from SAXS. Qualitatively, the distribution of the NPG pore size observed by SEM is consistent with the breadth of the scattering peak from the pre-annealed NPG shown in Figure 7.1. Using line scans from SEM images in Figure 7.2c, $R_p = 28.6 \pm 3.2\,nm$, which is statistically similar to the SAXS value of 27.5nm. Figure 7.2d depicts the AFM height image of the NPG across a 2 μm x 2μm area. The height image also captures the heterogeneity of pore sizes and gives $R_p = 25.4 \pm 5.2\,nm$. In summary, the SEM and the AFM images yield values of R_p that are in statistical agreement with SAXS measurements. Additionally, NPG pore size has a narrow distribution of pore sizes as visualized by SEM/AFM characterization as well as the peak width of SAXS.

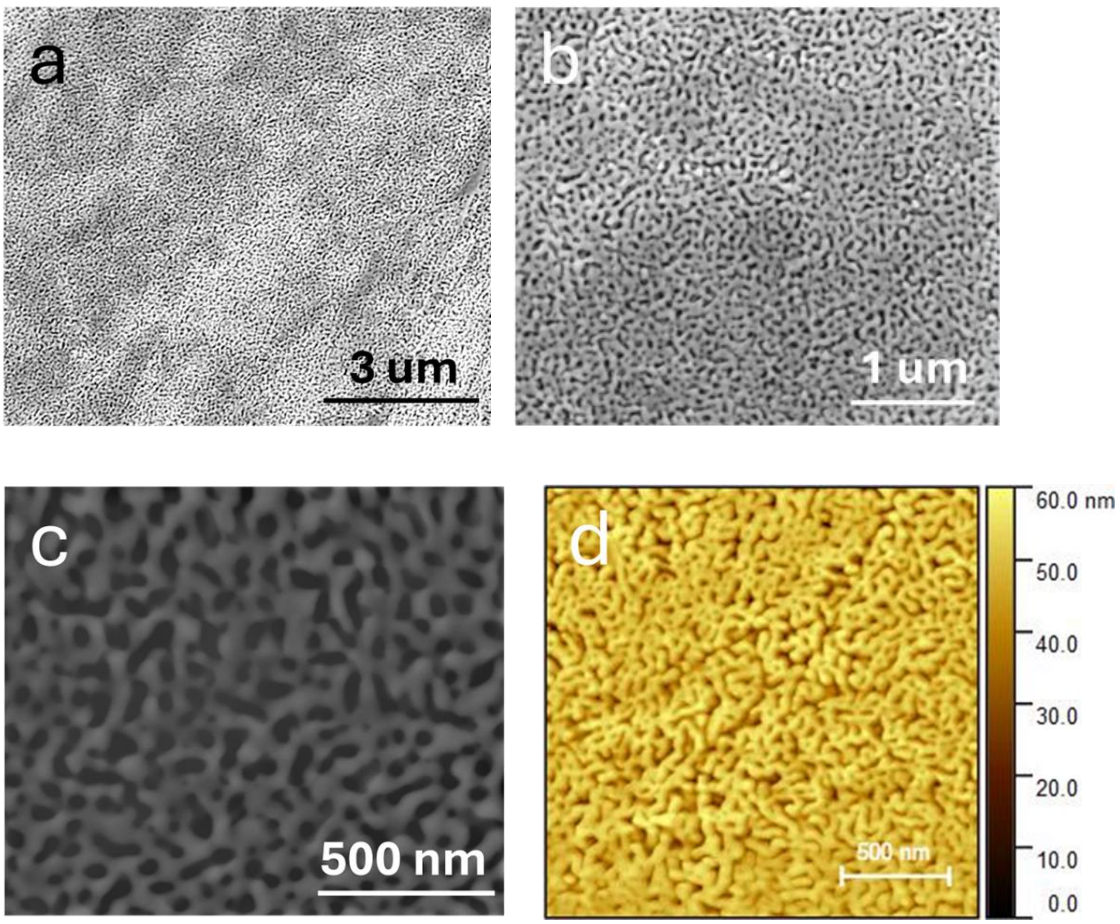

Figure 7.2. SEM images of pre-annealed NPG across different length scales. namely (a) 10 μm x 10 μm, (b) 5 μm x 5 μm and (c) 2 μm x 2 μm. The gold ligament and pores are the light and dark regions, respectively. (d) AFM topography image of NPG across 2 μm x 2 μm. The gold ligaments and pores are gold and dark, respectively.

The temperature dependence of P2VP infiltration through nanopores is described next. Figure 7.3 shows that infiltration time decreases strongly as temperature increases for P2VP-302k (green) and P2VP-940k (blue). The 80% infiltration time ($\boldsymbol{\tau}_{80\%}$) denotes the time for the underlying P2VP to reach a height of 80% of the NPG thickness, namely 96 nm. As shown in Figure 7.3, the $\boldsymbol{\tau}_{80\%}$ increases with M_w and reduced temperatures. As shown in our previous

publications, P2VP M_w is proportional to the infiltration rate such that $\boldsymbol{\tau}_{80\%} \sim M_w^{1.43}$, which agrees with Figure 7.3 that the higher the M_w is, the longer the $\boldsymbol{\tau}_{80\%}$ is. For instance, at 150°C, P2VP-302k possess a $\boldsymbol{\tau}_{80\%}$ of 16.81 mins, while P2VP-940k possess a $\boldsymbol{\tau}_{80\%}$ of 187.8 mins, which is almost 10x increase in time. Note that the $\boldsymbol{\tau}_{80\%}$ for P2VP-302k and P2VP-940k does not perfectly follow the precious publication trend of $\boldsymbol{\tau}_{80\%} \sim M_w^{1.43}$. This is due to the decreased pore size of the NPG, and increased fraction of smaller pores as shown in the AFM/SEM. The $\boldsymbol{\tau}_{80\%}$ also decreases non-linearly with reduced infiltration temperatures. P2VP-302k has a $\boldsymbol{\tau}_{80\%}$ of 590 min at 130°C, while the $\boldsymbol{\tau}_{80\%}$ is decreased 5x to 295 min at 135°C, and then decreased to 96.3 mins at 140°C. P2VP infiltration time inside NPG increases with enhanced M_w and decreased infiltration temperatures.

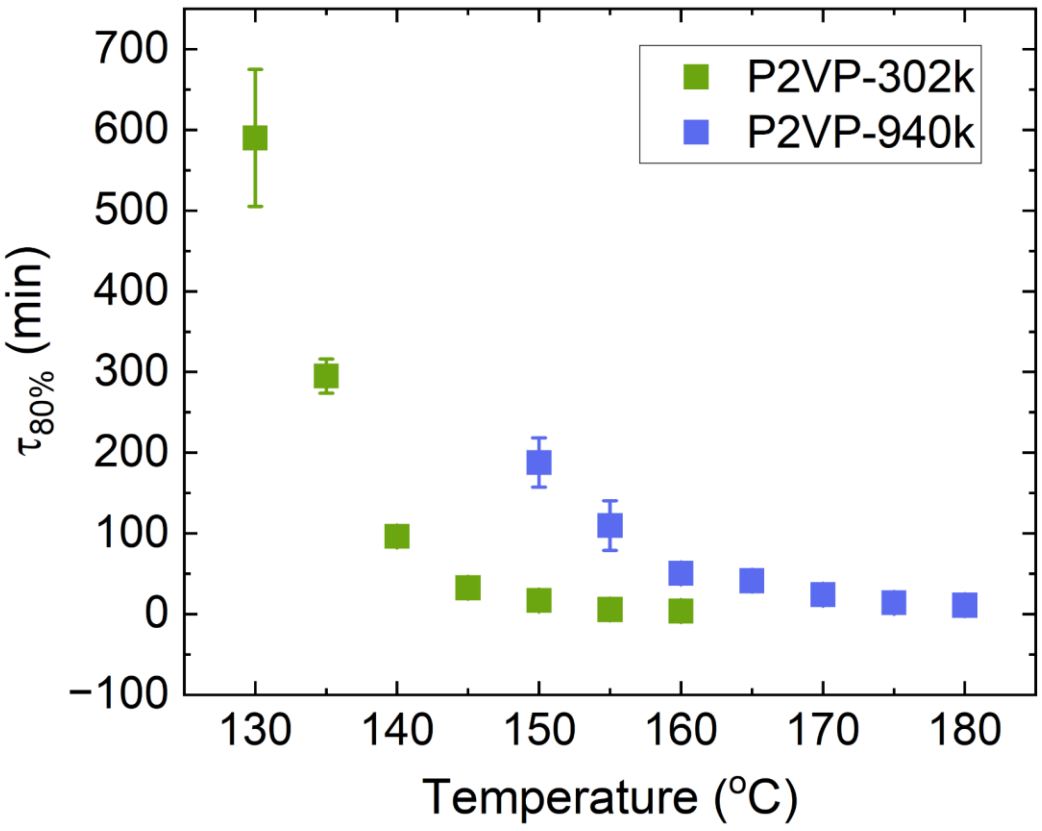

Figure 7.3. $\boldsymbol{\tau}_{80\%}$ versus P2VP-302k and P2VP-940k at different temperatures. P2VP-302k infiltrates at temperatures between 130 - 160°C, while P2VP-940k infiltrates at temperatures 150 - 180°C. $\boldsymbol{\tau}_{80\%}$ represents the infiltration time that the P2VP reaches 80% of the NPG height.

For P2VP-302k and P2VP-940k, the effective viscosities (η_{eff}) are lower than the bulk viscosities (η_{bulk}) at all temperatures. The η_{eff} can be calculated using a modified Lucas-Washburn Equation [47],

$$h^2 = \left(\frac{\Upsilon R_p \cos\theta}{4\,\eta_{eff}\,\sigma^2}\right) t \qquad \text{Eq. 7.3}$$

where the bulk fluid viscosity is replaced by the effective viscosity, η_{eff}. For the P2VP:NPG system, the Υ of P2VP is 37.9 mN/m [25], the average R_{pore} is 27.5 nm, σ is 1.5 [48], and θ between P2VP and gold [49] is 9°. Using these values, experimental data (e.g., Fig. 7.3) and Eq. 3, η_{eff} can be determined. As shown in Figure 7.4a, the P2VP-302k η_{eff} increases by over two orders of magnitude, from $1.8 * 10^6$ to $2.8 * 10^8$ $Pa * s$ as infiltration temperature decreases from 160°C to 130°C. For P2VP-940k, the η_{eff} increases from $5.18 * 10^6$ to $8.95 * 10^7$ $Pa * s$ as infiltration temperature decreases from 180°C to 150°C. η_{bulk} values were calculated from the literature [50]. For P2VP-302k, η_{bulk} increases from $3.00 * 10^6$ to $5.29 * 10^8$ $Pa * s$ as temperature decreases from 160°C to 130°C, whereas for P2VP-940k, η_{bulk} increases from $1.44 * 10^7$ to $6.17 * 10^8$ $Pa * s$ as temperature decreases from 180°C to 150°C. Figure 7.4a shows that at all temperatures for both M_w, η_{eff} is lower than the η_{bulk}. The difference ($\eta_{bulk} - \eta_{eff}$) is larger for P2VP-940k. This trend is reiterated by plotting the ratio ($\frac{\eta_{eff}}{\eta_{bulk}}$) as a function of temperature as shown in Figure 7.4b. In Figure 7.4b, $\frac{\eta_{eff}}{\eta_{bulk}}$ for both P2VP-302k and P2VP-940k at all temperatures are below 1. As previously noted, for P2VP infiltration into NPG, $\eta_{eff} > \eta_{bulk}$ for M_w < 180k Da, whereas $\eta_{eff} < \eta_{bulk}$ for M_w > 180k Da. In the present study, the M_w are 302k and 940k Da, which are above the threshold of 180k Da; thus, it is expected that the η_{eff} is lower than η_{bulk}. This study supports previous findings at a single temperature but shows that effective viscosity is more strongly reduced at a higher confinement ratio.

We further compare the behavior of $\frac{\eta_{eff}}{\eta_{bulk}}$ as a function of temperature for P2VP-302k and P2VP-940k. It is interesting to note that the η_{bulk} for P2VP-940k at 150°C ($6.17 * 10^8\ Pa * s$) and η_{bulk} for P2VP-302k at 130°C ($5.29 * 10^8\ Pa * s$) are similar to each other, but that η_{eff} for P2VP-940k is much lower than P2VP-302k. η_{eff} for P2VP-302k at 130°C is $2.81 * 10^8\ Pa * s$ while η_{bulk} for P2VP-940k at 150°C is $8.95 * 10^7\ Pa * s$, which is a decrease of nearly 4x. The change in η_{eff} with respect to η_{bulk} can be better visualized in Figure 7.4b where $\frac{\eta_{eff}}{\eta_{bulk}}$ for P2VP-940k is much lower than P2VP-302k. For P2VP-302k this ratio varies between 0.53 and 0.77 without any systematic trend with temperature. For P2VP-940k, the ratio is lower, slightly increasing from 0.15 to 0.36 as the temperature increases. This trend requires further exploration for systems with high confinement ratios over a broad temperature range. According to the previous research where the $\frac{\eta_{eff}}{\eta_{bulk}}$ is systematically studied as a function of M_w, as M_w increases, $\frac{\eta_{eff}}{\eta_{bulk}}$ decreases, which agrees with the two M_w trend in this study. However, interestingly, the $\frac{\eta_{eff}}{\eta_{bulk}}$ is relatively constant over its respective temperature range for P2PV-302k and P2VP-940k. CaRI studies of unentangled polystyrene (PS) and P2VP infiltrating into SiO_2 nanoparticle packings also found that $\frac{\eta_{eff}}{\eta_{bulk}}$ does not strongly depend on temperature, polymer-SiO_2 interfacial energy, and polymer M_w [25]. For P2VP-940k, the greater reduction in η_{eff} may be attributed to a lower fraction of highly absorbed chains on the NPG wall, which reduces the polymer-wall friction [21]. These studies show $\frac{\eta_{eff}}{\eta_{bulk}}$ remains relatively constant for P2VP-302k and P2VP-940k across the temperature range investigated and that η_{eff} is lower for the P2VP-940k system.

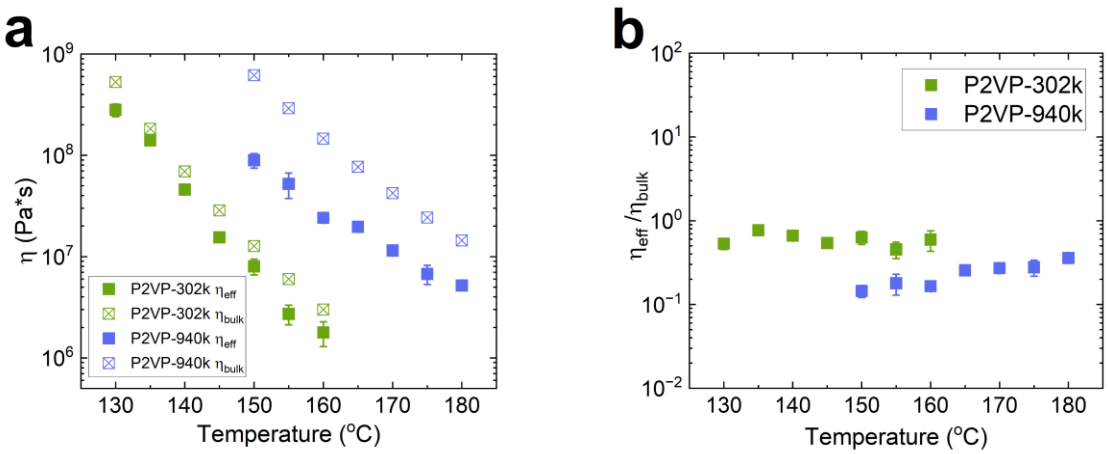

Figure 7.4. a. Effective viscosity (η_{eff}) and bulk viscosity (η_{bulk}) of P2VP-302k and P2VP-940k as a function of temperatures. η_{eff} are lower than η_{bulk} for all temperatures, implying that for both M_w P2VP travels faster in NPG as compared with in bulk. b. Using data from 4a, the ratio of $\frac{\eta_{eff}}{\eta_{bulk}}$ is plotted as a function of temperature. The ratio of $\frac{\eta_{eff}}{\eta_{bulk}}$ are below 1 for both M_w at all temperatures, and the $\frac{\eta_{eff}}{\eta_{bulk}}$ value decreases with M_w.

The temperature dependence of the shift factors, a_T, of P2VP-302k is next compared to the bulk behavior. Experimental a_T are calculated using $\frac{\eta_{eff,T}}{\eta_{eff,r}}$, where $\eta_{eff,T}$ is the effective viscosity at a given temperature in Figure 7.4, and the $\eta_{eff,r}$ is the effective viscosity at reference temperature, T_r = 160°C. The bulk P2VP log (a_T) can be calculated through the WLF equation with C1 and C2 parameters of 7.63 and 131.9 respectively [50]. Figure 7.5a shows log (a_T) plotted as a function of temperature for P2VP-302k (green), P2VP-940k (blue) and bulk P2VP (pink dotted line). The P2VP-302k shift factors (green) are in good agreement with literature values over the temperature range investigated. Figure 7.5b shows the best fits of the WLF shift factor predictions to the individual shift factors for P2VP-302k and P2VP-940k. In the WLF model,

C1 is related to the inverse of the free volume at T_g (C1 = $\frac{B}{2.303\, f_g}$), whereas C2 is the ratio of f_g to the thermal expansion coefficient (C2 = $\frac{f_g}{\alpha_f}$). The value of f_g is relatively constant across many polymers, ca. 0.0025 [34], and therefore in fitting log (a_T), C1 is kept constant while C2 is varied to optimize the fit. As shown in Figure 7.4b, the bulk parameters from the WLF are in good agreement with the P2VP-302k results where the best fit for C2 is 130.7 ± 2.1, in statistical agreement with the bulk C2 value of 131.9. As noted in Table 1, the P2VP-302k / NPG system has a Γ = 0.55, corresponding to moderately confined conditions for P2VP inside the pores. The agreement between bulk and measured shift factors suggests that moderate confinement does not perturb the thermal expansion coefficient (α) compared to the bulk. In summary, the bulk polymer temperature dependence behavior can be used to predict the viscosity dependence on temperature for moderately confined systems.

Infiltration of P2VP-940k into NPG indicates a reduced thermal expansion coefficient, and correspondingly a weaker dependence of viscosity on temperature. For P2VP-940k, Figure 7.5a shows that log (a_T) values are greater than WLF predicted values at high temperatures (i.e, 165℃ to 180℃). Figure 7.5b compares the experimental and WLF fit to log (a_T) using $C2_{P2VP-940k}$ = 220.9 ± 23.0 and $C2_{bulk}$= 131.9, respectively. The larger value of $C2_{P2VP-940k}$ captures the weaker temperature dependence of a_T and η_{eff}, which is captured in Figure 7.5b (blue symbols) and Figure 7.4a (solid blue symbols), respectively. We attribute this weaker dependence on temperature for P2VP-940k to the effect of confinement on thermal expansion. As shown in Table 1, the P2VP-940k / NPG system corresponds to a confined system where Γ = 0.97. Based on previous work, when P2VP infiltrates inside NPG, a physisorbed layer is formed.

As a result, the effective radius (R_{eff}) is reduced to $R_{eff} = R_p - \Delta R$. For P2VP-940k, R_g is 26.6 nm, whereas the NPG has a pore radius R_p = 27.5 nm (Figure 7.1). Including the formed physisorbed layer during infiltration, the confinement ratio (R_g/R_{eff}) is greater than 1, corresponding to a highly confined state where the infiltrating polymer down the center of the pore is strongly perturbed. Due to the high degree of confinement, the thermal expansion coefficient is reduced. A weaker temperature dependence would be accentuated at higher temperatures (further from T_g) as shown in Figures 7.4a (viscosity) and 7.5b (shift factors). Using $C2_{P2VP-940k} = 220.9 \pm 23.0$ and $f_g \cong 0.025$ [34], α_f is $1.13 * 10^{-4}$, which is less than that of bulk P2VP, $\alpha_f = 1.90 * 10^{-4}$. Thus, the weaker than expected temperature dependence of $\log(a_T)$ and η_{eff} is attributed to a reduction of the thermal expansion coefficient under high confinement conditions.

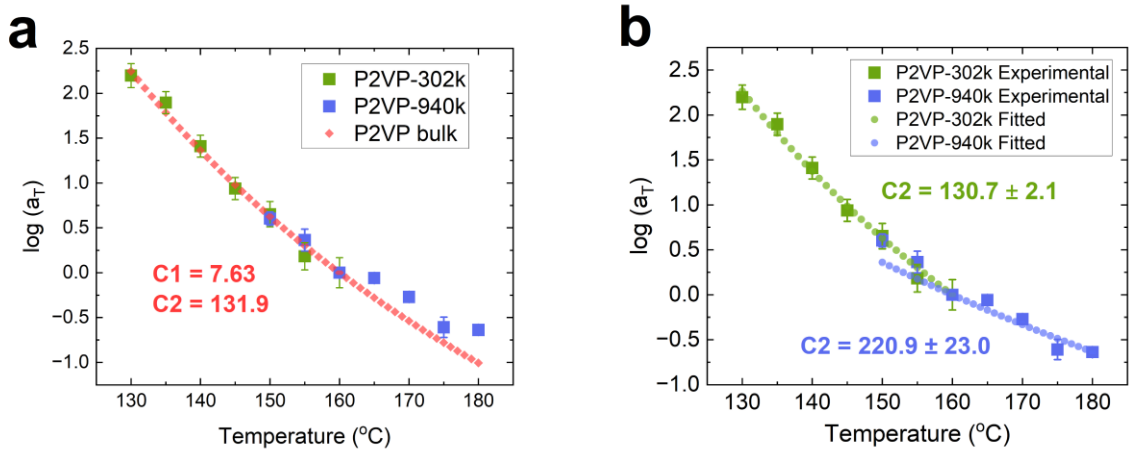

Figure 7.5. a. Temperature shift factor (a_T) of the P2VP-302k and P2VP-940k and compared with the bulk P2VP a_T. The bulk a_T agrees well for experimental P2VP-302k while is inconsistent with P2VP-940k. b. Experimental fit of the a_T while keeping C1 at the bulk value and varying C2. P2VP-940k exhibits a much enhanced C2 as compared to the bulk while P2VP-302k well agrees with the bulk C2.

The apparent activation energy ($\triangle H_{aa}$) is much lower for P2VP-940k, which partially accounts for the higher degree of enhanced kinetics as compared to P2VP-302k. The $\triangle H_{aa}$ can be expressed [51] through the derivative of ln a_T such that $\triangle H_{aa} = R * d\ lna_T/d\ (1/T)$, and through the differentiation, $\triangle H_{aa}$ can be calculated through the Equation 7.4 [51].

$$\triangle H_{aa} = \frac{2.303*R*C1*C2*T^2}{(C2+T-T_r)^2} \qquad \text{Eq. 7.4}$$

The Eq. 7.4 is found to be most reliable when $T - T_g$ is within 100℃ [51]. In this study, the temperature ranges is 130 - 180℃, and the P2VP T_g is 100℃ [50], thus this equation is applicable. As shown in the Figure 7.6, $\triangle H_{aa}$ for bulk P2VP, P2VP-302k in NPG, and P2VP-940k in NPG are plotted as a function of temperatures. The C2 analysis from Figure 7.5b are used to calculate and plot the P2VP in NPG $\triangle H_{aa}$. Since the $C2_{P2VP-302k}$ is statistically identical to the bulk, it is not surprising that the $\triangle H_{aa,P2VP-302k}$ aligns with the $\triangle H_{aa,P2VP\ bulk}$, implying that the energy barrier for P2VP to initiate movements within the system is almost the same for bulk P2VP and P2VP-302k. On the other hand, P2VP-940k in NPG exhibits a much reduced $\triangle H_{aa}$. For instance, $\triangle H_{aa,P2VP-302k} = 55.9\ kcal$ at 150℃ while $\triangle H_{aa,P2VP-940k} = 34.4\ kcal$, which is reduced by more than 30%. For the entire P2VP-940k temperature range (150-180℃), $\triangle H_{aa,P2VP-940k} < \triangle H_{aa,P2VP-302k}$. The much reduced $\triangle H_{aa,P2VP-940k}$ also accounts for the high $\eta_{bulk} - \eta_{eff}$ difference as indicated in Figure 7.4a. Activation energy is reduced for P2VP-940k, which results in the enhanced kinetics and reduced viscosity.

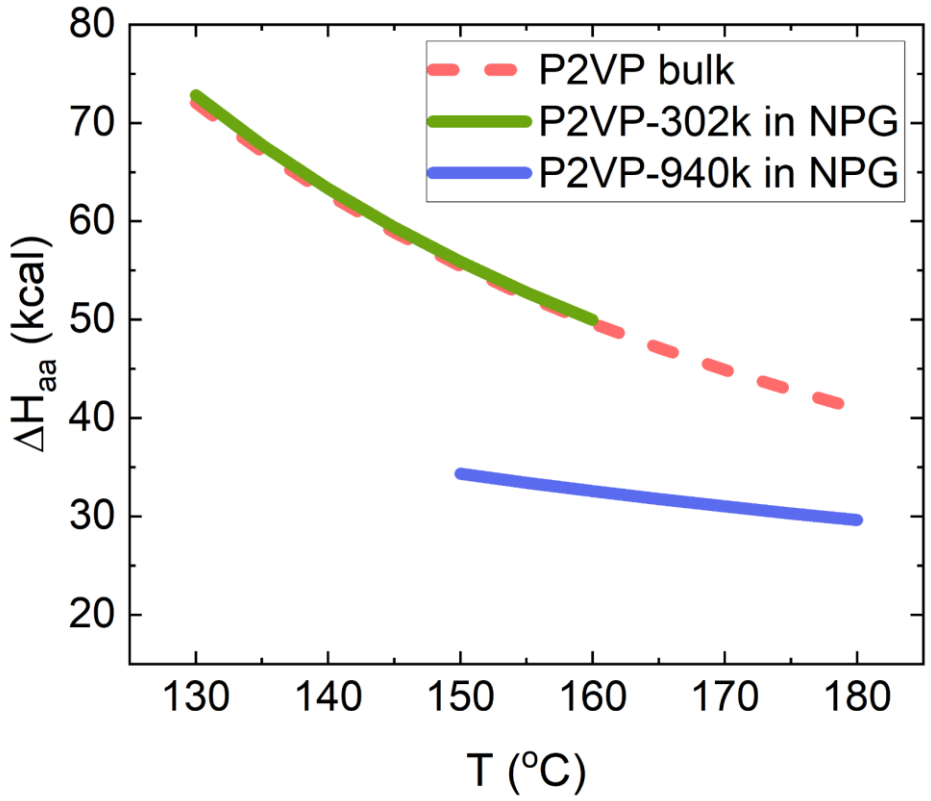

Figure 7.6. Apparent activation energy ($\triangle H_{aa}$) for bulk P2VP, P2VP-302k inside NPG, and P2VP-940k inside NPG. The reference temperature (T_r) for this calculation is 160°C. The $\triangle H_{aa}$ is much lower for P2VP-940k as compared to bulk P2VP and P2VP-302k.

7.4 Conclusion

In this work, poly(2-vinylpyridine) (P2VP) infiltration kinetics inside nanoporous gold (NPG) at different temperatures are investigated and analyzed. P2VP-302k (Γ = 0.55) and P2VP-940k (Γ = 0.97) are used to infiltrate into NPG at 130 - 160℃, and 150 - 180℃ respectively. The 80% infiltration times ($\boldsymbol{\tau}_{80\%}$) exhibit a nonlinear relationship with the temperature such that as temperature decreases, $\boldsymbol{\tau}_{80\%}$ increases. To better understand the infiltration kinetics in NPG at different temperatures, effective viscosity (η_{eff}) are calculated. η_{eff} for both M_w at all infiltration temperatures are reduced as compared to the bulk viscosity (η_{bulk}), implying that P2VP kinetics inside NPG is faster than in bulk. Additionally, η_{eff} is found to decrease with enhanced M_w while $\frac{\eta_{eff}}{\eta_{bulk}}$ remains relatively stable for each individual M_w across the experimental temperature range. The WLF analysis shows that the moderately confined P2VP-302k well agrees with the bulk P2VP WLF prediction, implying bulk WLF parameters can accurately predict the temperature dependence for weakly confined polymers. On the other hand, P2VP-940k deviates from the bulk WLF parameters, and additionally analysis shows that P2VP-940k exhibits a much enhanced C2 parameter, originated from the reduced thermal expansion coefficient (α_f), due to the P2VP-940k being more confined in spacing. Lastly, the apparent activation energy ($\triangle H_{aa}$) for P2VP-940k is found to be much smaller than that of P2VP-302k and the bulk P2VP, which explains for the much enhanced kinetics and the bigger difference in $\eta_{bulk} - \eta_{eff}$. This study enables a better understanding of temperature dependence of polymer kinetics under different degrees of confinement, providing insights of preparing nanocomposites at high filler loadings.

7.5 References

1. Balazs, A. C., Emrick, T. & Russell, T. P. Nanoparticle Polymer Composites: Where Two Small Worlds Meet. *Science* **314**, 1107–1110 (2006).

2. Guth, E. Theory of Filler Reinforcement. *J. Appl. Phys.* **16**, 20–25 (1945).

3. Kim, J. *et al.* Estimation of the concentration of nano-carbon black in tire-wear particles using emission factors of PM10, PM2.5, and black carbon. *Chemosphere* **303**, 134976 (2022).

4. Bilchak, C. R., Huang, Y., Benicewicz, B. C., Durning, C. J. & Kumar, S. K. High-Frequency Mechanical Behavior of Pure Polymer-Grafted Nanoparticle Constructs. *ACS Macro Lett.* **8**, 294–298 (2019).

5. Rittigstein, P. & Torkelson, J. M. Polymer-nanoparticle interfacial interactions in polymer nanocomposites: Confinement effects on glass transition temperature and suppression of physical aging: Polymer-Nanoparticle Interfacial Interactions. *J. Polym. Sci. Part B Polym. Phys.* **44**, 2935–2943 (2006).

6. Liu, Y. *et al.* Electro-thermal actuation in percolative ferroelectric polymer nanocomposites. *Nat. Mater.* **22**, 873–879 (2023).

7. Bilchak, C. R. *et al.* Polymer-Grafted Nanoparticle Membranes with Controllable Free Volume. *Macromolecules* **50**, 7111–7120 (2017).

8. Merkel, T. C. *et al.* Ultrapermeable, Reverse-Selective Nanocomposite Membranes. *Science* **296**, 519–522 (2002).

9. Glor, E. C., Ferrier, R. C., Li, C., Composto, R. J. & Fakhraai, Z. Out-of-plane orientation alignment and reorientation dynamics of gold nanorods in polymer nanocomposite films. *Soft Matter* **13**, 2207–2215 (2017).

10. Hore, M. J. A. & Composto, R. J. Nanorod Self-Assembly for Tuning Optical Absorption. *ACS Nano* **4**, 6941–6949 (2010).

11. Hore, M. J. A., Frischknecht, A. L. & Composto, R. J. Nanorod Assemblies in Polymer Films and Their Dispersion-Dependent Optical Properties. *ACS Macro Lett.* **1**, 115–121 (2012).

12. Takahashi, S. & Paul, D. R. Gas permeation in poly(ether imide) nanocomposite membranes based on surface-treated silica. Part 1: Without chemical coupling to matrix. *Polymer* **47**, 7519–7534 (2006).

13. Chevigny, C. *et al.* Polymer-Grafted-Nanoparticles Nanocomposites: Dispersion, Grafted Chain Conformation, and Rheological Behavior. *Macromolecules* **44**, 122–133 (2011).

14. Natarajan, B., Li, Y., Deng, H., Brinson, L. C. & Schadler, L. S. Effect of Interfacial Energetics on Dispersion and Glass Transition Temperature in Polymer Nanocomposites. *Macromolecules* **46**, 2833–2841 (2013).

15. Wagner, H. D. & Vaia, R. A. Nanocomposites: issues at the interface. *Mater. Today* **7**, 38–42 (2004).

16. Schadler, L. S., Brinson, L. C. & Sawyer, W. G. Polymer nanocomposites: A small part of the story. *JOM* **59**, 53–60 (2007).

17. Maguire, S. M., Chung, H.-J. & Composto, R. J. Polymer Blend Systems With an Added Solvent. in *Bijels* (ed. Clegg, P. S.) 73–113 (The Royal Society of Chemistry, 2020). doi:10.1039/9781839160974-00073.

18. Chung, H., Ohno, K., Fukuda, T. & Composto, R. J. Self-Regulated Structures in Nanocomposites by Directed Nanoparticle Assembly. *Nano Lett.* **5**, 1878–1882 (2005).

19. Krook, N. M. *et al.* Alignment of Nanoplates in Lamellar Diblock Copolymer Domains and the Effect of Particle Volume Fraction on Phase Behavior. *ACS Macro Lett.* **7**, 1400–1407 (2018).

20. Huang, Y.-R. *et al.* Polymer nanocomposite films with extremely high nanoparticle loadings via capillary rise infiltration (CaRI). *Nanoscale* **7**, 798–805 (2015).

21. Kong, W. *et al.* Capillary filling dynamics of polymer melts in a bicontinuous nanoporous scaffold. *J. Chem. Phys.* **160**, 044904 (2024).

22. Venkatesh, R. B. & Lee, D. Conflicting Effects of Extreme Nanoconfinement on the Translational and Segmental Motion of Entangled Polymers. *Macromolecules* **55**, 4492–4501 (2022).

23. Venkatesh, R. B. & Lee, D. Interfacial Friction Controls the Motion of Confined Polymers in the Pores of Nanoparticle Packings. *Macromolecules* **55**, 8659–8667 (2022).

24. Venkatesh, R. B. *et al.* Effect of polymer–nanoparticle interactions on solvent-driven infiltration of polymer (SIP) into nanoparticle packings: a molecular dynamics study. *Mol. Syst. Des. Eng.* **5**, 666–674 (2020).

25. Hor, J. L., Wang, H., Fakhraai, Z. & Lee, D. Effects of polymer–nanoparticle interactions on the viscosity of unentangled polymers under extreme nanoconfinement during capillary rise infiltration. *Soft Matter* **14**, 2438–2446 (2018).

26. Qiang, Y., Pande, S. S., Lee, D. & Turner, K. T. The Interplay of Polymer Bridging and Entanglement in Toughening Polymer-Infiltrated Nanoparticle Films. *ACS Nano* **16**, 6372–6381 (2022).

27. Qiang, Y., Turner, K. T. & Lee, D. Role of Polymer–Nanoparticle Interactions on the Fracture Toughness of Polymer-Infiltrated Nanoparticle Films. *Macromolecules* **56**, 122–135 (2023).

28. Ren, T. *et al.* Increase in the effective viscosity of polyethylene under extreme nanoconfinement. *J. Chem. Phys.* **160**, 024909 (2024).

29. Hor, J. L., Wang, H., Fakhraai, Z. & Lee, D. Effect of Physical Nanoconfinement on the Viscosity of Unentangled Polymers during Capillary Rise Infiltration. *Macromolecules* **51**, 5069–5078 (2018).

30. Shin, K. *et al.* Enhanced mobility of confined polymers. *Nat. Mater.* **6**, 961–965 (2007).

31. Tu, C.-H., Zhou, J., Butt, H.-J. & Floudas, G. Adsorption Kinetics of *cis* -1,4-Polyisoprene in Nanopores by *In Situ* Nanodielectric Spectroscopy. *Macromolecules* **54**, 6267–6274 (2021).

32. Tu, C.-H., Zhou, J., Doi, M., Butt, H.-J. & Floudas, G. Interfacial Interactions During In Situ Polymer Imbibition in Nanopores. *Phys. Rev. Lett.* **125**, 127802 (2020).

33. Yao, Y., Butt, H.-J., Zhou, J., Doi, M. & Floudas, G. Capillary Imbibition of Polymer Mixtures in Nanopores. *Macromolecules* **51**, 3059–3065 (2018).

34. Rubinstein, M. & Colby, R. H. *Polymer Physics*. (Oxford University Press, Oxford ; New York, 2003).

35. Maguire, S. M. *et al.* Effect of Nanoscale Confinement on Polymer-Infiltrated Scaffold Metal Composites. *ACS Appl. Mater. Interfaces* **13**, 44893–44903 (2021).

36. Biener, M. M. *et al.* ALD Functionalized Nanoporous Gold: Thermal Stability, Mechanical Properties, and Catalytic Activity. *Nano Lett.* **11**, 3085–3090 (2011).

37. Li, Y., Hart, J. L., Taheri, M. L. & Snyder, J. D. Morphological Instability in Topologically Complex, Three-Dimensional Electrocatalytic Nanostructures. *ACS Catal.* **7**, 7995–8005 (2017).

38. Fujita, T. *et al.* Atomic Observation of Catalysis-Induced Nanopore Coarsening of

Nanoporous Gold. *Nano Lett.* **14**, 1172–1177 (2014).

39. Ng, A. K., Welborn, S. S. & Detsi, E. Time-dependent power law function for the post-dealloying chemical coarsening of nanoporous gold derived using small-angle X-ray scattering. *Scr. Mater.* **206**, 114215 (2022).

40. Gomes, D. R., Turkin, A. A., Vainchtein, D. I. & De Hosson, J. Th. M. Bending of nanoporous thin films under ion radiation. *Thin Solid Films* **688**, 137419 (2019).

41. Lilleodden, E. T. & Voorhees, P. W. On the topological, morphological, and microstructural characterization of nanoporous metals. *MRS Bull.* **43**, 20–26 (2018).

42. Hu, K., Ziehmer, M., Wang, K. & Lilleodden, E. T. Nanoporous gold: 3D structural analyses of representative volumes and their implications on scaling relations of mechanical behaviour. *Philos. Mag.* **96**, 3322–3335 (2016).

43. Welborn, S. S., Van Der Meer, S., Corsi, J. S., De Hosson, J. Th. M. & Detsi, E. Using X-Ray Scattering to Elucidate the Microstructural Instability of 3D Bicontinuous Nanoporous Metal Scaffolds for Use in an Aperiodic 3D Tricontinuous Conductor–Insulator–Conductor Nanocapacitor. *ACS Appl. Mater. Interfaces* **13**, 11721–11731 (2021).

44. Welborn, S. S., Van Der Meer, S., Corsi, J. S., De Hosson, J. Th. M. & Detsi, E. Using X-Ray Scattering to Elucidate the Microstructural Instability of 3D Bicontinuous Nanoporous Metal Scaffolds for Use in an Aperiodic 3D Tricontinuous Conductor–

Insulator–Conductor Nanocapacitor. *ACS Appl. Mater. Interfaces* **13**, 11721–11731 (2021).

45. Wittstock, A., Biener, J. & Bäumer, M. Nanoporous gold: a new material for catalytic and sensor applications. *Phys. Chem. Chem. Phys.* **12**, 12919 (2010).

46. Michels, A. & Weissmüller, J. Magnetic-field-dependent small-angle neutron scattering on random anisotropy ferromagnets. *Rep. Prog. Phys.* **71**, 066501 (2008).

47. Masoodi, R., Pillai, K. M. & Varanasi, P. P. Darcy's law-based models for liquid absorption in polymer wicks. *AIChE J.* **53**, 2769–2782 (2007).

48. Luo, J.-W. *et al.* Macroscopic transport properties of Gyroid structures based on pore-scale studies: Permeability, diffusivity and thermal conductivity. *Int. J. Heat Mass Transf.* **146**, 118837 (2020).

49. Kunz, M. S., Shull, K. R. & Kellock, A. J. Colloidal Gold Dispersions in Polymeric Matrices. *J. Colloid Interface Sci.* **156**, 240–249 (1993).

50. Takahashi, Y., Ochiai, N., Matsushita, Y. & Noda, I. Viscoelastic Properties of Poly(2-vinylpyridine) in Bulk and Solution. *Polym. J.* **28**, 1065–1070 (1996).

51. Williams, M. L., Landel, R. F. & Ferry, J. D. The Temperature Dependence of Relaxation Mechanisms in Amorphous Polymers and Other Glass-forming Liquids. *J. Am. Chem. Soc.* **77**, 3701–3707 (1955).

CHAPTER 8. CONCLUSIONS AND FUTURE DIRECTIONS

8.1 Conclusions and Broader Future Directions

Understanding the polymer kinetics under confinement while fabricating an ultra-high nanofiller loading polymer nanocomposites (PNCs) is critical for industrial applications and the next generation advanced materials. To reach the high loading of PNCs, we utilized nanoporous gold (NPG) as the starting membrane template and infiltrated polymer inside to fabricate polymer infiltrated nanoporous gold (PING). These high loading PNCs possess enhanced mechanical properties [1], as well as unique optical properties [2,3] and structure and material stabilization [4].

This thesis presents fundamental science research on polymer kinetics under confinement and tunable optical properties of the resulting PNCs. In chapter 1-3, the general introduction, theoretical background for better understanding the thesis, and the experimental methods and characterization techniques are presented. In chapter 4, the polystyrene (PS) infiltration kinetics inside moderately confined NPG with a weak polymer-wall interfacial energy is investigated. Followed by chapter 4, chapter 5 delves into the poly(2-vinylpyridine) (P2VP) kinetics inside NPG, which possess a stronger polymer-wall interfacial energy. By the studies of chapter 4 and 5, the effect of interfacial energy on the polymer kinetics are well studied, extending PING for new possibilities for stimuli-response and ion conductive membranes. Chapter 6 introduces UV-Vis as a novel and facile tool to track polymer kinetics inside NPG. The optical properties of P2VP infiltrated NPG at different infiltration extents are measured and simulated, introducing this novel type of PNCs for optical sensing membranes. Chapter 7 investigates the temperature effect of the P2VP kinetics inside NPG. It is found that as the polymer is moderately confined,

the temperature dependence follows the bulk WLF performance; however when the polymer is more confined, the WLF parameter deviates from the bulk. The temperature dependence enables further machine learning studies and better predictions of PING fabrication processes under different conditions. The current chapter 8 discusses the future directions of the NPG-derived PNCs that are worth investigating.

8.2 Polymer grafted NPG

In this section, the polymer grafted NPG fabrication and characterization will be first introduced, followed by the future research directions of the grafted NPG membranes. Section 8.2.1 presents successful fabrication of 47k Da PEO graft onto the NPG (R_p = 27.5 nm). The grafting-to mechanism utilizes the thiol-gold chemistry. The successful grafting of linear PEO inspires future directions to graft loop, and interlocked loops to the NPG, which opens up doors for future advanced studies in polymer kinetics, stability and mechanical performances.

8.2.1 Polymer grafted NPG Fabrication and Characterization

Inspired by the thiol-gold chemistry, we fabricated polymer grafted NPG which enables plenty of future research. When a thiol molecule interacts with the gold surface, a strong covalent bond forms in between the sulfur end and the gold surface, thus forming self-assembled monolayers (SAMs) [5,6]. The thiolate SAMs on gold have found various applications in fields such as sensing [7], electronics [8] and surface patterning [9]. This section focuses on the use of thiol-gold chemistry to fabricate polymer-grafted NPG, which allows future research on polymer kinetics with modified surface interfacial energy. In the following section, the detailed logistics

of the polymer grafted NPG will be introduced and the future research directions will be discussed.

The polymer grafted NPG are first studied on a 2D flat surface. SH-PEO (M_w = 47 kDa) are dissolved in DI-H_2O with concentrations of 0.1 - 0.5 uM. Then, QCM measurements were performed using a flat gold quartz crystal and the frequency measurement is shown in the following Figure 8.1. The first 6 minutes were used to reach the equilibrium baseline, then the gold crystal started to be exposed to the SH-PEO solution. The change in frequency (Δf) rapidly decreases from t = 6 min to t = 10 mins, implying a fast bonding process. Then, after the Δf is completely stabilized (t = 29 min), DI-H_2O is used to rinse off the extra unbonded SH-PEO, which resulted in the little increase of Δf between t = 29 min to t = 40 min. After the unbonded polymer is completely rinsed off, the Δf is stabilized to ~ 13 Hz. The grafting density can thus be calculated using the Saubery Equation mentioned in Chapter 3. As the SH-PEO grafts onto the QCM gold crystal, the contact angle dramatically decreases. Before PEO grafting, the Au flat surface [10] is reported to have a contact angle of 64.4° while after grafting the contact angle decreases to 46.4°. SH-PEO grafting density onto gold surfaces is quantified using QCM and the water contact angle decreases upon grafting.

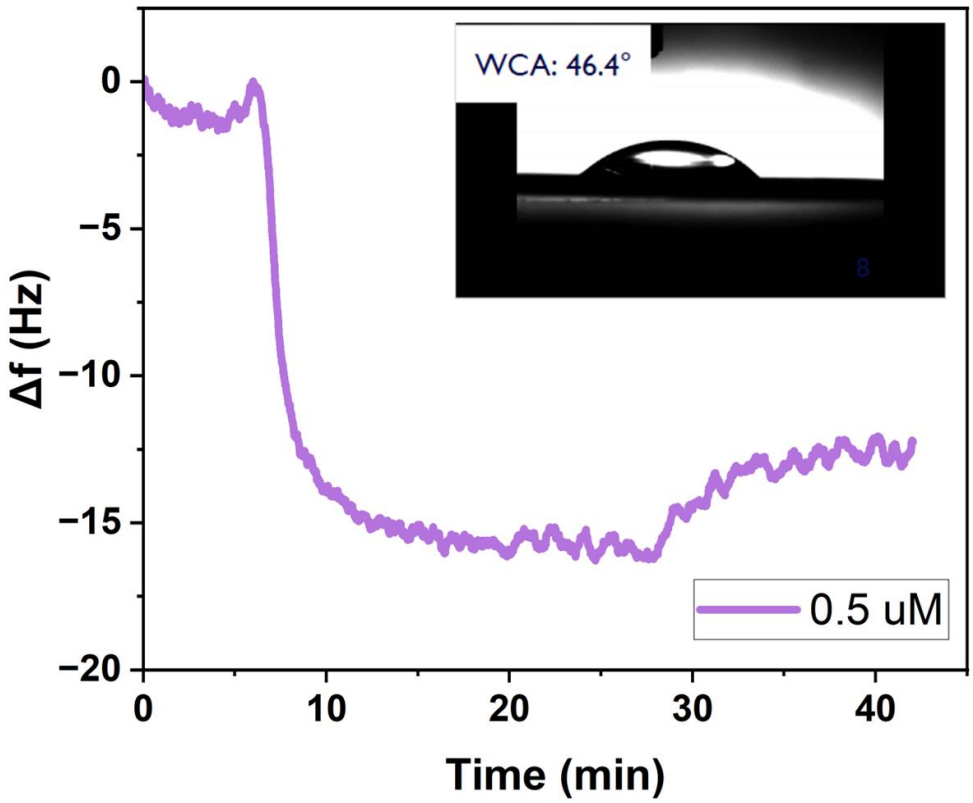

Figure 8.1. QCM-D measurement of 0.5 uM SH-PEO solution grafting onto planar Au QCM sensor. The inserted image is the resulting water contact angle measurement after the complete grafting.

The grafting densities, as well as the contact angles, are relatively consistent for SH-PEO grafting concentration of 0.1 - 0.5 uM given long enough time to equilibrate. As shown below in Table 8.1, the grafting density is relatively stable at 0.13 chains/nm^2, implying that at those concentration regimes, grafting density is independent of polymer concentration. The water contact angle, similarly, also implies a stable grafting density. By extrapolating the 2D flat gold

surface into the 3D gold surface (NPG), the NPG also experiences a stabilized grafting density in the concentration range of 0.1 - 0.5 uM.

Table 8.1. Grafting density and water contact angle at different grafting concentrations given a long even time. The grafting density and contact angle appears to be relatively consistent, being at 0.13 chains/nm^2 and 46^o respectively.

Concentration	Grafting Density (chains/nm^2)	Contact Angle
0.5 uM	0.147	45.5°
0.5 uM	0.135	44.3°
0.5 uM	0.103	46.4°
0.3 uM	0.166	46.2°
0.3 uM	0.145	46.9°
0.3 uM	0.107	45.6°
0.1 uM	0.151	46.3°
0.1 uM	0.117	44.8°
0.1 uM	0.122	46.5°

The thickness of the 47k Da. SH-PEO graft is measured to be 10.5 nm on a flat gold surface. The thickness of the SH-PEO on a gold wafer is measured by x-ray reflectivity (XRR) as shown in the following Figure 8.2. The gold wafer, where the SH-PEO is grafted to, is made by sputter coat ~ 50 nm gold nanoparticles on top of the silicon wafer. The fitting of the XRR results well captures the gold wafer nature, which is evidenced by 51.1 nm of gold coating atop of Si wafer as shown in Figure 8.2, validating the precision and accuracy of the fit. The PEO layer thickness is measured to be 10.5 nm, with a roughness of 1.8 nm. The calculated R_g of the PEO is 8.32 nm, with b = 1.1 nm and M_o = 137 g/mol [11]. Since $2R_g$ > PEO height, it can be implied

that the PEO grafts are in mushroom form, where the PEO melt chains collapse together towards the gold surface. Similarly, the PEO height information is carried over to PEO-NPG system.

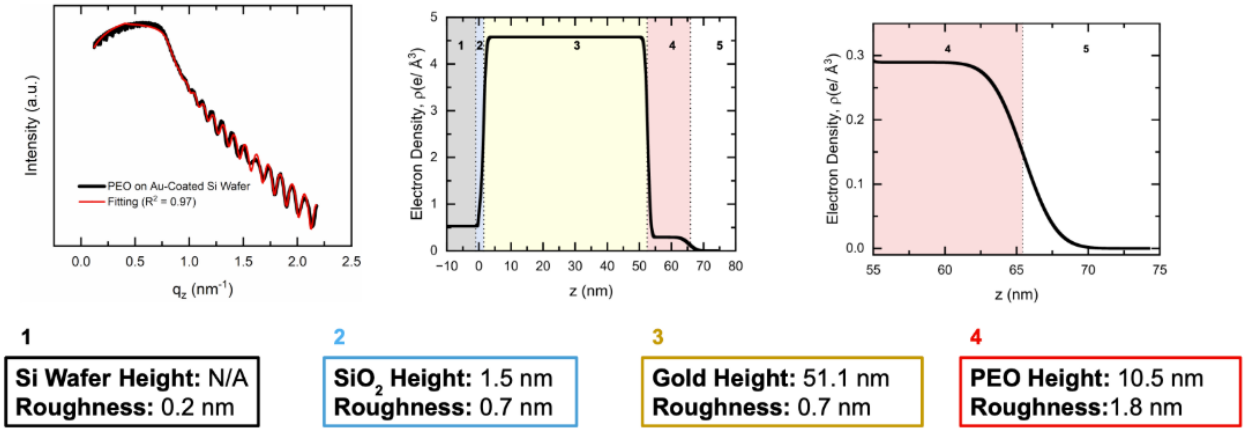

Figure 8.2. XRR analysis of SH-PEO grafted gold wafer. The analysis shows the SH-PEO graft thickness is 10.5 nm.

After quantifying the grafting density and the grafting thickness on the planar gold surface, SH-PEO is grafted onto the 3D bicontinuous NPG. Because the NPG is 50 vol% porous and it is hydrophilic, NPG can be lifted off from the glass substrate easily when in contact with water solution. To prevent NPG from detaching the substrate surface, a thin layer of 900k PS is spin coated onto the glass substrate and is annealed at 150°C for 1 min to induce ~5% infiltration extent inside NPG. The 5% infiltrated PS serves as an adhesive layer that well binds the substrate and the NPG together, even with the presence of water solution. Subsequently, the 5% infiltrated NPG are immersed into SH-PEO solutions for grafting for 24 h. After 24 h, the grafted samples are immersed into water for 10 min to remove unbonded polymer chains on the surface. After each of the precedingly described steps, the absorbance spectra are taken as shown in Figure 8.3. The plain NPG has a relatively weak peak, with the peak wavelength at 513 nm. After the PS

thin film is deposited underneath and infiltrates 5% inside the NPG, the peak wavelength increases to 520 nm and the peak shape becomes more apparent. The 5% PS infiltrated NPG is then immersed into SH-PEO solution of 0.1 uM and 0.05 uM concentration, followed by a complete water rinsing afterwards. Both 0.05uM and 0.1 uM grafting on NPG ligament induce a blue shift in absorbance peak position, from 520 nm to 515 nm. The change in the absorbance spectra implies that the SH-PEO has been successfully grafted onto the NPG.

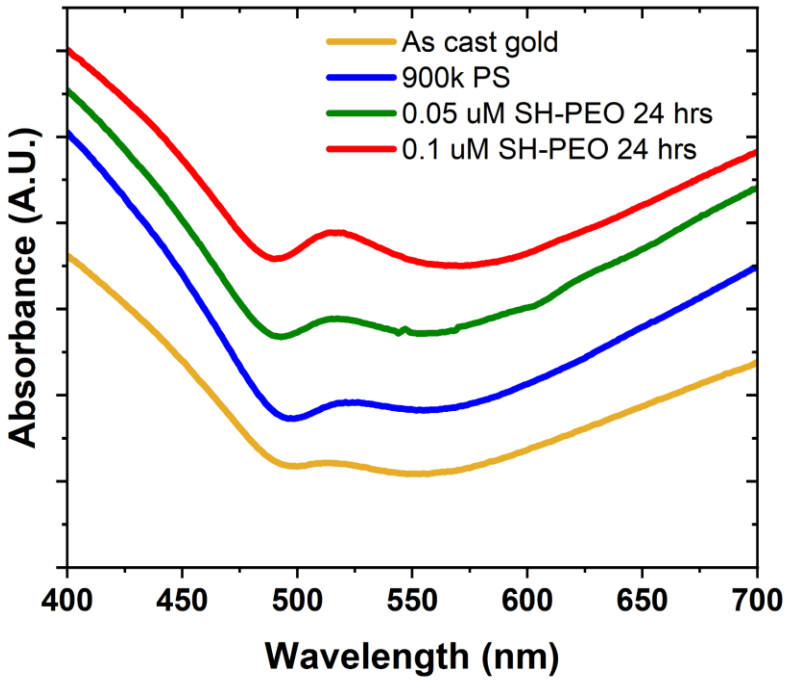

Figure 8.3. Absorbance spectra of plain gold, 900k-PS, SH-PEO grafted NPG at different concentrations.

To further investigate the effect of grafting thickness on absorbance spectra, DDA simulations are performed as shown in Figure 8.4. In the DDA simulation, a brush resembling P2VP (n = 1.54) is grafted onto the T shape gold ligament (described in Chapter 6) with

thickness varying between 0 to 15 nm. The brush is set to fully cover the T-shaped gold surface. As shown in Figure 8.4a, as the brush thickness increases, the peak gradually undergoes a red shift, and the shape becomes more apparent. When no P2VP brush is grafted to the surface, the absorbance spectra exhibit a peak position at 515 nm, while when the grafting thickness increases to 15 nm, the peak increases to 522 nm. As shown in Figure 8.4b, the peak position initially increases linearly with bigger grafting thickness, but when thickness reaches 10 nm, the boundary effect of grafting thickness on peak position saturates and remains constant at 522 nm. The shape analysis also agrees with the peak position analysis that the shape stops changing as the brush thickness reaches to 10 nm. The peak height, area under curve (AUC), and full width half maximum (FWHM) are analyzed in Figure 8.4c. Similar to the change in peak position, initially the shape parameters increase linearly with the grafting thickness, and when the saturation is reached (thickness = 10 nm), the shape parameters stop changing.

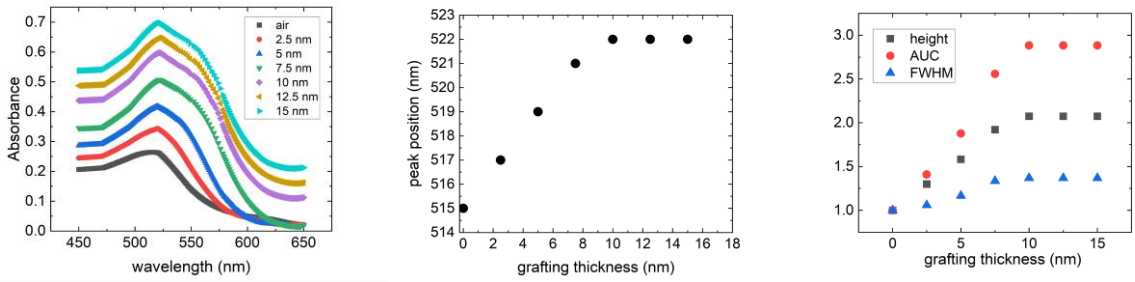

Figure 8.4. a. DDA simulation results of absorbance spectra at different grafting thickness. b. Absorbance peak position as grafting thickness from 0 to 15 nm. c. analysis of height, area under curve (AUC) and full width half maximum (FWHM) at different grafting thickness.

The DDA simulation further confirms the UV-Vis observation that SH-PEO are successfully grafted onto the NPG ligaments. As a result, the 2D gold wafer measurements could be

extrapolated onto the 3D NPG system. Thus, SH-PEO grafted NPG possess a grafting density of ~ 0.13 chains/nm^2, while the grafting thickness is 10.5 nm.

This previous section presents the successful fabrication and characterization of SH-PEO grafted NPG. The grafting density is found to be 0.13 chains/nm^2, and the grafting thickness is 10.5 nm. The grafting also found to decrease the water contact angle from 64° to 46°. In the following section 8.2.2, the future research directions of the polymer grafted NPG will be discussed in more detail.

8.2.2 Polymer grafted NPG Future Research Directions

Polymer grafts inside NPG decrease the NPG R_p, which could allow more research of highly confined polymers inside nanochannels. For instance, the graft height is measured to be 12.9 nm, so the effective radius (R_{eff}) of the NPG decreases accordingly such that $R_{eff} = R_p$ - graft height. As in the 8.2.1 section, NPG R_p = 27.5 nm, so the R_{eff} = 17.0 nm. According to the modified LWE in Chapter 2, the decrease in radius will induce a significant increase in viscosity. Simultaneously, the SH-PEO graft induces a change in interfacial energy between the infiltrating polymer and the wall. Different polymer (block copolymer, homopolymer) infiltration kinetics would be an interesting future direction to research to better understand the confinement effect and the interfacial energy effect.

Polymer grafted NPG could also be used to investigate the effect of entanglement on infiltration. When PEO graft on NPG is exposed to air, the graft resides as a mushroom shape. However, if the PEO graft is exposed to good solvent such as water or ethanol, the graft will become more linear and elongated. Thus, by utilizing solvent vapor annealing to infiltrate

polymers, the effect of entanglement on kinetics and mechanical strength can be further investigated.

8.3 Polymer interlock/loop modified NPG

Polymers can also be grafted onto NPG as individual loops or interlocked loops. For instance, instead of a mono-thiol terminated PEO chain, a di-thiol terminated PEO chain could be covalently bound to Au surface on both ends, resulting in loops of unknown radius. The PEO loop grafted NPG can be then used to investigate the polymer kinetics. After the PING is fabricated, the polymer stability and degradation, as well as mechanical properties, could be further investigated and compared to the bulk. The PEO loop allows future investigation of entanglement effects on kinetics and pathways to enhance polymer stability and strength. By interconnecting the individual loops, loop interlocks on the NPG ligament could be formed. The interlock polymers with different sizes inside the NPG can be used as a trapping net which could facilitate practical applications such as water/molecule filtration.

8.4 Summary

Based on the research findings from Chapter 4 - 7, multiple interesting aspects are proposed in this Chapter, including using polymer grafted NPG as the starting membrane template and fabricating individual or interconnected loops inside the NPG. There are other aspects that worth more research, such as the mechanical properties of PING and ion

conductivity of PING with different counterion concentrations. The promising properties of PING calls for further research.

8.5 References

1. Podsiadlo, P. *et al.* Ultrastrong and Stiff Layered Polymer Nanocomposites. *Science* **318**, 80–83 (2007).

2. Hore, M. J. A. & Composto, R. J. Nanorod Self-Assembly for Tuning Optical Absorption. *ACS Nano* **4**, 6941–6949 (2010).

3. Hore, M. J. A., Frischknecht, A. L. & Composto, R. J. Nanorod Assemblies in Polymer Films and Their Dispersion-Dependent Optical Properties. *ACS Macro Lett.* **1**, 115–121 (2012).

4. Maguire, S. M. *et al.* Effect of Nanoscale Confinement on Polymer-Infiltrated Scaffold Metal Composites. *ACS Appl. Mater. Interfaces* **13**, 44893–44903 (2021).

5. Xue, Y., Li, X., Li, H. & Zhang, W. Quantifying thiol–gold interactions towards the efficient strength control. *Nat. Commun.* **5**, 4348 (2014).

6. Bürgi, T. Properties of the gold–sulphur interface: from self-assembled monolayers to clusters. *Nanoscale* **7**, 15553–15567 (2015).

7. Chaki, N. K. & Vijayamohanan, K. Self-assembled monolayers as a tunable platform for biosensor applications. *Biosens. Bioelectron.* **17**, 1–12 (2002).

8. Heimel, G., Romaner, L., Zojer, E. & Bredas, J.-L. The Interface Energetics of Self-Assembled Monolayers on Metals. *Acc. Chem. Res.* **41**, 721–729 (2008).

9. Xia, Y. & Whitesides, G. M. SOFT LITHOGRAPHY. *Annu. Rev. Mater. Sci.* **28**, 153–184 (1998).

10. Kong, W. *et al.* Capillary filling dynamics of polymer melts in a bicontinuous nanoporous scaffold. *J. Chem. Phys.* **160**, 044904 (2024).

11. Rubinstein, M. & Colby, R. H. *Polymer Physics*. (Oxford University Press, Oxford ; New York, 2003).

Appendix A. Supplemental Information for Chapter 4

FWHM of SAXS Analysis

In the article, the d spacing of annealed NPG is directly characterized via SAXS as shown in Fig. 4.1a. However, as shown in the SEM and AFM analysis in Figure 4.1b and 4.1c, the pore size of the NPG is not constant. Indeed, the pore size is distributed among a range. In this section, we analyze the range of the NPG R_p via the Full-Width-Half-Maximum (FWHM) Approach on SAXS data. First, the measured annealed NPG data is fitted through a Gaussian function to enable the best fit. Then, the maximum intensity, where intensity = 470.66, is found at q = 0.00524 Å, corresponding to d = 148 nm. Afterwards, the half intensity point, where intensity = 235.33, is found at two q positions. From the lower end, where q = 0.00218 Å, the d_{upper} = 355 nm, implying that $R_{p,upper}$ = 89 nm. While at the higher end of q where q = 0.00829 Å, the d_{lower} = 93 nm which leads to $R_{p,lower}$ = 22.5 nm.

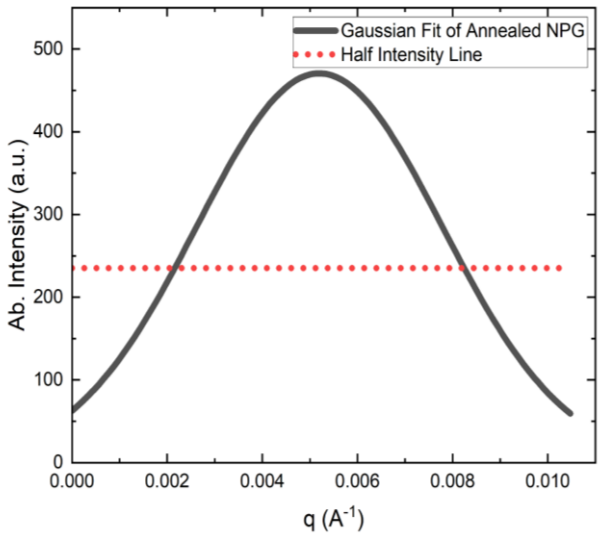

Figure A1. FWHM analysis of annealed NPG SAXS plot.

SEM Line Scans

Below in Figure A2 presents SEM line scan analysis of NPG annealed at 175℃ for 3 h. In the SAXS plot shown in Figure 4.1a, the average d-spacing for annealed NPG is 150 nm. The SEM line scan data well agrees with the SAXS analysis such that d = 146 ± 9 nm. Therefore, we further proved the accuracy of the annealed NPG d-spacing.

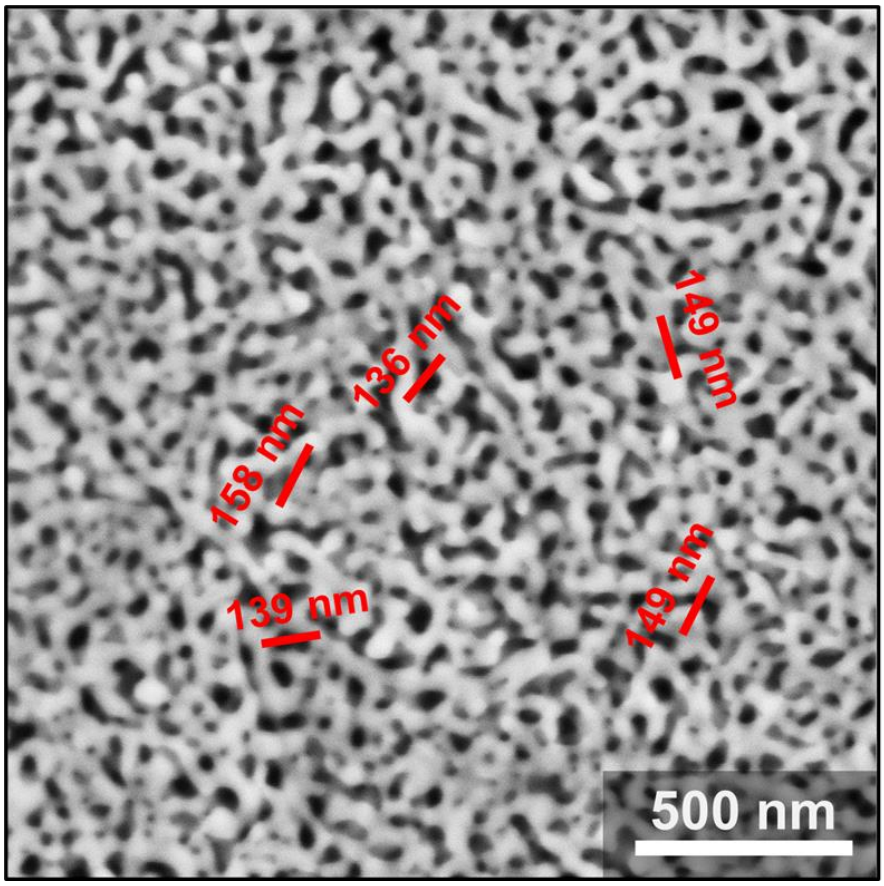

Figure A2. SEM line scans of annealed NPG

AFM 2D Correlation Graph

Fig. A3 presents the 2D correlation relationship of the annealed AFM height image in 4 directions, -45°, 0°, 45°, and 90°, as depicted in the AFM height image insert. The annealed NPG d can be calculated by measuring the average distance between the 2D correlation graph local minimums. The average d calculated from the AFM 2D correlation analysis utilizing the 4 directions mentioned above yields d = 114 ± 39 nm.

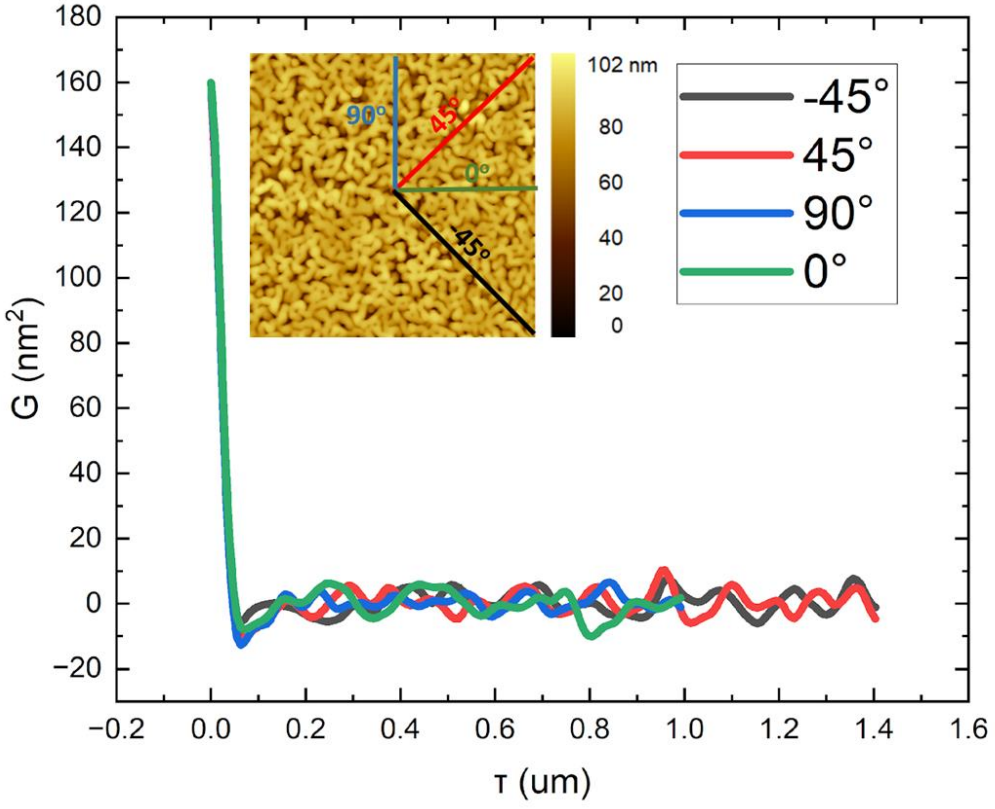

Figure A3. 2D correlation function of NPG AFM height image shown in Fig. 4.1. The x-axis represents the autocorrelation projection at certain angles. The d-spacing can be calculated by finding the peak-peak positions in the preceding graph.

Color Change of Infiltrated vs. Non-infiltrated

Below in Figure A4 it presents the color change of the composite before and after the complete infiltration. In Figure A4a, it shows the as prepared bilayer sample, in which the top NPG structure is bronze-ish gold. In part b, it shows the fully infiltrated sample, where the top most PING is more dimmer as compared to the part a. The change in the color as PING forms is also evidenced by the increase in the refraction index during the infiltration process through in situ ellipsometry measurement.

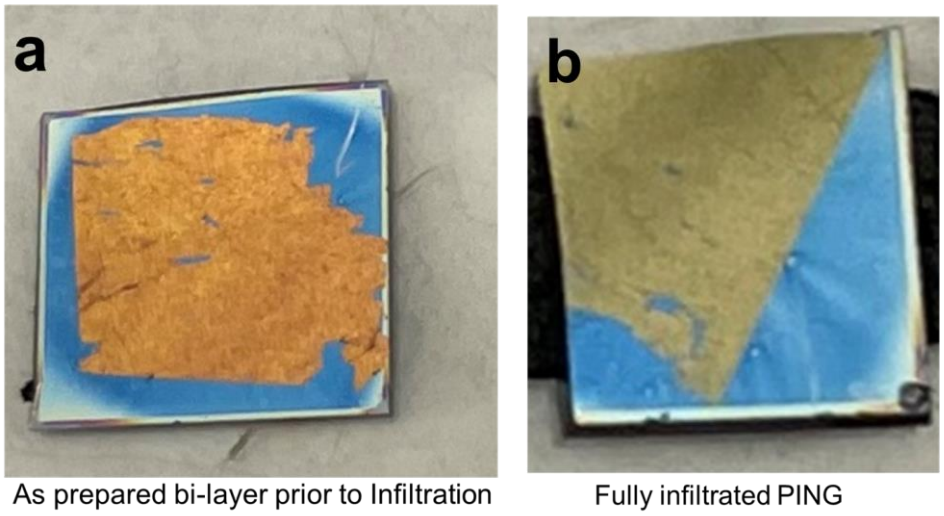

Figure A4. Color changes of PS infiltrated into NPG. a. picture of an as prepared bilayer; b. picture of fully infiltrated PING.

AFM Phase Images infiltrated vs. non-infiltrated

In the main text Figure 4.3, we have presented the AFM height images of the bilayer before annealing and the PING nanocomposite. In the Figure A5, we present the phase images of the as prepared bilayer, where NPG sits on top of PS, and the fully infiltrated PING. From those two images, we see that though the pores get filled up, after complete infiltration, there is not a top uniform wetting layer that covers the whole structure. This phenomenon also explains Figure 4.4 that the water contact angle (WCA) of the fully infiltrated PING is different from the WCA of PS thin film.

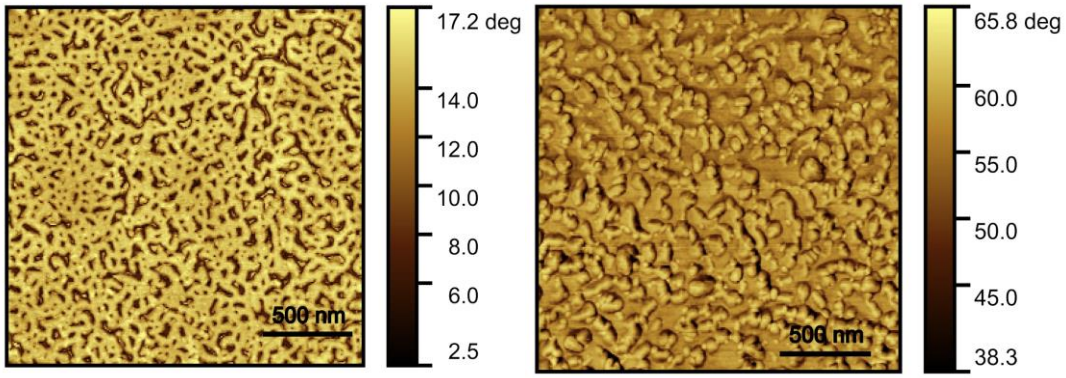

Figure A5. (left) AFM phase image of NPG atop of PS-400k; (right) AFM phase image of PS-400k fully infiltrated into NPG by annealing at 150°C for 3 h.

Dynamic Water Contact Angle on PING

Since in Figure 4.4, the final contact angle of a PING is not consistent with the contact angle of a thin PS film, we also performed dynamic water contact angle. As shown in Figure A8, the advancing contact angle (θ_{adv}) ≠ receding contact angle (θ_{rec}) ≠ static contact angle shown in Figure 4.4. The difference in the contact angle, $\Delta\theta = \theta_{adv} - \theta_{rec} = 29.6°$, is caused by hysteresis. Hysteresis effect is caused by the required activation energy for a droplet to move from a metastable phase to another metastable phase[2]. Hysteresis as visualized in Figure A6 implies that the PING surface is not perfectly smooth and the PS may not form a uniform wetting layer, which could both lead to difference in activation energy.

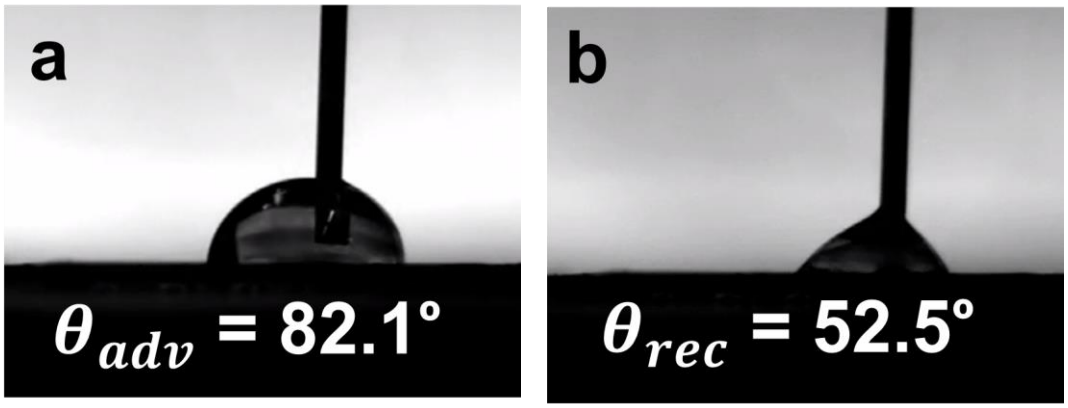

Figure A6. Dynamic water contact angle of PING. a. advancing water contact angle of PING; b. receding water contact angle of PING.

PS Bulk and Non-Equilibrium Viscosity During Infiltration Calculation

Bulk PS viscosity calculation. The bulk viscosity for entangled PS could be calculated at 150 °C using Equation A1[3–5]:

$$log\left(\frac{\eta_T}{\eta_{217}}\right) = 2.68 * 10^{16}\left(\frac{1}{T^6} - \frac{1}{490^6}\right) e^{-\frac{1330}{M}} \qquad \text{Eq. A1}$$

where in Eq. A1, η_{217} is the PS viscosity at 217 °C, T is temperature in Kelvins, and M is PS molecular weight. η_{217} for entangled PS can be calculated in Eq. A2[3–5]:

$$log\ \eta_{217} \cong 3.4\, log\, M - 13.40 \qquad \text{Eq. A2}$$

Non-equilibrium PS effective viscosity under confinement calculation. Effective viscosity (η_{eff}) could be calculated using the modified Lucas-Washburn Equation shown in Eq. 5. The total distance, h, traveled at time t could be calculated using the infiltration extent and the thickness of NPG (120 nm) measured by XS-SEM. The surface tension (γ) could be calculated by Equation A3[6,7].

$$\gamma = \gamma_\infty - \frac{k}{M^{2/3}} \qquad \text{Eq. A3}$$

Where γ_∞ is the surface tension that varies with temperature, k is a constant. From literature studies, for PS with M = 240,000 Da, γ is expressed as a function of temperature (in °C) through Eq. A4 and γ_∞ is expressed as a function of temperature shown in Eq. A5.

$$\gamma = \mathbf{34.6} - \mathbf{0.05}\,\boldsymbol{T}\ \frac{\boldsymbol{mN}}{\boldsymbol{m^2}} \qquad \text{Eq. A4}$$

$$\gamma\gamma_\infty = \mathbf{42.3} - \mathbf{0.071}\,\boldsymbol{T}\ \frac{\boldsymbol{mN}}{\boldsymbol{m^2}} \qquad \text{Eq. A5}$$

Thus, the surface tension of PS at 150 ℃ could be calculated through Eq. 3-5. Then, by substituting γ into Eq. 5 together with other parameters, we can calculate the PS effective viscosity at a certain M.

MD Simulations

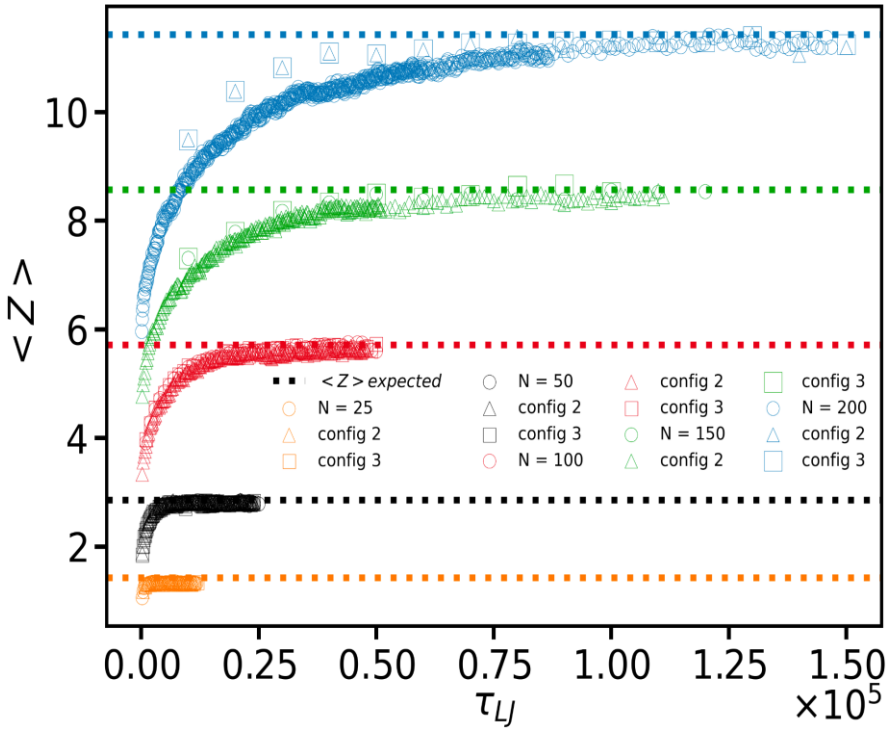

Figure A7. Entanglement statistics of polymer chains during equilibration.

The entanglement statistics during polymer equilibration for the three configurations of each polymer chain length are shown in Figure A7. The equilibrated N/N_e values are shown by the dotted lines. The number of monomers per chain are 25, 50, 100, 150, and 200, with N/N_e approximately equal to 1.5, 3.0, 6.0, 8.5, and 11.5, respectively.

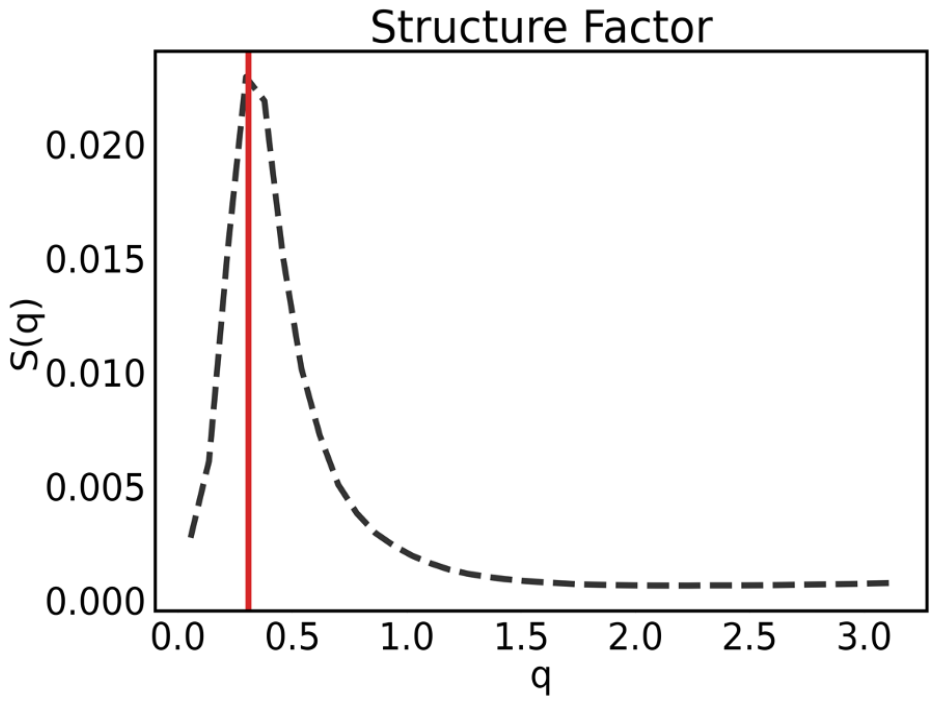

Figure A8. Structure factor of simulated nanoporous gold structure.

Figure A8 shows the structure factor of the simulated nanoporous gold structure. The red line marks $q_{max} = 0.308212$. The ligament-ligament distance d_{l-l} is calculated from the structure factor with the equation $d_{l-l} = (1.23 * 2\pi)/q_{max}$, where 1.23 is the form factor for the nanoporous gold structure. The ligament-ligament distance is defined as $d_{l-l} = 2R_{ligament} + 2R_{pore}$. Assuming equivalent values for $R_{ligament}$ and R_{pore} allows for calculation of the average pore radius via the equation $R_{pore} = d_{l-l}/4$. Using the calculated $q_{max} = 0.308212$ gives an average pore radius $R_{pore} = 6.27\sigma$.

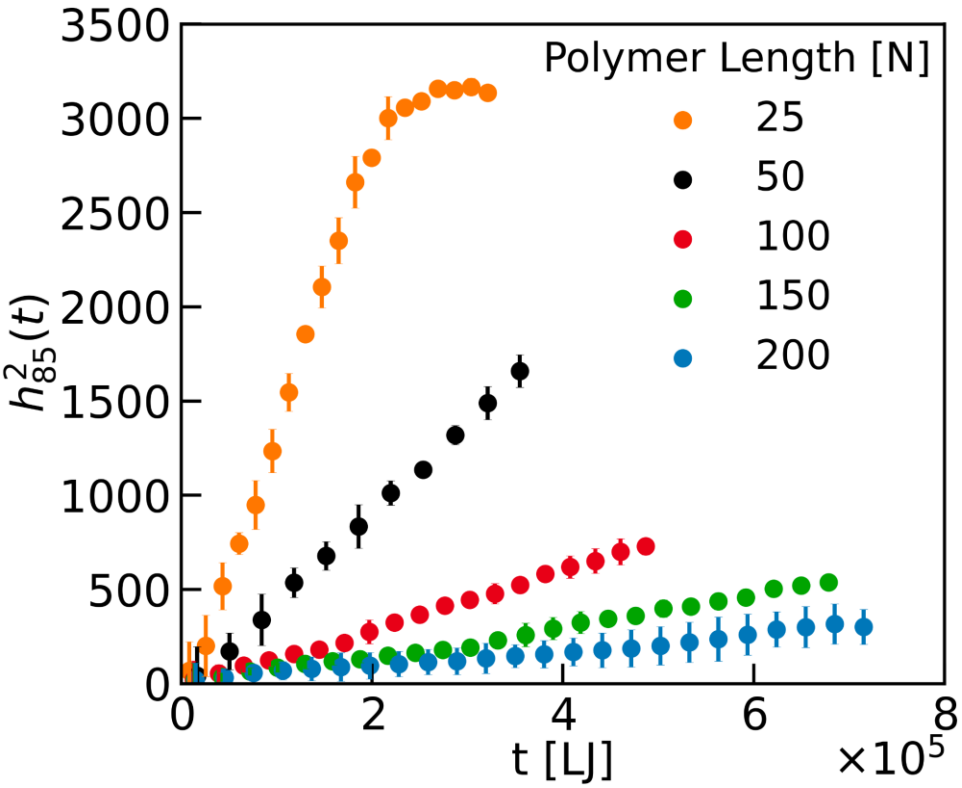

Figure A9. The square of the infiltrated polymer film height h_{85}^2 as a function of simulation time. Each color corresponds to a different polymer chain length, N, as noted in the legend. An average of triplicate runs is shown, with error bars included on the plots.

The infiltration of the bulk of the polymer is characterized via the z threshold z″, where $\int_0^{z''} \rho(z)dz = 0.85\rho_{total}$, or at which 85% of the total polymer density is contained. The difference between this height and the bottom of the nanoporous gold structure, $z'' - z_{gold}$, is referred to as $h_{85}(t)$. The change in the square of the infiltrated polymer film height as a function of simulation time is shown in Figure A9.

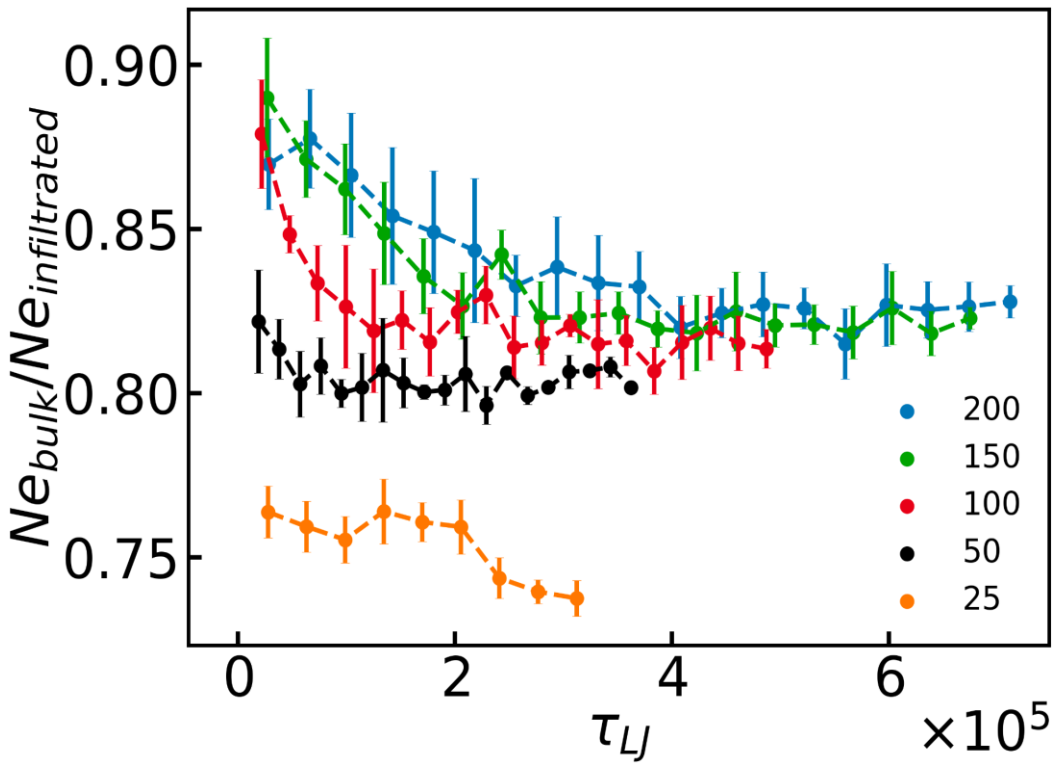

Figure A10. The ratio of bulk entanglement length versus infiltrated entanglement length , $\frac{Ne_{bulk}}{Ne_{infiltrated}}$, over the course of infiltration.

The ratio of bulk entanglement length versus infiltrated entanglement length during the course of infiltration is shown in Figure A10. The data at the final simulation point for each chain length was used to calculate $\frac{Ne_{bulk}}{Ne_{infiltrated}}$, as shown in Figure 4.9b in the main text.

References

1. Maguire, S. M. *et al.* Effect of Nanoscale Confinement on Polymer-Infiltrated Scaffold Metal Composites. *ACS Appl. Mater. Interfaces* **13**, 44893–44903 (2021).

2. Gao, L. & McCarthy, T. J. Contact Angle Hysteresis Explained. *Langmuir* **22**, 6234–6237 (2006).

3. Fox, T. G. & Flory, P. J. Viscosity—Molecular Weight and Viscosity—Temperature Relationships for Polystyrene and Polyisobutylene [1,2]. *J. Am. Chem. Soc.* **70**, 2384–2395 (1948).

4. Fox, T. G. & Flory, P. J. Second-Order Transition Temperatures and Related Properties of Polystyrene. I. Influence of Molecular Weight. *J. Appl. Phys.* **21**, 581–591 (1950).

5. Fox, T. G. & Flory, P. J. The glass temperature and related properties of polystyrene. Influence of molecular weight. *J. Polym. Sci.* **14**, 315–319 (1954).

6. Wu, S. Surface and interfacial tensions of polymer melts. II. Poly(methyl methacrylate), poly(n-butyl methacrylate), and polystyrene. *J. Phys. Chem.* **74**, 632–638 (1970).

7. Legrand, D. G. & Gaines, G. L. The molecular weight dependence of polymer surface tension. *J. Colloid Interface Sci.* **31**, 162–167 (1969).

Appendix B. Supplemental Information for Chapter 5

h^2 vs. t for the 85k and 940k p2vp

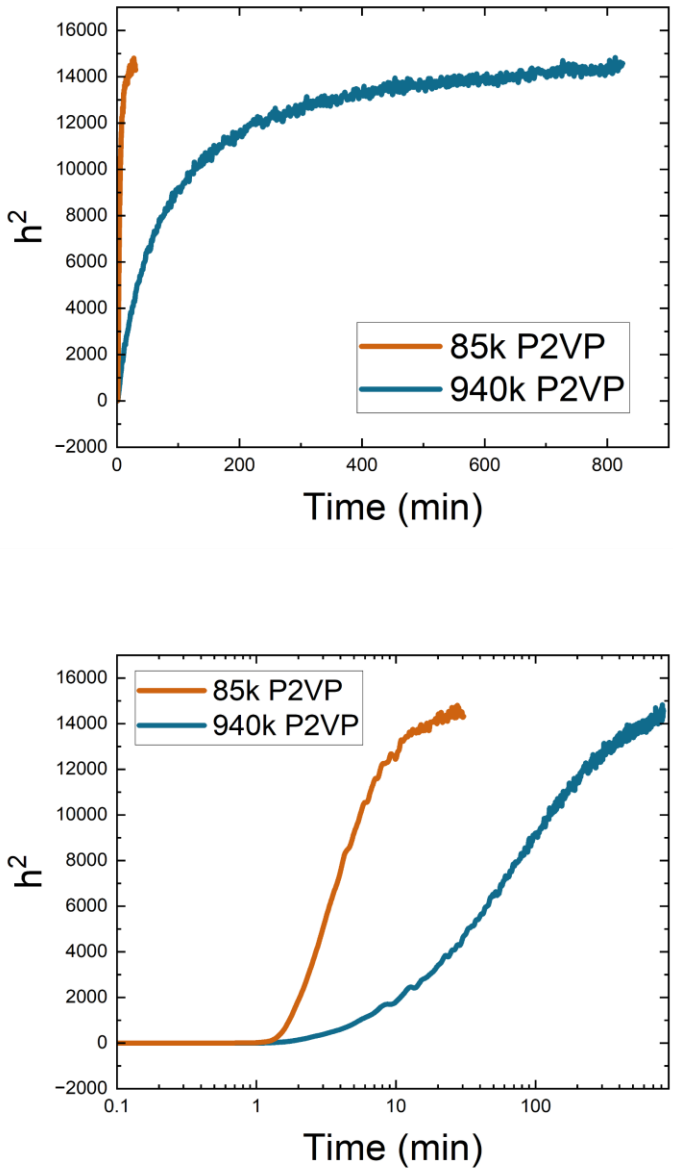

Figure B1. h^2 vs. t plot for 85k and 940k P2VP. (top) On a linear-linear plot; (bottom) On a linear-log plot. The thickness (h) of the NPG is 120 nm, thus the maximum h^2 is 14400.

PS-160k and P2VP-153k T_g Measurements

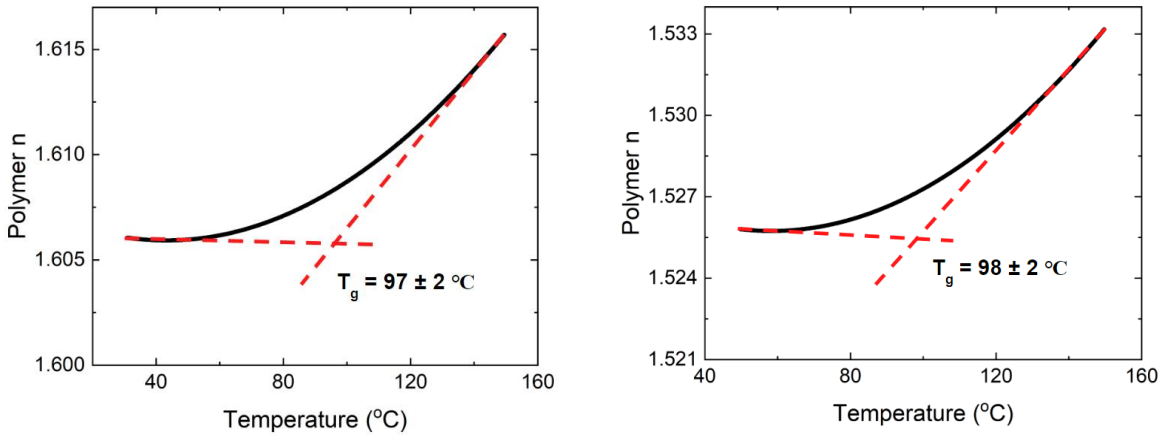

Figure B2. The polymer glass transition temperature (T_g) is measured using in-situ spectroscopic ellipsometry. (left) PS-160k refractive index as a function of temperature. The T_g is analyzed to be 97 ± 2 °C. (right) P2VP-153k refractive index as a function of temperature. The T_g is analyzed to be 98 ± 2 °C. The T_g is statistically identical between P2VP and PS.

AFM Height Images of PS/NPG Infiltrated NPG

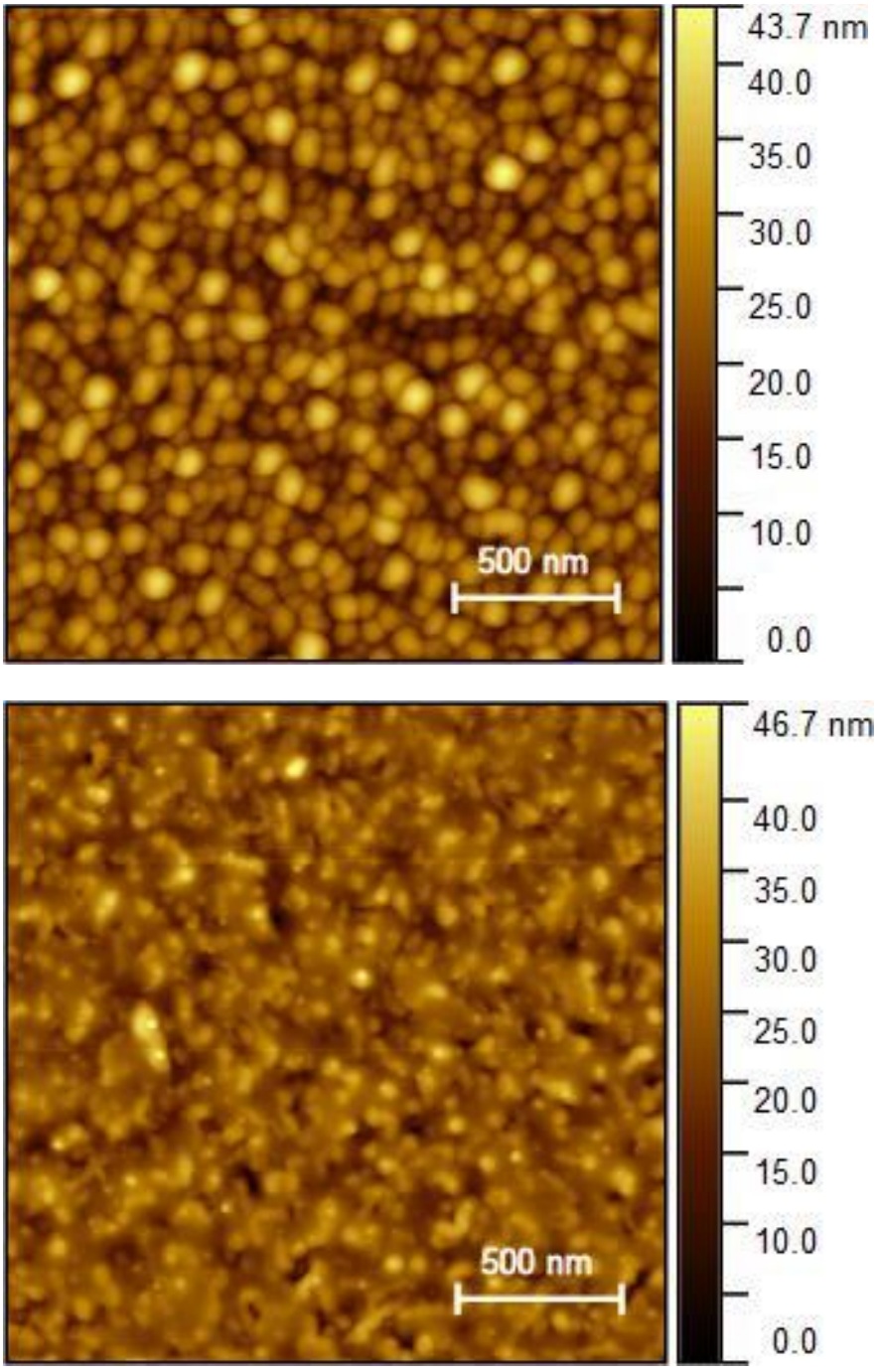

Figure B3. (top) AFM height image of P2VP-153k fully infiltrated NPG. (bottom). AFM height image of PS-168k fully infiltrated NPG. P2VP infiltrated NPG has blob structures on the surface while PS does not.

Water Contact Angle of P2VP Infiltrated NPG

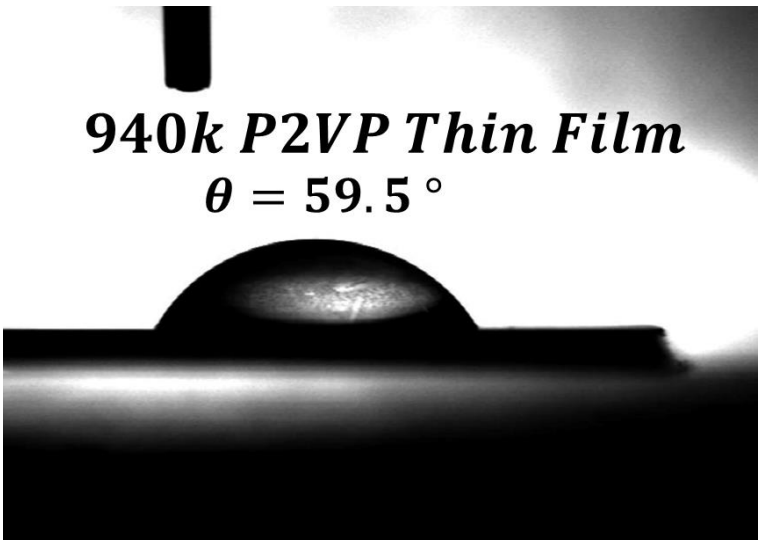

Figure B4. WCA of P2VP thin film. The water contact angle is 59.5°.

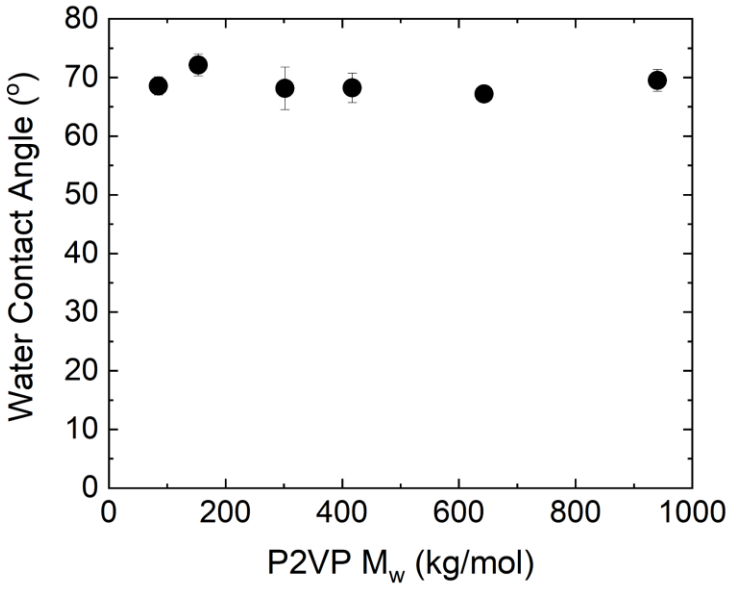

Figure B5. WCA of different M_w P2VP fully infiltrated NPG. The WCA remains relatively constant at 70° at various M_w.

Appendix C. Supplemental Information for Chapter 6

Atomic Force Microscopy and Image Analysis

Tapping mode AFM was performed using Bruker Icon AFM with non-contact tips (TAP300AL-G-50 radius of curvature < 10 nm, Ted Pella). Image analysis was performed using Gwyddion software. The images were leveled using mean field subtraction function. Background noise was removed using a 2^{nd} order polynomial background. Autocorrelation functions were performed on 1 x 1 μm^2 images with filters and background subtraction as described above.

Height Image

Figures C1-C3 show the AFM height images of the NPG composites at various stages of infiltration with various molecular weights. For as-cast NPG, the ligament structure was visible, with a constant pore diameter of around 100 nm. The as-cast composites displayed high surface roughness (~10-15 nm), whereas fully infiltrated NPG composite with P2VP displayed low surface roughness (~2-3 nm). The bi-continuous structure was also invisible in the fully infiltrated composites. Similarly, the height of the as-cast composite had a large range, whereas the fully infiltrated material had a small range for height. We interpret this phenomenon as polymer has filled all pores to the surface. The infiltration for each material involved thermal annealing at 140 °C for various times, followed by quenching on a metal plate to room temperature. Table C1 below shows the infiltration time for each P2VP molecular weight. We

note that this characterization method only probes the surface of the NPG film, and hence cannot provide information on the remainder of the composite, (e.g., if the polymer has filled half of the pore).

Table C1. P2VP Mw and their full infiltration time

Sample	100 % Infiltration Time
P2VP-79	10 min
P2VP-277	5 hours
P2VP-547	5 hours
P2VP-855	17 hours

A. B.

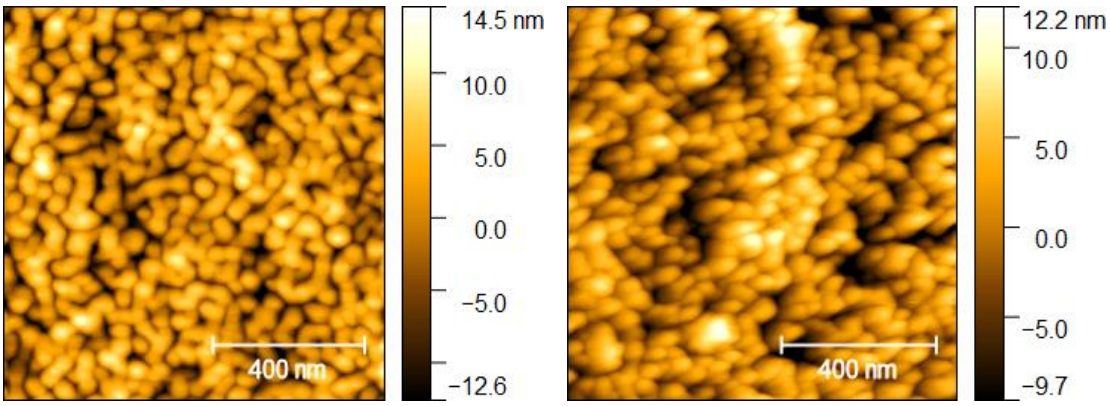

Figure C1: (A) AFM height image of as-cast P2VP-79:NPG composite. (B) Height image of fully infiltrated P2VP-79:NPG composite.

A. B.

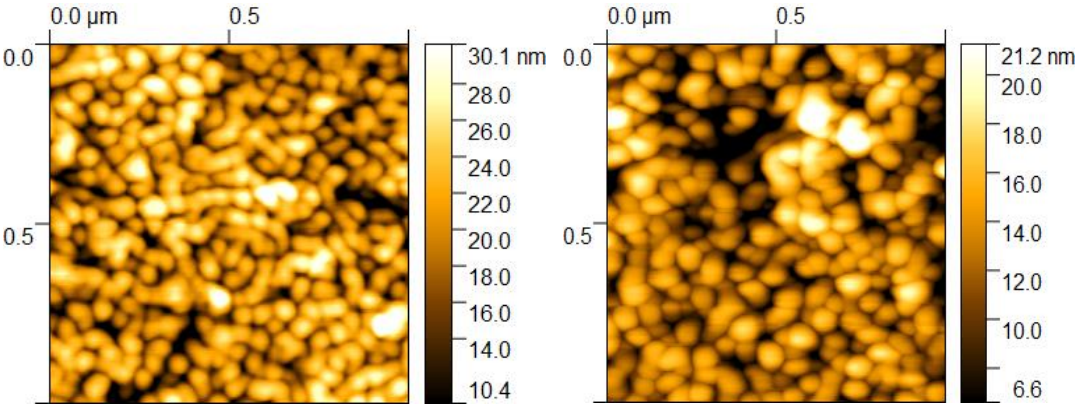

Figure C2: (A) AFM height image of as-cast P2VP-277:NPG composite. (B) Height image of fully infiltrated P2VP-277:NPG composite.

A. B.

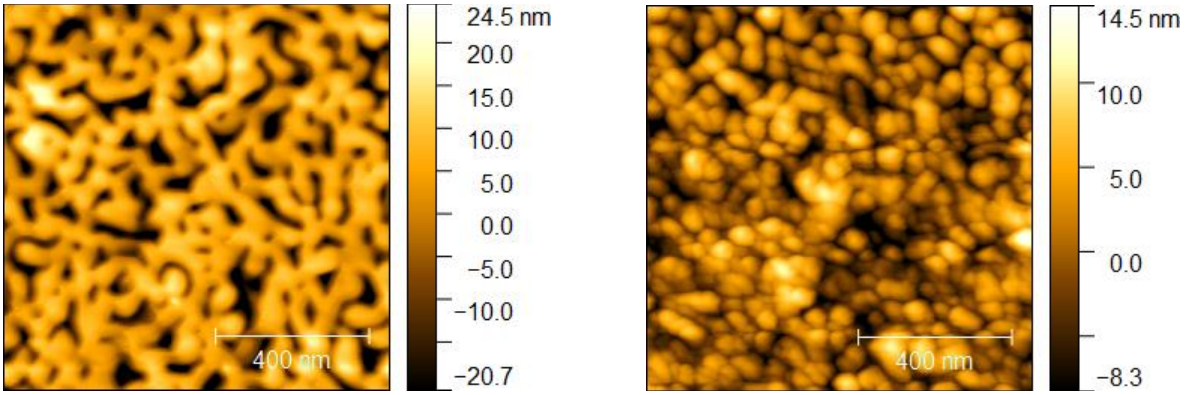

Figure C3: (A) AFM height image of as-cast P2VP-855:NPG composite. (B) Height image of fully infiltrated P2VP-855:NPG composite.

Phase Image

Figures C4-C7 show the AFM phase images of the NPG composites at various stages of infiltration with various molecular weights. For as-cast NPG, the ligament explored a high difference in degrees, indicating a significant phase lag from tapping hard materials. The fully infiltrated surface had lower difference in degrees, which showed that polymers have filled the pores, and potentially wets the gold surface as the tip explored smaller phase lag when tapping soft surfaces.

A. B.

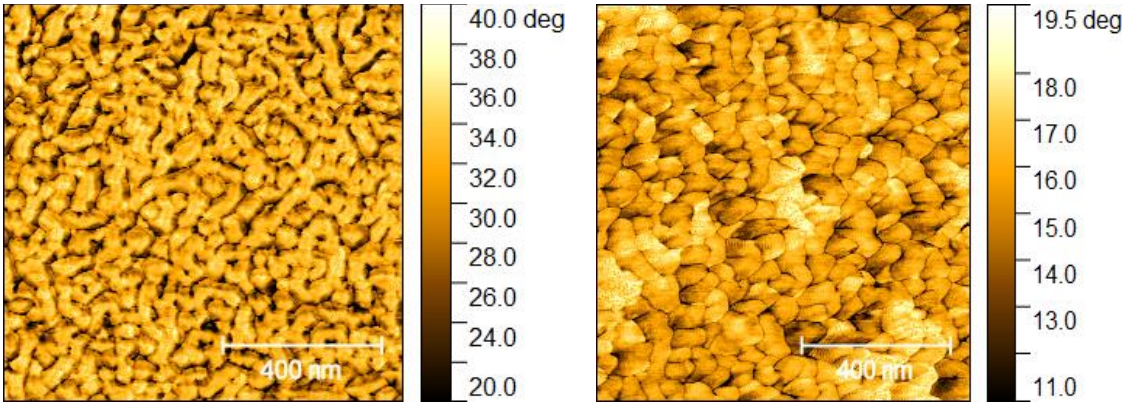

Figure C4: (A) AFM phase image of as-cast P2VP-79:NPG composite. (B) Phase image of fully infiltrated P2VP-79:NPG composite.

A. B.

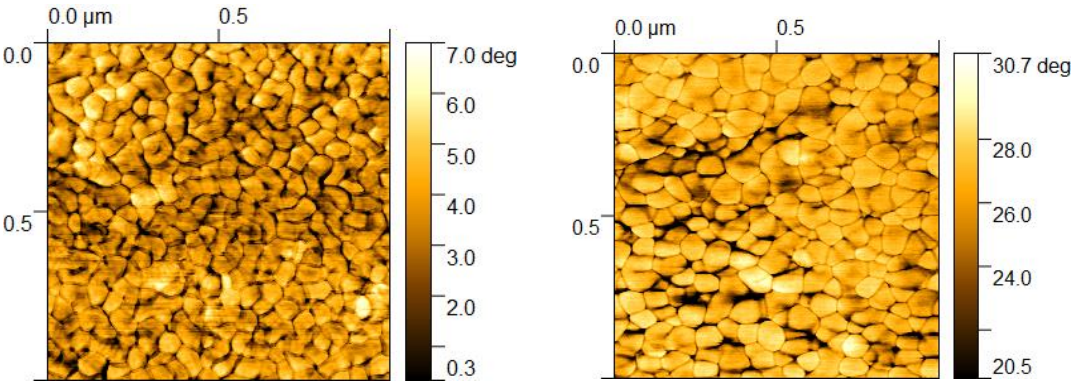

Figure C5: (A) AFM phase image of as-cast P2VP-277:NPG composite. (B) Phase image of fully infiltrated P2VP-277:NPG composite.

A. B.

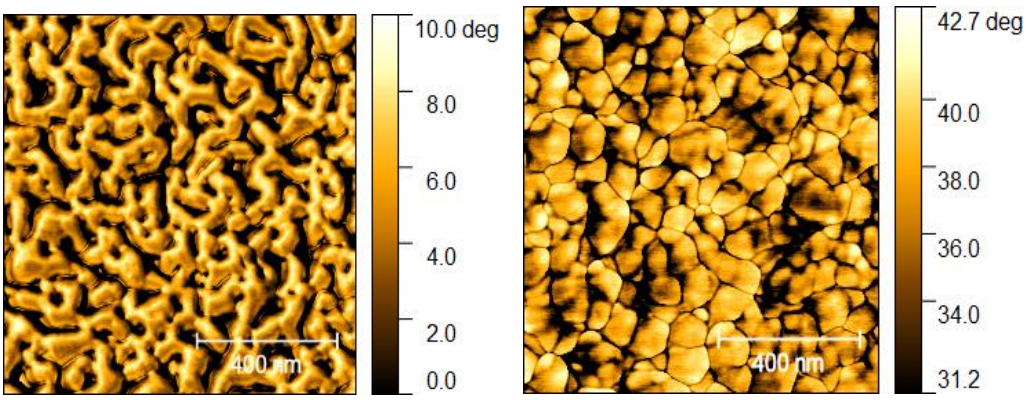

Figure C6: (A) AFM phase image of as-cast P2VP-547:NPG composite. (B) Phase image of fully infiltrated P2VP-547:NPG composite.

A. B.

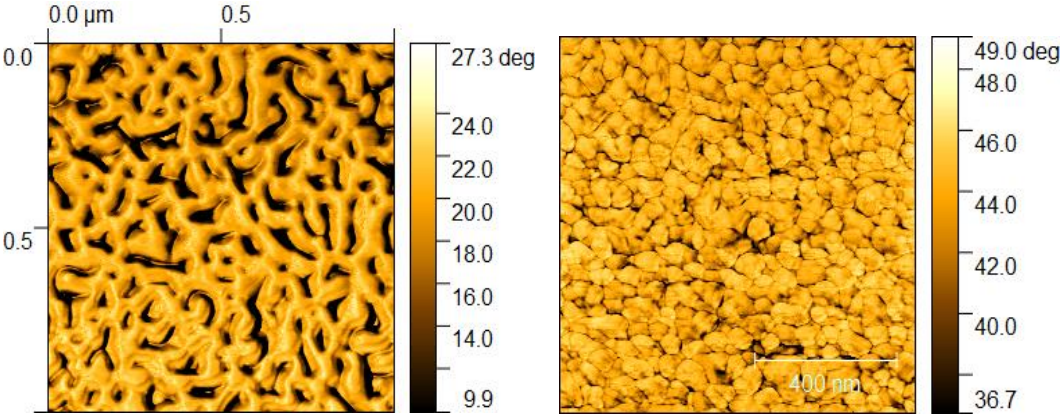

Figure C7: (A) AFM phase image of as-cast P2VP-855:NPG composite. (B) Phase image of fully infiltrated P2VP-855:NPG composite.

Surface Wetting Properties

Figure C8 shows the phase image of the water contact angle (WCA) of PS filled NPG composite and P2VP filled NPG composite. Each contact angle was an average of three measurements. As the contact angle is between gold's contact angle (65°) and PS contact angle (90°), we are certain that PS does not wet the surface yet forms a mushroom-like formation on the NPG surface. The P2VP filled composite's contact angle is similar to that of P2VP (67°). We acknowledge that since P2VP's WCA is similar to that of gold, WCA alone is not sufficient in proving the surface wetting property of P2VP. However, by combining the phase image data, we can infer this property.

A. B.

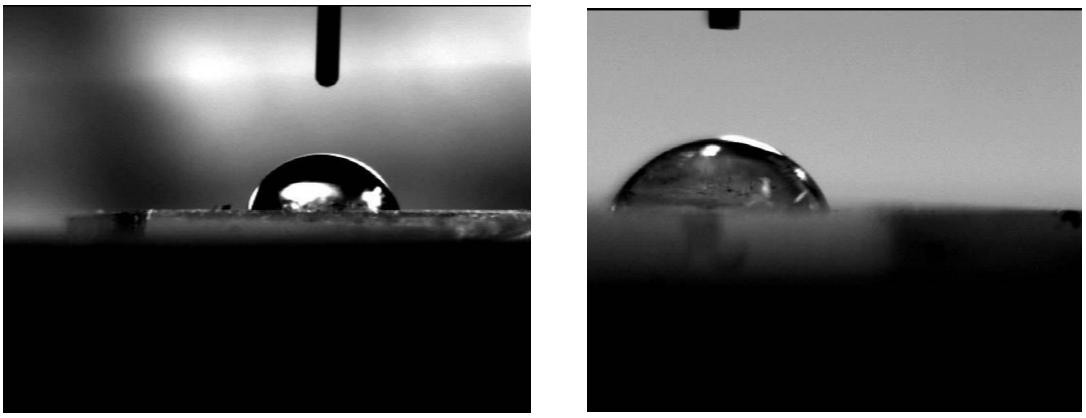

Figure C8: (A) WCA of PS filled composite, angle = 70.4 °. (B) WCA of P2VP filled composite, angle = 63.3°.

UV-Vis Measurements of Absorbance

Absorbance spectra of the glass substrate and the different polymer thin films were taken using Varian Cary Win 5000 UV-VIS-NIR Spectrophotometer with wavelengths ranging from 200-1000 nm. Figure C9 below shows the absorbance spectra of the different substrates.

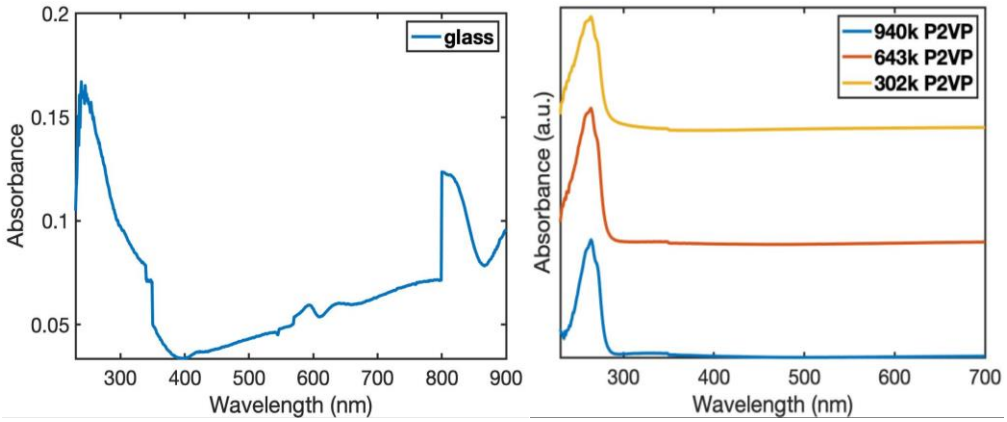

Figure C9: Absorbance spectra of the glass substrate and different P2VP thin films.

Absorbance spectra of each composite at different infiltration times were taken using Varian Cary Win 5000 UV-VIS-NIR Spectrophotometer with wavelengths ranging from 200-1000 nm. Each polymer composite's spectrum was taken from as-cast to full infiltration, with various time intervals in between. All polymer molecular weights have been used to test absorbance for 3 trials. The spectra showed a rightwards shift of the resonance peak, indicating that the refractive index of the material has changed at various stages of infiltration. We could then utilize the absorbance spectra to determine infiltration kinetics. Figure C10 below shows the absorbance spectra of different P2VP composites.

P2VP-79 P2VP-277

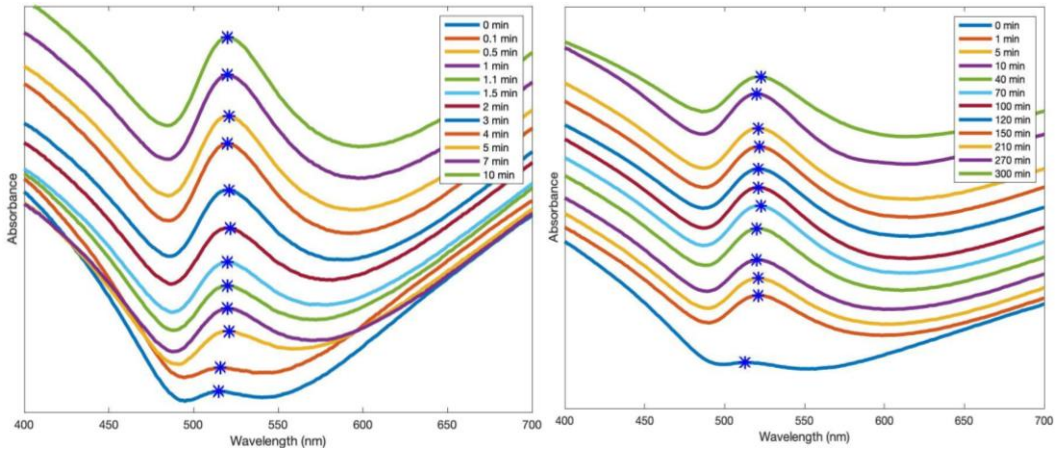

P2VP-855

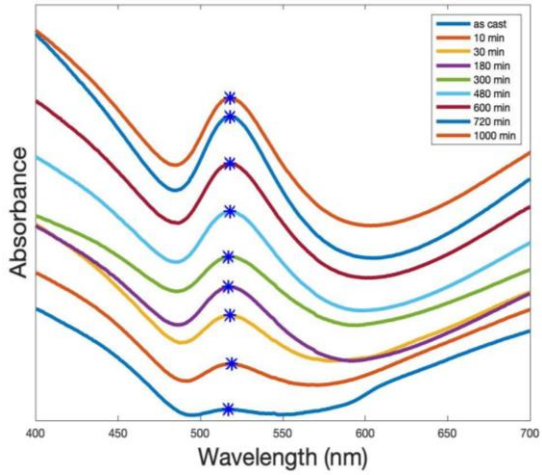

Figure C10: Absorbance spectra of different P2VP-NPG composites.

P2VP Infiltration Kinetics

It is also worth noting that as P2VP infiltrates into the pores, the absorbance increases, the peak width gets wider and therefore, the peak area gets larger. To determine infiltration kinetics, all three variables have been plotted against infiltration time, as shown in Figure C11, and the infiltration kinetics was determined using MATLAB curve fitting software. Figure C12 shows the infiltration extent vs time from all three variables. The 80% infiltration time is similar from each of the three methods (~3% difference), indicating that the usage of any variable to determine infiltration kinetics is acceptable. For best simplification, we used peak height vs time for all P2VP composites.

Peak Height

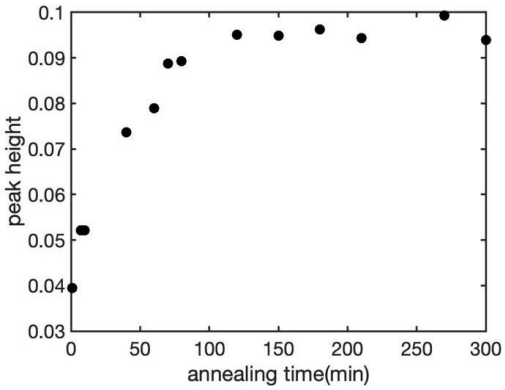

Peak Width

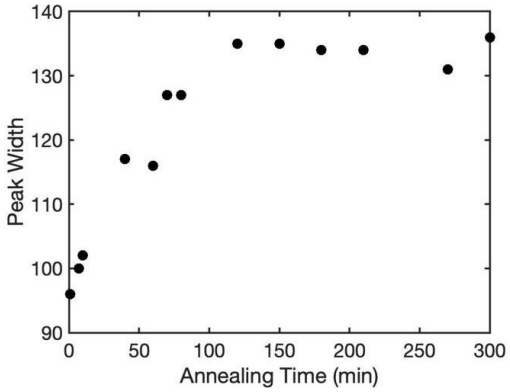

Peak Area

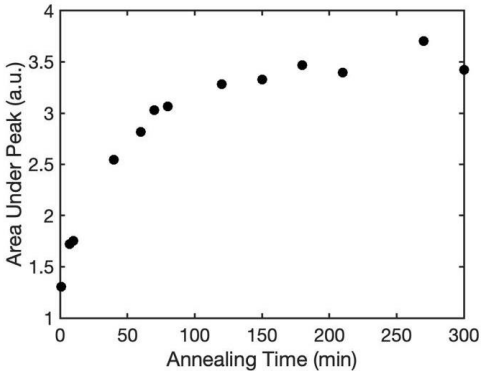

Figure C11: Peak height, width and area vs time for P2VP-547 composite.

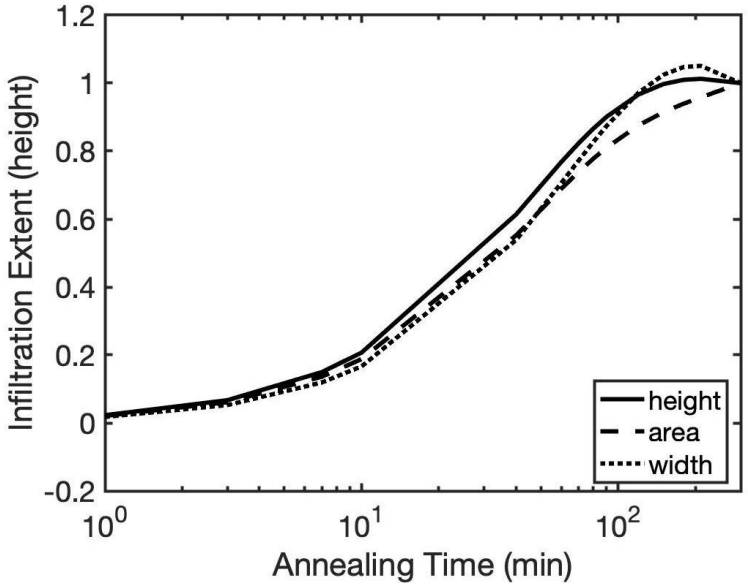

Figure C12: Infiltration extent vs annealing time of P2VP-547 composite.

DDA: Au Rod Absorbance Spectra in air, water, and P2VP

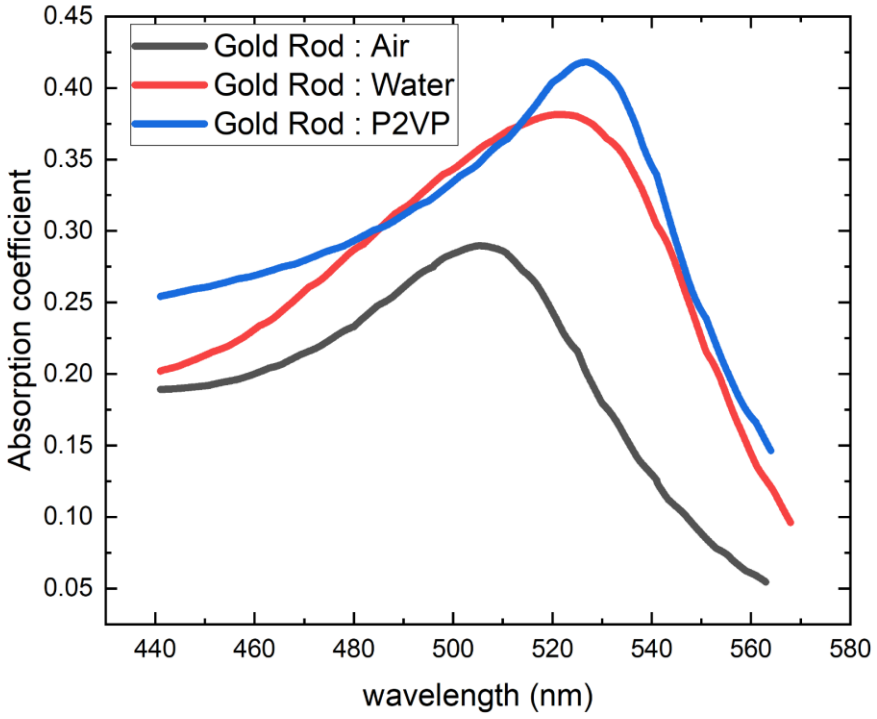

Figure C13. Gold Rod absorbance behavior in air, water and P2VP respectively.

DDA: Analysis on three different surrounding mediums

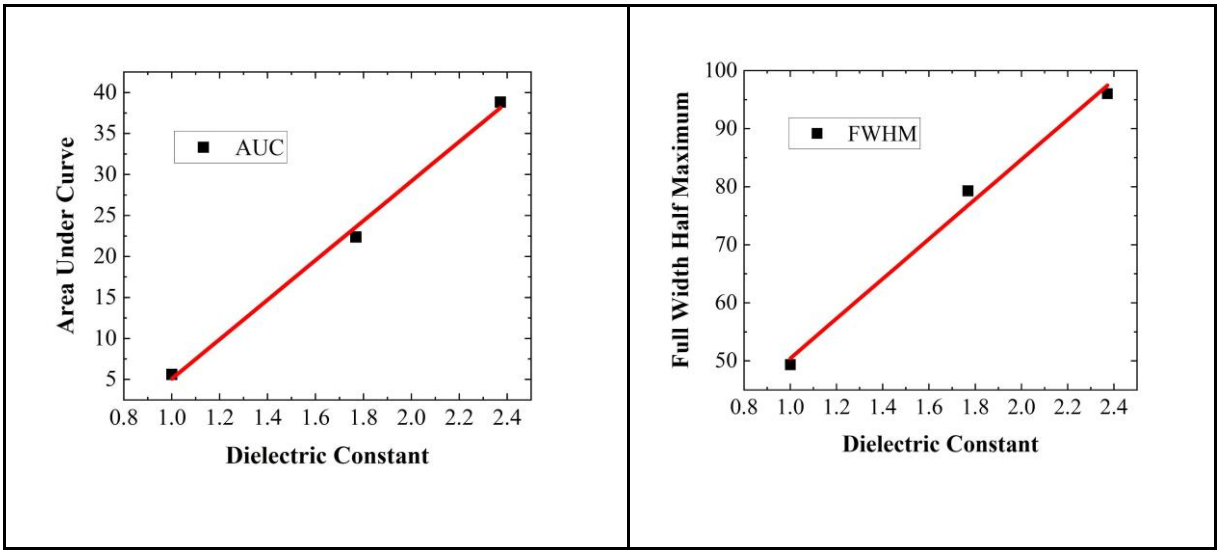

Figure C14. Relationships between (a) Area Under Curve (AUC) and (b) Full Width Half Maximum (FWHM) with dielectric constant, as the medium changes from air (n=1), water (n=1.33), to P2VP (n=1.54). Linear fitting with Pearson's r equal to (a) 0.99791, (b) 0.99573, and R-square(COD) equal to (a) 0.99582, (b) 0.99147.

DDA: Relationship of Infiltration Extent on Area Under Curve and Full Width Half Maximum

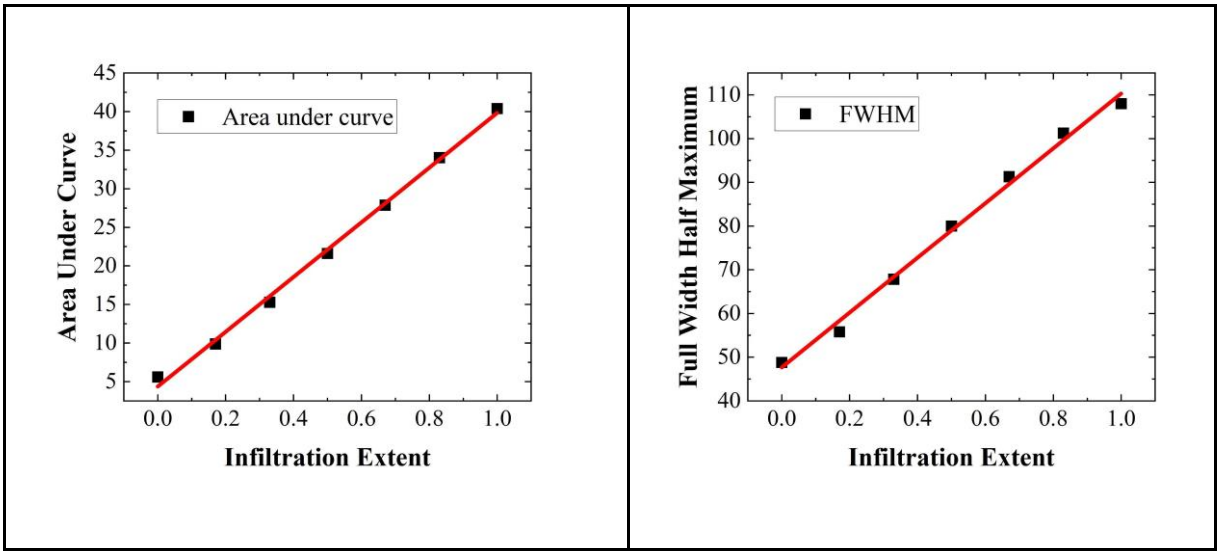

Figure C15. Area under curve and Full Width Half Maximum of NPG with different P2VP infiltration extents from DDA simulation. Linear fitting with Pearson's r equal to (a) 0.99843, (b) 0.9968, and R-square (COD) equal to (a) 0.99686, (b) 0.99361.

DDA: Calculated IE vs. IE for Area Under Curve and Full Width Half Maximum Analysis

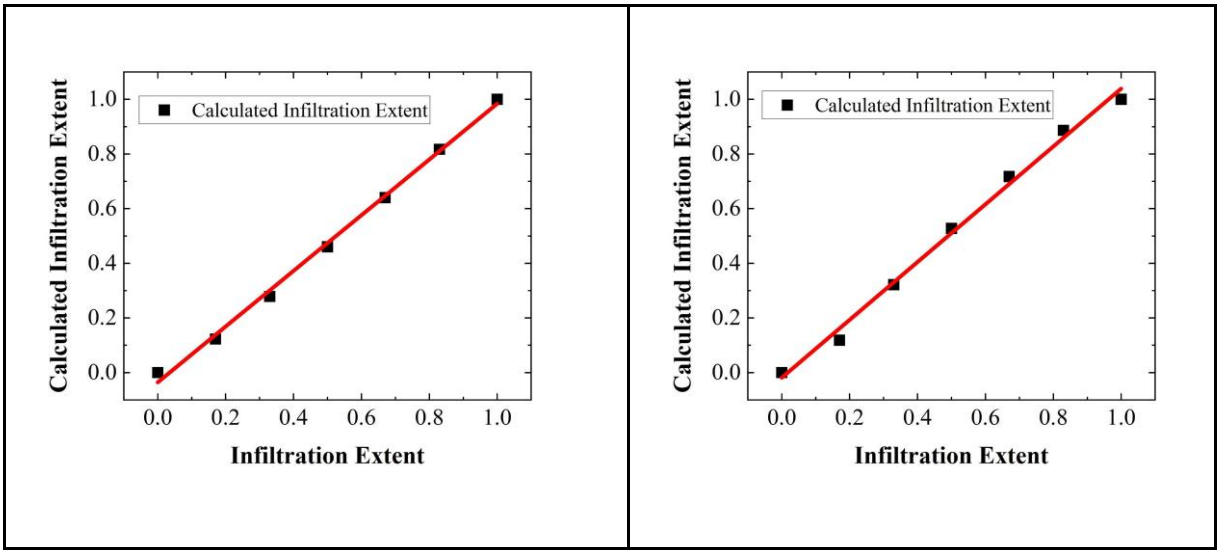

Figure C16. Plot of calculated infiltration extent from (a) area under curve and (b) full width half maximum vs. pre-defined infiltration extent. Slope of the linear fitting equal to (a) 1.01929, (b) 1.05831, with standard error of (a) 0.02558, (b) 0.03794

Reference

1. Purcell, E. M. & Pennypacker, C. R. Scattering and Absorption of Light by Nonspherical Dielectric Grains. *Astrophys. J.* **186**, 705 (1973).

2. Draine, B. T. & Flatau, P. J. Discrete-Dipole Approximation For Scattering Calculations. *J. Opt. Soc. Am. A* **11**, 1491 (1994).

3. Romann, J., Wei, J. & Pileni, M.-P. Computational Matching of Surface Plasmon Resonance: Interactions between Silver Nanoparticles and Ligands. *J. Phys. Chem. C* **119**, 11094–11099 (2015).

4. Johnson, P. B. & Christy, R. W. Optical Constants of the Noble Metals. *Phys. Rev. B* **6**, 4370–4379 (1972).

5. Genzel, L., Martin, T. P. & Kreibig, U. Dielectric function and plasma resonances of small metal particles. *Z. F*[illegible]*r Phys. B Condens. Matter Quanta* **21**, 339–346 (1975).

6. Ashcroft, N. W., Mermin, N. D. & Smoluchowski, R. *Solid State Physics*. *Phys. Today* **30**, 61–65 (1977).

7. El-Haija, A. J. A. Effective medium approximation for the effective optical constants of a bilayer and a multilayer structure based on the characteristic matrix technique. *J. Appl. Phys.* **93**, 2590–2594 (2003).